



HAL
open science

Design of synthetic diffractive structures for 3D visualization applications and their fabrication by a novel parallel-write two-photon polymerization process

Qiang Song

► **To cite this version:**

Qiang Song. Design of synthetic diffractive structures for 3D visualization applications and their fabrication by a novel parallel-write two-photon polymerization process. Optics / Photonics. Ecole nationale supérieure Mines-Télécom Atlantique, 2020. English. NNT : 2020IMTA0199 . tel-02945442

HAL Id: tel-02945442

<https://theses.hal.science/tel-02945442>

Submitted on 28 Sep 2020

HAL is a multi-disciplinary open access archive for the deposit and dissemination of scientific research documents, whether they are published or not. The documents may come from teaching and research institutions in France or abroad, or from public or private research centers.

L'archive ouverte pluridisciplinaire **HAL**, est destinée au dépôt et à la diffusion de documents scientifiques de niveau recherche, publiés ou non, émanant des établissements d'enseignement et de recherche français ou étrangers, des laboratoires publics ou privés.

THESE DE DOCTORAT DE

L'ÉCOLE NATIONALE SUPERIEURE MINES-TELECOM ATLANTIQUE
BRETAGNE PAYS DE LA LOIRE - IMT ATLANTIQUE

ÉCOLE DOCTORALE N° 596

Matière Molécules et Matériaux

Spécialité : Photonique

Par

QIANG SONG

Design of synthetic diffractive structures for 3D visualization applications and their fabrication by a novel parallel-write two-photon polymerization process

Thèse présentée et soutenue à IMT Atlantique (Brest), le 10 septembre 2020

Unité de recherche : Département optique

Thèse N°: 2020IMTA0199

Rapporteurs avant soutenance :

Pierre Ambs, Professor, Haute-Alsace University

Jana B. Nieder, Group Leader at INL-International Iberian Nanotechnology Laboratory, Portugal

Composition du Jury :

Président : Jean-Louis De Bougrenet, Professor, IMT Atlantique

Examineurs : Pierre Ambs, Professor, Haute-Alsace University

Jana B. Nieder, Group Leader at INL-International Iberian Nanotechnology Laboratory, Portugal

Frank Wyrowski, Professor, Friedrich Schiller University Jena, Germany

Directeur de thèse : Kevin Heggarty, Professor, IMT Atlantique

Contents

Contents	I
List of Figures	IV
Acknowledgement	i
Résumé.....	ii
Abstract.....	xii
Chapter 1 General Introduction	1
1.1 Diffractive optical elements	1
1.2 Thesis problematic	2
1.3 Thesis objectives	3
1.4 Organization of the thesis	4
1.5 Thesis contributions	4
1.6 List of Publications	5
Chapter 2 Diffractive optical elements	7
2.1 Main DOE types classifications	7
2.2 General introduction for DOE	10
2.3 DOE models.....	11
2.3.1 Thin Element approximation	11
2.3.2 Rigorous model in the thick DOE region	13
2.4 Formulae for free-space diffraction propagation	14
2.4.1 Helmholtz equation	14
2.4.2 The Angular Spectrum Method.....	15
2.4.3 The Rayleigh-Sommerfeld diffraction formula	17
2.4.4 Paraxial approximation diffraction models.....	18
2.5 DOE design algorithms.....	20
2.5.1 Unidirectional algorithms	21
2.5.2 Direct Binary Search.....	21
2.5.3 Bidirectional algorithm	25
2.6 Review of standard DOE fabrication techniques.....	26
2.6.1 Mask based photo-lithography.....	26

2.6.2	Maskless parallel direct writing photo-lithography	28
2.6.3	Electron Beam Lithography	30
2.6.4	2PP lithography	32
2.6.5	Parallel TPP lithography	34
2.7	Practical Considerations of DOE design.....	36
2.7.1	Considerations on pixelated structure	36
2.7.2	Considerations on duplicate DOE structures	38
Chapter 3	Design of visualization DOE under LED illumination.....	41
3.1	DOE projecting a 2D pattern under divergent illumination.....	42
3.1.1	Propagation model of the divergent illumination	42
3.1.2	Algorithm.....	43
3.1.3	Design results.....	44
3.1.4	Conclusion of divergent source illuminated DOE algorithm	46
3.2	Faceted gratings method	46
3.2.1	Principle	47
3.2.2	Algorithm description	49
3.2.3	Numerical simulation.....	52
3.2.4	Discussion.....	55
3.2.5	Conclusion for DBA security holograms.....	59
3.3	2D diffractive optically variable device.....	59
3.3.1	Principle	60
3.3.2	Design and Simulation.....	62
3.3.3	Conclusion for blazed gratings based OVDs.....	63
3.4	Fresnel DOE method for 3D floating holographic ‘image’	64
3.4.1	Algorithm for 2D floating hologram.....	65
3.4.2	Principle and configuration for 3D floating “image” hologram	68
3.4.3	Design procedure and numerical simulation.....	72
3.4.4	Discussion: Validity of the 3D effect	77
3.4.5	Conclusion of the FDOE method.....	79
3.5	3D image DOEs by Frequency multiplexing method.....	80
3.5.1	Design principle	80
3.5.2	Summary of the Frequency multiplexing method	82
Chapter 4	Modeling and optimizing optically thick DOEs	85
4.1	Introduction.....	85
4.2	Kogelnik theory	86
4.3	Rigorous theory for thick structure design.....	92
4.4	Algorithm and design results	96
4.5	Conclusion	104
Chapter 5	DOE fabrication and experimental analysis	105
5.1	Introduction.....	105
5.1.1	IMT Atlantique DOE fabrication and characterization facilities... ..	105
5.2	Experimental verification of the projection type 2D security holograms	

illuminated by a divergent light source.....	108
5.2.1 DOE sample test with divergent light illumination	108
5.2.2 Fabrication and experimental verification of the faceted grating array DOE	110
5.2.3 Fabrication and experimental verification of a 2D optically variable device	112
5.3 Experimental verification of the “floating 3D image” DOE	115
5.3.1 Experimental verification for faceted Fresnel DOEs.....	115
5.3.2 Experimental verification of Frequency multiplexing DOE design method	119
5.4 Conclusion	121
Chapter 6 Contributions to DOE fabrication facilities at IMT-A	123
6.1 Illumination system design for the current parallel direct write photoplotter 	124
6.2 Illumination system design for a new hybrid parallel write lithography machine	128
6.3 Illumination optical system design for the 2PP Photoplotter.....	136
6.3.1 The basic principle of 2PP	136
6.3.2 The experimental parallel 2PP photoplotter.....	139
6.4 Conclusion	145
Chapter 7 General Conclusion and Perspectives	147
Appendix.....	151
Bibliography	153

List of Figures

Figure 1-1- (a) Surface relief structure of a DOE. (b) Diffraction configuration of a DOE beam shaper.....	1
Figure 2-1- (a) Schematic of transmissive type ADOE. (b) Schematic of reflection type ADOE. (c) Schematic of transmissive type PDOE. (d) Schematic of reflection type PDOE.....	8
Figure 2-2- Configurations of the diffraction propagation of a DOE.	8
Figure 2-3- Alternative configuration of the Fourier type DOE beam shaper.	9
Figure 2-4- Typical Fourier type DOE and Fresnel type DOE(Gray level represents local phase).	9
Figure 2-5- Schematic of 2D DOE design. To solve the optimization problem, the propagation region is divided into two diffraction regions, where U_{inc} and U_{out} are the electric and magnetic field.	10
Figure 2-6- Structure of the M-level DOE. U_{inc} is the illuminating light, and U_l is the diffraction field after the DOE.	12
Figure 2-7- Geometry schematic of a binary phase grating diffraction.	13
Figure 2-8- The definition of the signal window of the output plane.	21
Figure 2-9- The flow chart of a basic DBS algorithm for DOE design.	22
Figure 2-10- Global optimization for converging to the global optimum.	22
Figure 2-11- The basic principle of particle swarm optimization.....	23
Figure 2-12- The general flow chart of PSO. The Pbest means the individual optimal solution in current iteration, and the Gbest is the global optimal solution.....	23
Figure 2-13- The principle flowchart of a general GA method. Here, $x_i(i=1,2,\dots,n)$ means one possible DOE solution.	24
Figure 2-14- Flowchart of IFTA based bidirectional method.	25
Figure 2-15- Basic lithography process of DOE fabrication using contact lithography.	26
Figure 2-16- Basic process for multi-level DOE fabrication.	27
Figure 2-17- The sketch of the projection photo-lithography process.	28
Figure 2-18- (a) the basic process of maskless photo-lithography.(b) Principle of maskless photo-lithography machine in IMT-Atlantique.	29
Figure 2-19- 3D plot of the DOE samples. (a) Fresnel Lens. (b) Blazed gratings. (c) Binary DOE.	30
Figure 2-20- (a) Basic process of EBL. (b) The principle of the EBL.....	31
Figure 2-21- The schematic of single beam TPP lithography system.....	32
Figure 2-22- The sketch of the parallel TPP lithography system	34

Figure 2-23- 3D blazed grating recently fabricated by parallel TPP process in the IMT-A cleanroom.....	35
Figure 2-24- The 2PP lithographic system with use of a PSLM [91].	35
Figure 2-25- (a) Target mask.(b) image pattern on photoresist base on lithography simulation.....	36
Figure 2-26- Output diffraction pattern for a DOE beam shaper with different pixel pitch. The pixel size reduces gradually from (a)-(c), while the their corresponded are shown in (b)-(d).	37
Figure 2-27- (a) DOE phase with isolated pixel.(b) DOE phase without isolated pixel.....	38
Figure 2-28- Variation pf output pattern (d, e, f) with the number of DOE periods illuminated by the incoming beam (a, b, c). Illumination of only one period leads to speckles on the output pattern.	38
Figure 3-1 Schematic of the divergent light shaping.	42
Figure 3-2- Flowchart of the proposed optimization method.	43
Figure 3-3- Convergence curve of proposed algorithm and standard IFTA.	45
Figure 3-4- Design result for the divergent source illuminated DOE algorithm. (a) The designed phase distribution. (b) The reconstructed pattern.	45
Figure 3-5- The schematic of the DBA principle for producing arbitrary patterns.	47
Figure 3-6- Schematic of the spherical wave decomposition.	48
Figure 3-7- Arrangement of vector k_{in} and k_{out}	49
Figure 3-8- Flowchart of the first part of DBA design algorithm.	50
Figure 3-9- Schematic of the diffraction angle optimization. The solid lines are the rays before exchange, and the dotted lines are the optimal rays after exchange.	52
Figure 3-10- The target image for DBA design.	53
Figure 3-11- Maximum deflection angle against the cumulated number of exchanges.....	53
Figure 3-12- Optical path in VirtualLab Fusion TM	54
Figure 3-13- Reconstructed result in VirtualLab Fusion TM software.	55
Figure 3-14- The calculated first order diffraction efficiency as a function of blazed grating period obtained by RCWA.	56
Figure 3-15- Blazed grating diffraction efficiency against the incident angle and groove depth.....	56
Figure 3-16- Configuration of the blazed grating. (a) continuous grating profile. (b) Multilayer profile used in RCWA simulations.....	57
Figure 3-17- spectrum of the used LED.....	58
Figure 3-18- the calculated first order diffraction efficiency as a function of incident wavelength obtained by RCWA.....	58
Figure 3-19- The configuration schematic of observing a transmissive OVD. ...	60
Figure 3-20- The configuration schematic for observing a reflective OVD.....	61

Figure 3-21-Diffraction patterns of different gratings.	62
Figure 3-22-Target image for OVD.	62
Figure 3-23-the designed OVD.....	63
Figure 3-24-Simulation results of the designed OVD. (a) Reconstructed result with rotation angle 6 degrees. (b) Reconstructed result with rotation angle -6 degrees.	63
Figure 3-25-The principle of producing a virtual object.(a) Fourier type hologram. (b) Fresnel type hologram.	64
Figure 3-26- Photograph of a Fresnel type transmissive DOE illuminated from behind by red divergent LED source.	65
Figure 3-27-The flowchart of the modified GSA in Fresnel domain.....	66
Figure 3-28-The configuration of the off-axis Fresnel DOE design.....	67
Figure 3-29-Fresnel hologram. (a) On-axis target; (b) Off-axis target; (c) On-axis Fresnel hologram; (d)Off-axis Fresnel hologram.	68
Figure 3-30-The configuration of the LED source and observer.	69
Figure 3-31-Principle of proposed FDOE calculation process.	70
Figure 3-32-Flowchart of the proposed iterative optimization process of FDOE. See text for a detailed description.	72
Figure 3-33-The definition of signal area in the diffracted image plane.	73
Figure 3-34-Target image for testing the algorithm’s convergence behavior.	75
Figure 3-35-Curve of the reconstruction’s RMSE against the iterations.	75
Figure 3-36- A Comparison of convergence behavior between the proposed algorithm and GS algorithm.....	75
Figure 3-37-Optimal phase map and the reconstructed result.	76
Figure 3-38-Assemble of the FDOE.	77
Figure 3-39-Schematic of imaging principle, (a) LED source is on the axis, (b) LED source is off axis.....	78
Figure 3-40-Simulated reconstruction image with different LED size. (a) Reconstructed result with coherent plane wave. Reconstructed results for LED size of (b) 1mm. (c)2mm.(d) 3mm.....	79
Figure 3-41-Schematic of the spatial frequency segmentation method.....	80
Figure 3-42-The principle of the zero padding technology for target image.....	81
Figure 3-43- Simulation results. (a) the simulation result without zero padding.(b) the simulation result with the zero padding.	82
Figure 4-1-Schematic of thick hologram with white light illumination.	85
Figure 4-2- Schematic of the VBG’s diffraction.	87
Figure 4-3-Vector diagram for a volume Bragg grating. (a) Incident light at the Bragg angle. (b) Incident light deviated from the Bragg angle.	88
Figure 4-4-The diffraction efficiency against the incident wavelength near the center wavelength for a VBG with a Bragg incidence.....	90
Figure 4-5-The diffraction efficiency against the incident wavelength with different spatial frequencies.	91

Figure 4-6- The proposed thick 3D diffractive structure to create wavelength selectivity.	92
Figure 4-7- (a) The amplitude of the diffraction field through the binary phase grating. The results are obtained using TEA model are compared with the RCWA simulation model. (b) The phase distribution of the diffraction field through the binary phase grating. The results obtained using TEA model are compared with RCWA simulation model.	93
Figure 4-8- Geometried schematic of the multi-layer grating diffraction.....	94
Figure 4-9- The Bragg like structure. A Multilayer structure with single material in air which can be fabricated using 2PP lithography. All the thicknesses t_l and transition points a_l, b_l in each layer are variables to be optimized.	97
Figure 4-10- The flowchart of the design algorithm for the synthetic Bragg like structure design.	98
Figure 4-11- The diffraction efficiency of the zeroth order against the number of harmonic orders used in the RCWA model.....	99
Figure 4-12- The FOM against iterations.	100
Figure 4-13- The optimal thick structure.	100
Figure 4-14- Optimization results for 650nm. (a) Intensity distribution inside the multilayer periodic structure. (b) Spectrum curve.	101
Figure 4-15- Light path view of 3D grating in VirtualLab fusion.	101
Figure 4-16- The setting parameters for the designed Bragg like structure in VirtualLab fusion software	102
Figure 4-17- Spectrum curve with different layer thickness errors.	103
Figure 4-18- Spectrum curve with different lateral errors.	103
Figure 5-1- Photograph of the photoplotter in IMT-A cleanroom.	106
Figure 5-2- (a) The basic DOE fabrication process in the IMT-A clearroom. (b) Spin-coater unit. (c) coating machine.	107
Figure 5-3- (a) 3D interferometric microscope for measuring the DOE profile. (b) Optical microscope. (c) SEM for submicron structure measurement. (d) Optical bench for DOE diffraction characterization.	108
Figure 5-4- (a) Experiment setup of testing the DOE sample. (b) Numerical simulation output pattern. (c) Experimental output pattern.	109
Figure 5-5- Maximum deflection angle against with the cumulated number of exchanges of the real DBA.	110
Figure 5-6- Surface structure and surface profile. (a) Partial view of the fabricated grating cell array. (b) Height profile of single fabricated grating cell. (c) Normalized theoretical first order diffraction efficiency against depth.	111
Figure 5-7- (a) Experiment setup. (b) The intensity distribution on the target plane as a result of illuminating the DBA with a green LED source. (c) Intensity distribution on target plane when illuminated by a white LED of a smart-phone.....	112
Figure 5-8- (a) Optical microscope photography of part of the OVD. (b)	

Interferometric microscope height map view of the boundary of the pi pattern and the background. (c) Interferometric microscope generated 3D view of the structure on the boundary.....	113
Figure 5-9 -Height map surface structure image and surface profile of the OVD blazed gratings.	113
Figure 5-10 -Experimental results.(a) Optically reconstructed result with tilt angle -6 degrees.(b) optically reconstructed result with tilt angle 6 degrees.	114
Figure 5-11 -View of the fabricated FDOE and real sample. (a) Microscope view of the part of the FDOE. (b) Photograph of the real sample etched into photoresist on the glass substrate.....	116
Figure 5-12 -Schematic diagram of the 3D floating virtual object reconstruction capture setup.	116
Figure 5-13 -Experiment setup for 3D floating virtual image reconstruction. Inset: spectrum of the LED source obtained using an Ocean Optics HR4000CG-UV-NIR. The center wavelength is 525nm.....	117
Figure 5-14 -One perspective of the 3D virtual object “cube” floating in air...	117
Figure 5-15 -Virtual image taken from different angles of the object “cube” with the FDOE is illuminated by the LED.....	118
Figure 5-16 -Setup for diffraction parameters measurement.	119
Figure 5-17 -The calculated hologram using Frequency multiplexing method. The inset is a part of the hologram.....	119
Figure 5-18 -Different angular virtual image views of the object “house” when the DOE is illuminated by a LED source.	120
Figure 6-1 - Schematic of the illumination system of the current parallel photoplotter in the cleanroom at IMT-A.	124
Figure 6-2 - Schematic of the experimental setup for measuring the farfield diffractive intensity distribution of the illumination system.....	125
Figure 6-3 -Farfield intensity distribution of the light from fiber end. The “ROI” corresponds to the SLM size and position.	125
Figure 6-4 -The principle of improving the illumination uniformity in the ROI. Each circle represents a copy of the farfield fiber output pattern.	126
Figure 6-5 - Numerical simulation of the DOE homogenized intensity distribution in the ROI.....	127
Figure 6-6 - (a) Experimental evaluation setup of the photoplotter illumination system. (b) The illumination intensity distribution without a DOE diffuser. (c) The illumination intensity distribution with the DOE diffuser.	127
Figure 6-7 -Schematic of the digital mask based lithography machine using an LCD-SLM.....	129
Figure 6-8 -Illumination optical configurations. (a) Schematic of the Critical illumination configuration. (b) Schematic of the Kohler illumination configuration.....	131
Figure 6-9 -The ZEMAX ray-tracing simulation of the illumination system for	

homogenizing the SLM in the hybrid lithography machine.	132
Figure 6-10- ZEMAX simulation of the modified illumination system for homogenizing the SLM.....	133
Figure 6-11- (a)The simulated intensity distribution on the SLM , a circle of diameter is 20mm (The diagonal length of the SLM is about 18mm). (b) The intensity distribution at the rear aperture of the microscope objective , a rough circle of diameter about 4mm.	133
Figure 6-12- Photography of the deigned LED based optical illumination system assembled into the prototype lithography machine.	134
Figure 6-13- Optical setup of the hybrid parallel write lithography machine..	135
Figure 6-14- Microscope images of the patterns fabricated using the 1PP arm of the hybrid parallel write lithography machine. (a) Test pattern (smallest lines are 1 micron width). (b) DOE sample.....	135
Figure 6-15- (a) One photon absorption process of the 1PP photoplotter. (b) Two-photon absorption process of the 2PP photoplotter.....	136
Figure 6-16- The intensity profile of the Gaussian light and squared Gaussian light.	137
Figure 6-17- (a)The simulated intensity distribution along the axis of one-photon absorption.(b) The simulated intensity distribution along the axis based on two-photon absorption.	138
Figure 6-18- Schematic diagram of the parallel 2PP photoplotter based on a beam splitter DOEs.....	140
Figure 6-19- SEM images of a parallel 2PP fabricated “T” like 3D structure array. (a) Top view of the whole 3D array. (b) Side view of part of 3D structures, showing the individual 3D “T” structure.	140
Figure 6-20- The DOE diffuser target pattern for parallel 2PP photoplotter illumination system.....	141
Figure 6-21- The optical system for parallel 2PP photoplotter.	142
Figure 6-22- Zemax simulation of the illumination module intensity distribution in the SLM plane. (a) without a diffuser. (b) with the DOE diffuser.	142
Figure 6-23- The photograph of the latest parallel 2PP photoplotter optical setup.	143
Figure 6-24- Microscope image of the fabricated grid pattern. (a) The fabricated grid pattern without a diffuser for homogenizing the LCD-SLM illumination (the step and repeated SLM patterns are visible). The red dotted line represents the contour of SLM. (b) The fabricated grid pattern with a diffuser for homogenizing the LCD-SLM illumination.	144
Figure 6-25- Partial microscope image of the written grid pattern.	144



Acknowledgement

The three years working in Optics Department of IMT Atlantique is challenge but still very exciting because I engaged in a promising research project. On the end of this PhD, I would like to thank all people who supported me during my PhD study. First, I would like to express my sincerest gratitude to my supervisor, Professor Kevin Heggarty at IMT Atlantique for accepting me into his group. Over the three years, Professor Kevin Heggarty gave me many advices and ideas. In addition, he also taught me skills of giving an excellent oral presentation which is significant in my further study. I am also grateful for Professor Kevin Heggarty for his help not only in diffractive optics research but also in personal training. I would like to acknowledge Professor Frank Wyrowski for giving me a chance to study one month in his applied computational optics group of Jena university.

I would also like to thank Jennifer Romer for helping me disposing various documents. With her help, I can work efficiently during the PhD study.

I would like to give my sincere thanks to Yoran Eli Pegion, Quentin Carlier, Thomas Le Deun, Luis Adrian Perez Covarrubias, Vasili Marshev for providing fruitful support. With their helps, life is more interesting.

Finally, I would love to express gratitude to my parents, my grandmother and girlfriend for their emotional support and understanding throughout my PhD study.

Résumé de la thèse

1.1 Introduction générale

Les éléments optiques diffractifs (EOD) sont généralement des dispositifs contenant une surface micro ou nanométrique avec un motif en relief complexe, comme le montre la figure 1. Ils ont attiré beaucoup d'attention au cours des quarante dernières années pour leur capacité extraordinairement polyvalente à manipuler les champs lumineux et pour leur volume compact. Comme ces structures de surface en relief sont faciles à produire en masse à l'aide de la technique éprouvée de nano-impression, elles sont également très utilisées dans le domaine industriel. La figure 1(b) illustre, par exemple, une configuration typique de mise en forme de faisceau par EOD. Étant donné que le front d'onde de la lumière incidente sur le EOD peut être facilement et diversement manipulé par la structure de surface en relief EOD, ces dispositifs sont de plus en plus utilisés dans un éventail d'applications toujours plus large, par exemple comme dans la mise en forme de faisceau laser, dans l'optique des modules d'illumination des équipements de lithographie optique ou comme séparateur de faisceau ou générateur de points qui sont apparus récemment dans les panneaux solaires et dans les applications de reconnaissance faciale des téléphones cellulaires. Par rapport au volume encombrant des éléments optiques réfractifs (ROE), les EOD compacts et plans peuvent également parfois réaliser avantageusement bon nombre des mêmes fonctions optiques que les ROE, comme les lentilles sphériques, les prismes et les lentilles de forme libre.

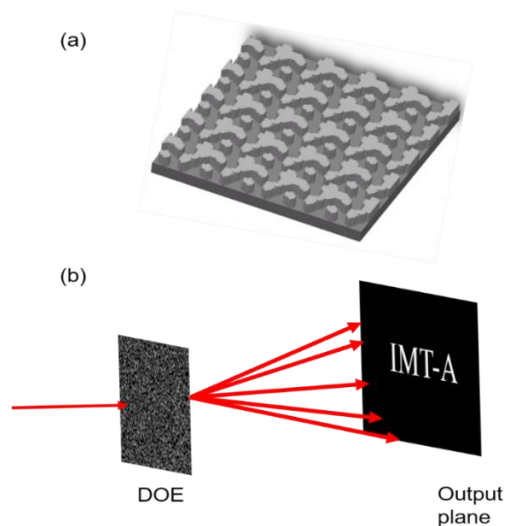


Figure 1-(a) Structure du relief de surface d'une EOD. (b) Configuration de la diffraction d'un façonneur de faisceau d'une EOD.

Les hologrammes pour l'enregistrement et l'affichage d'images 3D et de fronts d'ondes sont un autre type d'EOD et l'une des applications les plus frappantes qui ont également été étudiées depuis des décennies. Un hologramme traditionnel est réalisé en enregistrant, sur une plaque photosensible, le motif d'interférence entre le front d'onde d'un objet et un faisceau de référence

ii

à l'aide d'un banc optique. Comme ces hologrammes optiques traditionnels nécessitent des systèmes d'enregistrement optique compliqués, les chercheurs ont mis au point des hologrammes synthétisés par ordinateur (HSO) qui utilisent des méthodes de calcul numérique pour offrir une plus grande flexibilité et supprimer la nécessité d'un banc optique. Les hologrammes et les hologrammes générés par ordinateur sont largement utilisés dans les applications de sécurité optique sur les billets de banque, les documents d'identité et les marques pour les protéger contre les contrefaçons.

1.2 Problématique de la thèse

Malgré ces nombreux avantages et applications des EOD, plusieurs limitations dans la modélisation, la conception et la fabrication des EOD enregistrées optiquement (hologrammes conventionnels) et des EOD "synthétiques" ou générées par ordinateur, réduisent actuellement leurs performances et limitent leurs applications. Une première limitation est que les principaux modèles et algorithmes de conception, en particulier des EOD synthétiques, nécessitent très souvent l'utilisation d'une source laser. Cela impose fréquemment des restrictions pratiques à de nombreuses applications des EOD, en particulier dans les applications visuelles telles que les hologrammes de sécurité où les règles de sécurité oculaire sont importantes. Il existe clairement un besoin d'algorithmes de conception des EOD compatibles avec d'autres types de sources lumineuses, en particulier les sources LED extrêmement courantes (disponibles sur le smartphone dans la poche de chacun) qui sont divergentes, temporellement incohérentes et généralement d'une largeur spectrale beaucoup plus large que les lasers. Une deuxième restriction concerne la nature généralement 2D des figures de diffraction de sortie générés par les EOD classiques. Là encore, dans les applications de visualisation en particulier, telles que les hologrammes de sécurité et la réalité augmentée, la capacité à donner une impression visuelle convaincante de motifs en 3D serait un net progrès par rapport à la plupart des performances actuelles des EOD.

Une troisième limitation importante pour les techniques de conception et de fabrication des EOD habituelles est l'exigence de sources de lumière monochromatiques. Les EOD capables de travailler avec des sources de lumière blanche (telles que les LED blanches) et surtout celles capables de générer des modèles de sortie de couleur contrôlée à partir de telles sources seraient hautement souhaitables dans de nombreuses applications. Les hologrammes optiquement "épais" traditionnels (réseau de Bragg), tels que ceux enregistrés dans des émulsions argentiques ou des photopolymères, sont utilisés depuis de nombreuses années pour produire des hologrammes à haute efficacité de diffraction et spectralement sélectifs. Cependant, il existe peu d'équivalents parmi les hologrammes conçus et produits synthétiquement. Des modèles et des algorithmes pour la conception de structures d'EOD synthétiques "épaisses" sur le plan optique constitueraient à nouveau une avancée importante par rapport aux capacités actuelles. Une dernière limitation des performances actuelles des EOD est que nous ne disposons pas de technique de fabrication pratique facilement disponible pour la production de ces EOD synthétiques "épaisses" optiquement performantes. Si de telles structures pourraient en principe être réalisées à l'aide des techniques photo-lithographiques multicouches actuelles, la résolution

et le nombre de couches, et donc les efforts et les coûts requis, rendent cette approche peu rentable pour la plupart des applications. L'étude de voies alternatives pour la fabrication de structures d'EOD optiquement "épaisses" est donc un sujet de recherche important.

1.3 Objectifs de la thèse

Cette thèse vise à aborder les limites indiquées ci-dessus à travers plusieurs contributions à la conception, la fabrication et le test de structures d'EOD sélectives en longueur d'onde qui peuvent être observées à l'aide de sources LED divergentes et blanches, en vue d'élargir les applications à des domaines qui ne sont pas accessibles pour le moment. Les nouvelles structures auront des applications, par exemple, dans la protection des documents d'identification, des billets de banque et des marques contre la contrefaçon. Parmi celles-ci, une application importante est celle des hologrammes de sécurité plus sophistiqués avec la visualisation d'objets en 3D, où le dispositif peut produire un objet virtuel en 3D "flottant" à angle de vue multiple, perçu à proximité du substrat de l'hologramme. Une autre application potentielle importante concerne la visualisation 3D automobile, où les informations virtuelles pourraient être fusionnées dans la scène réelle : utile par exemple pour la conduite assistée. Comme indiqué ci-dessus, les structures optiques de volume (réseau de Bragg) peuvent réaliser de nombreuses fonctions optiques souhaitées, mais elles nécessitent un système d'enregistrement d'interférences optiques encombrant et une chimie complexe pour fabriquer des structures optiques aussi épaisses et à haute efficacité de diffraction. Les autres inconvénients de cette approche d'enregistrement optique sont qu'elle manque de souplesse de conception et qu'elle est peu adaptée à la production en série. L'approche de conception visée dans cette thèse devrait nous permettre d'optimiser des structures photoniques plus sophistiquées. Cela nous pousse à trouver une nouvelle voie pour fabriquer des structures aussi complexes. La question spécifique abordée est la suivante : "Pouvons-nous trouver un moyen efficace de fabriquer synthétiquement des dispositifs diffractifs aussi "épais" optiquement, qui évite d'utiliser le banc d'interférence optique et qui soit plus adapté à la production de masse ?

La nouvelle technique de fabrication mise au point est une extension des techniques photolithographiques à écriture directe massivement parallèles développées par le département d'optique de l'IMT Atlantique dans le cadre de doctorats précédents. Au début de ce doctorat, la résolution de fabrication du phototraceur à écriture parallèle de l'IMT Atlantique était limitée à environ 1 micron et, plus important encore, la machine ne pouvait fabriquer que des structures photoniques 2D ou 2,5D qui ne pouvaient pas obtenir une sélectivité de longueur d'onde à haut rendement. Pour permettre la fabrication de structures photoniques entièrement 3D avec une résolution submicronique, l'approche à écriture parallèle a été adaptée pour tirer parti des techniques de polymérisation à deux photons (2PP) afin de permettre la fabrication de structures 3D optiquement "épaisses". Ma contribution à la conception et à l'assemblage de ce nouveau phototraceur (dans le cadre d'un projet européen H2020 s'étendant bien au-delà de ma thèse) est principalement centrée sur la conception et le développement des modules d'illumination à haute uniformité basés sur des EOD.

1.4 Contributions de la thèse

Nous avons identifié un certain nombre de limitations des modèles/algorithmes de conception des éléments optiques diffractifs (EOD) et des techniques de fabrication des EOD qui réduisent actuellement les performances des EOD et restreignent leurs applications. Cela nous a permis de fixer les principaux objectifs de la thèse en vue de traiter ces limitations et de tenter de les surmonter ou de les réduire, améliorant ainsi les performances actuelles des EOD. Après avoir présenté, dans le chapitre 2, les principaux concepts, modèles, algorithmes de conception et techniques de fabrication des EOD afin de donner un aperçu de l'état actuel de l'art dans la communauté de l'optique de diffraction, nous avons abordé les limitations identifiées de manière systématique et développé les solutions suivantes.

1.4.1 EOD de Fresnel projetant un modèle 2D en utilisant un éclairage divergent

Cette approche était une extension de l'algorithme de base de l'IFTA pour permettre l'éclairage par une source de lumière LED divergente, temporellement incohérente mais presque monochromatique (voir figure 2). Cela a produit l'image de sortie souhaitée, mais avec une faible efficacité globale du système et des limitations sur la taille de l'EOD dues à la charge de calcul. Par exemple, un EOD de 20000×20000 pixels nécessite plus de 10 heures avec un PC standard. C'est pourquoi une autre stratégie de conception, avec une charge de calcul plus faible, basée sur des matrices à facettes, a été proposée.

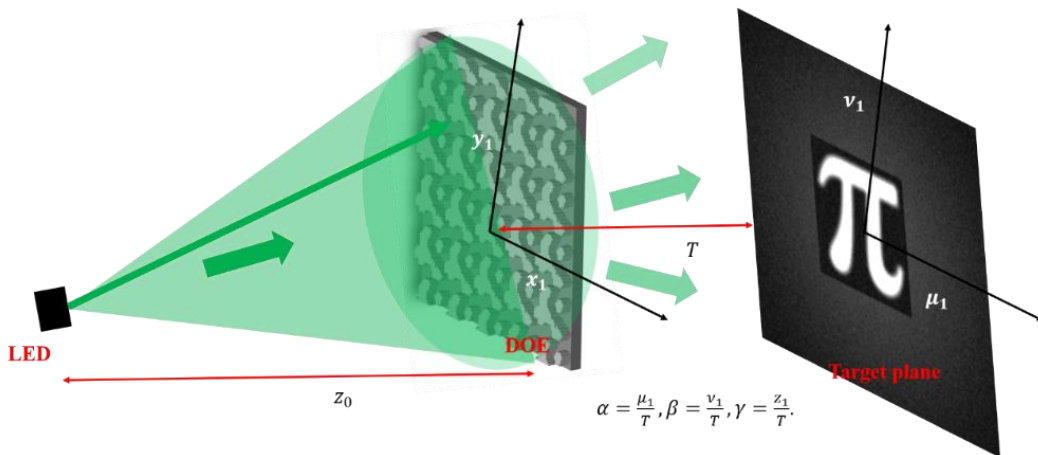


Figure 2- Schéma de la mise en forme divergente de la lumière.

1.4.2 Méthode des matrices à facettes

Dans cette méthode, une technique basée sur un réseau de diffraction blazé (DBA) a été décrite. Les paramètres du réseau de chaque facette ont été optimisés à l'aide d'un nouvel algorithme d'optimisation en deux étapes. Les résultats de la simulation numérique vérifient l'approche de conception. Les facteurs qui peuvent affecter le résultat de la conception ont également été identifiés et étudiés, ce qui fournit à un ingénieur optique un guide de conception en considérant les limites réelles de fabrication. Cette approche a également permis d'obtenir des images de sortie clairement visibles qui restent acceptables même lorsque les EOD sont éclairés par une LED blanche comme on en trouve sur presque tous les smartphones (voir figure 4).

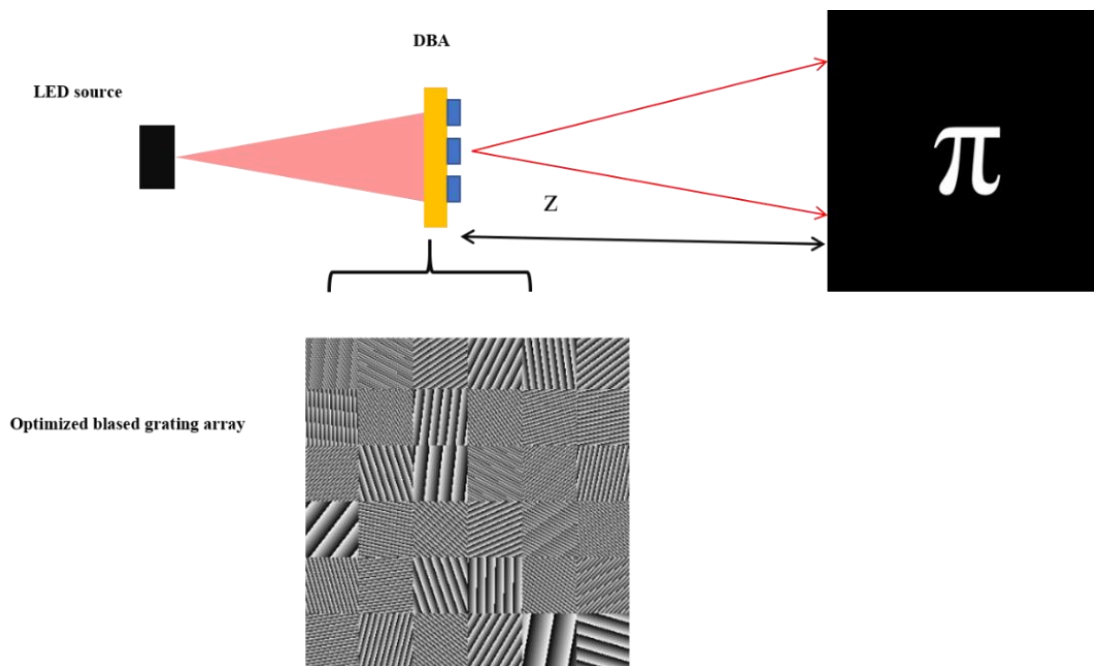


Figure 3- Le schéma du principe DBA pour la production de modèles arbitraires.

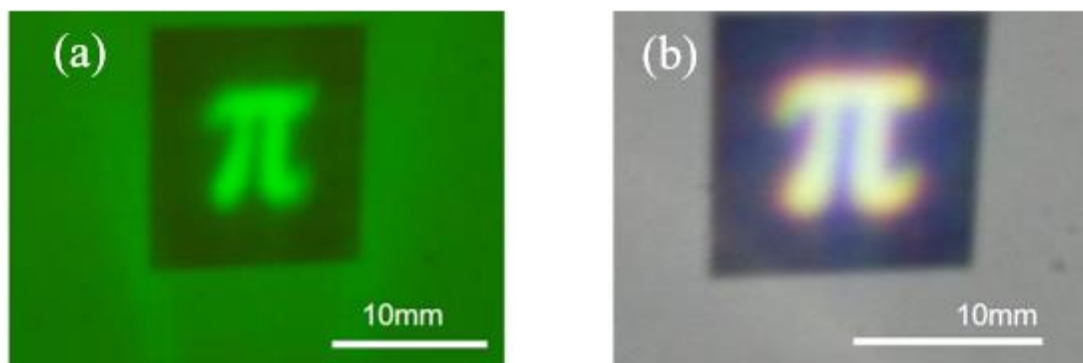


Figure 4- (a) La distribution de l'intensité sur le plan de la cible suite à l'éclairage du EOD avec une source LED verte. (b) Distribution de l'intensité sur le plan de la cible lorsque l'EOD est éclairée par une LED blanche d'un smartphone.

Les deux approches susmentionnées sont utilisées pour produire un modèle de projection en 2D. Les approches suivantes, destinées spécifiquement aux applications de visualisation, ont tenté de produire des images de sortie virtuelles plutôt que des images projetées sur un écran d'observation.

1.4.3 Méthode des EOD de Fresnel à facettes

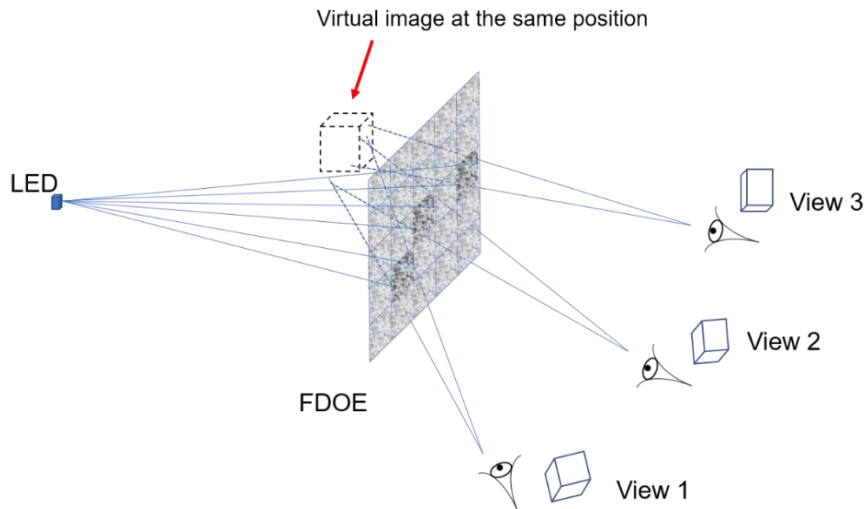


Figure 5- La configuration de la source LED et de l'observateur.

L'idée essentielle de la méthode est esquissée dans la figure 5. Elle montre la disposition de la source LED, de la FEOD et des observations. La source LED est placée derrière la FEOD de type transmissif. La structure diffractive globale est constituée d'une matrice d'EOD de Fresnel individuelles. Chaque EOD de Fresnel diffracte pour générer une vue du même objet 3D, mais observé sous un angle de vue légèrement différent. En optimisant soigneusement les angles pour chaque facette, lorsqu'un observateur déplace son œil d'un côté à l'autre du plan FEOD, il observe les différentes vues, générant les vues angulaires légèrement différentes de l'objet 3D. L'effet global est celui de l'observation d'un véritable objet 3D flottant. Ici aussi, les contraintes de charge de calcul ont limité la taille des EOD à quelques cm². Une dernière technique basée sur le multiplexage de fréquence spatiale a donc été mise au point, qui a permis de concevoir efficacement des EOD de grande surface (des dizaines de cm²) produisant la perception visuelle d'un objet virtuel 3D flottant à proximité de la surface d'une EOD éclairée par une source LED divergente.

1.4.4 Méthode de multiplexage des fréquences

Un algorithme de conception permettant de produire un impressionnant objet virtuel flottant en 3D basé sur la technique du multiplexage de fréquence spatiale a été proposé (voir figure 6). En calculant l'hologramme à l'aide de la formule de diffraction du spectre angulaire sans l'approximation paraxiale, un objet virtuel flottant peut être perçu derrière le substrat de l'hologramme. Contrairement à la méthode des hologrammes de Fresnel à facettes proposée dans la section précédente, la méthode démontrée est moins lourde à calculer puisqu'elle n'utilise qu'une seule transformation de Fourier (dans ce travail de simulation, le temps de calcul est de 20 minutes pour produire un EOD de 30 mm x 30 mm). Il s'agit donc d'une méthode précieuse pour le calcul d'hologrammes de grande taille. La taille de l'EOD peut être encore plus grande en utilisant une transformation de Fourier modifiée. Le champ de vue (FOV – Field of View) de cette EOD ne dépend que de la taille des pixels, ici le FOV est d'environ 22 degrés ce qui est le double du résultat de la méthode FEOD présentée.

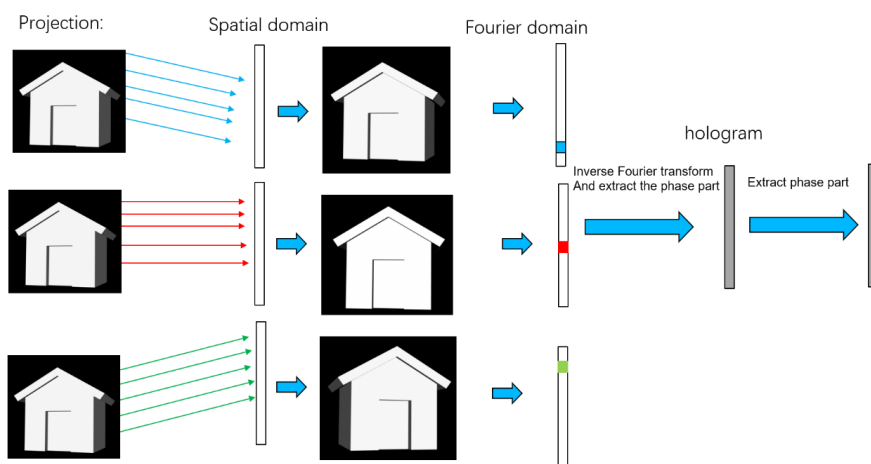


Figure 6- Schéma de la méthode de segmentation spatiale des fréquences.

Les méthodes de conception proposées fonctionnent mieux pour les sources de lumière monochromatiques puisque leurs conceptions sont basées sur le modèle TEA (Thin Element Approximation). Dans de nombreuses applications, une lumière blanche étendue est fréquemment utilisée pour éclairer les hologrammes de sécurité, par exemple la lumière d'éclairage d'un smartphone. Les performances optiques d'une EOD mince dépendent de la longueur d'onde, de sorte que la dispersion peut être importante lorsque les EOD sont éclairées par une lumière blanche. Habituellement, la façon de réduire cette dispersion est de produire un motif de cible plus petit, ce qui signifie que les ondes lumineuses diffractées par les hologrammes convergent vers le plan de la cible (de cette façon, la dispersion est faible). C'est un compromis utile du point de vue de l'ingénierie optique et qui produit déjà des EOD utilisables, mais le problème de la dispersion n'est pas fondamentalement abordé.

L'examen d'hologrammes historiques "épais" enregistrés optiquement (réseaux de Bragg) semble être un moyen efficace de résoudre le problème mentionné ci-dessus, mais des bancs d'interférences optiques compliqués et des résistances photosensibles spécifiques sont nécessaires. Le système lithographique 2PP massivement parallèle que nous développons actuellement commence à rendre possible la fabrication synthétique d'une EOD "épaisse" en 3D. Inspirées par cette nouvelle machine, nous avons étudié de nouvelles structures 3D épaisses en utilisant un algorithme d'optimisation heuristique. Comme les structures sont épaisses (le déphasage équivalent est supérieur à 2π), le modèle TEA n'est pas valide. Pour calculer le champ de diffraction avec précision, un modèle électro-magnétique rigoureux est nécessaire. Sur la base de cette théorie de diffraction rigoureuse, une nouvelle structure photonique a été proposée.

1.4.5 Conception de structures diffractives 3D de type Bragg

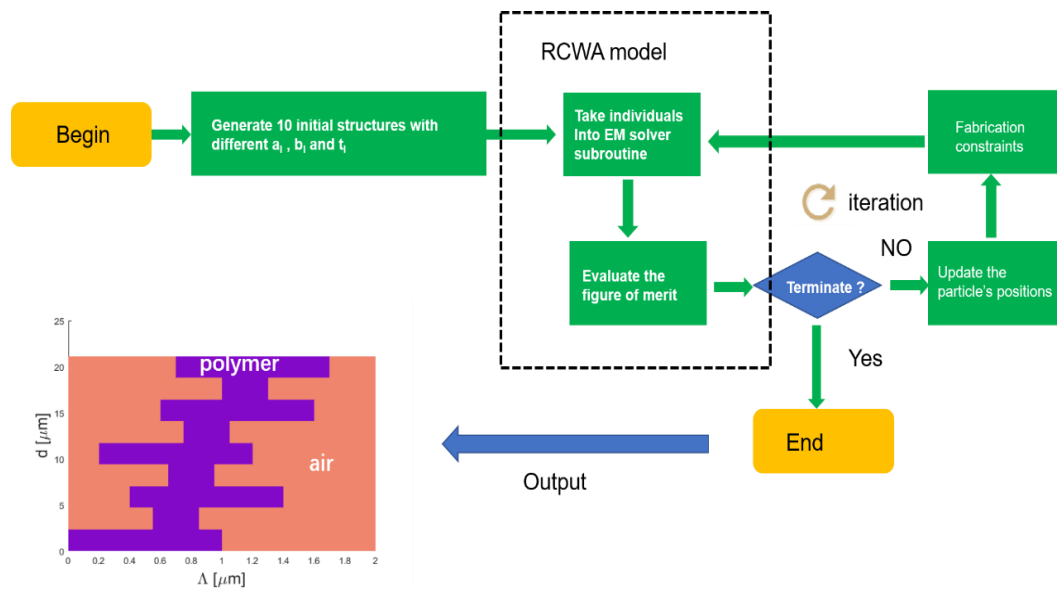


Figure 7- L'organigramme de l'algorithme de conception pour la conception de structures synthétiques de type Bragg.

Inspiré par les structures de réseau de Bragg en volume, une structure photonique de type Bragg a été proposée, spécialement adaptée à la fabrication par la technique de polymérisation à deux photons nouvellement disponible. Pour autant que nous sachions, c'est la première fois que de telles stratégies et structures de conception ont été signalées dans la communauté de l'optique. Un modèle RCWA multicouche a été présenté, mis en œuvre pour modéliser et concevoir la structure de type Bragg souhaitée en combinant le modèle RCWA et l'algorithme d'optimisation des essais de particules (voir figure 7). En outre, les limites de fabrication prévues de la lithographie 2PP ont été intégrées à l'algorithme de conception dans notre conception afin d'améliorer les performances de fabrication. Les résultats de la conception ont été vérifiés à l'aide du logiciel commercial VirtualLab FusionTM qui a démontré que la méthode de conception proposée peut être un moyen efficace d'optimiser de telles structures optiquement épaisses. La structure multicouche est destinée à être fabriquée par le système de fabrication parallèle 2PP actuellement en construction dans la salle blanche de l'IMT-A pour vérifier expérimentalement les performances des structures proposées.

1.4.6 Contributions aux installations de fabrication de l'EOD à l'IMT-A

Toutefois, la fabrication de ces micro et nanostructures entièrement en 3D est actuellement un défi de taille, car les techniques de fabrication traditionnelles (photolithographie par masque et écriture directe ou lithographie par faisceau électronique) se limitent généralement en pratique à la fabrication de structures en 2D ou 2,5D. La polymérisation à deux photons (2PP) est une technologie pour la fabrication de ces structures 3D complexes et à haute résolution, mais les vitesses de fabrication et les volumes d'écriture des 2PP sont actuellement fortement limités par l'approche séquentielle à faisceau laser unique. Pour résoudre ce problème, l'IMT Atlantique développe un phototraceur 2PP massivement parallélisé pour la fabrication rapide de structures

photoniques entièrement 3D de grande surface/volume. Ma contribution à ce projet s'est principalement concentrée sur la conception et l'assemblage des modules d'éclairage à haute uniformité basés sur des EODs. La conception du premier module d'éclairage était basée sur une source LED (voir figure 8). Étant donné le grand angle de divergence des LED, une lentille de condenseur asphérique à ouverture numérique élevée a été utilisée pour collecter la lumière. L'exigence d'uniformité élevée de la SLM a conduit à utiliser un diffuseur spécifique (conçu et fabriqué en salle blanche IMT-A). Une collimation supplémentaire a été utilisée pour se concentrer dans l'ouverture arrière du microscope afin d'améliorer l'efficacité énergétique.

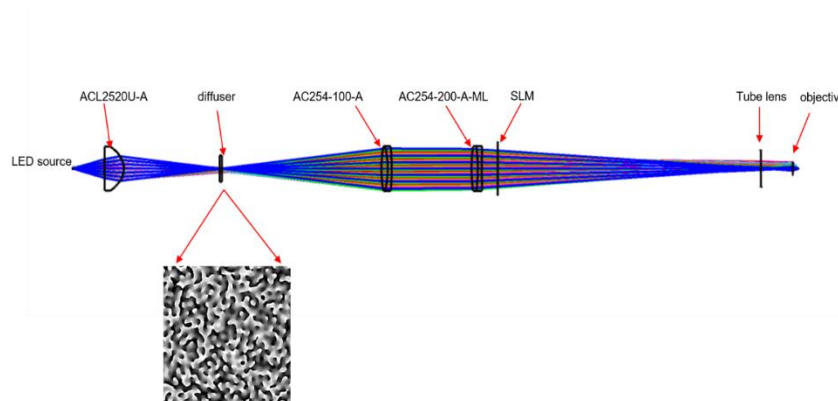


Figure 8-La simulation de ray-tracing ZEMAX du système d'illumination pour homogénéiser le SLM dans la machine de lithographie hybride.

Le deuxième module d'éclairage était basé sur une source laser pour une approche de polymérisation multi-photon (voir figure 9). Une technique similaire a été utilisée, mais elle a été compliquée par la nécessité d'adapter l'éclairage à la taille et à la forme du SLM. Le choix minutieux de l'image cible du diffuseur EOD nous a permis de modifier la forme de base du point rond sur le SLM en une forme rectangulaire plus uniforme et plus efficace.

Les premiers résultats obtenus récemment montrent que des structures entièrement 3D très prometteuses peuvent effectivement être fabriquées en parallèle par le nouveau phototraceur (voir figure 10). Il est prévu de fabriquer de nouvelles structures photoniques synthétiques en 3D épaisses.

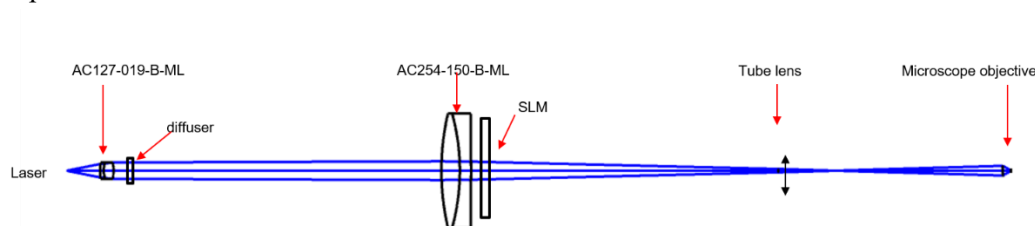


Figure 9- Le système optique du photo-traceur parallèle 2PP.

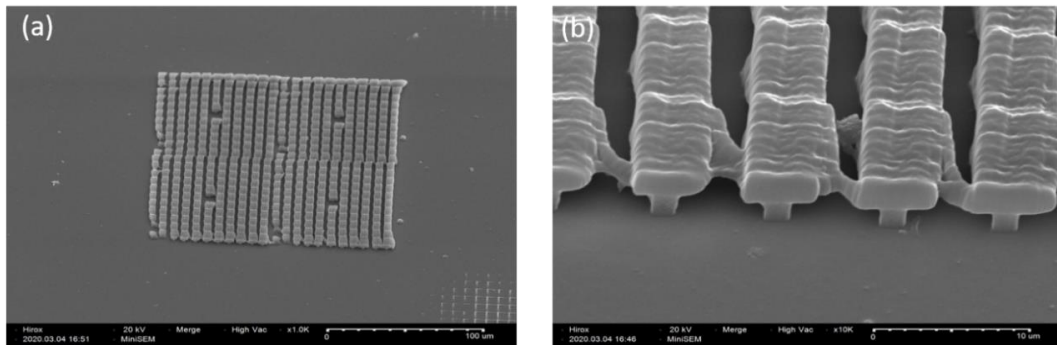


Figure 10- Images MEB d'un réseau de structures 3D en forme de "T" fabriqué en parallèle par 2PP. (a) Vue de dessus de l'ensemble du réseau 3D. (b) Vue latérale d'une partie des structures 3D, montrant la structure en "T" 3D individuelle.

1.5 Conclusion générale et perspectives

Dans cette thèse, nous avons principalement contribué les solutions suivantes aux limitations actuelles de la conception, fabrication et application des EOD :

- A. Design et vérification expérimentale de cinq algorithmes différents de conception d'EOD pour l'illumination par LED
 - 1) Projection d'image réelle : EOD de Fresnel pour éclairage divergent.
 - 2) Projection d'image réelle : EOD facetté à réseaux de diffraction.
 - 3) Image virtuelle 2D derrière le substrat du EOD : Fresnel EOD.
 - 4) Image virtuelle 3D derrière le substrat du EOD : EOD de Fresnel à facettes.
 - 5) Image virtuelle 3D derrière le substrat du EOD : EOD à multiplexage de fréquence spatiale.
- B. Conception et optimisation d'une nouvelle structure photonique synthétique 3D optiquement "épaisse" adaptée à la fabrication par polymérisation à deux photons.
- C. Conception de systèmes d'illumination à haute uniformité pour le photo-traceur IMT-A.

Ce nouveau phototraceur 2PP est clairement l'une des principales perspectives pour la poursuite des travaux de cette thèse. En particulier, en ce qui concerne les speckles laser qui sont encore observés dans certaines structures fabriquées. De nouvelles EOD homogénéisantes et un système permettant de faire vibrer la fibre de transmission du laser ont été identifiés comme des solutions prometteuses pour minimiser ces effets de speckle. De même, l'utilisation d'objectifs de microscope à O.N. plus élevés - et l'adaptation du système d'éclairage à ces objectifs - permettra de réduire la taille des structures réalisés.

Du côté de la modélisation/algorithmique, bien que nous ayons réussi à démontrer la génération de la perception visuelle d'un objet 3D flottant derrière la surface de l'EOD, la perception d'un objet virtuel 3D flottant devant le substrat de l'hologramme reste un objectif recherché depuis longtemps. Les travaux futurs se concentreront sur le développement d'algorithmes capables de produire l'impression d'un objet virtuel devant l'hologramme.

Abstract

Diffraction Optical Elements (DOEs) are now widely used in academic and industrial applications due to their ultra-thin, compact characteristics and their highly flexible manipulation of light wave-fronts. Despite these excellent properties, the scope of DOE applications is often limited by the fact that most DOEs are designed to generate only 2D projected patterns, and even more importantly, for use only with monochromatic, coherent, often collimated, laser sources. The cost and eye safety constraints of laser sources severely restrict DOE visualisation applications such as security holograms, and the 2D nature of the generated patterns limits virtual or augmented reality applications. To overcome these restrictions, this thesis targets the design and fabrication of wavelength selective 3D diffractive structures which can produce a perceived multiple view-angle “floating” 3D object behind the DOE substrate when illuminated by readily available and cheap white LED sources.

In an initial approach we develop and experimentally validate a series of novel design algorithms for conventional optically “thin” DOE structures under incoherent, divergent illumination; first to project 2D patterns, then to create virtual 2D images and finally virtual 3D patterns. In a second stage, we leverage the capacities of optically “thick”, Bragg-like structures to introduce spectral selectivity (towards colour output patterns) and improve diffraction efficiency. Since the thin element approximation is invalid when designing optically thick 3D photonic structures we develop a particle swarm optimization algorithm based on a rigorous diffraction model to design highly innovative optically thick synthetic diffractive structures.

The cost-effective fabrication of such proposed fully 3D micro- and nano-photonics structures is highly challenging when using current traditional lithographic techniques which are generally limited, in practice, to the fabrication of 2D or 2.5D structures. To this end, an advanced prototype massively parallelized two-photon polymerization (2PP) photoplotter for the fabrication of large area fully 3D photonic structures is currently being developed by the IMT Atlantique Optics Department. We present our contributions to the design and development of the critical, high uniformity illumination modules for the new prototype 2PP photoplotter.

The research and development in this thesis contributes to the broadening of DOE applications to fields which are currently inaccessible. The developed design methods can also find applications in holographic display fields such as automotive augmented reality.

Chapter 1 General Introduction

1.1 Diffractive optical elements

Diffractive optical elements (DOEs), usually a micro- or nano-patterned surface with a complex relief pattern as shown in **Figure 1-1(a)**, have attracted much attention over the past forty years for their extraordinarily versatile capacity to manipulate light fields and for their compact volume [1-5]. **Figure 1-1(b)** illustrates, for example, the diffraction configuration of a typical beam shaping DOE. Since the incident light wavefront on the DOE plane can be easily and variously manipulated by the DOE surface relief structure, such devices are increasingly being used in an ever increasing range of applications, for example as DOE beam shapers in laser beam shaping, in the illumination optics of optical lithography equipment or as beam splitter or dots generator that have recently appeared in solar cells and in cellphone face recognition applications [6-8]. Compared to the bulky volume of refractive optical elements (ROEs), compact, planar DOEs can also sometimes advantageously realize many of the same optical functions as ROEs such as spherical lenses, prisms and aspherical lenses [9-10].

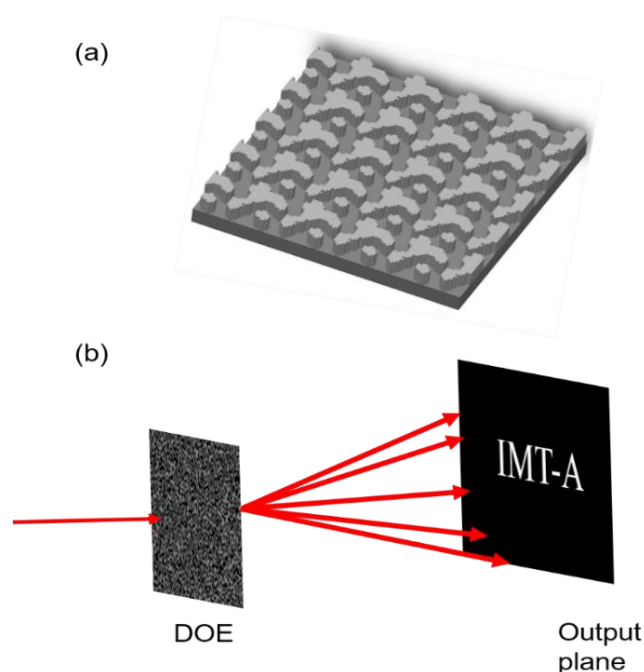


Figure 1-1-(a) Surface relief structure of a DOE. (b) Diffraction configuration of a DOE beam shaper.

Holograms for the recording and display of 3D images and wave-fronts are yet another form of DOE and one of the most striking applications that have also been investigated for decades. A traditional hologram is made by recording, on a photosensitive plate, the interference pattern between an object wavefront and a reference beam using an optical

bench. Since such traditional optical holograms need complicated optical recording systems, researchers developed computer generated holograms (CGHs) which use numerical calculation methods to give increased flexibility and remove the requirement for an optical bench. Both optically mastered holograms and CGHs are widely used in optical security applications on bank notes, identity documents and brands to protect against counterfeit [11-15].

1.2 Thesis problematic

Despite these many advantages and applications of DOEs, several limitations in the modeling, design and fabrication of both optically recorded (conventional holograms) and the increasingly prevalent “synthetic” or computer generated DOEs, currently reduce their performance and restrict their applications.

A first limitation is that the main models and algorithms for the design, particularly of synthetic DOEs, very often require the use of a collimated, coherent and monochromatic light source – usually a laser. This frequently imposes practical restrictions on many DOE applications, particularly in visual applications such as security holograms where eye safety regulations and cost constraints severely limit the use of laser sources. There is clearly a need for DOE design algorithms compatible with other types of light source, in particular the extremely common LED sources (available on the smartphone in everyone’s pocket) that are divergent, temporally incoherent and generally of a much wider spectral width than lasers.

A second restriction concerns the usually 2D nature of the output diffraction patterns generated by most current DOEs. Again, in visualisation applications especially, such as security holograms and Augmented Reality, the ability to display or give a convincing visual impression of 3D patterns would be a clear advance on most current DOE performance.

A third important limitation with many current DOE design and fabrication techniques is the requirement for monochromatic light sources. DOEs capable of working with white light sources (such as white LEDs) and especially those capable of generating controlled colour output patterns from such sources would be highly desirable in many applications. Traditional optically “thick” holograms (where the light modulation is performed in a volume whose thickness is greater than the light wavelength) such as those recorded in silver halide emulsions or photopolymers have been able to use Bragg grating based volume effects to produce high efficiency colour selective holograms for many years. However, there are few equivalents with the more flexible, synthetically designed and produced holograms. Models and algorithms for the design of optically “thick” synthetic DOE structures would again be an important advance on current capabilities.

A final limitation on present DOE performance, that is linked to the above point, is that we possess no readily available practical fabrication technique for the production of these potentially high performance optically “thick” synthetic DOEs. While such structures could in principle be realised using current multilayer photolithographic

techniques, the resolution and number of layers and hence the effort and cost required make the approach uneconomic for most applications. The investigation of alternative routes to the fabrication of optically “thick” DOE structures is therefore an important research topic.

1.3 Thesis objectives

This thesis aims to address the limitations indicated above through several contributions to the design, fabrication and test of wavelength selective DOE structures which can be observed using divergent and white LED sources, with a view to broadening the applications to areas which are not accessible at the moment. The new structures will have applications for instance in protecting identification documents, banknotes and brands against counterfeit. Among them, an important application is for more sophisticated security holograms with 3D object visualization, where the security device can produce a perceived multi-view angle “floating” virtual 3D object close to the hologram substrate. Another important potential application concerns automobile 3D visualization, where the virtual information could be merged into the real scene: useful for assisted driving.

As indicated above, volume optical structures (Bragg grating) can realize many of the desired optical functions, but they require a bulky optical interference recording system and complex chemistry to make such thick, high diffraction efficiency optical structures. Other downsides of this optical recording approach are that it lacks design flexibility and is little suited to mass production. The design approach targeted in this thesis should enable us to optimize more sophisticated 3D photonic structures. This in turn drives us to find a new path to fabricating such complex structures. The specific question addressed was: “Can we find an efficient way to fabricate such optically “thick” diffractive devices synthetically that avoids using the optical interference bench and is more suited to mass production ?”

The new fabrication technique developed is an extension of the massively parallel direct-write photolithographic techniques developed by the IMT Atlantique Optics Department through previous PhDs. At the start of this PhD the fabrication resolution of the IMT Atlantique parallel-write photoplotter was limited to approximately 1 micron, and more importantly the machine could only fabricate 2D or 2.5D photonic structures that could not obtain strong and high efficiency wavelength selectivity. To enable the fabrication of fully 3D photonic structures with sub-micron resolution, the parallel-write approach has been adapted to leverage two-photon polymerization (2PP) techniques to enable the fabrication of optically “thick” 3D structures. My contribution to the design and assembly of this new photoplotter (in the context of a EU H2020 project extending well beyond my thesis) is centred mainly on the design and development of the DOE based high uniformity illumination modules.

1.4 Organization of the thesis

The thesis contains seven chapters, organized as follows. After this General Introduction, in chapter 2, we will briefly introduce the various definitions of the different types of diffractive optical elements (DOEs) and classify them according to their working principle. We then present the various theoretical models, including scalar diffraction and vector diffraction theory, that can be used for DOE design. DOE optimization algorithms and current lithographic technologies are briefly compared and analyzed. This chapter also discusses some practical considerations of DOE design and introduces the main issues that this thesis aims to address.

In Chapter 3, we successively present three types of security hologram which can be observed under monochromatic divergent illumination. The first is a projection type security hologram which can produce a customized 2D diffraction pattern on a screen when illuminated by a divergent LED source. The second creates 2D target patterns on the surface of hologram substrate for direct observation rather than projection onto a screen. The third produces the visual perception of a “floating” virtual 3D object behind the hologram substrate.

A design algorithm for optimizing the parameters of novel, optically “thick” synthetic photonic structures based on a vector diffraction model is presented in chapter 4. In chapter 5, we experimentally verify the models and design algorithms presented in the previous chapters. The basic principle of the new parallel-write 2PP photoplotter currently under development at the IMT Atlantique to enable the fabrication of these new optically “thick” synthetic DOEs is presented in chapter 6 with, in particular, my contributions to the design, assembly and evaluation of a new illumination optical system for this photoplotter. Finally, we draw the major conclusions of the work of this thesis and propose some directions for future research.

1.5 Thesis contributions

1. Development of a DOE model and design algorithm for projection type security holograms under divergent light illumination. Experimental verification with a DOE fabricated using our parallel photoplotter in the IMT Atlantique cleanroom.
2. A method for the design and manufacturing of a diffractive blazed grating array (DBA) to produce a visual security feature when illuminated by a divergent Light emitting diode (LED) source, where the collective divergent angle is about 16 degrees. Experimental demonstration by a DOE sample fabricated in our cleanroom
3. Development and experimental verification of a technique for the optimization of a phase-only faceted Fresnel type diffractive optical element (FDOE) creating the visual perception of a “floating” virtual 3D object behind hologram substrate.

4. Design and fabrication of diffractive blazed grating based optical variable device for a security hologram application.
5. Design and fabrication of a phase only large area hologram (>30mm*30mm) for producing the visual perception of a “floating” virtual 3D object using a spatial frequency multiplexing method.
6. Development of a model and optimization algorithm, based on rigorous vector diffraction theory, for the design of synthetic optically thick photonic structures.
7. Design, assembly and evaluation of an improved uniformity illumination system for the current IMT Atlantique parallel photoplotter.
8. Design, assembly and evaluation of an high uniformity illumination system for the new IMT Atlantique 2PP parallel photoplotter.

1.6 List of Publications

Journals:

1. Qiang Song, Yoran-Eli Pigeon, Kevin Heggarty, “ Faceted Fresnel DOEs creating the perception of a floating 3D virtual object under divergent illumination”, *Optics Communications*, Vol.451, Issue15, pages:231-239(2019).
2. Qiang Song, Yoran-Eli Pigeon, Kevin Heggarty, “ Faceted gratings for an optical security feature”, *Applied Optics*, Vol.59, Issue 4, pp.910-917(2020).

Conferences:

1. Qiang Song, Yoran-Eli Pigeon, Xavier Theillier, Kevin Heggarty, “ An optimization approach of computer generated hologram(CGH) for divergent light shaping”, (Oral Presentation), *Digital Holography and Three-Dimensional Imaging*, 19-23 May, Bordeaux France, 2019
2. Qiang Song, Luis Adrian Perez Covarrubias, Yoran-Eli Pigeon, Kevin Heggarty, “Inverse design for wavelength selective thick diffractive optical element”, *Topical Meeting on Diffractive Optics*, 16-19, September, Jena, Germany, 2019.

Chapter 2 Diffractive optical elements

In the previous chapter, the basic principle of DOEs and CGHs as wave-front manipulating micro- and nano-structured surfaces was introduced. In this chapter, we present the main scientific and technical concepts behind the modelling, design and fabrication of DOEs, thus providing an indication of the current state of the art in the field. The aim here is to give only the level of detail required to follow our contributions presented in the succeeding chapters. For a more extensive treatment, the reader is directed to one of the general presentations of the maturing DOE field, for example in [1-3].

After a basic classification of the main DOE types, we will present the various diffraction and light propagation models (scalar and diffractive) used to design and simulate DOEs, along with their applicability regimes. We then summarize the main DOE design algorithms with their advantages and drawbacks. After a review of the principal DOE fabrication techniques we close the chapter with a discussion of some practical design considerations: how to design real-life DOEs which take fabrication and light source limitations into account, to improve practical DOE performance.

2.1 Main DOE types classifications

The different types of DOEs can be classified in numerous ways (see [2]). Here we will classify them mainly by the light modulation type and diffraction regime. DOEs or CGHs are often classified into two categories according to their light modulation: Amplitude modulation DOE (ADOE) and Pure phase DOE (PDOE) or low lossless DOEⁱ, see schematics shown in **Figure 2-1**.

ⁱ This classification applies best to thin DOEs modelled with the thin element approximation. More complex classification is required when using rigorous models which take propagation inside the DOE structure into account.

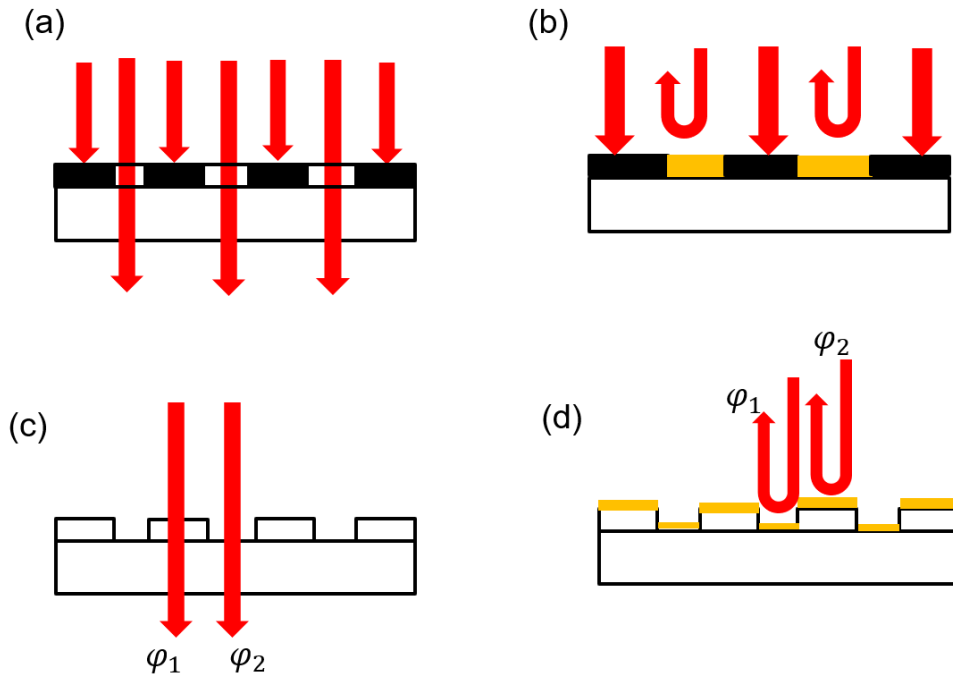


Figure 2-1- (a) Schematic of transmissive type ADOE. (b) Schematic of reflection type ADOE. (c) Schematic of transmissive type PDOE. (d) Schematic of reflection type PDOE.

An ADOE manipulates the incoming wavefront by modulating light transmission (transmissive DOE) or reflection (reflection DOE) for different zones (“pixels”) of the DOE, while PDOE manipulate the wavefront through controlling the phase delay of each zone (pixel). Since the incident light can totally pass through a PDOEs with no (or negligible) absorption, PDOEs can reach much higher optical efficiencies than ADOEs and they are therefore more effective. In this thesis, the PDOE is chosen as the research subject due to its high diffraction efficiency. Another useful DOE classification is that of diffraction regime or distance. Diffraction patterns can be observed in the Fresnel region or the far field region depending on the design method used for the DOE, as illustrated in **Figure 2-2**.

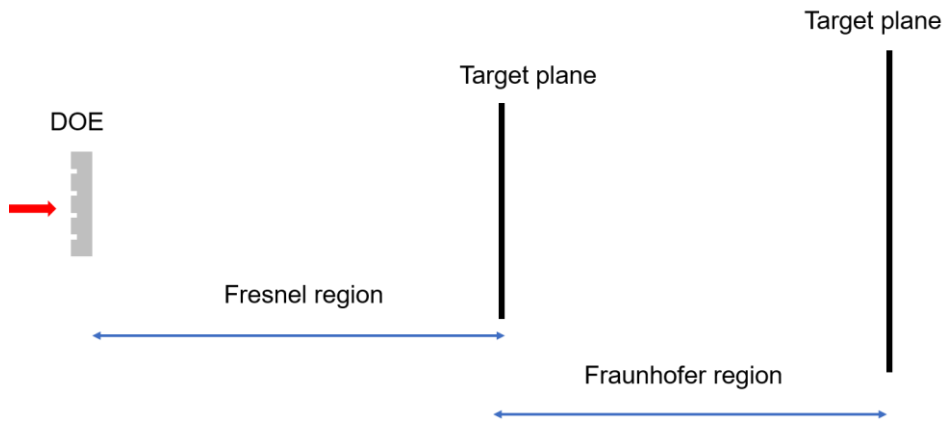


Figure 2-2- Configurations of the diffraction propagation of a DOE.

When a Farfield diffraction propagation operator (Fraunhofer diffraction method)

is used in DOE design, a far field pattern can be reconstructed by illuminating a plane wave on the DOE. This kind of DOE can be called Fourier type DOE, whose observation distance can be reduced by illuminating the DOE converging light or using a convex lens (see **Figure 2-3**).

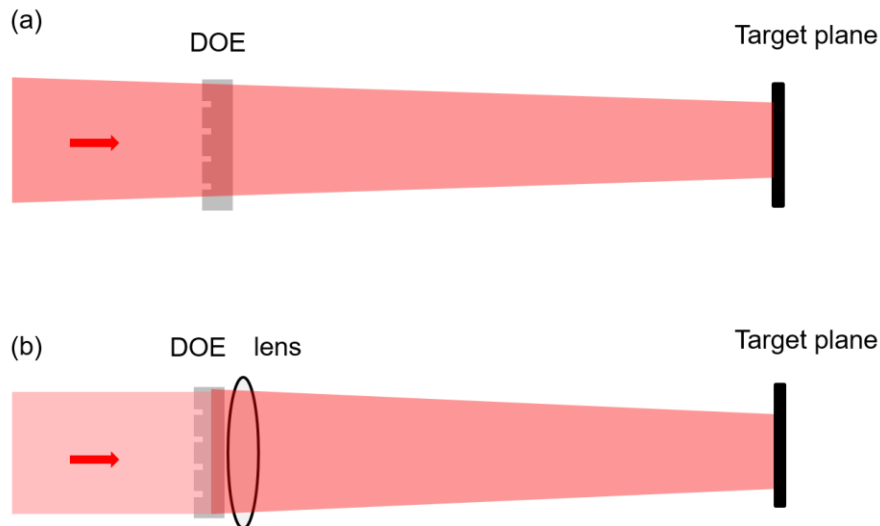


Figure 2-3-Alternative configuration of the Fourier type DOE beam shaper.

A Fourier type DOE can be used as beam splitter and beam shaper. On the other hand, if a Fresnel diffraction or angular spectrum propagation operator (angular spectrum diffraction propagation) is utilized, a Fresnel type DOE is formed after design. Fresnel DOE can be used in realizing security holograms which can produce a floating virtual object behind the hologram substrate, and as micro-lens for light homogenization and light field displays [16-20]. **Figure 2-4** depicts examples of Fourier and a Fresnel DOEs.

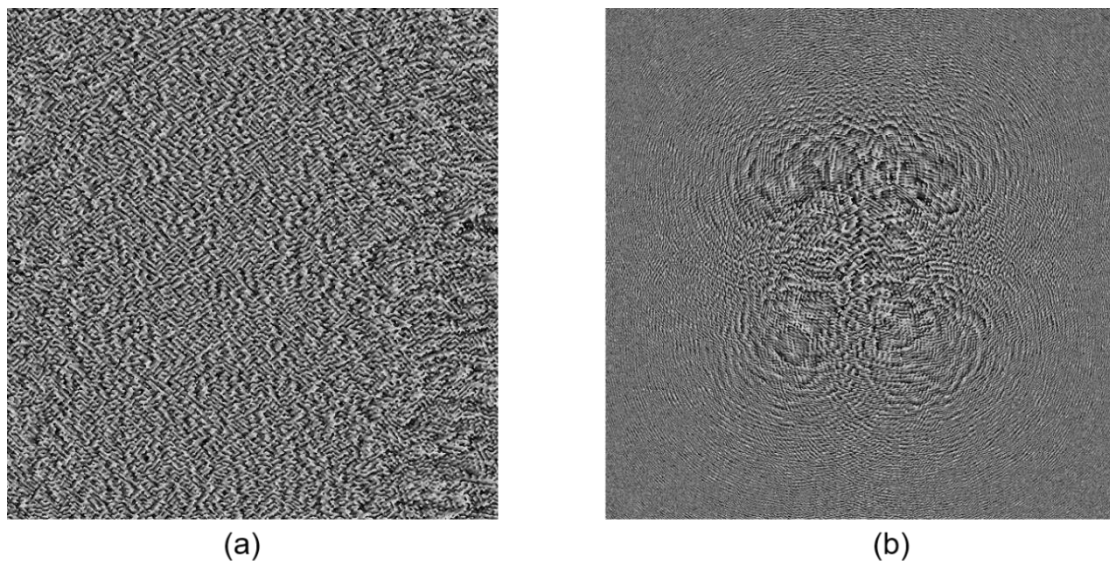


Figure 2-4- Typical Fourier type DOE and Fresnel type DOE (Gray level represents local phase).

The effective optical thickness of most DOEs is around one wavelength, such DOEs

are called thin DOEs. If the optical thickness of a DOE is much higher (larger than five wavelengths) than that of a thin DOE, they can be regarded as optically thick DOEs, which usually have wavelength selective effect.

When the feature size of a thin DOE is much bigger than the wavelength (10 times the wavelength), the simpler scalar diffraction model is commonly used to compute the diffraction pattern. For the scalar diffraction model, the components of the electromagnetic field are regarded as the same, so coupling effects between these components are neglected. When the feature size reduces down to the subwavelength range, a full-wave analysis method such as FDTD [21] or RCWA [22, 23] must be used to calculate all the electromagnetic components. The design of a DOE belongs to the phase retrieval problem set, the algorithm for optimizing the DOE's surface relief structure should be developed to reconstruct the output pattern as close as possible to the target pattern, if possible by incorporating the photo-lithographic fabrication limitations.

In the following sections, the calculation method for the vector diffraction and scalar diffraction models are presented based on Maxwell's equations. The selection criteria of the vector diffraction model are described. The various diffraction propagation methods used in this thesis are also demonstrated and compared in detail. These models are the core of the iterative algorithms we have developed to compute and optimize the topology of the diffractive optical elements (DOEs).

2.2 General introduction for DOE

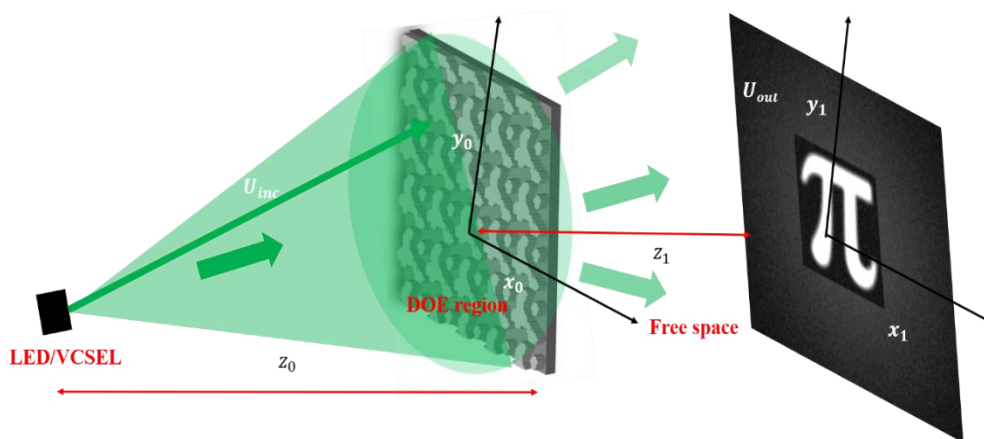


Figure 2-5- Schematic of 2D DOE design. To solve the optimization problem, the propagation region is divided into two diffraction regions, where U_{inc} and U_{out} are the electric and magnetic field.

Figure 2-5 depicts the schematic of a typical DOE for beam shaping in two dimensions, where U_{inc} is the illuminating light field, which is usually a plane, converging or divergent spherical wave. The incident light wave U_{inc} is modulated by the complex amplitude of the DOE in the DOE region. After the light and DOE's surface

relief interaction, the outgoing diffraction light is free space propagated from the DOE to the observation plane, then $U_{out}(x, y)$ is obtained on the observation plane. The DOE design problem is fundamentally to find the optimal solution of the DOE transmittance function such that the reconstruction result formed in the target plane is as close as possible to the target pattern. The diffracted field at the DOE plane and the observation plane are $U_0(x_0, y_0; 0)$ and $U_{out}(x_1, y_1; z)$, the sampling intervals Δ_1 and Δ_2 on DOE plane and target plane are chosen to satisfy Nyquist sampling theorem. To get a rigorous solution of this diffraction field, Maxwell's equations are used. In this thesis, the propagation process is in linear, isotropic and nondispersive medium without charges $\rho=0$ and currents ($J=0$). The diffracted field $U_0(x_1, y_1; 0)$ comprises electric field component E and magnetic field component H , which can be expressed as below[24]:

$$E(r, t) = \mathbf{E}_0(r)e^{-i\omega t} \quad (2.1)$$

$$H(r, t) = \mathbf{H}_0(r)e^{-i\omega t} \quad (2.2)$$

Substituting eq.(2.1) and eq.(2.2) into the Maxwell's functions:

$$\nabla \times \mathbf{H}_0 + ik_0 \varepsilon \mathbf{E}_0 = 0 \quad (2.3)$$

$$\nabla \times \mathbf{E}_0 - ik_0 \mu \mathbf{H}_0 = 0 \quad (2.4)$$

$$\nabla \cdot \varepsilon \mathbf{E}_0 = 0 \quad (2.5)$$

$$\nabla \cdot \mu \mathbf{H}_0 = 0 \quad (2.6)$$

In the above equations, the electric and magnetic fields are represented by E_0 and H_0 . The operators \times means the vector cross product, and \cdot represents vector dot product. And, $\nabla = (\frac{\partial}{\partial x} + \frac{\partial}{\partial y} + \frac{\partial}{\partial z})$. The permittivity and permeability of the propagating medium are represented by ε and μ , respectively. From eq.(2.3)-eq(2.6), the six components ($E_{0x}, E_{0y}, E_{0z}, H_{0x}, H_{0y}, H_{0z}$) are usually numerically solved by using Finite -Difference-Time-Domain (FDTD) [21] or Rigorous Coupled wave Analysis (RCWA) methods [22]. In general, full wave methods are used in calculating the diffraction field in the DOE region, and free-space diffraction propagating operators are used to calculate the far-field diffraction pattern.

2.3 DOE models

2.3.1 Thin Element approximation

According to the thin element approximation (TEA) model, the light field diffracted inside the DOE structure is ignored. In addition, the illuminating light is transmitted through the DOE structure without absorptions without changing diffraction direction. The light field after passing through the DOE's surface structure can be computed approximately as the multiplication of the transmission function of the DOE structure $T(x_0, y_0)$ with the incident light field U_{inc} with [25, 26]

$$U_1(x_0, y_0; 0) = T(x_0, y_0)U_{inc} \quad (2.7)$$

Usually, $T(x_0, y_0)$ is a complex function, which is expressed by

$$T(x_0, y_0) = A(x_0, y_0) \exp(j\varphi(x_0, y_0)) \quad (2.8)$$

Where $A(x_0, y_0)$ is the amplitude modulation by the DOE, and $\varphi(x_0, y_0)$ is the phase delay because of the passing through the DOE structure. Considering the high diffraction efficiency requirement, pure phase type DOEs are always used in this thesis. This means the $A(x_0, y_0)$ is usually set as constant (1) within the DOE contour (see **Figure 2-5**, the DOEs usually have a square aperture) without considering absorption or Fresnel reflection on the surface of the DOEs. **Figure 2-6** shows an M levels pure phase type DOE which is illuminated by a plane wave at normal incidence in free-space. The effective optical path difference (OPD) between the two separate isotropic medium thicknesses for a step height of Δh can be written as $\Delta OPD = (n-1)\Delta h$. So, the phase shift between the two layers can be expressed as $\Delta\varphi = k \cdot (n-1)\Delta h$. Here, k is the wave number, and n is the refractive index of the DOE. If the DOE has an M-level structure, the total DOE thickness should be $h = (M-1)\Delta h$, resulting in:

$$h = \frac{M-1}{M} \frac{\lambda}{n-1} \quad (2.9)$$

This kind of approximation is valid when the DOE's thickness corresponded to a phase shift smaller than 2π and its feature size is significantly larger than the wavelength (> 5 wavelengths) [26]. In these conditions, polarization effects can usually also be ignored because the output light fields for different polarization states are almost identical when the TEA model is valid. When these conditions are not satisfied, the diffraction field inside the DOE will reduce the calculation accuracy. In such cases, vector diffraction models such as FDTD or RCWA have to be used to get the exact calculation results of DOEs.

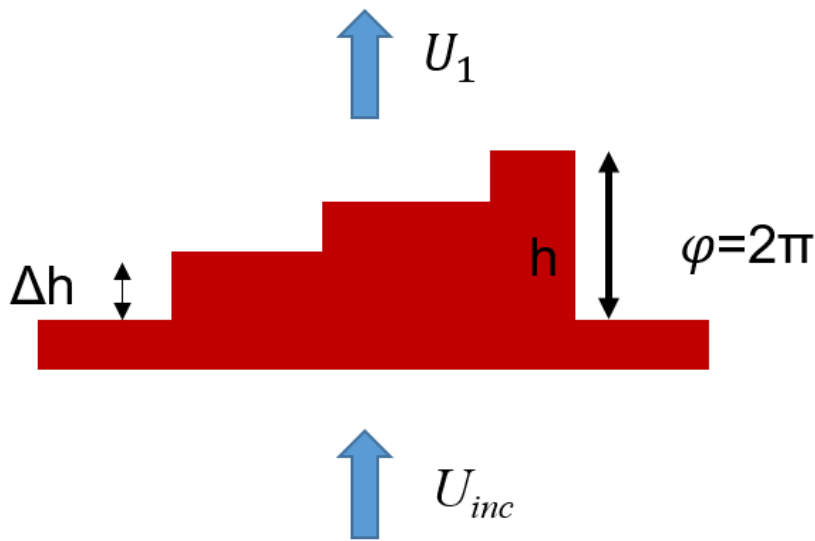


Figure 2-6-Structure of the M-level DOE. U_{inc} is the illuminating light, and U_1 is the diffraction field after the DOE.

2.3.2 Rigorous model in the thick DOE region

Except for the thin structure mentioned above, when the size of structures in the DOE or gratings becomes comparable to the wavelength of the incident light, the IFTA [27-29] based on the thin element approach, which is one of the most popular algorithms, cannot be applied to optimize the DOE because rigorous method have to be applied. The FDTD [21], FEM [30], RCWA [23] methods all offer rigorous EM solvers which can be used in calculating the diffraction field inside the DOE structure. But, the FDTD and FEM methods are often limited to a small scale, about ten times the wavelengths because of calculation load.

RCWA also called Fourier Modal Method (FMM) is a semi-analytical solution which can be applied for infinite periodic structures with a lower the calculation complexity and load. In this thesis, we aim to design large area thick DOE structures for wavelength selectivity. Periodic structures can be repeated to give large area photonics structures, so the FMM was chosen to optimize a single period of thick structures. The basic principle of RCWA is described here, more details can be found in the literature [22].

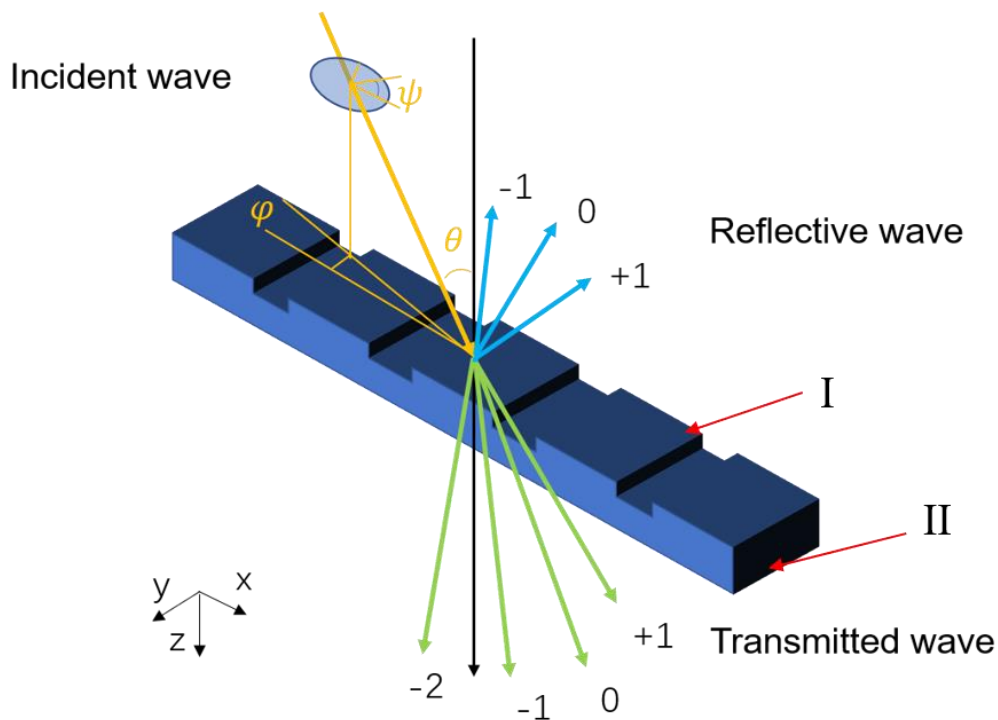


Figure 2-7- Geometry schematic of a binary phase grating diffraction.

The geometry schematic of the binary phase relief grating is sketched in **Figure 2-7**. In **Figure 2-7**, the grating structure is in region I and the substrate is in region II. The incident light is assumed to be a plane wave expressed using u_0 , θ is the incident angle, ψ represents the polarization angle, and φ means the azimuth angle. The ambient refractive index of is n_1 , the refractive index of the grating area is represented

by n_2 , the grating thickness is d , and the grating periods along the x and the y directions are depicted by Δ_x, Δ_y , respectively.

To simplify the illustration of the vector diffraction model for a binary grating, we assume that $\varphi = 0$, $\psi = 90^\circ$ (TE polarization state). Therefore, the incident electric field on the binary grating can be given as:

$$\vec{E}_0 = \vec{u} \exp(-j\vec{k}_0 \cdot \vec{r}) \quad (2.10)$$

In eq.(2.10), \vec{u} is expressed as below.

$$\vec{u} = (\cos \psi \cos \theta \vec{e}_x + \sin \psi \vec{e}_y - \cos \psi \sin \theta \vec{e}_z) = \sin \psi \vec{e}_y \quad (2.11)$$

Where, $k_0 = \frac{2\pi}{\lambda}$, λ is the wavelength of light in the vacuum. The harmonic diffraction orders along the x -axis and y -axis are denoted by m, n , respectively. The maximum number of harmonic diffraction orders along the x -axis and y -axis are M and N . Therefore, the total number of diffraction orders are $I = 2M + 1$, $J = 2N + 1$ in two directions, respectively. The number of the Fourier expansion order of the binary grating is the same as the harmonic diffraction order. The normalized electric fields in regions I and II can be expressed as below.

$$\vec{E}_I = \vec{E}_0 + \sum_{m,n} \vec{R}_{m,n} \exp(-j\vec{k}_{I,m,n} \cdot \vec{r}) \quad (2.12)$$

$$\vec{E}_{II} = \sum_{m,n} \vec{T}_{m,n} \exp[-1i \times \vec{k}_{II,m,n} \cdot (\vec{r} - \vec{d})] \quad (2.13)$$

In eq.(2.12) and eq.(2.13), $\vec{R}_{m,n}$, $\vec{T}_{m,n}$ are the reflection electric field and the transmission electric field of each harmonic diffraction order in the grating region I and substrate region II, respectively. $\vec{R}_{m,n}$, $\vec{T}_{m,n}$ can be obtained by solving the differential Maxwell's equation using the FMM incorporating the periodic boundary conditions of the binary grating. The reflected and transmitted waves of each level are shown in **Figure 2-7**. Here, we have briefly introduced the vector diffraction model of the binary grating, a more detailed model description for multilevel grating can be found in [31].

Once the light field near to the DOE plane has been obtained, the diffraction field in the Fresnel or Fourier regions can be calculated using free-space propagation method since the vector diffraction model is usually not applicable in this region due to the heavy computation complexity. The far field is calculated by combining the result of TE polarization state and TM polarization state. In the next section, the most common diffraction propagators will be described.

2.4 Formulae for free-space diffraction propagation[6]

2.4.1 Helmholtz equation

Since the propagation medium is homogeneous in the free-space region, the polarization coupling effect can be neglected. Therefore, Maxwell functions can be simplified to an elegant scalar wave equation as below [24].

$$\nabla^2 u(r, t) - \frac{n^2}{c} \frac{\partial^2}{\partial t^2} u(r, t) = 0 \quad (2.14)$$

Usually, $u(r, t)$ can be expressed as

$$u(r, t) = A(r) e^{-j\varphi(r)} e^{-j\omega t} \quad (2.15)$$

Where $A(r)$ and $\varphi(r)$ are the amplitude and phase delay of the light wavefront, respectively. Substituting eq.(2.15) into eq.(2.14), the Helmholtz equation is obtained as follow.

$$(\nabla^2 + k^2)U(\mathbf{r}) = 0 \quad (2.16)$$

Where, k is the wave number. Eq.(2.16) is usable in any monochromatic light propagation in a homogenous dielectric medium. The diffraction propagation of an electromagnetic field in free-space can be solved correctly using the Helmholtz equation. Through further derivation this scalar equation can be simplified to an more useful formula: the angular spectrum expression.

2.4.2 The Angular Spectrum Method

Through solving the Helmholtz function (eq. (2.16)), the angular spectrum method (ASM) formula can be obtained. In the terms of ASM, the diffraction field emitted from the source plane can be decomposed into numerous harmonic plane waves propagating according to their direction cosines. In this situation, this calculation method has another name which is the angular spectrum of plane waves [32, 33]. The angular spectrum in K -space (spatial frequency space) of the diffraction field on the observation plane can be calculated by using a Fourier Transform (FT) [3] :

$$A(f_x, f_y; z) \propto \iint_{-\infty}^{+\infty} U(x_2, y_2; z) \exp[-j2\pi(f_x x_2 + f_y y_2)] df_x df_y \quad (2.17)$$

Where, z is the distance between the light source plane and the observation plane, and f_x, f_y are the spatial frequencies. The FT operator can be regarded as a decomposition of a complicated light source into a collection of harmonic plane waves. Therefore, the spatial light field distribution on the observation plane can be expressed using an Inverse Fourier Transform (IFT) its corresponded spectrum:

$$U(x_2, y_2; z) \propto \iint_{-\infty}^{+\infty} A(f_x, f_y; z) \exp[j2\pi(f_x x_2 + f_y y_2)] df_x df_y \quad (2.18)$$

In eq. (2.17) and eq. (2.18), the proportionality symbol \propto is used because the constant complex number in front of the diffraction integral is neglected. This operation is reasonable since only the intensity information of the light field can be detected using the state-of-the-art measurement method. The measured intensity can be normalized without affecting the intensity distribution.

In general, the light field $U(x_2, y_2; z)$ should also obey the Helmholtz equation. By substituting eq.(2.18) into eq.(2.16), and further derivation, the solution of the spectrum can be written as [3]:

$$A(f_x, f_y; z) = A(f_x, f_y; 0)H(f_x, f_y; z) \quad (2.19)$$

Where $H(f_x, f_y; z) = \exp(jkz\sqrt{1 - \lambda^2(f_x^2 + f_y^2)})$ is the Transfer function which can produces phase delay when the light propagates. $A(f_x, f_y; 0)$ is the Fourier transform of the light field at the source plane. The diffraction field on the observation plane is expressed by:

$$U(x_2, y_2; z) \propto \iint_{-\infty}^{+\infty} A(f_x, f_y; 0)H(f_x, f_y; z) \exp[j2\pi(f_x x_2 + f_y y_2)] df_x df_y \quad (2.20)$$

Further, the ASM can be calculated directly as below, using a FT operator

$$U(x_2, y_2; z) \propto IFT[A(f_x, f_y; 0)H(f_x, f_y; z)] \quad (2.21)$$

In practice, all the direction cosines of the harmonic wave that can propagate should be real. Those harmonic waves that can only propagate smaller than a few wavelengths from the source plane are evanescent waves. Therefore, to remove the contribution of the evanescent light field, a circ function should be added into eq. (2.21). Hence, eq.(2.21) can modified as follow:

$$U(x_2, y_2; z) \propto IFT \left[A(f_x, f_y; 0)H(f_x, f_y; z) \cdot \text{circ} \left(\lambda \sqrt{f_x^2 + f_y^2} \right) \right] \quad (2.22)$$

The sampling distance is δ_{in} at the source plane, therefore the spatial frequencies f_x, f_y should be sampled with $\delta_f=1/(N\delta_{in})$ according to the discrete FT property. The main drawback of the ASM is that the sampling distance at the source plane and the output plane should be the same ($\delta_{out}=\delta_{in}$) which often limits the numerical simulation to a small region. Moreover, the transfer function $H(f_x, f_y; z)$ must be adequately sampled to reduce the frequency aliasing effect. Therefore, the phase term in the transfer function must satisfy the sampling condition [34, 35]. Without loss of generality, here we only consider one-dimension. The sampling condition can be expressed as follows.

$$\frac{1}{2\pi} \left| \frac{\partial \varphi_H}{\partial f} \right|_{max} \leq \frac{1}{2\delta f}, \quad \varphi_H = 2\pi z \sqrt{\lambda^{-2} - f^2} \quad (2.23)$$

By substituting $|f|_{max} = N\delta f/2$, $\delta_f=1/(N\delta_{in})$ into eq.(2.23), the valid propagation distance z is obtained as below.

$$z \leq \frac{N\delta_{in}^2}{\lambda} \sqrt{1 - \frac{\lambda^2}{4\delta_{in}^2}}, \delta_{in} \geq \lambda/2 \quad (2.24)$$

According to eq.(2.24), the ASM is only valid for short propagation distances without producing numerical artifacts. In other words, this diffraction propagating method is limited to the calculation of light field calculation near to the DOE [34]. An effective method to extend the propagation distance of the ASM is the zero-padding technique [35]. Generally, the padding factor is 2, which means the $\delta_{in} = 1/(2N\delta_{in})$. By using analogous derivation, the diffraction distance should satisfy $z \leq 2 \frac{N\delta_{in}^2}{\lambda} \sqrt{1 - \frac{\lambda^2}{4\delta_{in}^2}}$, which is two times that without the zero padding technique.

2.4.3 The Rayleigh-Sommerfeld diffraction formula

The Rayleigh Sommerfeld (RS) diffraction formula is derived from a model of the Huygens-Fresnel principle, which is expressed as [3] :

$$U_i(x_i, y_i) = \frac{1}{j\lambda} \iint U_0(x, y; 0) \left(jk - \frac{1}{r} \right) \frac{e^{jkr}}{r^2} dx dy \quad (2.25)$$

In eq.(2.25), r is the distance between an arbitrary point $P_0(x, y)$ at the DOE plane to an arbitrary point $P_i(x_i, y_i)$ in the target plane.

$$r = \sqrt{(x_i - x)^2 + (y_i - y)^2 + z^2} \quad (2.26)$$

Eq.(2.25) can be calculated as a convolution of the light field $U_0(x, y; 0)$ at DOE plane with an impulse response function in the propagating medium [36].

$$h(x, y; z) = \left(jk - \frac{1}{r} \right) \frac{e^{jkr}}{r^2} \quad (2.27)$$

To reduce numerical artifacts, the phase term of the impulse response $h(x, y; z)$ needs to be adequately sampled. Since the propagation distance is much larger than the wavelength, the phase term can be approximated to

$$\varphi_h = kr + \pi/2 \quad (2.28)$$

where $r = \sqrt{z^2 + x^2}$. By using a derivation method similar to that mentioned above, the propagating distance should satisfy the follow condition [35]:

$$z \geq \frac{N\delta_{in}}{\lambda} \sqrt{1 - \frac{\lambda^2}{4\delta_{in}^2}}, \delta_{in} \geq \frac{\lambda}{2} \quad (2.29)$$

According to the eq.(2.29) and eq.(2.24), we can see that these validity regions are complementary. That's to say RS diffraction formula can be used for the case when the

ASM is invalid. The RS formula belongs to the set of scalar nonparaxial diffraction propagation operators. In most practical DOE applications, the far field distribution is the most useful. Therefore, it makes sense to get a modified far field RS formula by using single FT operator. Eq.(2.26) can be modified as below by use of a first-order Taylor expansion [37].

$$\begin{aligned}
 r &= \sqrt{(x_i - x)^2 + (y_i - y)^2 + z^2} \\
 &= \sqrt{x_i^2 + y_i^2 + z^2} + \left(x_i \left[\frac{\partial r}{\partial x_i} \right] + y_i \left[\frac{\partial r}{\partial y_i} \right] \right) \\
 &= \sqrt{x_i^2 + y_i^2 + z^2} - \frac{xx_i + yy_i}{\sqrt{x_i^2 + y_i^2 + z^2}}
 \end{aligned} \tag{2.30}$$

Then, letting $k_x = \frac{x_i}{\lambda(x_i^2 + y_i^2 + z^2)^{1/2}}$, $k_y = \frac{y_i}{\lambda(x_i^2 + y_i^2 + z^2)^{1/2}}$. The diffraction field on the target plane can be expressed in K-space as below.

$$U_i(k_x, k_y) = \frac{(1 - \lambda^2 k_x^2 - \lambda^2 k_y^2)}{i\lambda z} \exp\left\{i \frac{2\pi}{\lambda} z (1 - \lambda^2 k_x^2 - \lambda^2 k_y^2)^{-\frac{1}{2}}\right\} \times F\{U_0(x, y)\} \tag{2.31}$$

From eq.(2.31), we can see that the diffracted light field can be calculated by implementing single FT operator. This modified formula is very useful for designing wide diffraction angle DOEs.

In practical DOE optimization, the Iterative Fourier Transform Algorithm (IFTA) [29] is commonly used. Therefore, fast diffraction calculation methods are required. Although the modified RS formula is accurate, but it is slow for IFTA design. In many applications, the DOE's diffraction angle is not large (smaller than 30 degrees). Therefore, it is helpful and possible to modify the RS formula to get a paraxial formula for DOE design.

2.4.4 Paraxial approximation diffraction models

Paraxial Angular spectrum Method

Considering small diffraction angles, the angular spectrum can be rewritten as [38]:

$$U(x_2, y_2; z) \propto \iint_{-\infty}^{+\infty} A(f_x, f_y; 0) H(f_x, f_y; z) \exp[j2\pi(f_x x_2 + f_y y_2)] df_x df_y \tag{2.32}$$

Where $H(f_x, f_y; z) = \exp[-jk\lambda z(f_x^2 + f_y^2)]$ is the paraxial transfer function, The equation is the paraxial form of the non-paraxial ASM which is only valid under paraxial approximation. For fast calculation, $U(x_2, y_2; z)$ can written in a single FT operator as below.

$$U(x_2, y_2; z) \propto IFT[A(f_x, f_y; 0)H(f_x, f_y; z)] \tag{2.33}$$

Similarly, the sampling condition for one dimension should be [34]:

$$\frac{1}{2\pi} \left| \frac{\partial \varphi_H}{\partial f} \right|_{max} \leq \frac{1}{2\delta f}, \quad \varphi_H = -k\pi z f^2 \quad (2.34)$$

From eq.(2.34), the validity region of the paraxial transfer function is $z \leq \frac{N\delta_{in}^2}{\lambda}$, which means that the paraxial ASM can only be used for numerical simulations for short propagation distances.

To expand the paraxial diffraction distance, some approximation for the distance r should be used in a modified RS formula, resulting in Fresnel diffraction approximation.

Fresnel approximation

In the Fresnel approximation, we assume that the propagation distance z is much larger than the wavelength and aperture. Therefore, the RS formula can be modified as [3]:

$$U_i(x_i, y_i) = \frac{1}{j\lambda} \iint_{-\infty}^{+\infty} U_0(x, y, 0) \frac{e^{jkr}}{r^2} dx dy \quad (2.35)$$

Since the propagation distance z is far enough at a small diffraction angle (less than 10 degrees), r in the denominator is approximately equal to z . In addition, in the exponential term r can be written approximately as follow by using binomial expansion method

$$r \approx z + \frac{(x_i-x)^2+(y_i-y)^2}{2z} \quad (2.36)$$

Substituting r in eq.(2.36) into eq.(2.35), the diffraction field on the target plane can modified as below.

$$U_i(x_i, y_i) = \iint_{-\infty}^{+\infty} U_0(x, y, 0) \exp \left[j \frac{k}{2z} [(x_i - x)^2 + (y_i - y)^2] \right] dx dy \quad (2.37)$$

We can continue to simplify the equation by extracting the constant phase term out of the integral, and rearranging the equation. Then the Fresnel diffraction formula for the paraxial approximation is obtained as follows.

$$U_i(x_i, y_i) = \iint_{-\infty}^{+\infty} U_0(x, y, 0) \exp \left[j \frac{k}{2z} (x^2 + y^2) \right] e^{-j \frac{2\pi}{\lambda z} (xx_i + yy_i)} dx dy \quad (2.38)$$

Eq (2.38) can also be evaluated using single FT operator:

$$U_i(x_i, y_i) = \frac{e^{jkz}}{j\lambda z} \exp \left[j \frac{k}{2z} (x_i^2 + y_i^2) \right] FT \left\{ U_0(x, y, 0) \exp \left[j \frac{k}{2z} (x^2 + y^2) \right] \right\} \quad (2.39)$$

According to the discrete FT property, the sampling distance in the target plane can be expressed as:

$$\delta_2 = \frac{\lambda z}{N\delta_1} \quad (2.40)$$

The sampling requirement for Fresnel propagation is [39].

$$\delta x \left| \frac{\partial \varphi_h}{\partial x} \right|_{max} \leq \pi, \quad \varphi_h = kx^2/2z \quad (2.41)$$

By solving eq.(2.41), we can obtain the validity region for Fresnel diffraction propagation as below:

$$z \geq \frac{N\delta_{in}^2}{\lambda} \quad (2.42)$$

Compared to the validity region for paraxial ASM, the regions are complementary. If an optical engineer wants to generate a far-field diffraction pattern using a Fourier type DOE, the Fresnel propagation formula can be further simplified by using the Fraunhofer approximation.

Fraunhofer approximation

In general, if the light field is produced in the far-field, the distance z should be much larger than the aperture size of the DOE. It means the quadratic phase term $\exp \left[j \frac{k}{2z} (x^2 + y^2) \right]$ is near to constant (1) across the whole aperture. Therefore, the Fresnel propagation formula can be simplified further as below [3]:

$$U_i(x_i, y_i) \propto \iint_{-\infty}^{+\infty} U_0(x, y, 0) e^{-j \frac{2\pi}{\lambda z} (xx_i + yy_i)} dx dy \quad (2.43)$$

From eq.(2.43), we can recognize a direct FT of the incident light field. This is called Fraunhofer diffraction. The validity region can be obtained by similar consideration as:

$$z \gg \frac{2D^2}{\lambda} \quad (2.44)$$

Where D is the diameter of the effective aperture. Because Fraunhofer diffraction is only a special case of Fresnel diffraction, the sampling criterion is the same as eq. (2.40). Usually, the Fraunhofer diffraction pattern is obtained in the far-field, but it can also be obtained by implementing a converging illumination or placing a positive lens near to the DOE. The wavefront positive lens or converging spherical wave is equivalent to the phase term $\exp \left[-j \frac{k}{2z} (x^2 + y^2) \right]$ [3].

2.5 DOE design algorithms

The basic diffraction propagation models have been presented, they constitute one part of the DOE or CGH design process. Another important part is the design algorithm. In general, the quality of a DOE is evaluated according to the specific application. Usually, the figure of merit (FOM) is defined using the diffraction efficiency

$$\eta = I_{signal}/I_{incident}, \quad \text{and the mean square error } MSE = \frac{1}{MN} \sum_1^M \sum_1^N (I_{rec} - I_{target})^2 \quad [40].$$

Where I_{signal} and $I_{incident}$ are the diffracted light power in the signal window and the total power of the incident light, respectively, where the signal window [7] is defined in

Figure 2-8. I_{rec} and I_{target} are the diffracted light power of the reconstruction and target images, respectively.

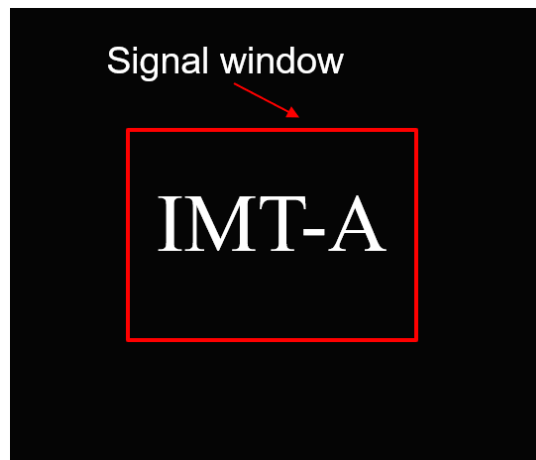


Figure 2-8-The definition of the signal window of the output plane.

Over the past forty years, many DOE design algorithms have appeared. Here, the mainstream algorithms for DOE design are illustrated. The algorithms for DOE calculation can be divided into two categories. The first are unidirectional algorithms, and the second are called bidirectional algorithm. The mainstream unidirectional algorithms include direct binary search (DBS) [41,42], optimal-rotation-angle [43], particle swarm optimization (PSO) [44,45], genetic algorithm(GA) [46-48]. The most popular bidirectional algorithm is IFTA [29] and its modified forms [49,50].

2.5.1 Unidirectional algorithms

Unidirectional algorithms are widely used in Fresnel and Fourier type DOE design [51], where the diffraction field can only be calculated in the forward direction during the DOE design.

2.5.2 Direct Binary Search

The basic principle of Direct Binary Search (DBS) is to scan all of the phase levels of the DOE in a pixel by pixel method, and accept the phase level for each pixel giving the optimal reconstructed pattern. The optimal DOE solution can be reached at the expense of a huge number of iterations using DBS method. This drawback limits DBS approach which can only be applicable in DOE design with small number of pixels for example a DOE beam splitter. In practical DOE design the DBS begins with a random phase solution [51]. Then, one pixel of the DOE is chosen at a time to change the phase level if it contributes positively to the figure of merit of the reconstructed result. The DBS optimization process repeats until no single pixel alteration. By using this method,

the modified DBS can converge to an optimal DOE solution within a smaller number of iterations. The detailed flowchart of the DBS is illustrated in **Figure 2-9**. However, these algorithms usually fail to find the global optimal DOE phase solution.

To reach a global optimum (see in **Figure 2-10**), more complex algorithms have been developed, for example PSO [44] and GA [46].

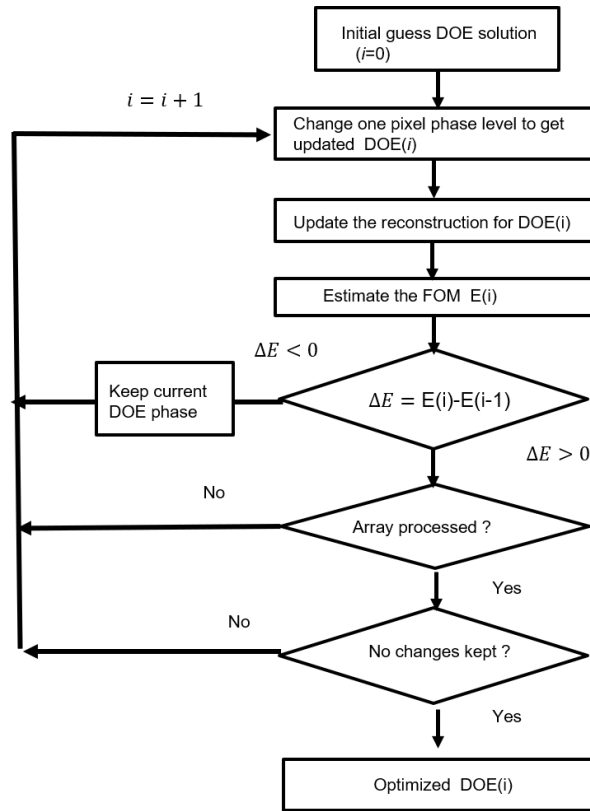


Figure 2-9-The flow chart of a basic DBS algorithm for DOE design.

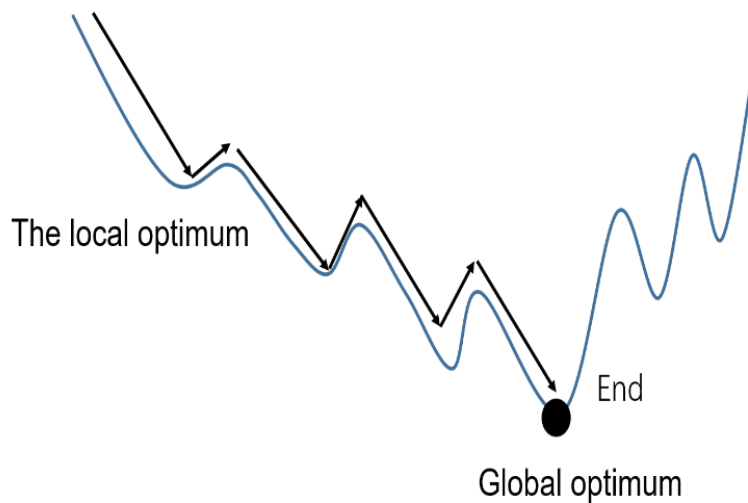


Figure 2-10-Global optimization for converging to the global optimum.

Particle swarm optimization

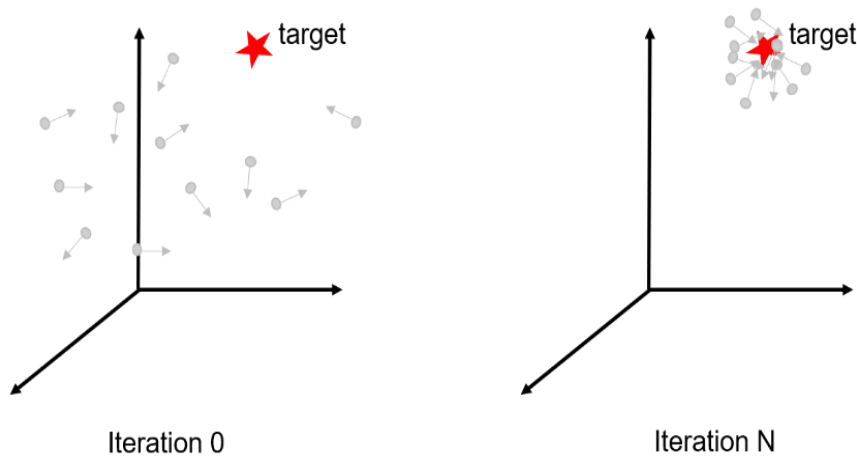


Figure 2-11-The basic principle of particle swarm optimization.

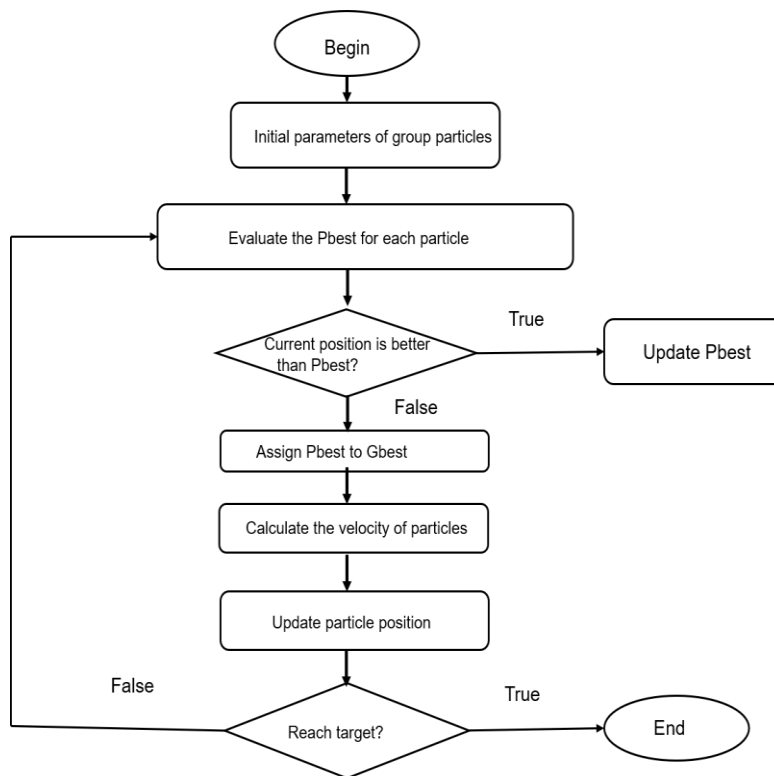


Figure 2-12- The general flow chart of PSO. The Pbest means the individual optimal solution in current iteration, and the Gbest is the global optimal solution.

PSO was first proposed by Kennedy and Eberhart , and has been widely applied to the inverse design of photonic structures [52-54]. The inspiration originates from an analogy with the processes followed by bird group’s foraging. In the basic PSO model, the possible solution can be abstracted as an individual particle without mass and volume in N dimensional space. Each particle has its own velocity, position, and figure

of merit in the N dimensional search space. In the beginning of PSO, a group of particles are initialized with random velocities and positions. Then, each particle moves toward to the current optimal particle in the searching space. After several iterations, the best solution can be found out. According to the mathematical model of PSO, we can regard one DOE estimation as a particle. The best solution is obtained when a swarm of particles moves to the optimal destination. Compared to DBS, PSO can jump out of a local optimum (see **Figure 2-10**). But, one disadvantage is that PSO converges slowly due to its random pixel change. On the other hand, the final optimum solution is always dependent on the initial input estimations. To help understand the basic PSO algorithm, **Figure 2-11** shows the basic principle, and the **Figure 2-12** depicts the general flowchart of the PSO.

Genetic Algorithm

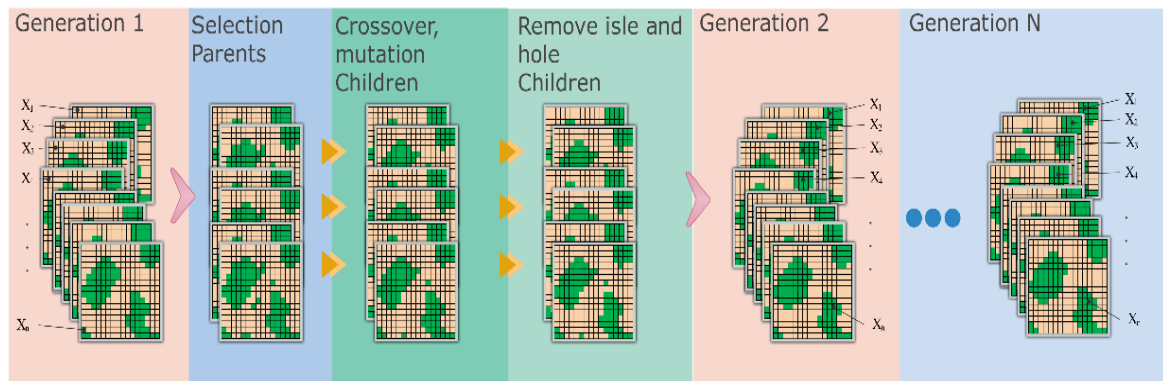


Figure 2-13- The principle flowchart of a general GA method. Here, $x_i(i=1,2,\dots,n)$ means one possible DOE solution.

Another important global algorithm is the famous genetic algorithm [47] and its modified versions. The basic flowchart is shown in **Figure 2-13**. This method originates from natural evolution, the central idea is “survival of the fittest”. The algorithm mimics evolution by using crossover, selection and mutation. Similar to the PSO, GA uses a large number of DOE estimate solutions to produce the first generation. First, the forward diffraction propagation formula is used to calculate the diffraction field of all the DOE estimate solutions on the target plane; then, the figure of merit is evaluated to select the higher performance DOE estimate solution from the first generation. After this process, new generations are produced by introducing individual cross-overs and mutations. These steps are repeated until an optimum is found. Usually, a few mutations are introduced to the iterations to avoid stagnation effects. Through these operations, GA can converge to the globally optimal DOE solution. Similar to PSO, this algorithm depends strongly on the initial estimations, and on the parameters selection for DOEs with a crossover and mutation. In addition, it converges slowly which is not suitable for DOE with a large number of pixels, but well adapted to the grating type DOE design such as beam splitters. In fact, optical engineers usually combine the DBS and PSO to

get a better solution than when only one type unidirectional algorithm is used. Because PSO and GA are both dependent on the initial estimations, DBS is often used to generate the improved initial DOE estimate solutions for GA or PSO. In this way, a global DOE solution can be found more efficiently. Despite, this bidirectional algorithm is still more suitable for large size DOE.

2.5.3 Bidirectional algorithm

In most applications, such as beam splitter [55], beam shaper [56] and DOE diffuser design [57], the DOE's phase map can be inversely computed from the complex amplitude field at the target plane. However the DOE performance is often low by using this direct method. To address this problem, a bidirectional algorithm can be a good choice for the optical engineer, because the iterative method can significantly reduce the reconstruction error through several iterations. The basic IFTA method is presented in **Figure 2-14** [58]. The initial estimation for the target field is usually obtained by taking the target pattern's amplitude value, and adding random phase values ranging from $0-2\pi$. After parameter initialization, the inverse diffraction operation is used to calculate the light field in the DOE plane. To take the limitation of real photolithography fabrication techniques, some compulsory fabrication constraints, such as soft phase quantization and isolated pixel removal technique in the DOE plane should be incorporated into the standard IFTA method during the iterative design process. In the next step, the forward diffraction operator is implemented to obtain the current diffraction field in the target plane, and the figures of merit are calculated from this output pattern to evaluate the current performance. If the figures of merits are not sufficient, the diffraction field is updated according to the specific target pattern constrains. Usually, the algorithm converges after about hundred iterations.

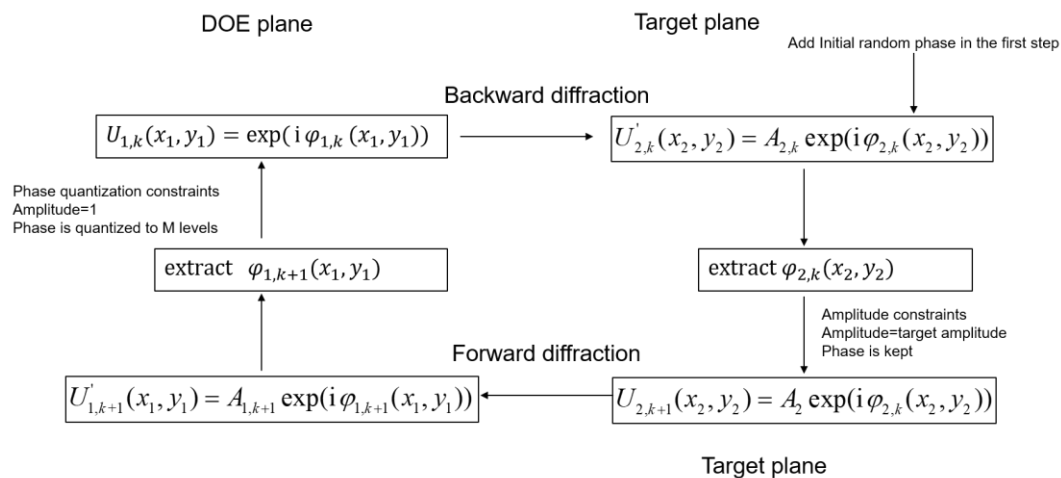


Figure 2-14- Flowchart of IFTA based bidirectional method.

Compared to unidirectional methods, bidirectional algorithms are fast and more

efficient for large pixel number DOE design. Bidirectional algorithm for multilevel DOEs can also achieve a better optical performance than the binary DOE. But the fabrication limit should also be considered during the DOE design. So, the general fabrication methods and their limits are demonstrated in the next section.

2.6 Review of standard DOE fabrication techniques

2.6.1 Mask based photo-lithography

Mask based photo-lithographic technology is widely used in industrial semiconductor integrated circuits manufacture, such as the electron chips of computers and cellphone. With the developing of optical technology, the most famous advanced lithography equipment company ASML [59] has currently reached the resolution of 5nm using an extreme ultraviolet lithography (EUV) system. Inspired by this idea, similar technology is used for fabricating DOEs with a lower resolution compared to the highest performance ASML lithography machine. The basic binary DOE fabrication processes are briefly described below. First, a cleaned wafer or glass substrate is prepared to be coated with photo-resist by using spin coater. The photoresist is a viscous, liquid solution, which can be laid down in a uniform single layer by fast spinning of the substrate. The coated photoresist's thickness depends on the spin coater's speed and resist viscosity. After this step, the mask pattern produced by laser beam [60] or electron beam lithography (EBL) [61] is transferred usually onto the photoresist through contact projector illuminated by ultraviolet light, see **Figure 2-15**

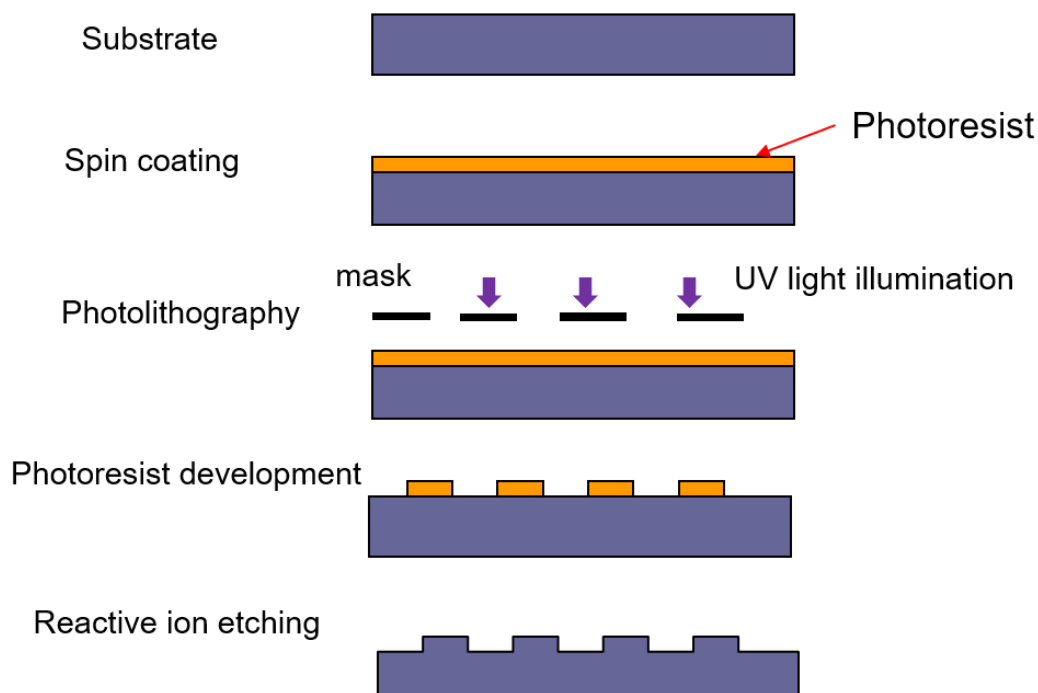


Figure 2-15-Basic lithography process of DOE fabrication using contact lithography.

Usually, there are two kinds of photoresist, one is positive photoresist which becomes soluble when exposed after ultraviolet light in the developer, while another one is called negative photoresist in which unexposed areas are soluble in the developer. After the etching process in developer, the mask's pattern is transferred in the photoresist layer. Then, a reactive ion beam etching (RIE) is used to etch into the substrate according to the required depth, and remove the residual photoresist. This fabrication method can also be used to fabricate multi-level DOEs, by repeating the fabrication process is for binary DOE described above. The etched substrate is coated and exposed again to produce a secondary mask, then repeat this process to get the desired number of levels. The eight-level DOE's basic lithographic process is shown in **Figure 2-16**.

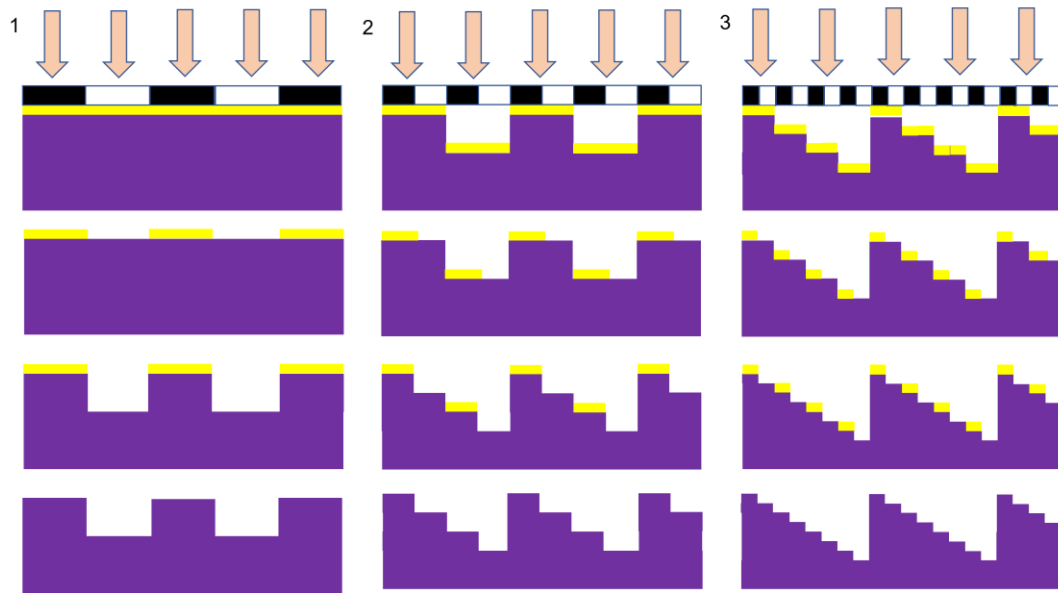


Figure 2-16-Basic process for multi-level DOE fabrication.

Figure 2-17 is a schematic of a projection photo-lithography system. The light source emits deep ultra-violet light, which is homogenized and collimated by a condenser lens system. The modulated light is then transmitted through the mask and the projector lens transfers the layout pattern from the mask onto the wafer. An immersion medium, such as deionized water is often used between the projection lens and the wafer to further enhance the resolution. In addition, other resolution enhancement techniques (RET), such as off axis illumination (OAI) [62, 63] are often used to improve the resolution. Source mask optimization (SMO) [64-66] is also often implemented to compensate the system's optical proximity effect. Mask based photo-lithography is high performance for DOE mass production. But the disadvantage is the need for multiple lithography processing steps to make multi-level DOEs (see **Figure 2-16**). In addition, the photomasks are produced by EBL, which increases the production cost compared to the binary DOEs. On the other hand, though the multi-level DOEs have higher diffraction efficiency and higher fidelity than binary DOEs, the

multiple limitations of photomask alignment process can introduce errors which reduce the DOE performance in practice. From the perspective of a DOE manufacturer, a new design DOE should be verified as soon as possible, as this can accelerate the product iteration process. For these reasons, maskless (for example in which the mask is replaced by micro-display screen which can program the needed mask pattern) lithography tools are highly attractive. In the next subsection, a detailed description of our home-built maskless photo-lithography machine in the IMT-Atlantique (IMT-A) clean room is presented.

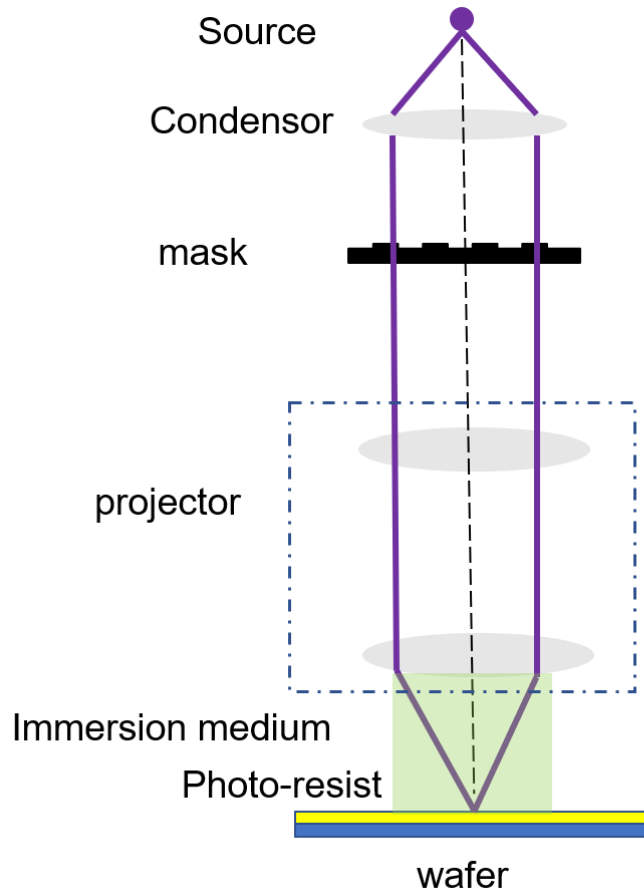


Figure 2-17-The sketch of the projection photo-lithography process.

2.6.2 Maskless parallel direct writing photo-lithography

Figure 2-18 describes the basic principle of the maskless parallel direct-write photo-lithography used in our cleanroom [67]. In **Figure 2-18 (a)** shows the basic lithography process consisting of three main steps. The glass substrate is cleaned with ultrasonic water cleaning, and then heated for 15 minutes at a temperature of 120 degrees to remove the residual water on a hot plate. The next step is the spin coating of a photoresist layer onto the cleaned glass substrate. In this thesis, the photoresists used are from the S1800 series which are positive photoresists from Micro Resist Technology. According to the different viscosities, photoresist S1805 is suitable for binary DOEs

and photoresist S1813 is used for making multi-level DOEs. The spin coating speed is chosen to give a uniform and different thickness photoresist layer according to the DOE design wavelength. The deviation of the uniformity of our spin-coating process is approximately 30nm. The etch depth is dependent on the DOE operating wavelength λ and the refractive index of the resist. According to the thin element approximation (TEA), the groove depth of the surface relief structure can be written as $d = \frac{N-1}{N} \frac{\lambda}{2(n_{material}-n_{air})}$, N is the number of phase levels, usually N is eight considering the compromise with fabrication limitations $n_{material}$ is the refractive index of photoresist. λ is the design wavelength. For example, at a wavelength of 532nm and for a photoresist refractive index of 1.66 at this design wavelength. According to this formula, the maximum etch depth d for an 8-level DOE is about 691nm. The spin coating speed is 3200rpm, giving a photoresist thickness about 1.3 μ m; this depth is enough for etching the DOE. The coated substrate is baked for 2 minutes at temperature of 120 degrees to extract the solvent, and then cooled down to room temperature. After that, exposure is implemented using our home-built parallel maskless direct-write photo-lithography machine shown in **Figure 2-18 (b)**: an updated version of the system demonstrated in [67]. In **Figure 2-18 (b)**, the light source is LED based with a center wavelength of 435nm corresponding to the optimal resist sensitivity. The divergent light is first collimated and homogenized by using group of illumination lens and our designed DOE diffuser (see Chapter 6). Then, the collimated and uniform light field is modulated depending on the designed phase pattern loaded on the 1920 \times 1080 pixels Spatial Light Modulator (SLM) and de-magnified onto the surface of the photoresist on the precision moving platform through the objective lens group. The exposure is implemented with a lookup table (LUT) to establish a linear relation between the addressed gray phase level on the SLM and the etch depth. The demagnification of the objective lens is 5. The projection area of SLM is small, around 5.7mm*3.2mm. So large size DOEs are manufactured by stitching different SLM images side by side (1cm²/min) by moving the stage in x and y direction with an accuracy of better than 250nm.

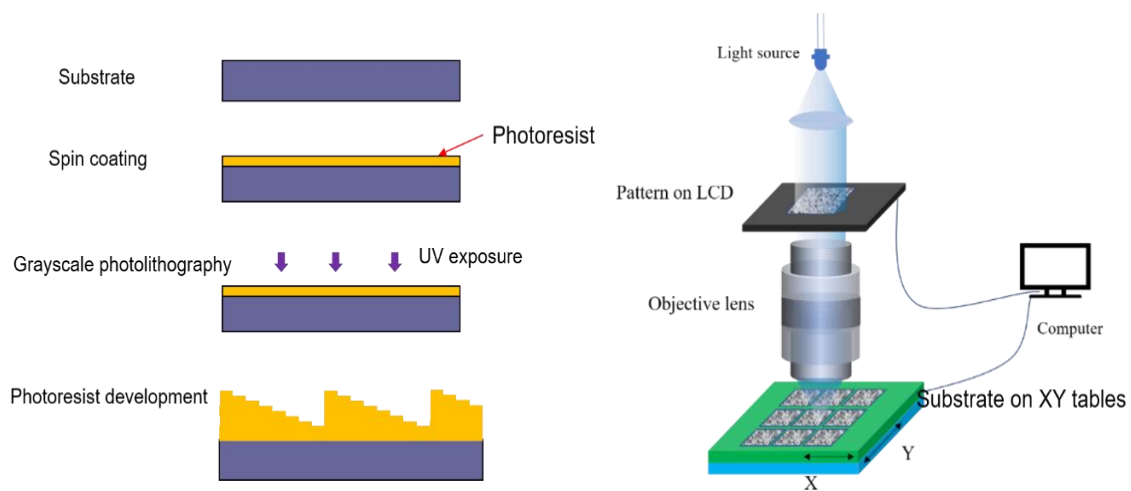


Figure 2-18- (a) the basic process of maskless photo-lithography.(b) Principle of maskless photo-lithography machine in IMT-Atlantique.

The last steps are to develop the exposed photoresist in a chemical solution for 2 minutes, followed by rinsing and blow drying. When the all procedures are finished,

the fabricated sample is measured using an interferometric microscope to get the 3D profile information, a schematic example 3D plot is given in **Figure 2-19**.

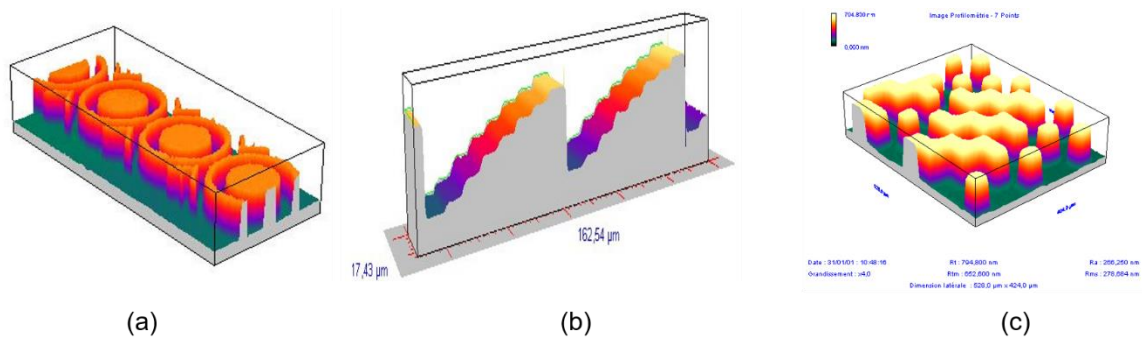
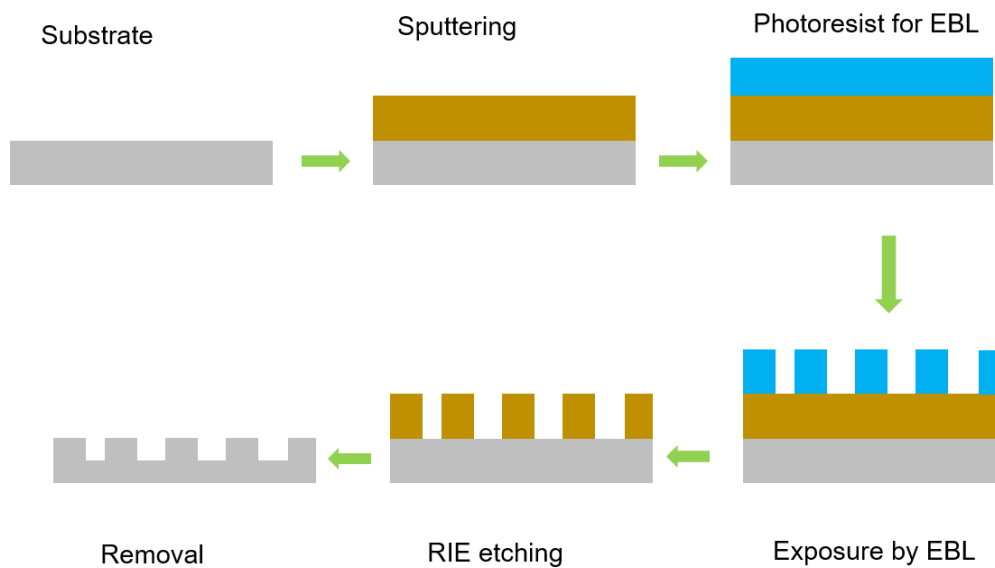


Figure 2-19- 3D plot of the DOE samples. (a) Fresnel Lens. (b) Blazed gratings. (c) Binary DOE.

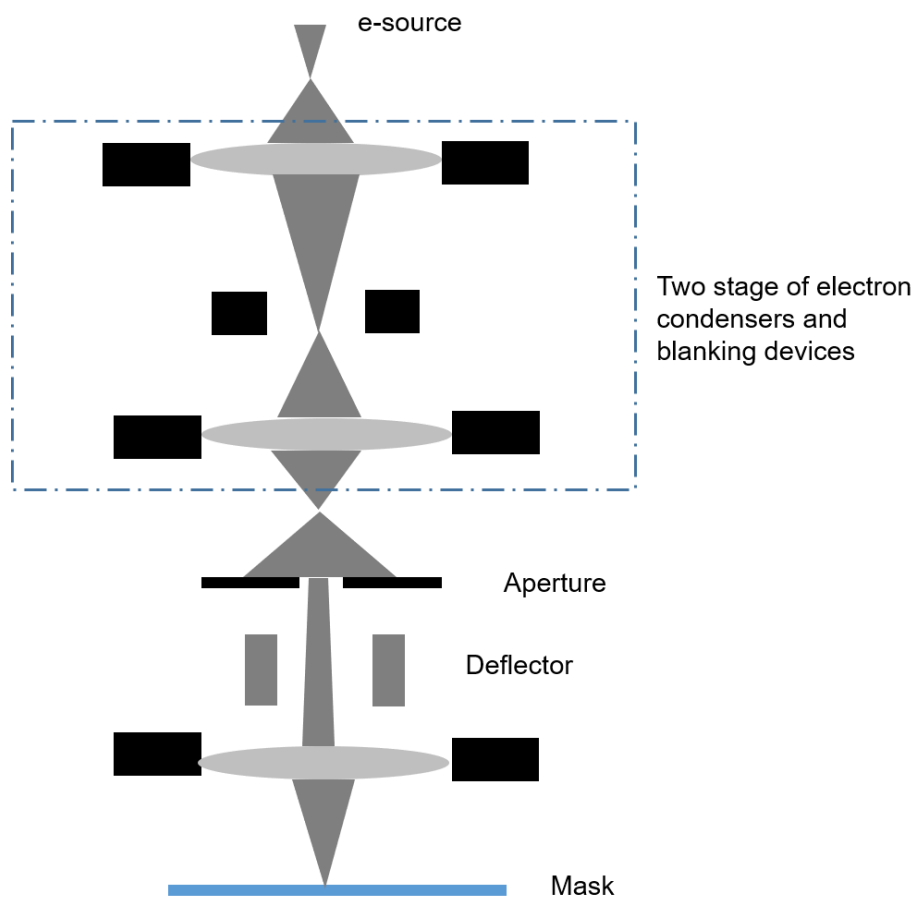
The described fabrication method above is fast and highly efficient, especially for DOE prototyping verification for industrial application. The main current limitation is the fabrication resolution of approximately 0.75 micron which is insufficient for fabricating the subwavelength structures which work at visible spectrum. To address this limitation, the EBL technology can be used. EBL has already been widely used for fabricating submicron structures such as wide diffraction angle DOEs [68], photonic crystals [69], meta-surface structure [70-72] and so on.

2.6.3 Electron Beam Lithography

When the required feature size is reduced to subwavelength dimensions, electron patterning machines are needed. EBL has already been widely used for fabricating subwavelength device, such as wide angle DOE [68], and meta-surface holograms [73-76] in the visible spectrum. Its basic working principle is similar to direct-write lithography (for example Heidelberg DWL 66+) [77], but the exposure source is an electron beam. EBL can focus the write spot down to sizes below 100nm, even down to 5nm recently. A typical fabrication process of EBL is shown in **Figure 2-20(a)**. A metallic layer is first sputter deposited on the cleaned substrate to avoid electric charging. Then, the photo-resist is coated on the metallic layer using a spin coater. The most frequently used photoresists are Poly-methylmethacrylate (PMMA) and Hydrogen silsesquioxane (HSQ), which are negative resists. The photoresist is exposed by deflecting the electron beam and moving the translation stage, see **Figure 2-20 (b)**. The exposed photoresist is developed to etch the pattern in the photoresist layer. After that, Reactive Ion Etch (RIE) is used to transfer the pattern in the photoresist into substrate and remove the residual photoresist and the metallic layer.



(a)



(b)

Figure 2-20- (a) Basic process of EBL. (b) The principle of the EBL.

Figure 2-20 (b) shows the principle of EBL, it consist of the electron beam

condensers and deflectors. Typical machines manufacturers are Raith [78], JEOL [79] and Hitachi [80]. One limitation that must be kept in mind, is that the final feature size is dependent on the resolution of RIE. Although, EBL has a small resolution, it still has several drawbacks. The infrastructure costs are high, and the writing time is long for large size DOE because of its single beam exposure technique. In addition, the proximity effect needs customized software to pre-compensate the mask profile which increase the overall cost.

Another common drawback of both EBL and maskless parallel direct lithography is that they cannot fabricate fully 3D micro-structure. 3D photonic structures are more attractive since they can open routes to new optical effects (for example wavelength selectivity) and new potential application. Can we find a way to fabricate 3D structure with a high resolution below than 100nm? Two-photon polymerization (2PP or TPP) lithography appears to be an effective way. In next subsection, the 2PP technique is introduced.

2.6.4 2PP lithography

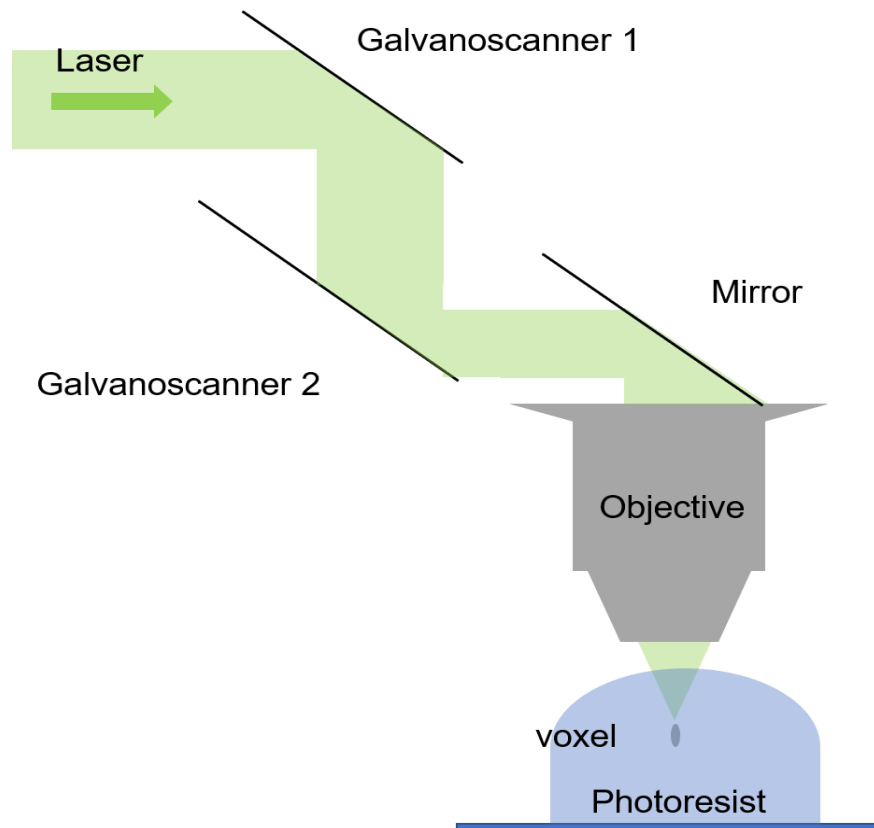


Figure 2-21- The schematic of single beam TPP lithography system.

Three dimensional (3D) photonics structures due to their flexible manipulation of light, including DOEs [81], photonic crystal [82], MOEMS [83], Micro-lens array [84] have gained extensive attraction recently in the optics community. All of these

promising devices make higher requirements on lithographic fabrication. Particularly, the fabricated feature size should be reduced to nano scale ($<100\text{nm}$) when a photonic device works in visible spectrum. The limitations of traditional lithographic techniques are now gradually being realized since these traditional lithographic techniques are restricted to the direct fabrication of 2D or 2.5D structures. 2PP lithography is a good candidate to address this problem as it can fabricate an arbitrary 3D structures layer by layer [85,86]. 2PP is a third order non-linear optical effect (depends on the square of the light intensity) based on the simultaneous absorption of two identical photons by a photo-sensitive material. Thus, it is possible to produce a subwavelength spatial resolution beyond diffraction limits as the absorption profile for the 2PP process is narrower than the beam profile of a one photon polymerization process.

A spiral 3D structure fabricated using 2PP lithography technique in 1997 brought the possibility of addressing successfully the above-mentioned issues [85]. Since then, 2PP lithography technique has gradually been applied to fabricating various complicated 3D micro/nano-structures [87,88]. It was a milestone in 2PP lithography community that a micro-bull with feature size of 120nm beyond the diffraction limit was successfully fabricated in 2001. Hereafter, 2PP techniques sprang up in fabricating 3D photonic structures.

The basic principle of 2PP lithography system is illustrated in **Figure 2-21**. The standard 2PP lithographic system consists of a pulsed laser which can produce femtosecond pulses of light, two scanners, suitable photoresists for 2PP, a precise moving stage and a computer to synchronize them. The laser used for 2PP is usually a high power mode-locked Ti: sapphire laser as the 2PP threshold is high (Third-order nonlinear optical effect). To excite 2PP, tight focusing is often needed using a high numerical aperture (NA) objective (for example an objective lens with NA of 1.4 for fabricating subwavelength structures). The photoresist should be sensitive to the 2PP process, such as polymers, where the polymerization process only happens in the region of focus point.

3D photonic structures can be polymerized in a photo-sensitive polymer resist for example inorganic-organic resin OrmoComp® (micro resist technology GmbH, Berlin, Germany). by scanning the focus in three dimensions within the resist.

Despite these advantages of fabricating 3D photonic structures using single beam 2PP lithography, the main drawback at present are the long writing times compared to parallel maskless direct writing lithography systems such as our home built direct write photoplotter (see **Figure 2-18**) as the writing beam must be scanned voxel by voxel to polymerize a 3D structure. For this reason, 2PP lithographic systems are limited to fabricating a very small 3D structures (typically $100\text{s } \mu\text{m}^3$). In addition, for most 2PP lithography system, a femtosecond laser is used which is high cost. To address this limitation, researchers have proposed different ways to parallelize 2PP fabrication to accelerate the 3D fabrication speed. The next subsection presents the state of the art of the current parallel 2PP lithography machines.

2.6.5 Parallel TPP lithography

It has recently become clear that ultrashort pulsed lasers can supply much higher laser power than the threshold requirement of a single beam 2PP lithographic process. Inspired by this development, it is now possible to split a laser beam into numerous separate beams with uniform power where each beam's light power is high enough to reach TPP threshold.

In this way, 2PP fabrications can be accelerated dramatically. There are many methods to split the incident beam, these methods can be divided into two categories. The first belongs to the refractive optical element (ROE), the other is DOE or CGH. Thanks to their high energy efficiency and compact volume, DOEs are usually used in the parallel 2PP lithographic system [89,90]. The example schematic of parallel 2PP lithography system is shown in **Figure 2-22**, the relay optics is a “4F” system which images the DOE phase or CGH to the pupil plane of the objective. After focusing by a high NA objective a customized pattern forms on one layer inside the photoresist. The inset shows an example 5 by 5 spot array, which can be used to polymerize a large area 3D periodic optical device with subwavelength feature sizes by moving the stage accurately according to the design to fabricate for example a micro-lens array or a blazed grating.

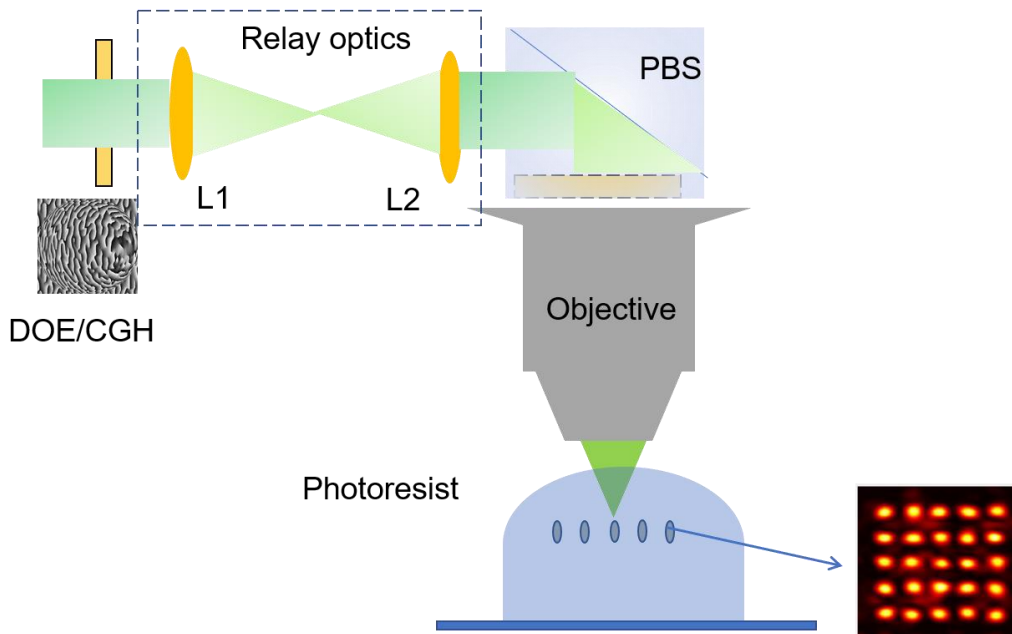


Figure 2-22- The sketch of the parallel TPP lithography system.

Figure 2-23 is an example 3D blazed grating fabricated using parallel 2PP lithography technique in our cleanroom at IMT-A.

With this method, it is becoming possible to simplify 3D photonics structure fabrication without the high cost of EBL.

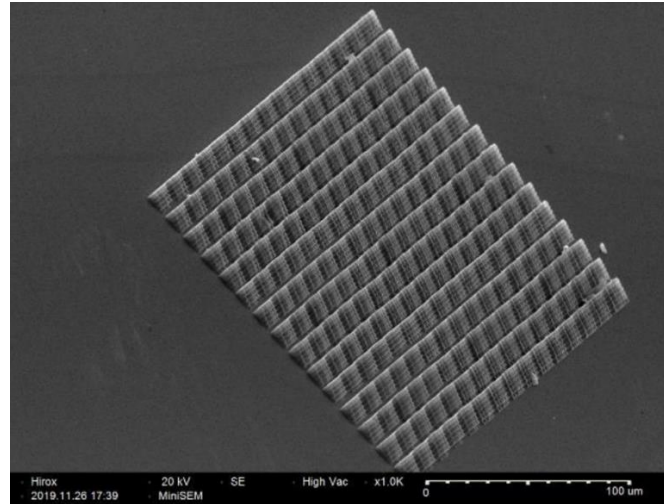


Figure 2-23- 3D blazed grating recently fabricated by parallel TPP process in the IMT-A cleanroom.

However, as we know, DOEs can only produce static patterns on the target plane, which is not suitable for dynamic manufacturing of a complex 3D micro-structures. A phase modulating SLM (PSLM) widely used in holographic display, can be used directly as a reconfigurable DOE in 2PP lithography systems. An example of 2PP lithographic system based on PSLM is shown in **Figure 2-24**.

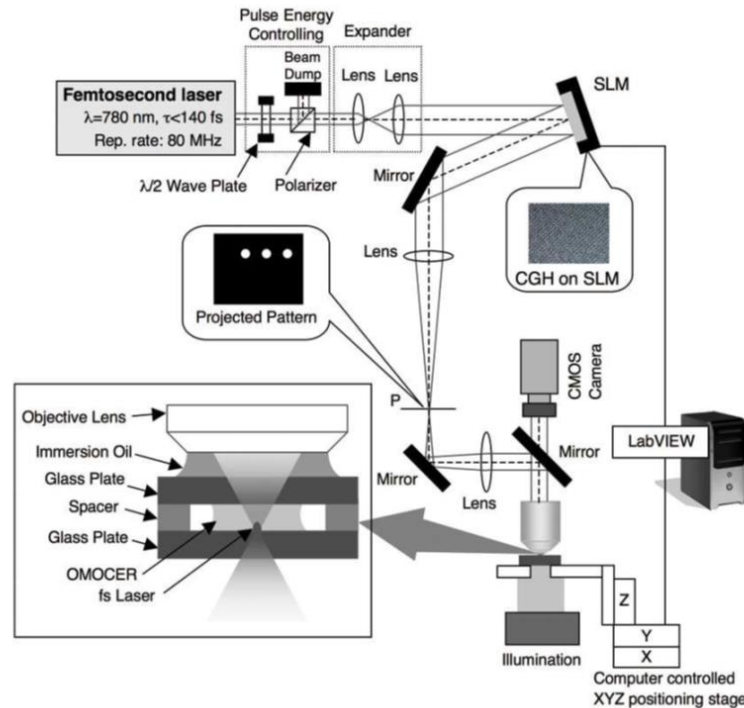


Figure 2-24-The 2PP lithographic system with use of a PSLM (Reprinted with Permission from [91] © The Optical Society).

In addition to using CGHs to split the incident light beam, researchers also developed algorithms specifically for the display of reconfigurable CGHs on a phase-modulating

SLM (Spatial Light Modulator) to project 2D or 3D light spot patterns directly into the photoresist. In this way, arbitrary 3D structures can be fabricated faster and more efficiently by projecting different spot patterns synchronised with substrate translations in x , y and z . However, the resolution of designed pattern is necessarily lower than that of the SLM because CGH coding needs phase freedom and amplitude freedom to obtain a high signal to noise ratio (SNR) reconstructed pattern. In addition to this inefficient use of available SLM Space Band Width Product (SBWP), speckle noise problems frequently occur. To reduce the laser speckle noise, the time multiplexing technique is often used, but at the cost of increased fabrication time.

To solve the problems above mentioned, we have proposed a new approach in which a standard (and hence cheap and high performance) amplitude modulation SLM is used to display an amplitude modulated pattern which is imaged by projection optics without wasting resolution compared to that of the phase SLM. A system based on this approach is currently being built in the IMT Atlantique clean rooms: a more detailed description of this system is given in chapter 6.

2.7 Practical Considerations of DOE design

2.7.1 Considerations on pixelated structure

In the previous section, the state of the art of current lithography technology was presented. With these advanced tools high resolution DOEs can be fabricated, but, optical proximity effect (OPE) which appears in any lithographic system and which directly influences the final exposure and decreases the resolution of the fabricated device [92]. OPE is an effect linked to diffraction and system optical aberrations which rounds the shape of the written pattern. An example of OPE is shown in **Figure 2-25**, **Figure 2-25 (a)** is the target mask, and **Figure 2-25 (b)** is the written image pattern whose corners are rounded. The lithography simulation process using Abbe imaging theory [93] is based on the diagram schematic of **Figure 2-17**.

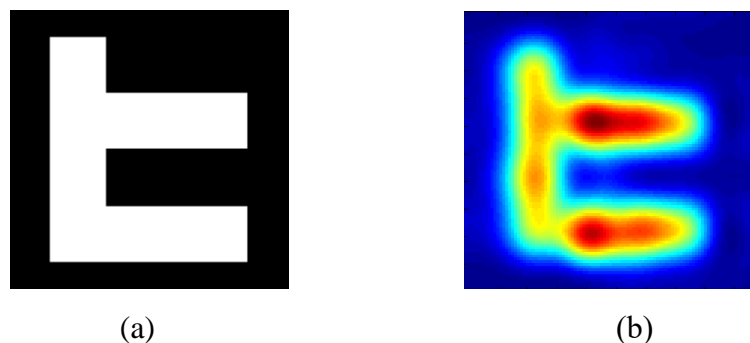


Figure 2-25- (a) Target mask.(b) image pattern on photoresist base on lithography simulation.

Due to OPE, a DOE's real optical performance is lower than that of the ideal calculated design results.

One effective way to reduce this problem is to make such that the fabricated pixel size is several times (at least two times) bigger than the fabrication resolution limit. For example, our current single photon parallel photo-plotter's resolution is experimentally 0.75 microns at the IMT-A, the minimum feature size should therefore be large than 1.5 microns. However, sampling the DOE pattern with large pixels does not full use of the machine's resolution capabilities, so leads to a diffraction result with many higher diffraction orders as shown in **Figure 2-26**. In **Figure 2-26** (d) and (e), the diffraction patterns contain many higher diffraction orders which reduce the real conversion diffraction efficiency of the designed DOE in the signal region, and produce more noise around the signal region. **Figure 2-26** (f) shows the reconstructed result without higher diffraction orders in the calculation window, that means the issue for an oversampled DOE pattern can be successfully addressed by oversampling the DOE pattern and reducing the fabrication pixel size.

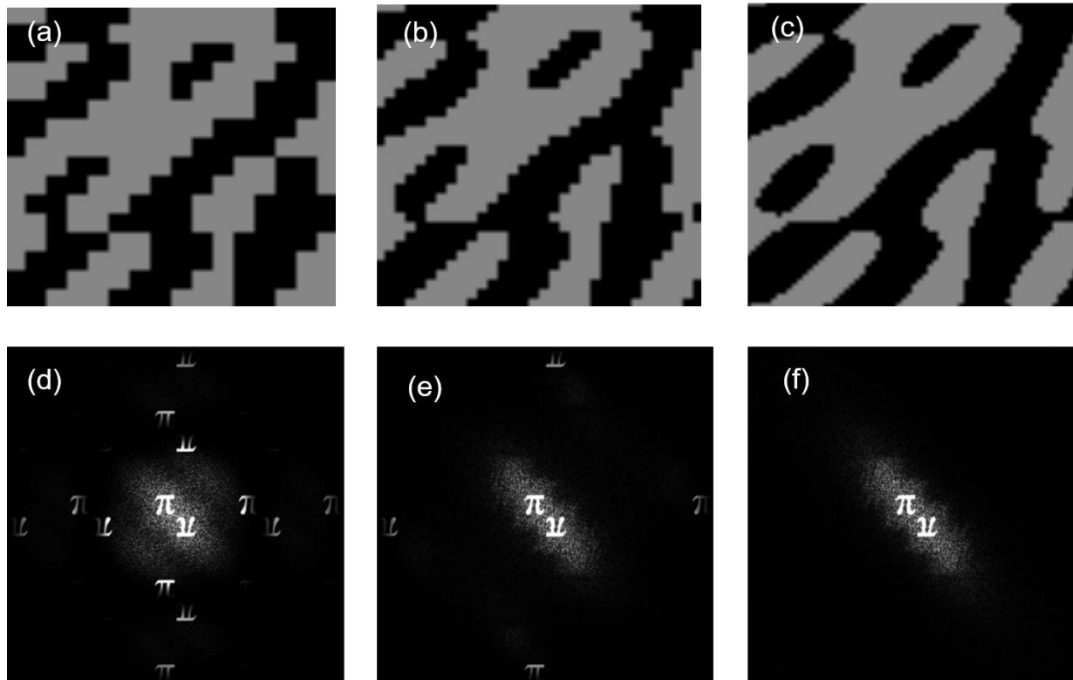


Figure 2-26- Output diffraction pattern for a DOE beam shaper with different pixel pitch. The pixel size reduces gradually from (a)-(c), while the their corresponded are shown in (b)-(d).

Another important practical factor in DOE design is the presence of isolated pixel structures which will produce stray light and stronger zeroth order due to their incorrect fabrication. A commonly used technique to avoid isolated pixel is based on zero padding method of the target pattern. This design method provides high amplitude freedom, and gives the design algorithm more freedom to put the noise outside the signal region, so converges to a much better solution with fewer isolated pixels. Such techniques reduce the fabrication burdens. But the calculation is heavy which needs more memory resources, and on the other hand it can only obtain small diffraction pattern.

In addition to the commonly used isolated pixels removing methods mentioned above,

another isolated pixel removing technique can also be considered for use in DOE design. A smoothing filter (usually Gaussian filter which is similar to the PSF of the mask lithography system) is imposed in the DOE plane to remove the isolated pixels, **Figure 2-27** depicts the design results.

But the optical engineer should notice that this method has a drawback which is difficult convergence to a good solution because the phase freedom is limited in the DOE plane.

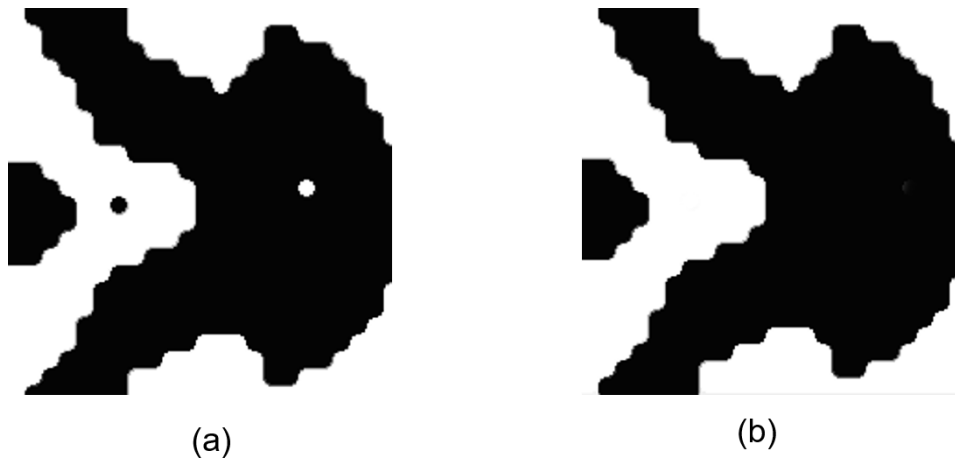


Figure 2-27- (a) DOE phase with isolated pixel. (b) DOE phase without isolated pixel.

2.7.2 Considerations on duplicate DOE structures

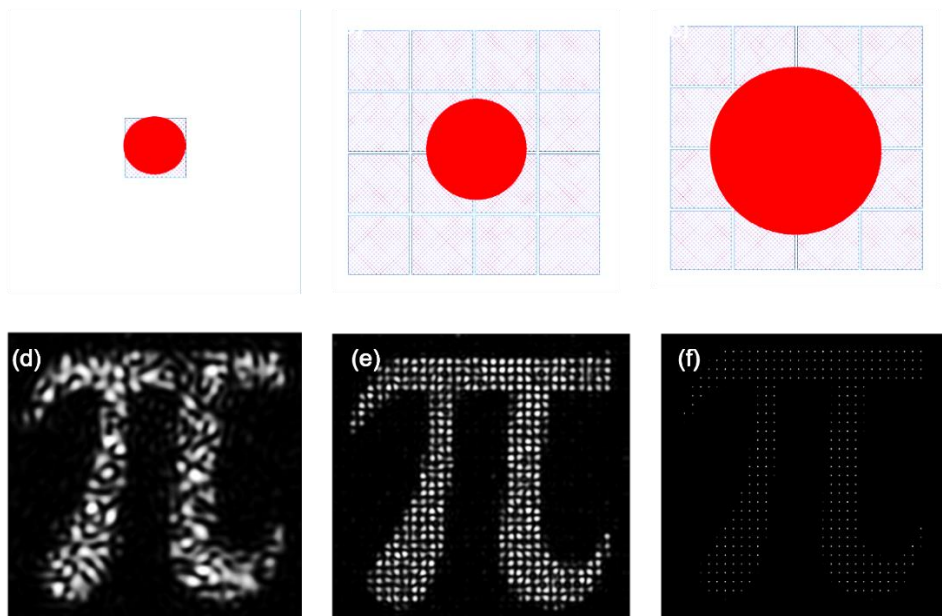


Figure 2-28- Variation of output pattern (d, e, f) with the number of DOE periods illuminated by the incoming beam (a, b, c). Illumination of only one period leads to speckles on the output pattern.

Figure 2-28 shows some reconstructed diffraction patterns obtained under different illumination configurations, where the red circle represents the illumination region and the rectangular shape depicts the DOE period. If the illuminating region is smaller than the DOE period (see **Figure 2-28(a)**), speckle noises is obvious in the diffraction pattern at the observation plane [94], see **Figure 2-28 (d)**.

One effective solution is to use an expanded beam illuminate several periodic of the DOE, see **Figure 2-28 (b)** and **(c)**. The speckle noise in the real diffraction pattern are reduced gradually. Speckle noises is essentially invisible when four DOE periods are illuminated (see **Figure 2-28 (f)**).

This reason for the behavior observed resulted in **Figure 2-28** is the finite beam size of the illumination configuration, which it is often regarded as infinite in the DOE design algorithm [6]. In fact, the real diffraction pattern in the observation plane is the ideal designed reconstructed diffraction field convolved with the Fourier Transform of the illumination aperture. By using this calculation technique, each pixel of the diffraction pattern is widened by the airy disk pattern of the illumination beam. These airy disk patterns can interfere if they overlap in the target image. Since the phase of DOE pixels is randomly assigned in the DOE design process, this interference produces a random distribution of maxima and minima between the spots in an observation screen, called speckles. When the illumination area is bigger, airy disk is smaller to this overlap occurs, thus reducing the speckle noise in the diffraction pattern.

From the perspective of an optical engineer, the practical factors mentioned above should all be considered in order to find a good compromise to give a realistic design based on the available lithographic fabrication tool. The next chapter is dedicated to present some real DOEs design techniques we have developed, for visualization application under LED illumination.

Chapter 3 Design of visualization DOE under LED illumination

Optical security technologies have gained extensive attentions in the optics community because of the distinctive visual effects of optical security components, and the large market in which they are widely applied in protecting identification documents, bank notes, and brands against counterfeit [95]. Among these technologies, security holograms are the most important as they are almost impossible to copy without intensive knowledge access to advanced lithographic fabrication tools and the corresponding design algorithms. However, much conventional optical security hologram fabrication is based on interference recording techniques, the details of the design method and fabrication skills have gradually become known to the public, which has made security holograms easier to counterfeit.

Thus, it is imperative to continuously develop novel and more complicated designs and technologies for advanced optical security holograms in order to stay ahead of counterfeiting. According to the descriptions of the previous chapter, pure phase DOEs are designed by using computer programming without the need of optical interference bench, which makes them suitable for producing security holograms with various virtues of ultra-compactness, lightweight, high diffraction efficiency and flexible manipulation of the amplitude/phase of incident light. DOEs are generally used to create 2D diffraction patterns on a far field or near field observation plane. In general, a coherent source laser is used to reconstruct the 2D diffraction pattern designed by a DOE. However the use of such source is inconvenient and can be dangerous for human vision perception, especially for the observation of security holograms. Therefore, there is a strong requirement for producing optical security features observable with a safer source such as LEDs which are both universally available in daily life, and safe for the human eye. To resolve the problem, our aim in this chapter is to use pure phase DOEs to design devices suitable for LED source illumination. In addition, security holograms which can produce new visual perceptions are continually needed for modern anti-counterfeiting protection. A particularly sought-after effect is a DOE producing perceived a floating 3D virtual object under readily available illumination, because 3D floating virtual object can provide observers with a perception close to real life.

In this chapter, DOE design methods and algorithms for creating a variety of 2D and 3D visualization effects under LED illumination are presented in detail based on the diffraction models presented in the previous chapter.

3.1 DOE projecting a 2D pattern under divergent illumination

3.1.1 Propagation model of the divergent illumination

Research into divergent light illumination have mainly been concentrated in refractive or reflective optical element (ROE) for a long time [10]. Although, these ROE based methods can produce an asymmetric pattern with a freeform lens or facet surface structure, their bulk volume and thickness limit their applications. DOEs are therefore a good choice to address this problem. But there is very little relevant research work about the DOE design with divergent incoherent light. To resolve this problem, we developed the following calculation model for divergent light illumination [56]. The schematic is sketched in **Figure 3-1**.

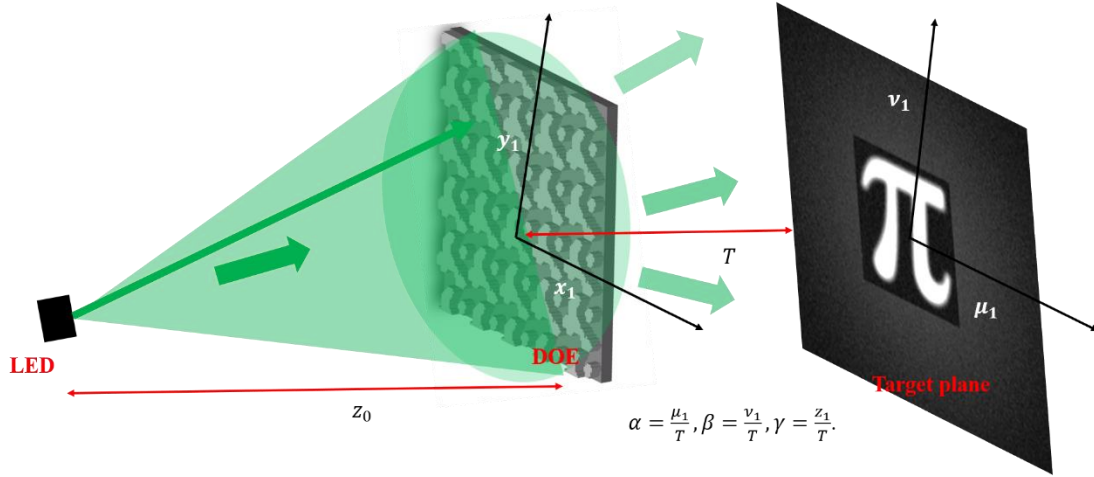


Figure 3-1 Schematic of the divergent light shaping.

Based on Fresnel diffraction formula in chapter 2, the diffraction field on the observed plane can be expressed as

$$u_t(\alpha, \beta; T) \approx \frac{\gamma \exp(jkT)}{j\lambda T} \int_{-\infty}^{\infty} u_0 \varphi(x_1, y_1; 0) \times \exp\left[-\frac{j2\pi}{\lambda}(\alpha x_1 + \beta y_1)\right] dx_1 dy_1 \quad (3.1)$$

$$u_0 \sim A \frac{z_0}{z_0 \sqrt{1 + \frac{x_1^2}{z_0^2} + \frac{y_1^2}{z_0^2}}} \frac{e^{jkz_0}}{z_0} \quad (3.2)$$

$$\alpha = \frac{\mu_1}{T}, \beta = \frac{\nu_1}{T}, \gamma = \frac{z_1}{T}. \quad (3.3)$$

Where u_0 is the illumination field of the LED source, φ is DOE transmission function, (x_1, y_1) and (μ_1, ν_1) represent the orthogonal coordinates of the DOE plane and the observation plane, z_0 is the distance between the source plane and DOE plane, $T = \sqrt{\mu_1^2 + \nu_1^2 + z_1^2}$. Usually, the distance between the DOE and observed plane is far larger than DOE size, so eq. (3.1) can be simplified as

$$u_t(\alpha, \beta; R) \approx \frac{\gamma \exp(jkT)}{j\lambda T} FT[u_0 \varphi(x_1, y_1; 0)] \quad (3.4)$$

From eq. (3.4), the diffraction field on the observed plane can be calculated using single 2D Fourier transform. Similarly, the diffraction field on the DOE plane is obtained with a single inverse Fourier transform, expressed in eq. (3.5).

$$u_0 \approx \frac{j\lambda T}{\gamma \exp(jkT)} \frac{FT^{-1}[u_t(\alpha, \beta; R)]}{\varphi} \quad (3.5)$$

According to eq. (3.4) and eq. (3.5), the diffraction field can be calculated directly using single forward Fourier transform and an inverse Fourier transform between the two domains. Therefore, the DOE phase can be optimized with a modified IFTA.

We model the LED as an extended source which can be treated as an array of Gaussian beams following the approach described for example in [2] (see page 321).

3.1.2 Algorithm

The classical IFTA (see Chapter 2) is one of the most popular algorithms, which has been widely used in phase retrieval problems and optimization of DOEs. Numerically, the Gerchberg-Saxton algorithm (GSA) is a forward and inverse Fourier transformation process of a complex function between real space and Fourier space, in which the constraints are applied to the computed wave-front based on a prior knowledge. Generally, the standard GSA is often used for plane wave shaping and valid only in the paraxial region. In this application, the model is modified as a divergent illumination is used. The proposed strategy is to use the scalar non-paraxial diffraction formula as the propagating function between the two domains, and introduce the divergent source model in the object space and the modified constraint in the Fourier space, as shown in **Figure 3-2**.

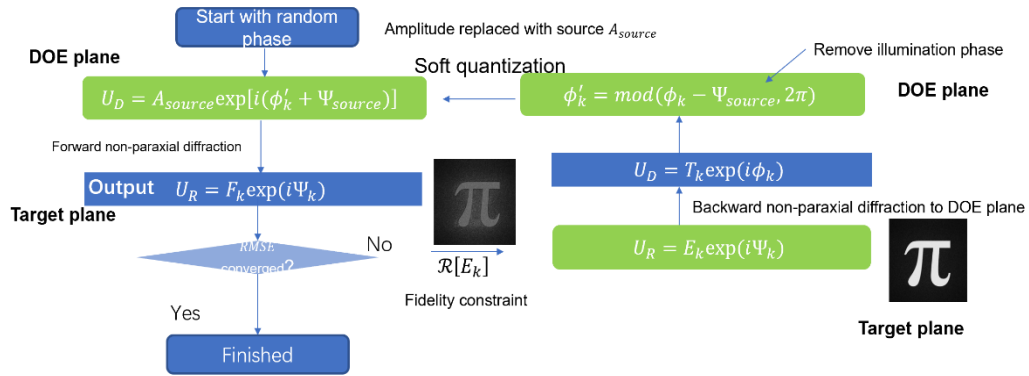


Figure 3-2-Flowchart of the proposed optimization method.

The design algorithm processes are presented as follows according to **Figure 3-2**.

1. To begin the iteration optimization process, a random phase range from $0-2\pi$ is imposed to the initial DOE phase Φ'_k , and multiplied by the input complex amplitude, then the proposed forward non-paraxial diffraction operator is applied to calculate the complex amplitude in the output plane.

2. In this design, the figure of merit is the root mean square error (RMSE) which is defined in eq. (3.8). If the RMSE is accepted, the iteration ends, otherwise a fidelity constraint (eq. (3.6)) is applied to obtain the modified complex amplitude in the output plane which is given in eq. (3.6).
3. The modified complex amplitude is then propagated back to the DOE plane by using the inverse non-paraxial diffraction formula eq. (3.5).
4. In the DOE plane, the illumination phase is removed and the amplitude is replaced with the incidence amplitude. Then, the iteration repeats 1-3.

Through the iterations, if the RMSE converges to an acceptable value or the assigned maximum iteration number is approached, the optimization process ends. Therefore, the optimal DOE phase Φ'_k is found.

In general, the standard GS algorithm usually falls into local optima, leading to low performance design results. To address the problem, the constraints are modified on the target plane. The constraint in the k th iteration is implemented by modifying $|E_k|$ such that

$$\mathcal{R}[E_k] = \begin{cases} \mathcal{E}_k [\mu_k (\omega_1 E_{target} - \omega_2 E_k)] & \Omega \in \text{signal window} \\ E_k & \Omega \notin \text{signal window} \end{cases} \quad (3.6)$$

$$\mathcal{R}[\mu_k] = \frac{E_{target}}{E_k} \mu_k, \quad \mathcal{E}_k = \frac{\sum_{\Omega_s} E_{target}}{\sum_{\Omega_s} E_k} \quad (3.7)$$

In eq.(3.7), the subscript k indicates the number of iterations, E_{target} is the target amplitude in the Fourier domain, ω_1 and ω_2 are empirical parameters, μ_k and \mathcal{E}_k are weighting factors. Usually, the figure of merit (FOM) of a DOE is defined as

$$\text{RMSE} = \frac{\iint (E_{target} - \gamma |E_k|)^2}{\iint E_{target}^2} \quad (3.8)$$

$$\gamma = \left(\frac{\iint E_{target}^2}{\iint |E_k|^2} \right) \quad (3.9)$$

3.1.3 Design results

A binary target " π " was used to demonstrate the proposed algorithm. In this design, the distance between LED source and DOE plane is 50mm, and the effective area of the LED illumination DOE was 12mm \times 12mm with pixel size of 0.75 μ m, the collective divergence angle was around 14 degrees. The fabricated phase levels are quantized, so the surface relief of the DOE should be divided into several levels. In theory, the higher the number of phase levels, the better the reconstructed image quality. But DOE fabrication performance must also be considered. Usually, eight levels are a good engineering compromise. To get a high quality reconstructed diffraction pattern, a soft

quantization method was incorporated into the proposed algorithm. A convergence curve compared to the typical GSA is shown in **Figure 3-3**.

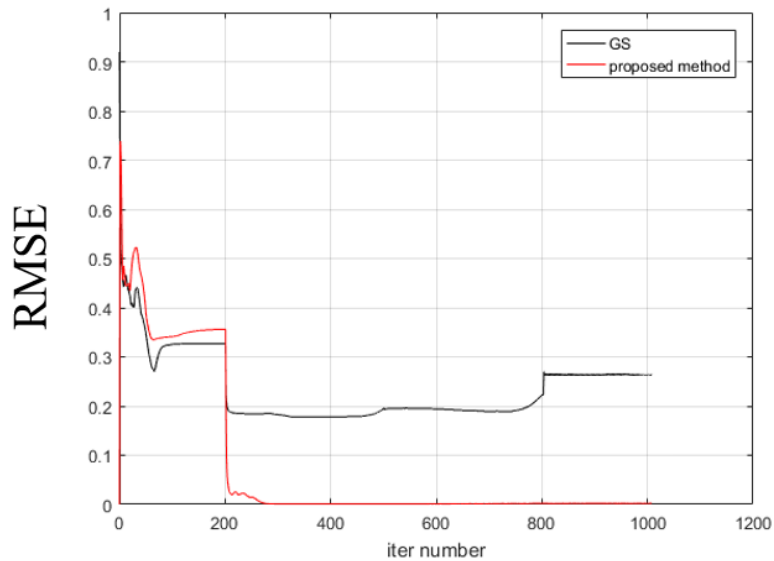


Figure 3-3-Convergence curve of proposed algorithm and standard IFTA.

From **Figure 3-3**, the RMSE of the GSA falls into a local optimum after 200 iterations, then it even goes higher after 800 iterations. Our developed algorithm converges after 200 iterations although it has a small fluctuation at the beginning. With the proposed algorithm, the design results are shown in **Figure 3-4**.

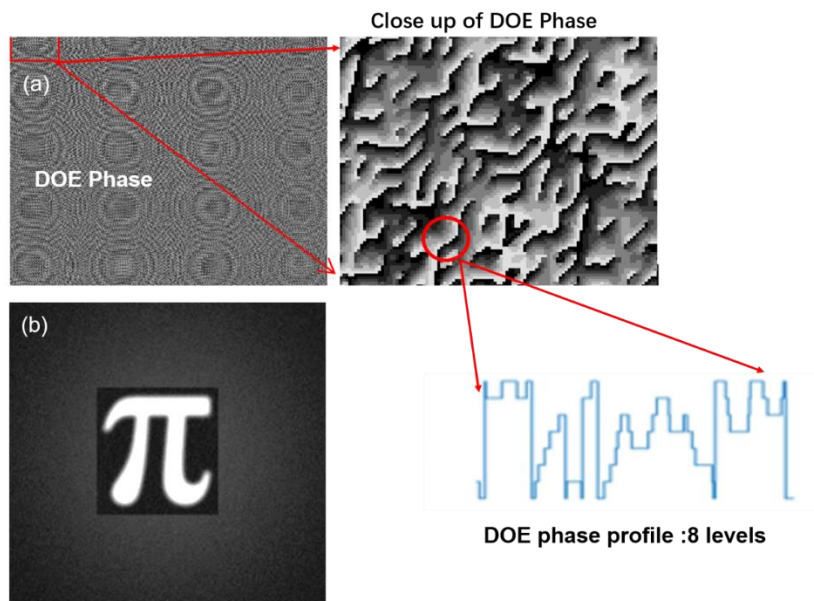


Figure 3-4-Design result for the divergent source illuminated DOE algorithm. (a) The designed phase distribution. (b) The reconstructed pattern.

Figure 3-4 (a) is the designed phase with eight levels, see the inset at bottom right-hand corner in **Figure 3-4**. The reconstructed pattern is demonstrated in **Figure 3-4** (b), which is similar to the target image. After optimization, we used our home-built photoplotter to fabricate the 16000×16000 pixels eight phase level DOE. The corresponding experimental reconstructions are demonstrated in Chapter 5. The results show good agreement with the simulation results.

3.1.4 Conclusion of divergent source illuminated DOE algorithm

In summary, a diffraction propagation model for divergent illumination has been proposed. Since the diffraction field in the two domains can be computed using simple Fourier transform, the modified GSA method for DOE design was presented incorporating a soft quantization algorithm. The optical experiment result is close to the numerical design simulation, demonstrating that the proposed method can effectively shape the divergent light from an LED. The proposed design method could also find applications in the design of diffractive optical elements for computational imaging. On the other hand at present, only 5% of light emitted by the highly divergent LED source can be captured by DOE, limited by DOE fabrication, therefore the real energy conversion is not high. Nevertheless the output image is still sufficient visible for use as a security hologram feature.

However, the DOE calculation load is heavy, so is not suitable for big DOE design (for example a DOE with 20000×20000 pixels needs more than 10 hours using a standard PC). The next section presents another lower calculation load design strategy based on faceted gratings.

3.2 Faceted gratings method

In the previous section, a DOE design method for producing a 2D diffraction pattern for a security feature application was demonstrated. However, it is still a heavy computation work to design such kinds of DOEs especially since the number of sampling points becomes large when illuminated with divergent light. This indicates that the approach is not the most suitable for divergent light sources. Another solution for LED light shaping is based on the element cells method as described for instance in [96] and implemented in the “Lighting Toolbox” of the commercial LightTrance software package [116]. However, little information is given in these references of the approach used to optimise the parameters of the element cells and no device fabrication or experimental verification is given. Here, we propose and demonstrate a specific technique for the optimisation of the gratings in the different elemental cells (facets) and confirm its effectiveness through device fabrication and experimental verification.

In this section, we present an efficient DOE design algorithm and fabrication to produce a new kind of diffractive blazed grating array (DBA) which can solve the

problems imposed by the divergent LED source, especially that of designing large size DOEs that are now feasible due to improved fabrication techniques [95].

3.2.1 Principle

The functional principle schematic of the approach is shown in **Figure 3-5**. The faceted gratings (FG) consists of an array of blazed grating cells, where each grating cell has a designated spatial period P and orientation angle φ . A diffraction pattern is obtained from the superposition of the first diffraction order spots of each blazed grating when illuminated by a narrow spectrum divergent LED source. The diffraction pattern, is projected onto a screen at a distance z . Usually, the distance is much larger than $\lambda z/p$, thus the diffraction result can be described by scalar Fresnel diffraction. In our case, we choose blazed gratings because multi-level blazed gratings can obtain high diffraction efficiency in the first diffraction order.

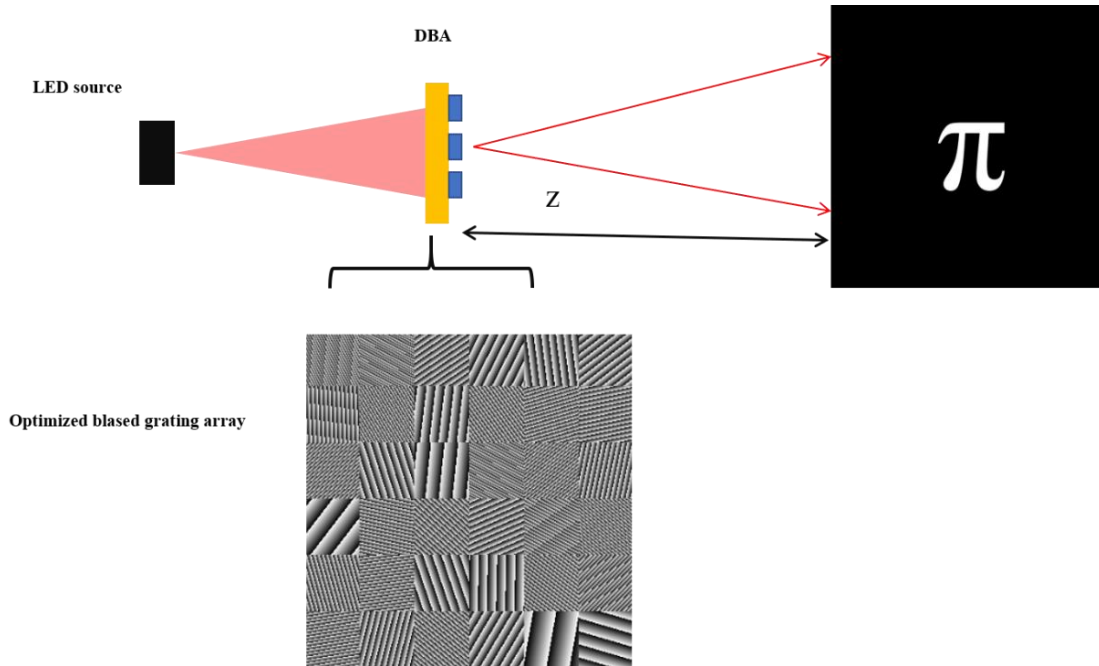


Figure 3-5-The schematic of the DBA principle for producing arbitrary patterns.

From **Figure 3-5**, the electric field $U_{out}(X,Y)$ of the target plane can be described in Eq.(3.10).

$$E(X,Y) = e^{jk\frac{X^2+Y^2}{2z}} FT(E_{in}e^{jk\frac{x_0^2+y_0^2}{2z}}) \quad (3.10)$$

In eq. (3.10), FT means the Fourier transform, z is the distance between the faceted gratings plane and target plane, (x_0, y_0) and (X, Y) represent the orthogonal coordinates in the DBA plane and target plane. The incident spherical wave can be divided into many plane waves, as shown in **Figure 3-6**. Each blazed grating introduces a linear phase shift of the wave-front, and the light incident on the grating cell array is modelled as a piece-wise plane wave extracted from the divergent spherical wave. Based on the thin-element approximation approach, the electric field behind each grating cell can be expressed as:

$$E_{in} = \frac{A}{r} e^{\frac{jkr}{r}} e^{j(k_x x_0 + k_y y_0)} \quad (3.11)$$

Where A and k represent the amplitude and wave vector of the incident light, and r is the distance from source to the DBA. k_x and k_y are the grating vectors in the X and Y directions, respectively.

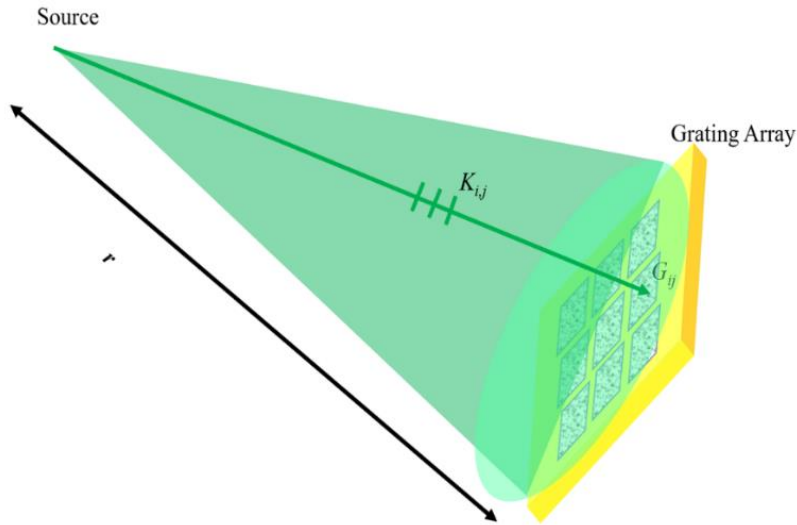


Figure 3-6-Schematic of the spherical wave decomposition.

Here, K_{ij} means the wavevector at the (i,j)-th grating, G_{ij} represents the (i,j)th grating. If each grating cell is small enough, the wave on each unit can be approximated as a plane wave. The incident angle on each grating cell is expressed as shown in eq.3.12

$$\theta_{ix} = \tan^{-1} \frac{x_i}{r}, \quad \theta_{iy} = \tan^{-1} \frac{y_i}{r} \quad (3.12)$$

In eq. (3.12), x_i and y_i are the global coordinates of each grating cell's center, and r is the distance between light source and the diffractive element. In the case of a single grating, let us consider an arbitrary grating cell of the optical element. Figure 3-7 depicts the schematic of the divergent light incident onto the grating cell (wave vector k_{in}) and the light diffracted from the grating cell toward the target plane (wave vector k_{out}). We assume that the grating is 100% efficient, the absolute values of vector k_{in} and k_{out} are the same, equal to $2\pi/\lambda$, but the directions are different. Here, λ is the design wavelength.

The coordinates k_{in} of each grating cell are known, so the direction cosine of the incident light can be calculated. The grating's conical diffraction formalism is described as below [95].

$$\alpha_{out} + \alpha_{in} = \frac{m\lambda}{P} \sin\varphi , \quad \beta_{out} + \beta_{in} = \frac{m\lambda}{P} \cos\varphi \quad (3.13)$$

In eq. (3.13), the α_{in} , β_{in} are the direction cosines of incident light in the x and y directions, respectively, and m is the diffraction order, in this work, $m=1$. α_{out} , β_{out} are the direction cosines of output light in the x and y directions, respectively. Parameter P is the period of the current grating cell, and φ is the grating's orientation angle, see **Figure 3-7**. Consequently, the angular position of a single point on the target plane is controlled by the spatial period and orientation angle φ of the individual grating cell. Based on Eq.(3.10)-(3.13), the period and the orientation angle of each grating can be optimized iteratively, until the desired irradiance distribution is obtained on the target plane.

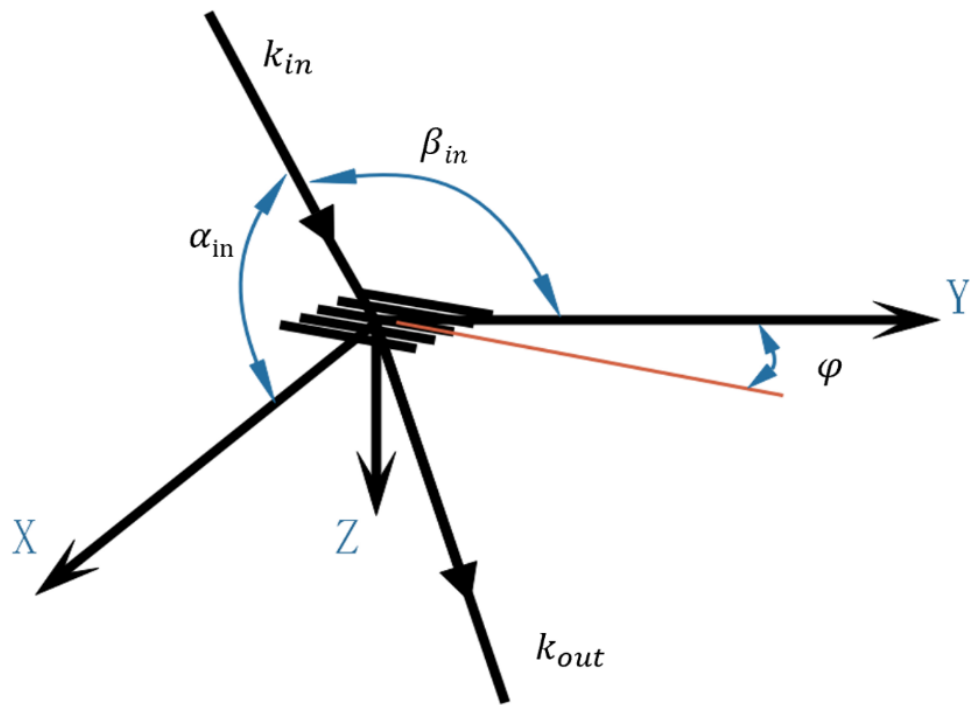


Figure 3-7-Arrangement of vector k_{in} and k_{out} .

3.2.2 Algorithm description

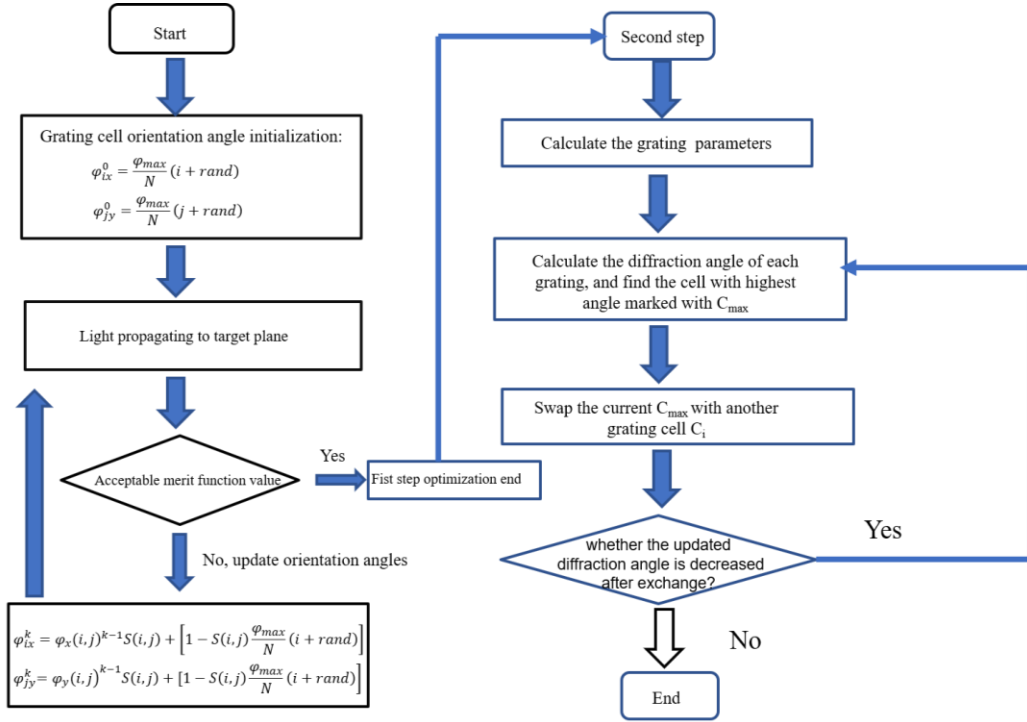


Figure 3-8-Flowchart of the first part of DBA design algorithm.

The iteration flowchart is shown in **Figure 3-8**. The detailed process is described below, where the algorithm is divided into two parts. In the first part, the initial parameters are obtained by implementing an iterative method. The second part of the proposed algorithm reduces the maximum diffraction angle of DBA cells. The second part is very important, because it simplifies fabrication and so improve real life DOE performance: the bigger the period of the grating cell, the better the fabrication quality. Here, we use a binary target pattern “ π ” to develop the algorithm. The DBA has a total size of $M \times N$ (rows x columns) cells. The maximum target intensity can be recorded as “1”, and the size of the target pattern is $P \times Q$ pixels.

The total number of the grating cell K should be larger than $P \times Q$ to get the correct target pattern. Mathematically, it is an inverse problem to obtain each grating cell’s parameters. The inverse problem thus reduces to calculating the grating function matrix G from equation $\Gamma G = F(x, y)$. Here, the operator Γ represents the diffraction propagation in eq. (3.10), and $F(x, y)$ represents the target matrix. Grating matrix G can be defined as below in eq.(3.14). The element $G_{i,j}$ is written as $(\varphi_{ix}, \varphi_{iy})$.

$$G = \begin{bmatrix} G_{11} & \cdots & G_{1N} \\ \vdots & \ddots & \vdots \\ G_{N1} & \cdots & G_{NN} \end{bmatrix} \quad (3.14)$$

The iterative optimization reduces the residual function $\|\Gamma G - F\|$. For each target point, the corresponding number of grating cells can be calculated as $K = M \times N /$

(P×Q). At the beginning, the initial orientation angle of each grating cell is set randomly. The orientation angle of each cell's grating can be written as :

$$\varphi_{ix}^0 = \frac{\varphi_{max}}{N}(i + rand) \quad (3.15)$$

$$\varphi_{jy}^0 = \frac{\varphi_{max}}{N}(j + rand) \quad (3.16)$$

Considering the high diffraction efficiency requirement, blazed gratings are used. The initial transmission function of each blazed grating cell can be expressed as

$$t_{ij}(x_0, y_0) = e^{i\frac{2\pi}{P}(\cos\varphi_{ix}^0 + \sin\varphi_{iy}^0)} \quad (3.17)$$

Combining eq. (3.10) , (3.11) and eq.(3.17), the diffractive output light field distribution is calculated as

$$E_t = \sum_{i,j}^{N,N} e^{jk\frac{x^2+y^2}{2r_{ij}}} FT[e^{j(k_{in,x}^i x_0^i + k_{in,y}^j y_0^j)} t_{i,j}(x_0^i, y_0^j) e^{jk\frac{x_0^i{}^2 + y_0^j{}^2}{2r_{ij}}}] \quad (3.18)$$

In eq. (3.18), X, Y are the global coordinates in the X and Y directions in the target plan, and x_0^i and y_0^j are the local coordinates in the x_0 and y_0 directions of grating cell $G(i,j)$, respectively. The divergent light source can be decomposed into harmonic plane waves

in K -space, see **Figure 3-6**. So, $e^{j(k_{in,x}^i x_0^i + k_{in,y}^j y_0^j)}$ is regarded as a plane wave incident on the cell of coordinate indices (i, j) , and the merit function on the target plane can be defined as

$$MSE = \frac{\sum_{N,N} \sum (I_t - I_{target})^2}{N \times N} \quad (3.19)$$

Where in eq.(3.19), $I_t = E_t * conj(E_t)$ is the output pattern obtained at the current iteration index. When the intensity of certain point on the target plane is lower than the target value, its corresponding grating cell's coordinate index is fixed and stored for the current iteration. Otherwise, its corresponding grating index is abandoned. When all the grating cell's indices are found, we can fix the cell matrix, and begin the next iteration. Here, we define an “ S ” matrix as a storage matrix to store the fixed grating cell's indices. The orientation matrix updates following equations:

$$\varphi_{ix}^k = \varphi_x(i, j)^{k-1} S(i, j) + \left[1 - S(i, j) \frac{\varphi_{max}}{N}(i + rand) \right] \quad (3.20)$$

$$\varphi_{jy}^k = \varphi_y(i, j)^{k-1} S(i, j) + \left[1 - S(i, j) \frac{\varphi_{max}}{N}(i + rand) \right] \quad (3.21)$$

The new updated orientation angle for each grating cell will be entered into the next iteration. This iteration process ends when the merit function value is accepted or the maximum iteration number is reached. The results of the first step optimization are not the optimal solutions; cells with high diffraction angle gratings should have their diffraction angles reduced to improve fabrication performance. To do this, the second

step of the proposed algorithm is executed which we call the exchange step.

To clearly understand this exchange method, the flowchart and schematic of the exchange method are shown in **Figure 3-9**. The details of the second optimization process are summarized below.

1. Calculate the current diffraction angle of each grating cell, and find out the the cell with the highest diffraction angle marked with C_{max} . The grating cell C_{max} corresponds to the target point T_{max} in the target plane, see **Figure 3-9**.
2. Calculate the diffraction angles between the current target point T_{max} and all other grating cells, then sort their values from smallest to largest.
3. Swap grating cell C_{max} and grating cell C_i , i.e. let the grating cell C_{max} correspond to target point T_i , and the grating C_i correspond to target point T_{max} .
4. Check the diffraction angle values after exchange:
 - a) If the new diffraction angle has increased, the exchange is cancelled, then swap the C_{max} with the next grating cell, until all the remaining grating cells have been changed.
 - b) If the updated diffraction angle is decreased after the exchange, the algorithm goes to step 5.
5. If the exchange of current grating cell C_{max} doesn't happen, the algorithm ends. If the exchange happens, the algorithm goes to step 1, and updates the C_{max} .

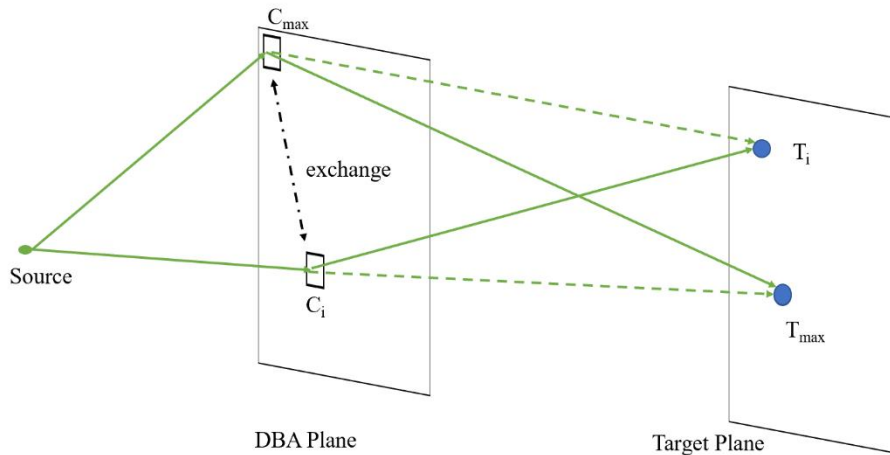


Figure 3-9-Schematic of the diffraction angle optimization. The solid lines are the rays before exchange, and the dotted lines are the optimal rays after exchange.

3.2.3 Numerical simulation

In order to verify the feasibility of the proposed design method, we performed the following numerical simulations. To reduce calculation time, a binary pattern “ π ” with

image size 40×40 pixels was used to verify the design method in the numerical simulation. This target image is shown in **Figure 3-10**. In this simulation test, considering the computation load, pixel size of each grating cell is $3\mu\text{m}$, each grating cell contains 60×60 pixels and the number of the cells is 30×30 . The total size of DBA is $5.4\text{mm} \times 5.4\text{mm}$. A LED wavelength of 525nm was used as the light source, here, the distance from source to DBA plane is 100mm , this distance cannot be too far because the energy from the divergent light source decrease rapidly. The propagation distance is 200mm from DBA to the target plane.

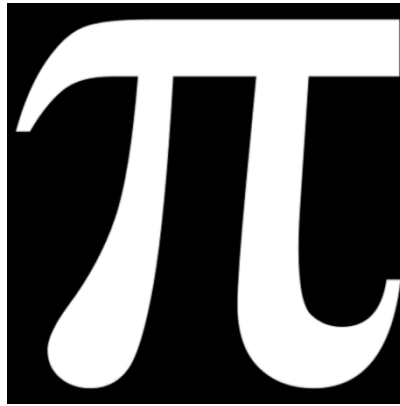


Figure 3-10- The target image for DBA design.

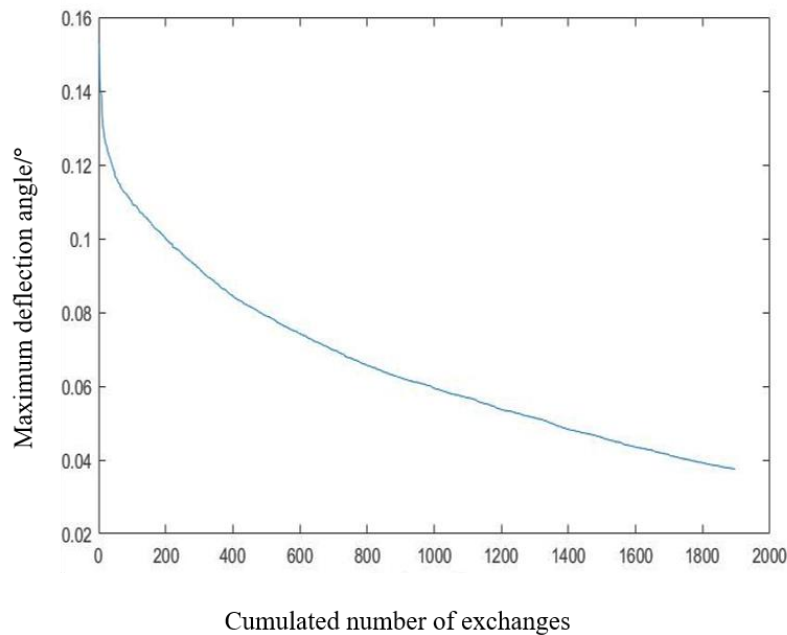


Figure 3-11-Maximum deflection angle against the cumulated number of exchanges.

The maximum diffraction angle against the number of exchanges is plotted in **Figure 3-11**. The final numerical simulation results with these parameters are demonstrated in **Figure 3-13**.

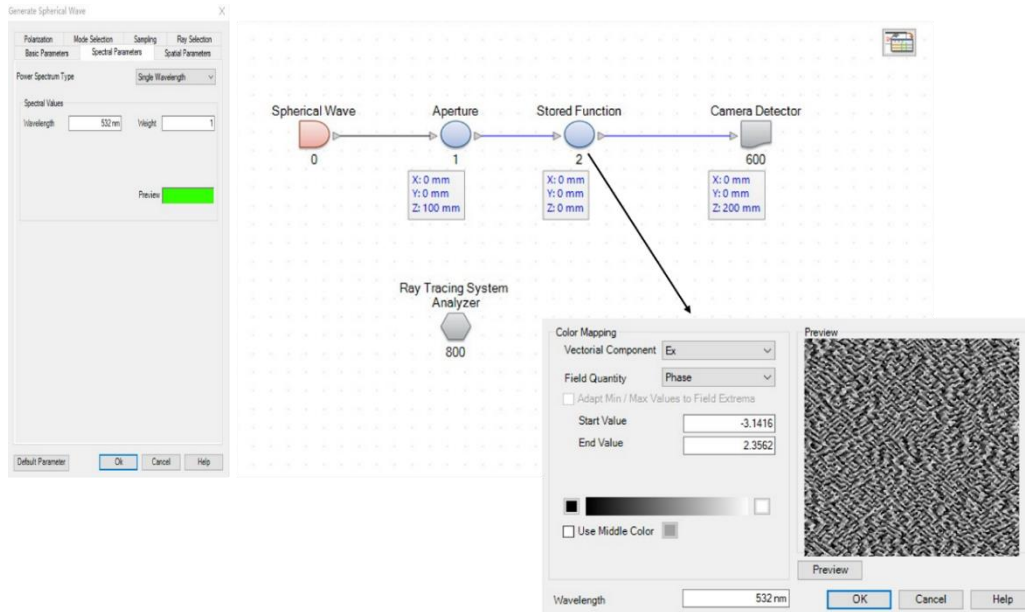


Figure 3-12-Optical path in VirtualLab Fusion™.

To validate the design result, the final optimal phase map of the diffracted reconstructed result was tested in VirtualLab Fusion™ software to verify the proposed method. VirtualLab Fusion™ (VL) is a famous and authoritative commercial advanced field tracing software, which is widely used in DOE design, subwavelength grating design, illumination optics design and various optical system simulations [116].

Figure 3-12 shows the basic settings in the VirtualLab Fusion™ simulation, the optical system consists of a spherical wave, an aperture, a stored function with the phase function of our faceted grating array DOE and a camera detector. The aperture is used to limit the beam size of the incident light, and the stored function box is to store the designed phase, see the inset at the lower right. The incident light's polarization state, wavelength, and sampling can also be modified, see the inset on the left of Figure 3-12. The propagation method can be modified according to the optical engineer's real requirements, such as far field operator, Fresnel operator, angular spectrum operator and so on. In this simulation work, the propagation method was selected as 'automatic propagation operator', which can automatically choose the operator according to setting parameters.

Classical field tracing was used for the simulation engine. The simulation result is obtained is shown in Figure 3-13. From Figure 3-13, we can see the speckle noise on the target since we implemented this numerical field tracing using a divergent coherent light source model in VirtualLab Fusion software. A more complicated source mode of LED source is not yet available. This speckle noise is suppressed when a low coherence degree LED source is used in real experiments, see Chapter 5. Through these numerical simulations in VirtualLab fusion software, we were able to validate the proposed design method.

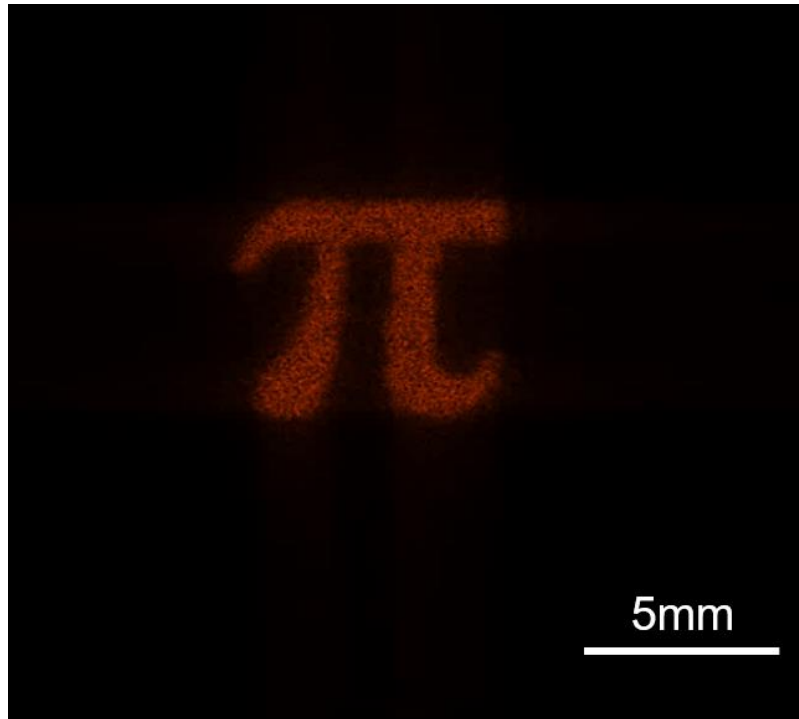


Figure 3-13-Reconstructed result in VirtualLab Fusion™ software.

3.2.4 Discussion

This section focused on an optimization algorithm to design blazed grating array structures for use under incoherent divergent illumination particularly suited to security hologram applications. The numerical simulation results demonstrate that the proposed structure functions well. However, for this to be the case, a number of interdependent optical system parameters must be chosen correctly. Such parameters include source-DBA distance, DBA size and grating cell size. We now discuss how these different and sometimes conflicting factors affect system design, with the aim of providing some simple design guidelines for optical engineers.

The most important overall consideration is to maintain the blazed grating period of the individual cells within the bounds imposed by their performance and fabrication limits. The second optimization step of the proposed algorithm helps towards this aim, but overall system design is also very important. **Figure 3-14** shows the practical first order diffraction efficiency of a blazed grating against grating period for normal incidence.

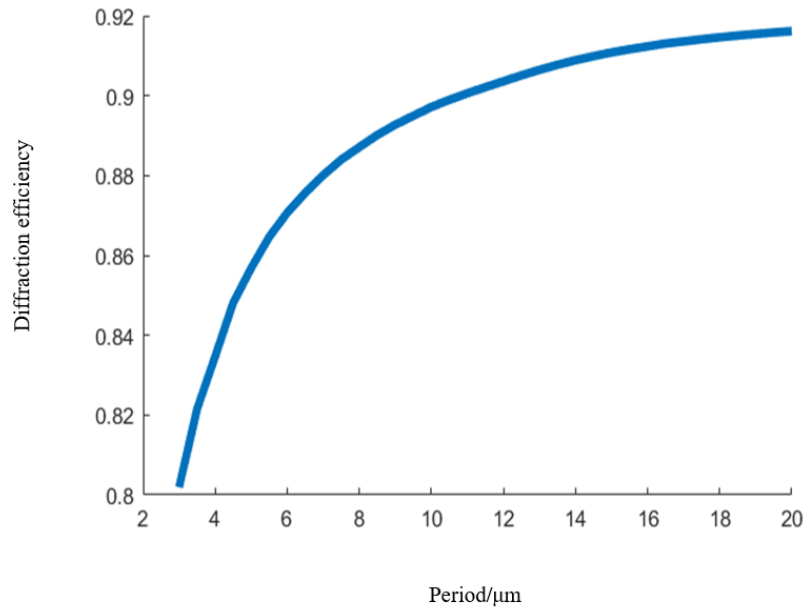


Figure 3-14- The calculated first order diffraction efficiency as a function of blazed grating period obtained by RCWA.

Figure 3-15 shows the dependence of blazed grating diffraction efficiency on grating groove depth (a good guide to DBA fabrication and replication accuracy) and incident illumination angle when keeping the grating’s spatial period fixed.

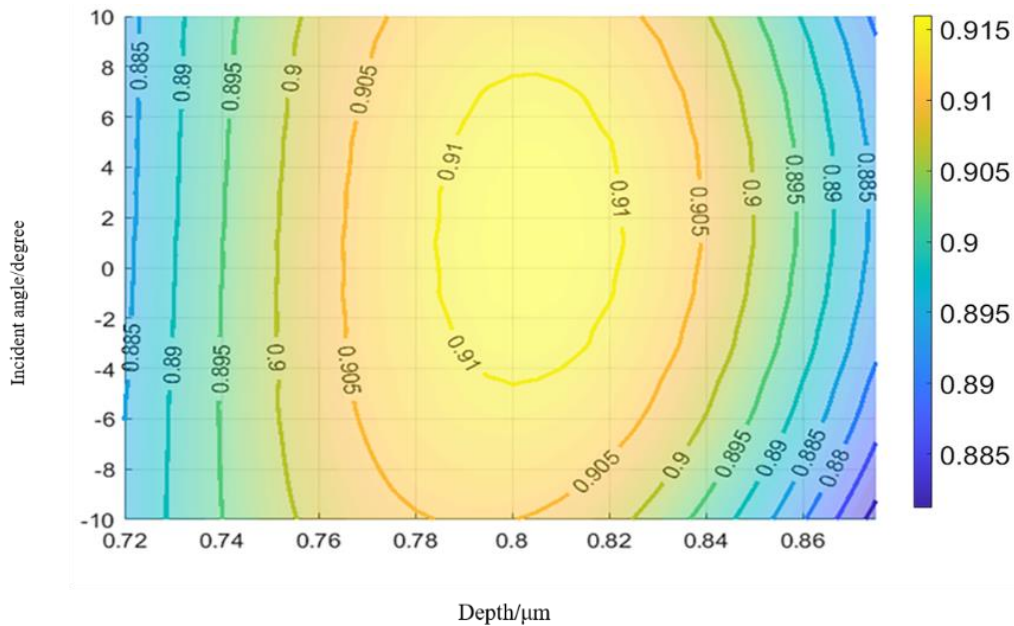


Figure 3-15- Blazed grating diffraction efficiency against the incident angle and groove depth.

Both figures are obtained using the RCWA model because the thin element approximation of scalar theory is no longer accurate for small grating periods and off-normal illumination. In the RCWA calculation, the continuous profile was sliced into several layers (20 layers in this simulation), see **Figure 3-16**.

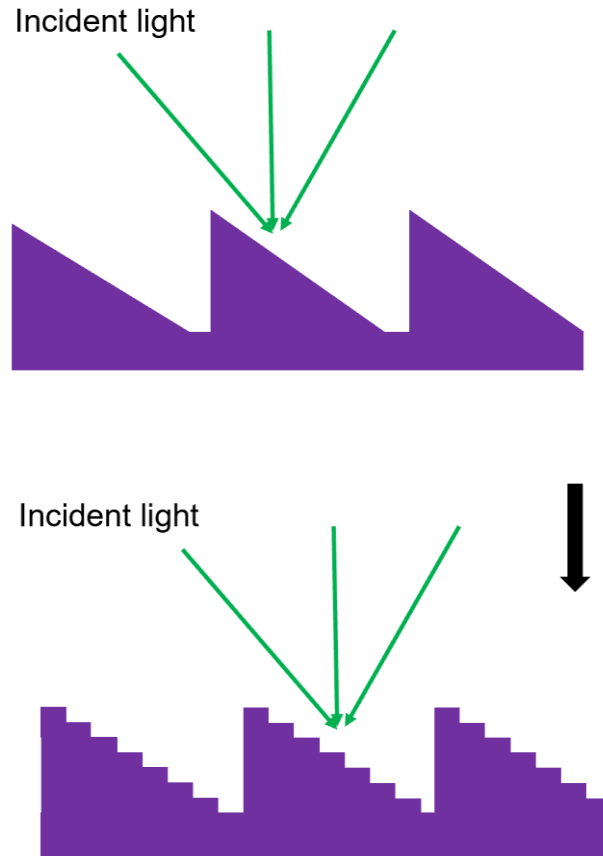


Figure 3-16-Configuration of the blazed grating. (a) continuous grating profile. (b) Multilayer profile used in RCWA simulations.

From **Figure 3-14** and **Figure 3-15** it is clearly that, to maintain high diffraction efficiency (greater than 85%), the grating period should be greater than roughly $5\mu\text{m}$ and incident angles should be less than about 10 degrees. These considerations have a direct influence on usable DBA size and source-DBA distances: a DBA with lateral dimensions of the order of cm should be illuminated by a source at distances of tens of cm. These values are perfectly compatible with our security hologram application, where holograms are usually held at arm's length. Of course, the further the DBA is placed from a divergent source, the less light it will capture which will reduce the intensity of the diffracted image. The optimal DBA size and position will thus be an engineering compromise based on these competing factors.

Another important system design consideration is the DBA size. If the cell is too large, we can no longer approximate the light from the divergent source to be a plane wave across the cell. If the cell is too small, the diffracted spot size (determined by the cell aperture) in the output image will increase in size, limiting the complexity and resolution of the output image. The output intensity distribution of each spot is given by

$$D_{spot} = d^2 \text{sinc}\left(d \frac{x}{\lambda z}\right) \text{sinc}\left(d \frac{y}{\lambda z}\right) \quad (3.22)$$

In eq. (3.22), d is the size of the grating cell, z is the distance between the DBA and

the image plane, and λ is the wavelength. With the DBA sizes and distances indicated above, cell dimensions on the order of 100 μm offer a good engineering compromise, with the added advantage that the cells are then barely visible by direct eye observation.

Normalized intensity

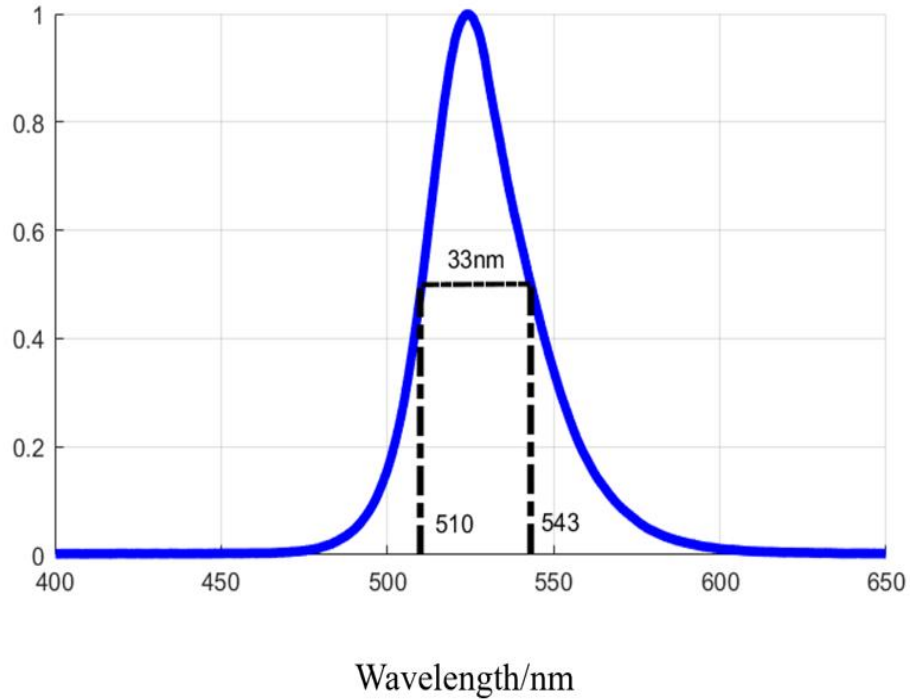


Figure 3-17-spectrum of the used LED.

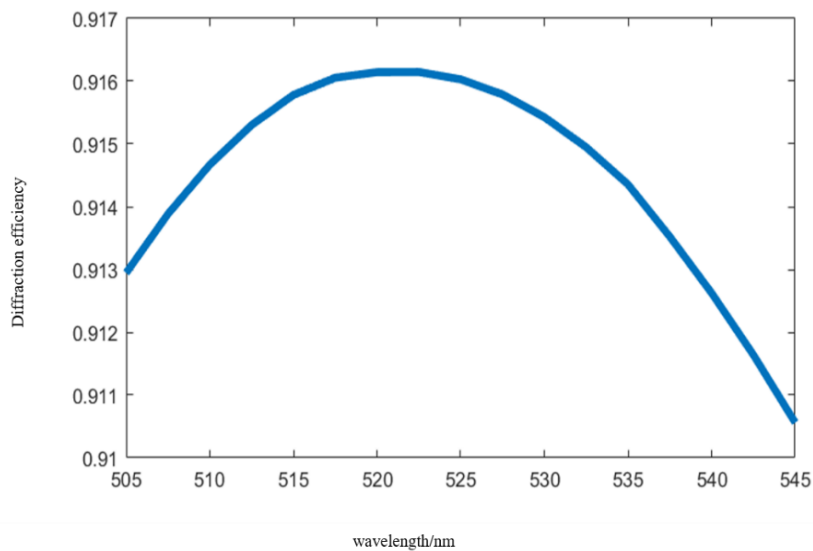


Figure 3-18-the calculated first order diffraction efficiency as a function of incident wavelength obtained by RCWA.

A final consideration is DBA performance with non-monochromatic divergent

sources such as readily available smartphone white LEDs. The LED used in our experimental system had a measured Full Width Half Maximum Spectral Width (FWHM) of 33nm. The spectrum of the LED is shown in **Figure 3-17**. **Figure 3-18** shows that over such spectrum ranges the diffraction efficiency of the blazed grating varies very little. For a white LED, the wavelength variation of the grating diffraction angle and diffraction efficiency produces color fringing in the output pattern. However, as system design considerations and the algorithm optimization tend to keep diffraction angles low (<10 degrees), these effects are limited and the desired pattern remains clearly recognizable (see Chapter 5).

3.2.5 Conclusion for DBA security holograms

In this section, a DBA based method for a projection type optical security hologram has been described. The grating parameters of each unit were optimized using a novel two-step optimization algorithm. The numerical simulation results verify the design approach. In addition, the factors which can affect the design result have also been identified and studied in a discussion section, which provides an optical engineer with a design guide by considering the real fabrication limits. Since the optical security component developed in this section is also a surface relief structure of a single polymer material, it can be replicated in mass production by using standard roll-to-roll nano-imprint technology. The design algorithm developed here should enable the extension of the application of optical security elements to a broader realm and facilitate extensive developments in other research fields of the optics community, such as light shaping, specific illumination for lithography and microscope systems.

In the previous two sections, we proposed two strategies for producing projection type security holograms. In advanced security holograms applications, holograms which can create the perception of a 3D floating security feature are highly sought after. The next section will introduce a design method which can produce such a security feature on the surface of hologram also based on blazed gratings structures.

3.3 2D diffractive optically variable device

In the previous sections, two different methods were presented to make a projection type security hologram. One drawback of these techniques is that the projection type DOEs need a screen to show the security pattern. In general, an optical security pattern which appears on the document surface is much easier to verify for an observer. In the security hologram community, dot-matrix holograms are a frequently used technique [97]. The dot-matrix hologram is comprised of many small bright dots, which are usually called 'diffractive pixels'. Usually, the diffractive pixel cannot be seen by the naked eye due to its small aperture dimension, which is below 80 μm . The diffractive pixels are filled with diffraction gratings which produce a visual image effect on the

dot-matrix hologram's surface when they are illuminated, for example by a LED source. The pattern can change when an observer tilts or flips the hologram substrate, such holograms are called optically variable devices (OVD).

Usually, an OVD is fabricated by using an interference setup, but it is very difficult to make complex gratings. Unlike this conventional fabrication, we use our home-built parallel photo-plotter to fabricate more complicated gratings. Thanks to this advanced facility, we can make more advanced OVDs.

As we know, OVDs have been widely used for more than 20 years. Here we present the technique as an important learning step to make more advanced 3D holograms using our developing 2PP lithography machine in the near future. With use of our developing parallel 2PP lithography machine, we will fabricate fully 3D subwavelength gratings to obtain 3D color visual effects (see Chapter 4 and 5). Hence, we will present the initial steps towards this goal by introducing the OVD design method and numerical simulation results using our home-built diffraction ray tracing software.

3.3.1 Principle

OVDs can be classified into two types, the transmissive type OVD is shown in **Figure 3-19**, or the reflective type OVD shown in **Figure 3-20**. In the **Figure 3-19**, the configuration consists of an illumination source, an OVD, and an observer. The OVD is usually patterned with areas containing gratings of either different pitches or different orientations, see in **Figure 3-19**. When an observer tilts the OVD, the different bright pattern can be perceived on its surface for specific illumination and observation angles.

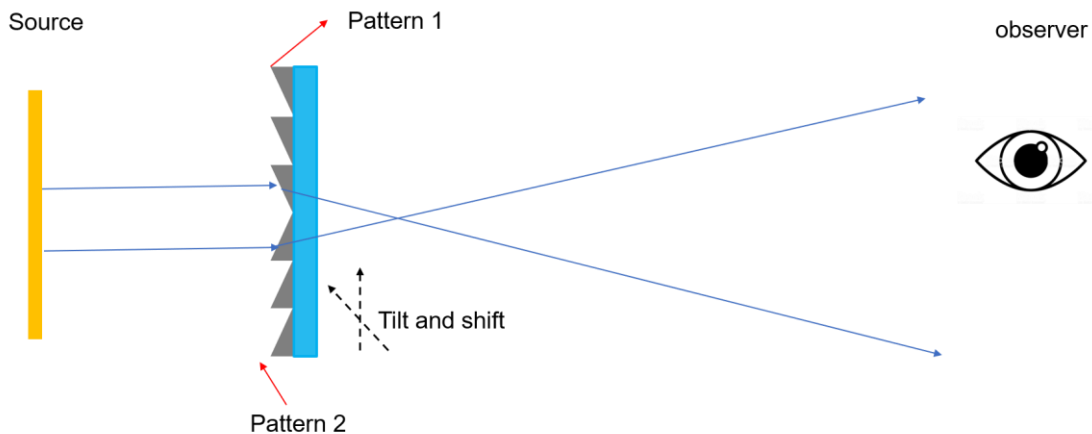


Figure 3-19-The configuration schematic of observing a transmissive OVD.

In a similar way with to transmissive type OVDs, the different pattern images can be observed by tilting the OVD, see **Figure 3-20**. On the surface of OVDs, binary, sinusoidal and the blazed gratings are frequently used to produce the specific diffraction effects. The comparison between two different types grating are depicted in **Figure 3-21**. For binary grating, the diffraction patterns are symmetrical, for example, the power of $+1^{\text{st}}$ diffraction order equals that of the -1^{st} diffraction order. The response is non-symmetrical for a multi-level phase grating, where power is almost all contribute in the 1^{st} diffraction order for grating pitches greater than about 5 microns. The

diffraction efficiency of these gratings can be predicted by combining the TEA model and scalar diffraction theory. The diffraction efficiency of an amplitude grating can be written as [26]

$$\eta_m = \left| \frac{\sin(m\pi c)}{m\pi} \right|^2 \quad (3.23)$$

Where m is the index of the diffraction orders, and c is the grating duty cycle. Generally, c is equal to 0.5, the first order diffraction efficiency of an amplitude grating is about 10% with a strong zeroth order (about 25%) and several higher orders. Obviously, it cannot be used in this application due to low efficiency and the visual interference of the higher diffraction orders.

A multilevel pure phase grating is frequently used in the design due to its high diffraction efficiency. The diffraction efficiency of such gratings based on the scalar TEA model can be written as [26]

$$\eta_m^L = \left[\frac{\sin(\pi(m-k)) \sin(\frac{m\pi}{L})}{\sin(\frac{\pi(m-k)}{L}) m\pi} \right] \quad (3.24)$$

Where L is the number of phase levels, and k is a factor for characterizing the etching depth error. When the grating has a perfect etch depth, $k=1$. According to eq. (3.24), the greater the number of phase levels, the higher the diffraction efficiency. Actually, it is often counter production to make a grating with more than 8 levels using traditional lithography techniques, since etch depth errors generally reduce the diffraction efficiency dramatically and damage the reconstructed pattern quality. When $L=8$, the efficiency of the first diffraction is around 95%, which can be regarded as a quasi-analog profile. and sufficient for this application. Next, the design process is introduced.

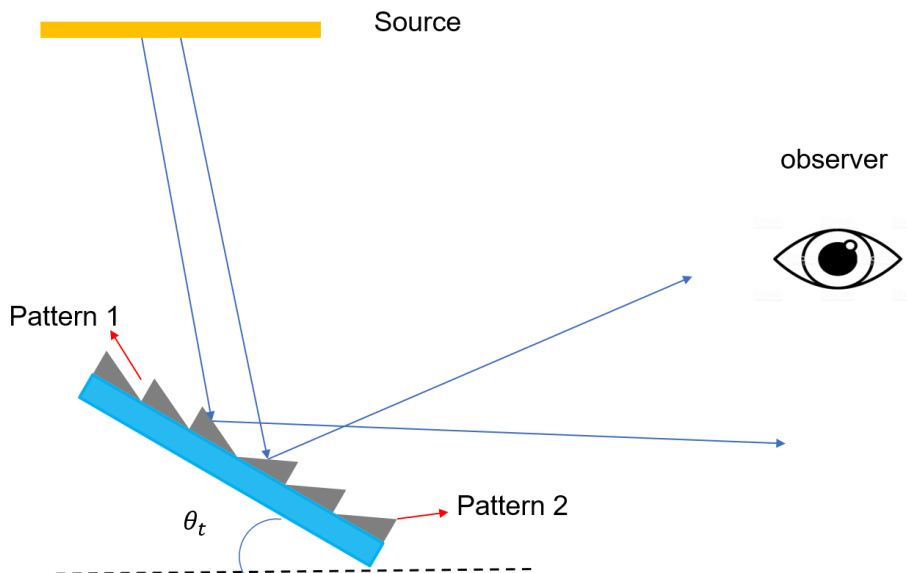


Figure 3-20-The configuration schematic for observing a reflective OVD.

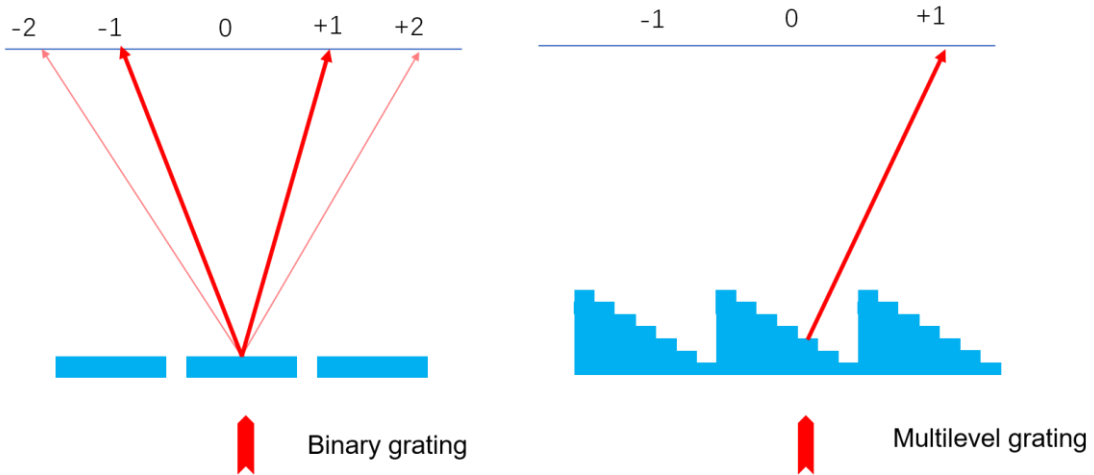


Figure 3-21-Diffraction patterns of different gratings.

3.3.2 Design and Simulation

The test target binary pattern 'π' we wish to make appear on the OVD is shown in **Figure 3-22**. The pattern is binary, white is for pattern feature, and the black is for background. So, two oppositely oriented multi-level gratings are used in this design, one for the security feature, the other for the background.

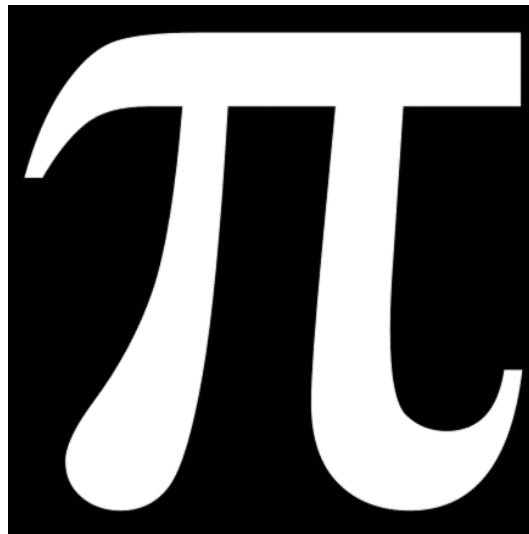


Figure 3-22-Target image for OVD.

In this design, the used pixel size was $0.75\mu\text{m}$ limited by our current photo-plotter's fabrication performance. The reflection type OVD was preferred since it is more convenient for observation. The chosen grating period was $6\mu\text{m}$ with an 8 levels phase grating. The target image is designed by 'M(x, y)'. The designed OVD component pattern T can be synthesized as

$$T(x, y) = M(x, y) * grating_1 + (1 - M(x, y)) * grating_2 \quad (3.25)$$

In eq.(3.16), $grating_1$ is patterned into the region of $M=1$, while the $grating_2$ is patterned into the area of $M=0$ (background), see them in **Figure 3-23**

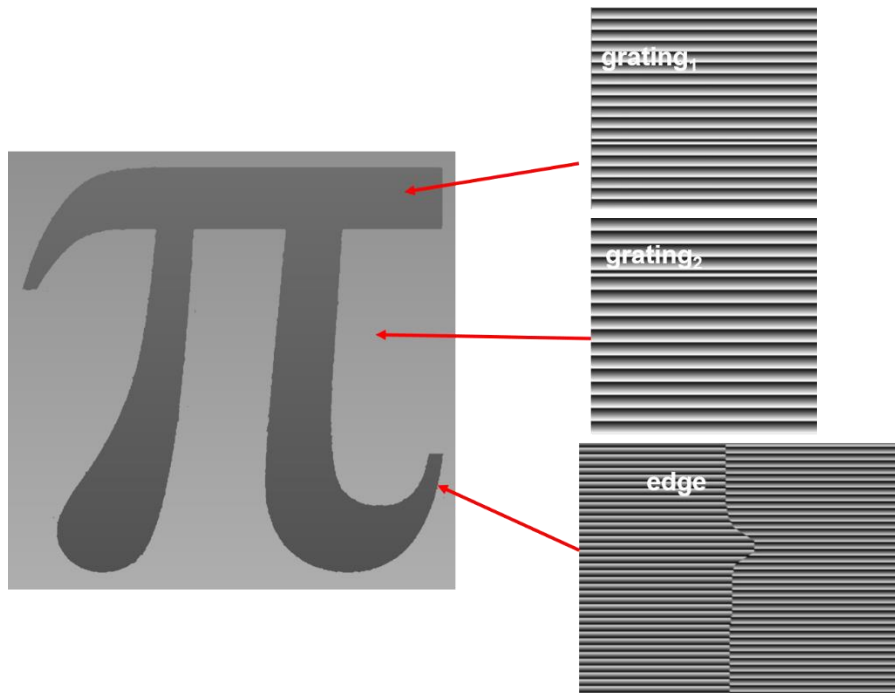


Figure 3-23-the designed OVD.

To verify the proposed design, a numerical simulation of the optical response was conducted using a new diffraction raytracing software developed by Doctor Yoran Pigeon in our group at IMT Atlantique. In the simulation, the illumination light was a square white LED source (210mm width) at a distance of 1500mm from the OVD to simulate an overhead fluorescent tube light source, and the observer was located at 500mm (arm's length) from the OVD. The results in **Figure 3-24** confirm that the design principle is verified. The corresponding experimental results are demonstrated in Chapter 5.

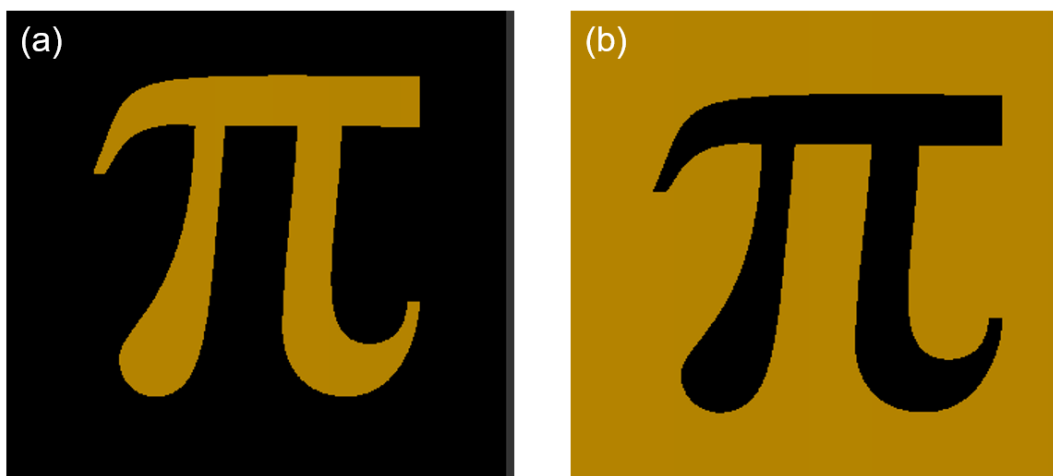


Figure 3-24-Simulation results of the designed OVD. (a) Reconstructed result with rotation angle 6 degrees. (b) Reconstructed result with rotation angle -6 degrees.

3.3.3 Conclusion for blazed gratings based OVDs

In summary, in this section a blazed grating based design method for creating a security pattern on the surface of a OVD has been demonstrated. Through the ray tracing simulation result, the design method has been validated, the observed bright pattern changes when the OVDs are tilted by an observer. As for the techniques proposed in previous sections, the OVD is also a surface relief component. Therefore, it can be replicated using the same fabrication tool mentioned before. Since it does not need a screen to show the security pattern, it can conveniently be applied to banknote and brands for anti-counterfeit. Actually, such technique is well known and relatively common. Here, we used it to learn how to design patterned OVDs. This is a learning step towards to developing more innovative OVDs producing the visual effect of a 3D object.

In the next sections we will describe a new design method and an optimization algorithm for producing faceted Fresnel hologram that give the perception of a “floating” 2D or 3D object close to hologram substrate.

3.4 Fresnel DOE method for 3D floating holographic ‘image’

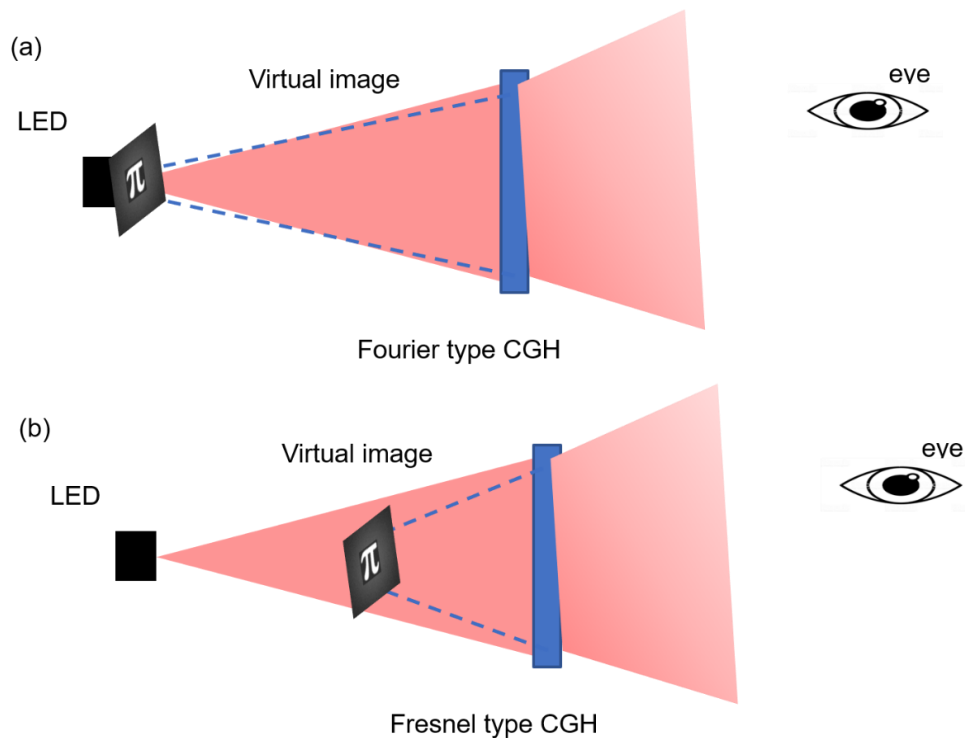


Figure 3-25-The principle of producing a virtual object. (a) Fourier type hologram. (b) Fresnel type hologram.

In this section, a design method based on off-axis Fresnel DOEs is used to create the visual impression of a 3D floating holographic image. Before we demonstrate the design strategy, its original spirit is presented first.

As indicated in Chapter 2, there are two kinds of CGHs: the Fourier type holograms and Fresnel type holograms. As is well known to optical engineers, the Fourier type hologram is used to project the desired pattern in the far field, while the Fresnel type hologram can reconstruct the target in the near field. Interestingly, when a Fourier type hologram is illuminated by a divergent LED source, a virtual image of the CGH target pattern can be seen at the source plane, see **Figure 3-25(a)**. The reason is that the light diffracted by a Fourier DOE is divergent, which also can be considered as a set of harmonic waves. When these plane waves are received by the human eye (an advanced camera), the human's brain perceives the light emitted as coming from an extended source of the form of the image coded in the hologram. For Fresnel DOE, the optical power of the DOE shifts the image from the source plane, see **Figure 3-25 (b)**. A real experimental result is presented in **Figure 3-26**. The shift distance is presented in detail in the next section. Inspired by this interesting phenomenon, we developed the 3D floating image by combining the off-axis Fresnel DOE designs and synthetic hologram techniques.

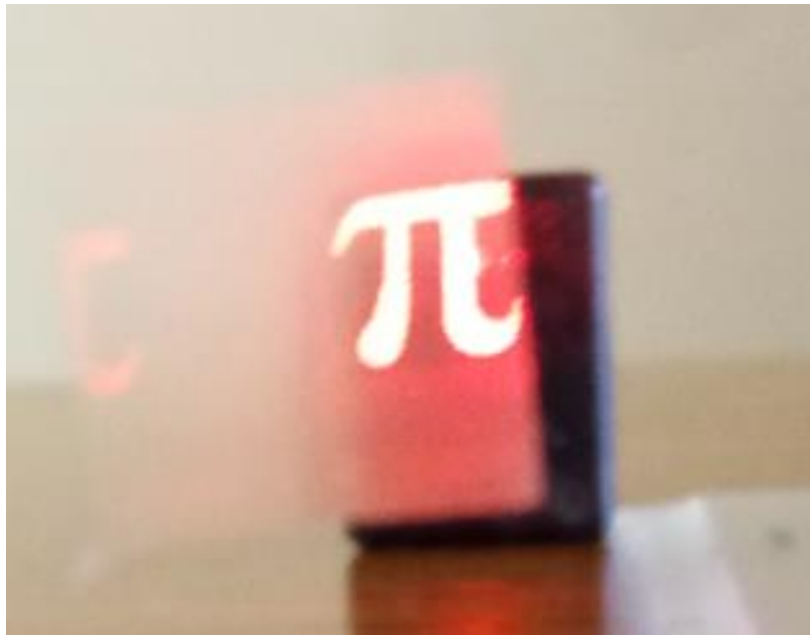


Figure 3-26- Photograph of a Fresnel type transmissive DOE illuminated from behind by red divergent LED source.

3.4.1 Algorithm for 2D floating hologram

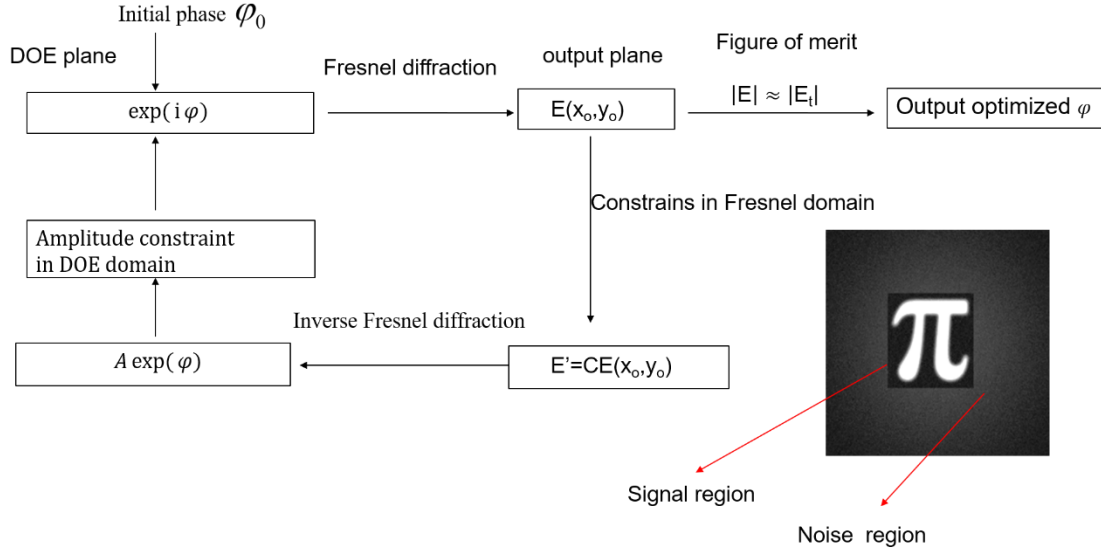


Figure 3-27-The flowchart of the modified GSA in Fresnel domain.

The basic flowchart of the DOE design approach in the Fresnel domain is shown in **Figure 3-27**. The standard GSA is based on the far field operator- Fourier transformation and inverse Fourier transformation. Therefore, the GSA should be modified using a Fresnel diffraction operator, see **Figure 3-27**. The Fresnel diffraction formula was described in Chapter 2, and its inverse form can be obtained easily. Here, we re-write the forward Fresnel diffraction and inverse Fresnel diffraction formula in eq. (3.26) and eq. (3.27).

$$U_i(x_i, y_i) = \frac{e^{jkz}}{j\lambda z} \exp \left[j \frac{k}{2z} (x_i^2 + y_i^2) \right] FT \left\{ U_0(x, y, 0) \exp \left[j \frac{k}{2z} (x^2 + y^2) \right] \right\} \quad (3.26)$$

$$U_0(x, y, 0) = \frac{j\lambda z}{\exp(jkz)} \exp \left[-j \frac{k}{2z} (x^2 + y^2) \right] FT^{-1} \left\{ U(x_i, y_i) \exp \left[-j \frac{k}{2z} (x_i^2 + y_i^2) \right] \right\} \quad (3.27)$$

The modified algorithm is presented as below. Usually, the amplitude of incident light is uniform during the design, the amplitude is set as constant 1 here. Before the iteration process begins, the initial DOE phase φ_0 is set as a random phase in the ranged $0-2\pi$. Then, a Fresnel diffraction propagation method is used to calculate the diffraction field $E(x_o, y_o)$ in the observed plane. The algorithm is modified using a zero-padding expansion method, which can be divided into two regions. In the signal region, a constraint factor is imposed on $E(x_o, y_o)$ to get the modified $E'(x_o, y_o)$, while the diffraction field is retained in the noise region. $E'(x_o, y_o)$ can be written as

$$E'(x_o, y_o) = \begin{cases} cT(x_o, y_o) & (x_o, y_o) \in \text{Signal reigion} \\ E(x_o, y_o) & \in \text{Noise region} \end{cases} \quad (3.28)$$

Where T is the amplitude field of the target image. The constraint c is a feedback factor, more detailed information can be found in reference [18]. The inverse Fresnel diffraction propagation formula is conducted to compute the diffraction field in the

DOE domain. In this design, the input illumination field was set as a plane wave, as amplitude constraint sets amplitude part of the field to 1 while retaining the phase information, then updates the phase φ . After several iterations, if the reconstructed amplitude $|E(x_o, y_o)|$ is close enough to the amplitude of the target $|E_t(x_o, y_o)|$, or the maximum number of iterations is reached, the iteration process end. Then, the optimized phase is obtained.

When an off-axis target pattern is required, the configuration can be modified as shown in **Figure 3-28** according to the specified shifting distance c_x, c_y .

To illustrate the difference between on-axis Fresnel holograms and off-axis Fresnel holograms, two types of holograms were calculated based on the design algorithm. They are shown in **Figure 3-29**. In this calculation, the design wavelength was 633nm, the pixel size of the DOE was $7.5\mu\text{m}$, the total number of sampling points was 1024, and the distance from DOE plane to the target plane was 120mm. From **Figure 3-29**, we can see the phase changes slowly in the center region for an on-axis Fresnel hologram, while it changes slowly in the corner (here upper right) for an off-axis Fresnel hologram corresponding to the target pattern.

In the following, we will present the detailed design method for producing the “floating” object effect using off-axis faceted holograms.

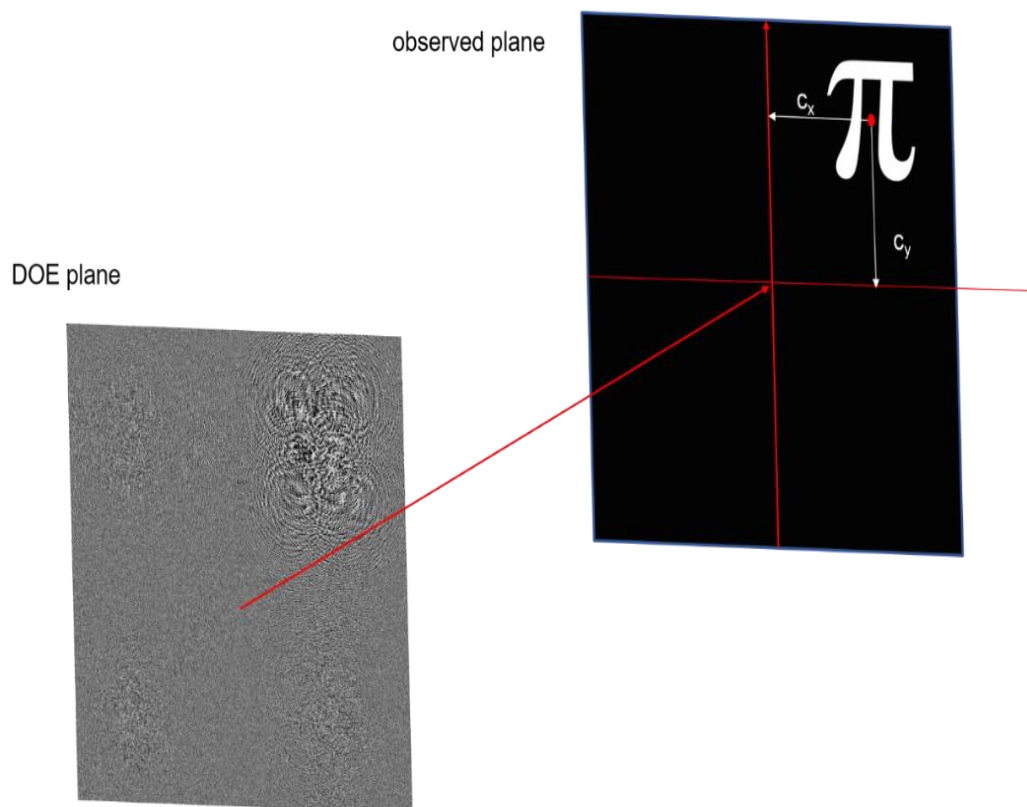


Figure 3-28-The configuration of the off-axis Fresnel DOE design.

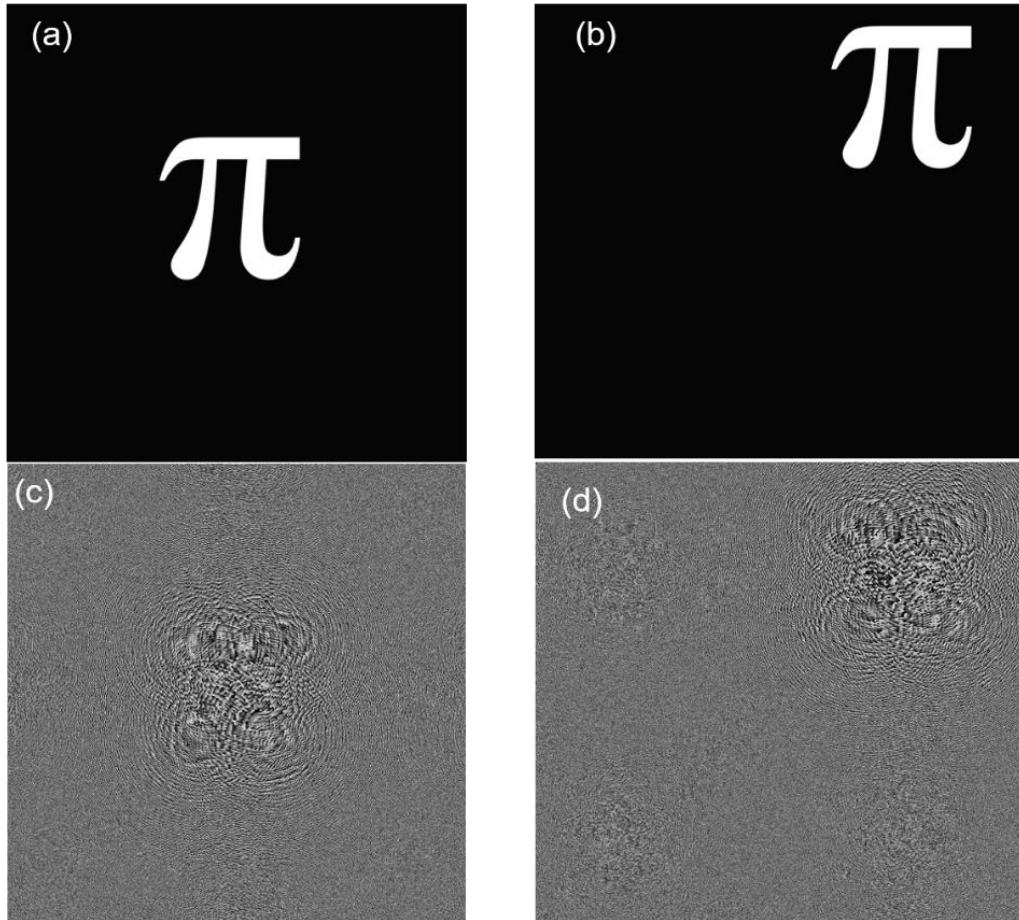


Figure 3-29-Fresnel hologram. (a) On-axis target; (b) Off-axis target; (c) On-axis Fresnel hologram; (d) Off-axis Fresnel hologram.

3.4.2 Principle and configuration for 3D floating “image” hologram

Since 3D views are more realistic for human perception, researchers have been engaged in developing holograms producing 3D visual effects for a long time. Optical recording of interference patterns is a direct way to make holograms generating real or virtual 3D image scenes, but the drawbacks of this approach also limit its applications because a complex optical interference setup is required and it is almost impossible to produce holograms of nonphysical objects [117]. Computer generated holography is more a flexible way for generating holograms compared to the traditional optical recording techniques because it can not only simulate the process of interference with a computer program but can also produce arbitrary nonphysical patterns using specific algorithms. Previous research tried to generate CGHs of simple 3D objects by superposing several holograms, each hologram generating for example a 3D image hologram [118], a 2D image slice at a different plane [119], or each hologram producing a different “tilted planar segment” of a 3D object [120]. However, in such approaches the 3D visual effect was limited by the limited number of planes or slices. A recent research of producing large size 3D hologram using ray-tracing method was proposed

[121]. But the diffraction efficiency is low since the hologram was binarized. On the other hand, a laser source was used to reconstruct the hologram thus the eye safety is also an important concern. Here our approach is not to generate a 3D light distribution but to generate the visual perception of a 3D object by combining CGHs producing different 2D views of a 3D object as seen from different directions.

In this section, we present a novel design technique which consists of faceted Fresnel DOEs to create a perception of floating 3D virtual object behind the hologram substrate when illuminated a divergent LED source [18]. Here, we name these DOE faceted pure phase Fresnel DOEs (FDOEs). As explained in previous sections, a LED source is used because it is less dangerous for visual perception than a laser source and more compact because no beam-expanding optics are needed to illuminate the whole area of the fabricated FDOE. The basic principle of the faceted Fresnel DOE is that on the surface of the FDOE, each DOE facet diffracts the incident light toward to the observer's position. Such that each facet generates an image that comes from a different angle. It therefore belongs to the off-axis type DOE. When the FDOE is illuminated by a divergent LED source, a floating 3D virtual image appears to be formed behind the FDOE an impression reinforced by moving the observer's head along the DOE; an observer can perceive different views of the virtual 3D object "hanging" in space.

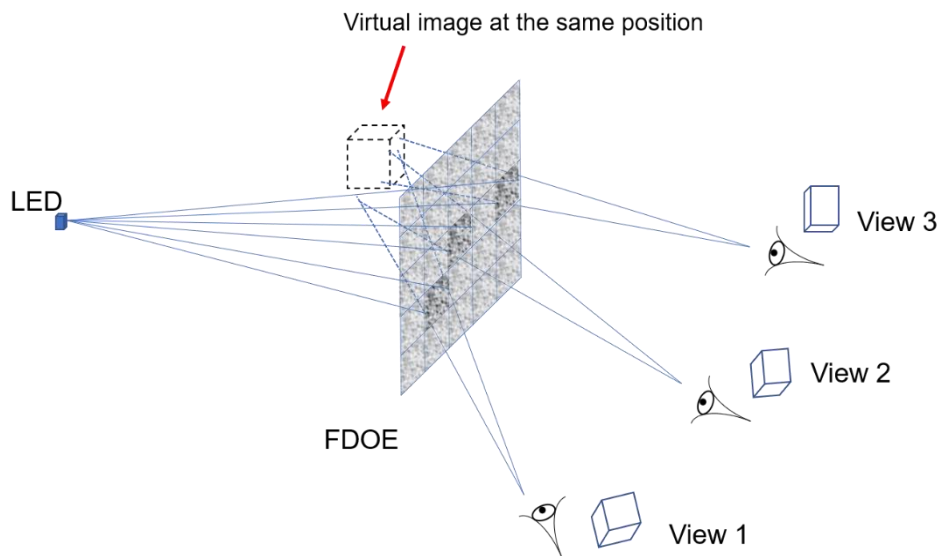


Figure 3-30-The configuration of the LED source and observer.

The essential idea of the method is sketched in **Figure 3-30**. **Figure 3-30** shows the layout of observations around the LED source and the FDOE. The LED source is placed behind the transmissive type FDOE. The overall diffractive structure is separated into a matrix of individual Fresnel DOEs. Each Fresnel DOE diffracts to generate a view of the same basic 3D object, but seen from a slightly different viewing angle. By carefully optimizing the angles for each facet, when an observer moves their eye from side to side at the FDOE plane, they observe the different views, generating the slightly different angular views of the 3D object, see **Figure 3-30**. The overall effect is that of observing a real 3D floating object. To make sure the observer has the impression that each view comes from the same object in the same position, the different DOE facets

must generate their reconstructed images with the correct off-axis offset. The lateral displacement of each reconstructed image should be calculated carefully. The basic calculation principle is shown below in **Figure 3-31**.

The global coordinates of the FDOE plane are denoted by (x_0, y_0) , and the local coordinates of the m -th DOE are denoted by (x_m, y_m) . The distance between the FDOE plane and the virtual image plane is denoted by $-z$, where z is a positive value, the distance is a negative value. The complex amplitude distribution of the (m, n) -th DOE on the FDOE plane can be described as follow:

$$H_{m,n}(x_m, y_n) = A_{source} \exp [j\varphi_{m,n}] \quad (3.29)$$

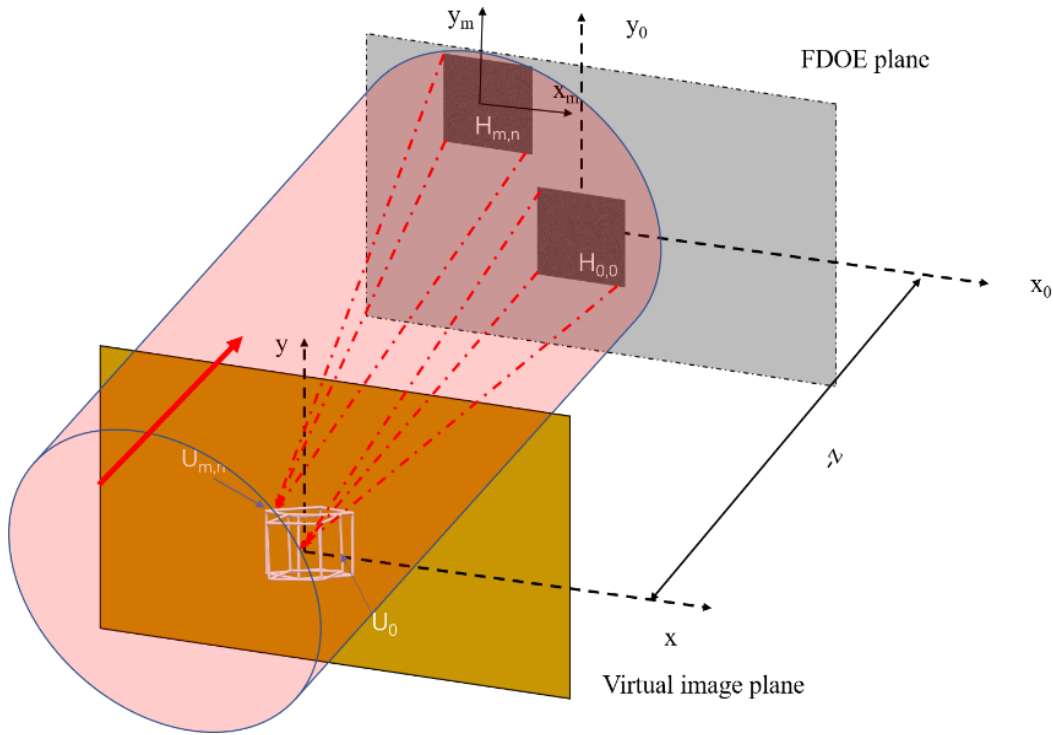


Figure 3-31-Principle of proposed FDOE calculation process.

where A_{source} and φ_m are the amplitude of the incident light and, the m -th DOE's phase distribution, respectively. According to Fresnel diffraction theory, the diffracted field distribution of the $(0,0)$ -th DOE at the virtual image plane can be expressed as

$$U_0(x, y) = \frac{\exp(-jkz)}{-j\lambda z} \exp \left[j \frac{k}{-2z} (x^2 + y^2) \right] \iint H_{0,0} e^{\frac{jk}{-2z} [x_0^2 + y_0^2]} dx_0 dy_0 \quad (3.30)$$

In eq. (3.30), $k=2\pi/\lambda$ is the wave number in free space, λ is the design wavelength, and x_0, y_0, x, y , are the coordinates in **Figure 3-31**. In order to generate the reconstructed virtual image of the (m, n) -th DOE towards the same position as that of the $(0,0)$ -th DOE, eq. (3.30) should be modified slightly. See **Figure 3-31**, x_m and y_n can be expressed as

$$x_m = x_0 + mP_{DOE} \quad (3.31)$$

$$y_n = y_0 + nP_{DOE} \quad (3.32)$$

In eq. (3.31) and eq. (3.32), P_{DOE} represents the facet size of the FDOE, m and n are the displacement along the x_0 axis and the y_0 axis, respectively. According to Fresnel diffraction theory, the complex amplitude distribution $U_{m,n}(x, y)$ in the virtual image plane contributed by the wavefront from the (m, n) -th DOE can be calculated as

$$U_{m,n}(x, y) = \frac{\exp(-jkz)}{-j\lambda z} \iint H_{m,n}(x_m, y_n) e^{\frac{jk}{-2z}[(x-x_m)^2+(y-y_n)^2]} dx_m dy_n \quad (3.33)$$

Substituting eq.(3.31) and eq.(3.32) into eq.(3.33), we obtain

$$U_{m,n}(x, y) = \frac{e^{-jkz}}{-j\lambda z} e^{\left[\frac{jk}{-2z}(x^2+y^2)\right]} e^{\frac{jk(mP_{DOE}x+nP_{DOE}y)}{z}} \\ \times \iint H_{m,n}(x_m, y_n) e^{\frac{jk}{-2z}[(x_0+mP_{DOE})^2+(y_0+nP_{DOE})^2]} e^{\frac{jk}{-2z}(xx_0+yy_0)} dx_0 dy_0 \quad (3.34)$$

Where, f_x, f_y are defined as

$$f_x = \frac{x}{\lambda z} \quad f_y = \frac{y}{\lambda z} \quad (3.35)$$

With the 2D Fourier transform (\mathcal{F}_{2D}), eq. (3.34) can be simplified as

$$U_{m,n}(x, y) = \frac{e^{-jkz}}{-j\lambda z} e^{\frac{jk}{-2z}(x^2+y^2)} e^{\frac{jk(mP_{DOE}x+nP_{DOE}y)}{z}} \cdot \mathcal{F}_{2D} \left[H_{m,n} e^{\frac{jk}{-2z}[(x_0+mP_{DOE})^2+(y_0+nP_{DOE})^2]} \right] \quad (3.36)$$

According to eq. (3.36), the diffracted field of the off-axis Fresnel DOE can still be expressed in a 2D Fourier transform format. Therefore, it can be computed quickly with the Fast Fourier transform method. Sampling constraints for the Fresnel diffraction calculation should also be considered. According to the Nyquist sampling rule, the absolute value of the propagation distance z should satisfy the condition below:

$$z > \frac{N\Delta p^2}{\lambda} \quad (3.37)$$

Here, in eq. (3.37), N is the number of sampling points and Δp is the DOE pitch. Generally, it is a phase retrieval problem to get the DOE phase. In this work, a modified iterative Fourier transform algorithm was implemented to design each off-axis Fresnel type DOE, which belongs to the IFTA family. The proposed method optimized the image quality and the fabrication performance simultaneously by incorporating a soft quantization in the iterative algorithm. The fabricated phase levels are quantized, so the surface relief of the DOE should be divided into several levels. As before eight phase levels were chosen as a good practical compromise between performance and ease of fabrication. The details of the design procedures are provided below.

3.4.3 Design procedure and numerical simulation

The flowchart of the proposed design approach is shown in **Figure 3-32**. The stack of different viewing angle target images is obtained from a 3D model using a visualization toolkit [98]. Each target image is input to the DOE optimization algorithm. This iterative algorithm can be divided into three stages, the so called three-part IFTA. The first stage is the standard Gerchberg-Saxton (GS) algorithm, it is implemented to get the rough phase solution, the GS operation process involves the back and forth transformation of signals between the input DOE plane and diffracted image plane.

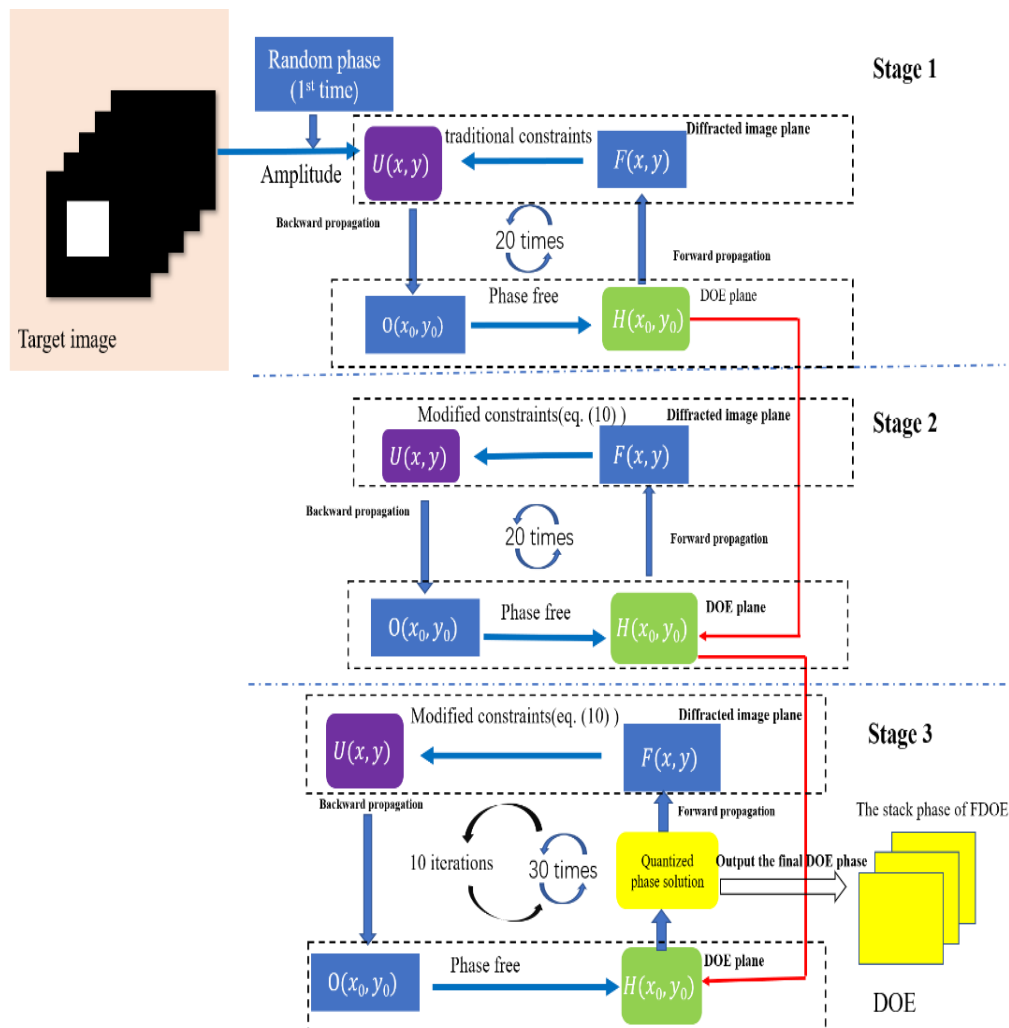


Figure 3-32-Flowchart of the proposed iterative optimization process of FDOE. See text for a detailed description.

The GS iteration process itself can be described in four basic steps:

1. The process starts from the diffracted image plane. An initial random phase is generated in the range $0-2\pi$, and then multiplied by an amplitude matrix with the current viewing angle target image to form the initial complex amplitude.
2. This field is propagated to the FDOE plane using inverse Fresnel diffraction field

propagation.

3. The amplitude of the wave-front $O(x_0, y_0)$ is replaced by the intensity distribution of the source amplitude, while the wavefront phase is retained, to form the updated complex amplitude $H(x_0, y_0)$ at the DOE plane.ⁱⁱ

4. Propagating the result back to the diffracted image plane, the phase obtained from the Fresnel diffraction propagation is combined with the corresponding view image amplitude.

The process then repeats from step 1. Based on the above steps, the phase is optimized for 20 iterations, then the algorithm goes on to the second stage, where the iteration process is similar to the GS algorithm, but the constraint strategy applied on the diffracted image plane is different to the conventional GS algorithm, here we use:

$$|U_k| = \begin{cases} 2\beta_k |F_{target}| - |F_k|, & F_k \in S \\ |F_k|, & else \end{cases} \quad (3.38)$$

Where, F_k is the reconstruction result of the k -th iteration, F_{target} is the target amplitude, β_k is a weighting factor, and S is the signal area, see **Figure 3-33**.

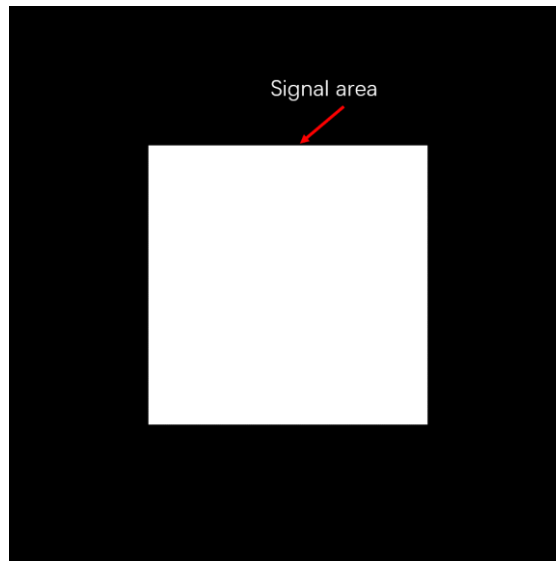


Figure 3-33-The definition of signal area in the diffracted image plane.

For a more detailed depiction of the modified amplitude constraint, we refer the interested readers to our previous published work [7].

The optimization process then goes into the third stage; this stage is called the iterative soft quantization method. The soft quantization is a stepwise iterative quantization method [27]. In this part, the iterative process is similar to that of the second stage, but another loop is introduced into it. This process of iteration can be

ⁱⁱ Note that in what follows, we assume that the DOE facets are illuminated by plane waves. Illuminating such a DOE with spherical wave will simply shift the position of the observed image along the optical axis; see discussion part for more details.

divided into 10 cycles, each cycle includes 30 iterations. The soft quantization operation can be described as follows:

First, we define φ_1 as

$$\varphi_1 = \frac{\varphi_{phase}^k}{\frac{2\pi}{Levels}} \quad (3.39)$$

$$\varphi_{phase}^{ik} = \varphi_1, \quad -\frac{\varepsilon_p}{2} \leq \varphi_1 - round(\varphi_1) < \frac{\varepsilon_p}{2} \quad (1 < p < 10) \quad (3.40)$$

In eq. (3.40), φ_{phase}^k is the un-quantized phase of the k -th iteration, $Levels$ is number of phase levels, φ_{phase}^{ik} represents the quantized phase in eq. (3.39). The quantity ε_p increases with the inner loop index p , the maximum loop range is $p=10$ in this work. p is an empirical parameter. Here, the collection of the values used for ε_p in this work is

$$\begin{aligned} \varepsilon_1 = 0.15, \varepsilon_2 = 0.3, \varepsilon_3 = 0.45, \varepsilon_4 = 0.6, \varepsilon_5 = 0.7, \varepsilon_6 = 0.8, \varepsilon_7 = 0.85, \\ \varepsilon_8 = 0.9, \varepsilon_9 = 0.95, \varepsilon_{10} = 1, \end{aligned} \quad (3.41)$$

So, in this way, the phase can be gradually quantized into eight levels with a high quality reconstructed image, and adapted to the fabrication constraints. The iterative calculation stops when the error between the intensity distribution on the reconstructed plane and target image is small enough, or the maximum number of iterations is reached. The root mean square error (RMSE) can be defined as

$$RMSE = \frac{\iint (U_{target} - \gamma |U_K|)^2}{\iint U_{target}^2} \quad (3.42)$$

where γ is a scale factor, which can be written as

$$\gamma = \left(\frac{\iint U_{target}^2}{\iint |U_K|^2} \right) \quad (3.43)$$

When the calculations of all the DOE facets are finished, the set of DOE phases are assembled to get the final FDOE.

To test and verify the numerical simulations, a 3D “cube” object was used to generate the different viewing angle images. In this simulation, a set of views in the same horizontal plane are used. To examine the convergence behavior of the proposed optimization algorithm, one view of these image is selected as the target image, this image is shown in **Figure 3-34**, it is the center view of the 3D object. The RMSE value is plotted against the iteration numbers in **Figure 3-35**. In this numerical simulation work, the wavelength was 525nm, the DOE pixel pitch was 0.75 μ m, the number of sampling points was 3600 in each DOE facet, and the distance between the FDOE plane and the virtual image was set as -120mm. According to eq. (3.42), the RMSE curves were calculated with different numbers of iterations in the soft quantization stage. For

example, 50 iterations are needed in the soft quantization step, the total number of iteration is 540 (20 in the first stage, 20 in the second stage, 500 in the third stage).

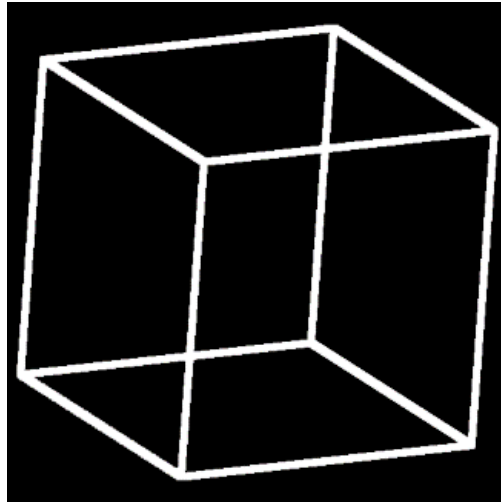


Figure 3-34-Target image for testing the algorithm's convergence behavior.

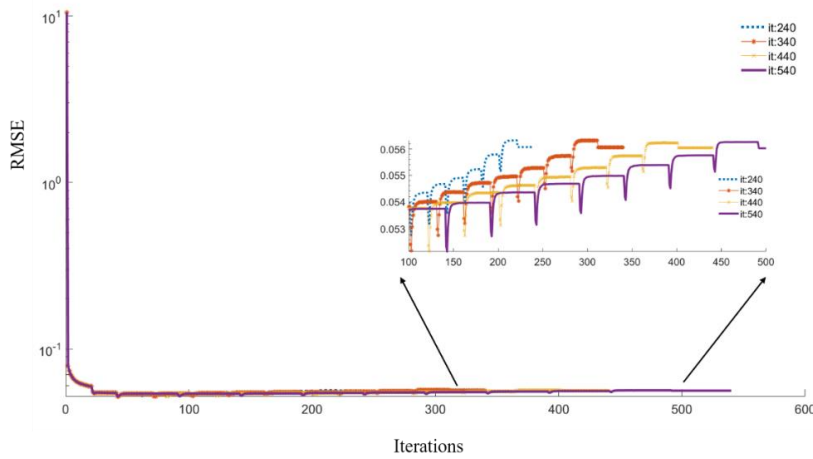


Figure 3-35-Curve of the reconstruction's RMSE against the iterations.

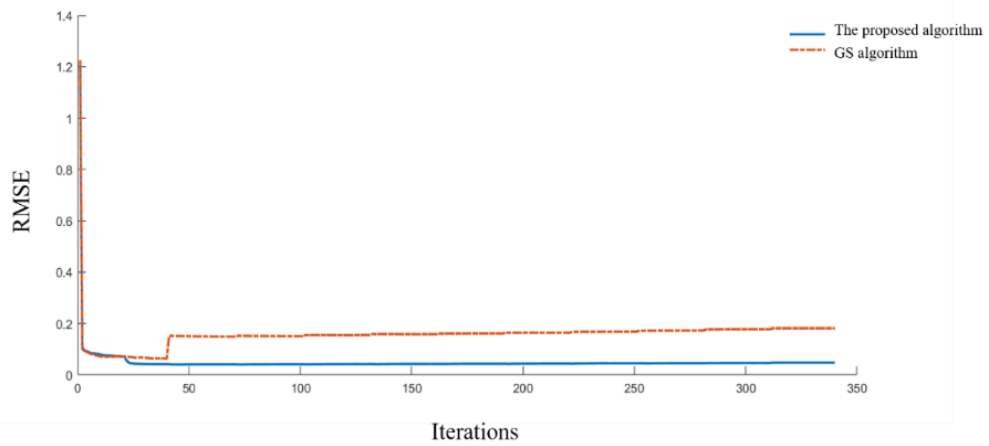


Figure 3-36- A Comparison of convergence behavior between the proposed algorithm and GS algorithm.

In **Figure 3-35**, the RMSE is small enough when the total number of iterations is 340. To further compare the convergence behavior between the standard GS and the proposed algorithm in this work, the RMSEs of the two algorithms are plotted in **Figure 3-36** against the iteration number. The results indicate that the proposed algorithm converges to a smaller RMSE than GS algorithm when the soft quantization process is implemented.

As there are many separate DOEs to calculate in the whole FDOE, the GPU is used to accelerate the calculation speed; the iteration optimization time is about 120 seconds for each facet on a computer equipped with Intel Core™ I7-8750H CPU@2.2GHz, GPU GTX1060 and the computation platform was MATLAB software. The final optimized DOE facet is shown in **Figure 3-37(a)**. The inset is a cross section of the phase map distribution in the red circle. It clearly indicates an eight phase-level structure. The simulated reconstructed virtual image is shown in **Figure 3-37(b)**. The reconstructed image is similar to the target image in **Figure 3-34**. But the reconstructed image is a bit darker than the target image, because the calculated diffraction efficiency is about 82%, part of the energy being lost as noise. The diffraction efficiency is defined as:

$$\eta = \frac{\sum_M \sum_N I(I \in S)}{\sum_M \sum_N I} \quad (3.44)$$

where I is the intensity distribution of the target plane, M and N are the number of sampling points in the X and the Y direction, respectively. S is the signal window.

For our application, the aim was to generate horizontal parallax 3D views. 11 off-axis Fresnel type DOE elements were used. The total size of the FDOE is 29.7mm×2.7mm, it can be regarded as the system eye-box. However, this is too small to be convenient in the vertical direction, as an observer will no longer see the virtual object if their eye moves beyond this small area. The pupil size of human eye is between 6mm~8mm, so the vertical direction should be expanded to satisfy this size. To address this problem, we developed a simple method to increase the vertical eye-box size. The assembly is shown in **Figure 3-38**.

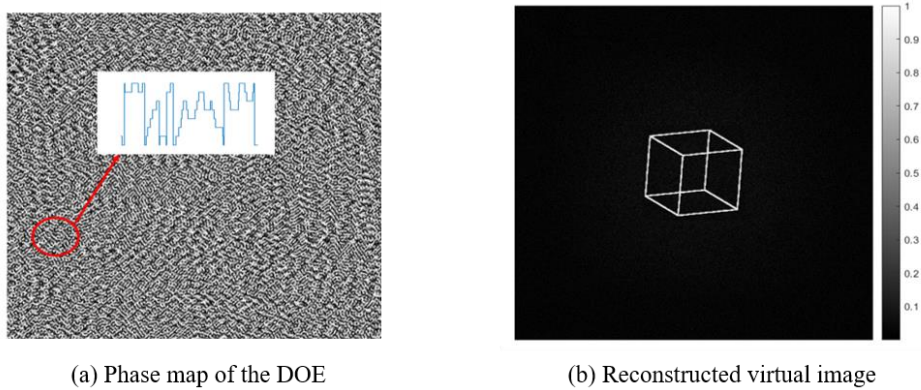


Figure 3-37-Optimal phase map and the reconstructed result.

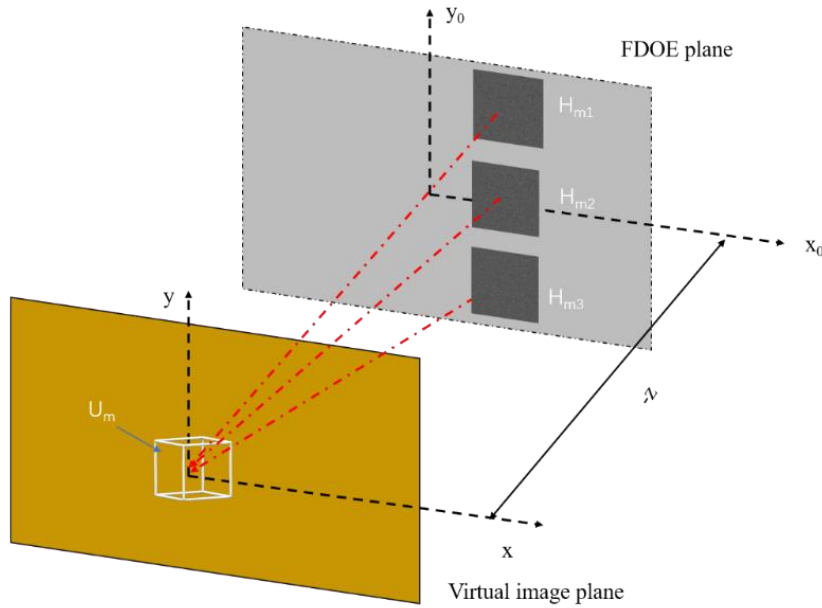


Figure 3-38-Assemble of the FDOE.

In Figure 3-38, the elements H_{m0} , H_{m1} and H_{m3} generate the same virtual image U_m at the same position. When the observer moves their eye in vertical direction, they can still see the same virtual image at a specific view angle. In this way, the eye-box can be expanded in the vertical direction, and the final size of the FDOE is $29.7\text{mm} \times 8.1\text{mm}$. Due to the use of divergent illumination and DOE fabrication limitations, the LED source (zeroth order) is visible to the observer through the DOE. If the FDOE are designed with an on-axis target, this visibility of the LED source perturbs the desired image. To avoid this, an off-axis configuration is used. An FDOE designed with the algorithm mentioned above, was fabricated by using our home-built photo-plotter was presented in Chapter 5. Next, we provide the discussion part of this design method.

3.4.4 Discussion: Validity of the 3D effect

In this section, we have presented the design process for a diffractive structure, based on an array of computer generated off-axis Fresnel phase holograms. When illuminated by a readily available LED source, the overall structure gives an observer the perception of a floating 3D object in space behind the hologram substrate. The design model has been described and confirmed through numerical simulation.

An important factor in generating the impression of a 3D object is the position of the LED source. In this work, the FDOE we designed is a shift-invariant component. Since the light propagation model used here is a linear transformation; the observed result is not sensitive to the position of the LED source. Mathematically and optically, the function of an off-axis Fresnel type DOE can be decomposed into three linear components: a spherical lens, a Fourier type DOE and a blazed grating phase. The

blazed grating phase component is used to shift the image laterally to the desired position. In **Figure 3-39(a)**, when the LED source is on the axis of DOE1, the virtual image is still formed on the axis because there is no blazed grating component in DOE1. The position of the generated virtual image can be calculated with the geometrical imaging formula as below.

$$d_{image} = \frac{f_{fresnel}d_s}{d_s - f_{fresnel}} \quad (3.45)$$

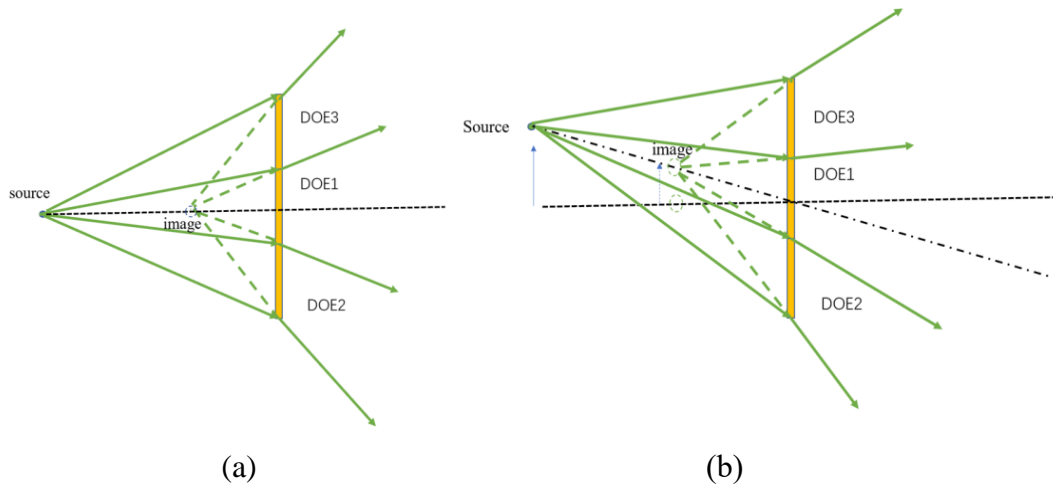


Figure 3-39-Schematic of imaging principle, (a) LED source is on the axis, (b) LED source is off axis.

Where $f_{fresnel}$ is the designed focal length of the Fresnel type DOE whose value in our design was -120mm, d_s is the distance between the source and the FDOE plane.

Since facets DOE2 and DOE3 are off axis, they contain a blazed grating component, so, their corresponding virtual image is deflected to the same position as the image produced by DOE1.

When the LED source is moved with respect to its original position (see **Figure 3-39 (b)**), the virtual image will move in the same direction, this process is similar to a lens imaging system, because the DOE's Fresnel lens component works as a lens. In this situation, the corresponding images generated by DOE2 and DOE3 just move in the same way.

However an additional complication should be noticed, the LED source is a divergent source, and the intensity shows a cosine roll off with the divergence angle. The bigger the divergence angle, the weaker the intensity. Therefore, the shifting distance of the LED source cannot be too far from the original position. Otherwise the observed object will appear with reduced and uneven intensity.

Another important factor is the spatial coherence of the LED source [99], the size of the LED cannot be too big; otherwise, the reconstructed image will not be sharp due to the reduced degree of spatial coherence. To show how the size of the LED affects the reconstruction image quality, the qualitative analysis was conducted with the results shown in **Figure 3-40**. As we expected, the reconstructed image is smeared when the size of the LED increases, small LED size produces good results. In our real application, the used LED (for example smartphone LED) size is typically around 1mm×1mm, and

the distance from the LED source to FDOE plane is more than 150mm, so the LED source can be still regarded as ‘point source’.

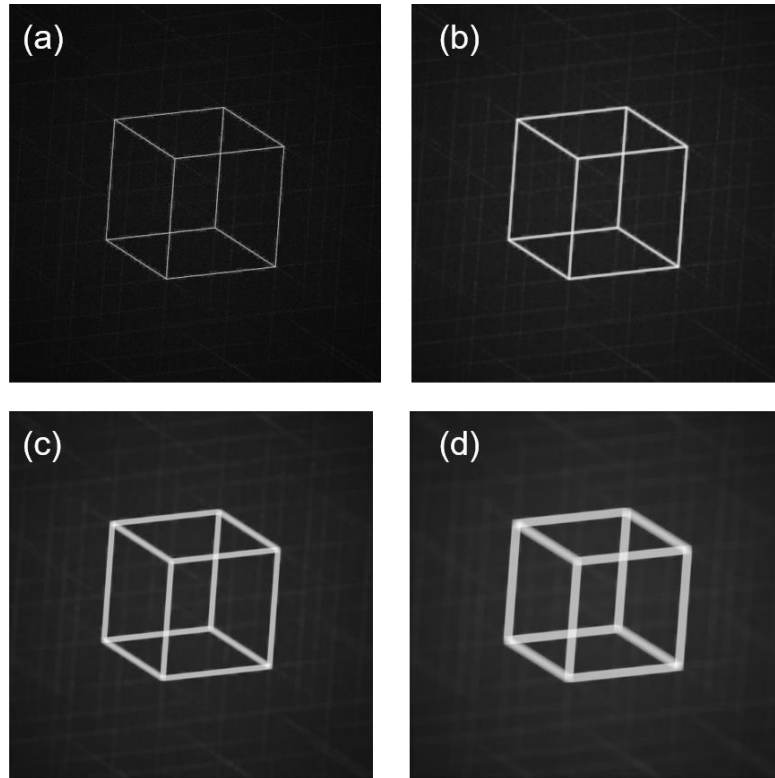


Figure 3-40- Simulated reconstruction image with different LED size. (a) Reconstructed result with coherent plane wave. Reconstructed results for LED size of (b) 1mm. (c) 2mm. (d) 3mm.

3.4.5 Conclusion of the FDOE method

In summary, in this section we have developed a design approach for phase-only faceted DOEs producing the visual impression of a horizontal moving 3D virtual object floating behind the hologram substrate. The design model for the FDOE has been validated through numerical simulation and experiments, the experimented results are presented in chapter 5. The convincing 3D virtual object can be perceived though a horizontal displacement of the observer’s eye exclusively when the FDOE is illuminated by a divergent LED source. Once again, as the FDOE is a surface relief diffractive structure, it can be replicated using mature roll-to-roll nanoimprint techniques for mass production. Therefore, the FDOE developed in this section can find important applications in advanced anti-counterfeiting protecting of bank notes and ID cards. The developed approach of the modified GS algorithm may also be applicable potentially in practical holographic 3D display applications. However, the calculation was heavy when large holograms are needed. The available fabrication resolution was not full used in the consideration of these off-axis Fresnel DOE method. To address these problems, a spatial frequency segmentation method was presented in the next

section.

3.5 3D image DOEs by Frequency multiplexing method

3.5.1 Design principle

In the previous section, we discussed the design method producing a perceived floating 3D virtual object using multiple holographic elements (facets) based off-axis Fresnel DOEs. It can produce an impressive 3D effect, but, the main drawback is the heavy calculation load of the iterative algorithm which limits its applications to relatively small size DOEs (a few cm²). To resolve this problem, the following spatial frequency segmentation technique was investigated [100]. It requires the calculation of only a single Fourier transform without any iterative calculations. The schematic of the principle is sketched in **Figure 3-41**.

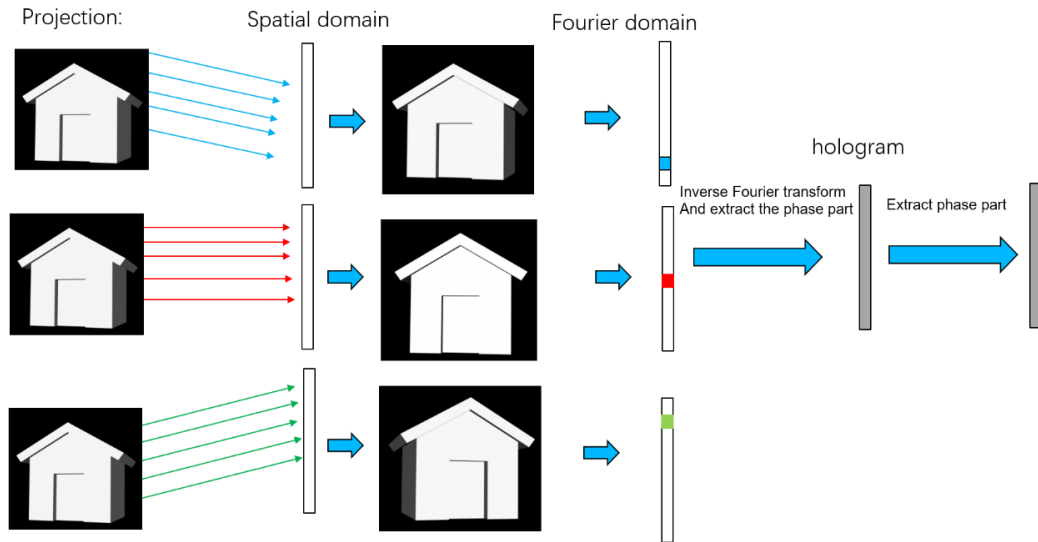


Figure 3-41-Schematic of the spatial frequency segmentation method.

The calculation process can be divided into three steps. The first step is called the parallel projection process, the second step is to inverse Fourier transform the assembled components in the Fourier domain, and the third step is to extract the phase part to make a pure phase hologram. In the first step, the projection of the target object is along the direction corresponding to its view angle, see **Figure 3-41**. Here, the lines with different colors represent the different view angles in **Figure 3-41**. In a second step, since the calculation method is based on the spatial frequency domain, the angular spectrum propagation operator is used to calculate the light field. In this way, the complex field in the Fourier domain can be expressed in eq. (3.46).

$$H(f_x, f_y) = \sum_{i,j} O(f_x^i, f_y^j) \exp [j2\pi z \sqrt{\frac{1}{\lambda^2} - f_x^{i2} - f_y^{j2}}] \quad (3.46)$$

Where λ is the wavelength, f_x^i and f_y^j are the (i, j) th spatial frequency corresponding to that of the projection angle, which can be written as

$$f_x^i = \frac{\cos\alpha_x^i}{\lambda}, f_y^j = \frac{\cos\alpha_y^j}{\lambda} \quad (3.47)$$

where $O(f_x^i, f_y^j)$ is the angular spectrum of the target object, $\cos\alpha_x^i$ and $\cos\alpha_y^j$ are direction cosines in the X and Y directions, respectively, and z is the distance between object plane and hologram plane (in this simulation, z is 50mm). In the third step, the light field in the hologram plane is calculated using an inverse Fourier transform, and the phase part is extracted to get the final hologram design as below.

$$h(x, y) = \text{angle} \left[FFT^{-1} \left(H(f_x, f_y) \right) \right] \quad (3.48)$$

Where *angle* indicates extraction of the phase part of the complex amplitude. Here, we let the amplitude part be constant one. This operation enables us obtain a higher diffraction efficiency DOE than that presented in reference [100].

In general, the reconstructed results show many higher diffraction orders around the signal area when the angular spectrum propagation method is used. One way to suppress this effect is to use the zero-padding technique on the target image as shown in **Figure 3-42**.

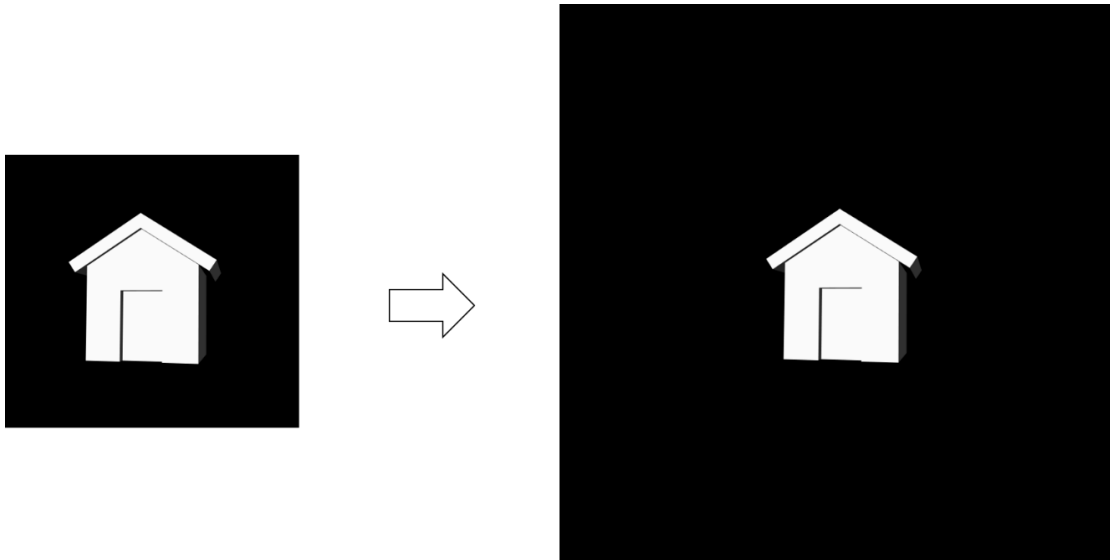


Figure 3-42-The principle of the zero-padding technology for target image.

The corresponding simulation results are shown in **Figure 3-43**. The higher diffraction orders are obvious **Figure 3-43** (a), while the higher orders have almost disappeared in **Figure 3-43**(b). To validate the reconstruction performance with the proposed technique, a hologram was fabricated with our home-built photo-plotter at IMT-A. The sampling of the hologram is 20000×20000 with a pixel size 1.5 μ m, and the design wavelength was 633nm. With this DOE pixel size, the field of view (FOV)

can be 22 degrees. The number of components in the Fourier domain is 1×15 . The calculated hologram size was $30\text{mm} \times 30\text{mm}$ in this simulation work, and the time cost is about 20 minutes using a standard Personal computer. The experimental results are demonstrated in Chapter 5, verifying the proposed method.

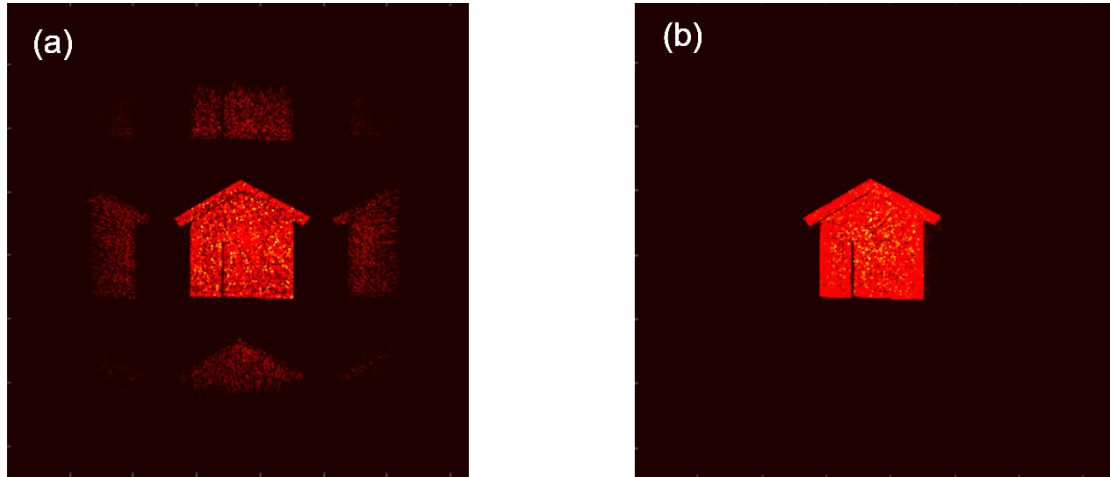


Figure 3-43- Simulation results. (a) the simulation result without zero-padding. (b) the simulation result with the zero padding.

3.5.2 Summary of the Frequency multiplexing method

In conclusion, a design algorithm of producing an impressive 3D floating virtual object based on the space frequency multiplexing technique was demonstrated in this section. By calculating the hologram using the angular spectrum diffraction formula without the paraxial approximation, a floating virtual object can be perceived behind the hologram substrate, see the experimental result presented in Chapter 5.

Unlike the faceted Fresnel holograms method that proposed in previous section, the demonstrated method is less calculation load since it only uses a single Fourier transformation (in this simulation work, the calculation time is 20 minutes for producing a $30\text{mm} \times 30\text{mm}$ DOE). Therefore, it is a valuable method for calculating large size holograms. The DOE size can be larger still by using a modified Fourier transformation [101]. The FOV of this DOE only depends on the pixel size, here the FOV is about 22 degrees which is twice the result of the FDOE method presented in the previous section.

In this design work, the high diffraction orders can also be suppressed in the observation window using the zero-padding technique (see **Figure 3-43**), which can provide a better reconstructed image quality. Similar to the FDOE, the presented DOE in this section is also a surface relief structure which can also be replicated using standard roll-to-roll nanoimprint technique for mass production.

In addition, the presented design method could also be a good candidate for practical holographic 3D display application due to its fast hologram calculation.

3.6 Conclusion

In this chapter, several novel design approaches have been proposed for DOEs producing real and virtual 2D and 3D images when illuminated by readily available temporally incoherent divergent light source such as LEDs. Such DOEs are particularly attractive for security hologram applications. Numerical simulations were conducted to validate all the design methods. The fabricated DOE can be reconstructed with a simple LED source which makes it possible for an observer to recognize the security feature without using special auxiliary tools.

However, the proposed design methods work best for monochromatic light sources since their designs are based on the TEA model. In many applications, an extended white light is frequently used to illuminate the security holograms, for example the illumination light of a smartphone. The optical performance of a thin DOE depends on the wavelength, so dispersion can be important when the DOE are illuminated by white light. Usually, the way to reduce this dispersion is to produce a smaller target pattern that means the light waves diffracted by the holograms converge to the target plane (in this way, the dispersion is small). This is a useful compromise from the perspective of optical engineering and already produce very usable DOEs, but the problem of dispersion is not fundamentally addressed.

In fact, looking at historical, optically recorded “thick” holograms (Bragg gratings) appears to be an effective way to resolve the problem mentioned above, but complicated optical interference benches and specific photosensitive resists are needed. The massively parallel 2PP lithographic system which we are currently developing is starting to make possible the synthetic fabrication of a 3D “thick” DOEs. Inspired by this new machine, new thick 3D structures have been investigated by using a heuristic optimization algorithm. Since the structures thick (the equivalent phase shift is larger than 2π), the TEA model is invalid. To calculate the diffraction field accurately, the electro-magnetic rigorous model is needed. In the next chapter, such a new 3D structure is presented and novel design methods obtained by combining the rigorous vectorial model with an optimization algorithm are described in detail.

Chapter 4 Modeling and optimizing optically thick DOEs

4.1 Introduction

In the previous chapter, we presented several different kinds of DOE algorithms for designing security and 3D visualization holograms. However, as discussed in section 3.6, these DOEs are all based on the TEA model, thus the corresponding devices are wavelength sensitive which often reduces their performance when observed with white light illumination. To resolve this problem, wavelength selective devices are highly required. Volume holograms are good candidates because of their phase shift of more than 2π . But their drawbacks also restrict them as we mentioned in the previous section. Now that the fabrication of thick 3D structures is becoming possible in our cleanroom, this drives us to think about new design approaches for the synthesis of thick DOE.

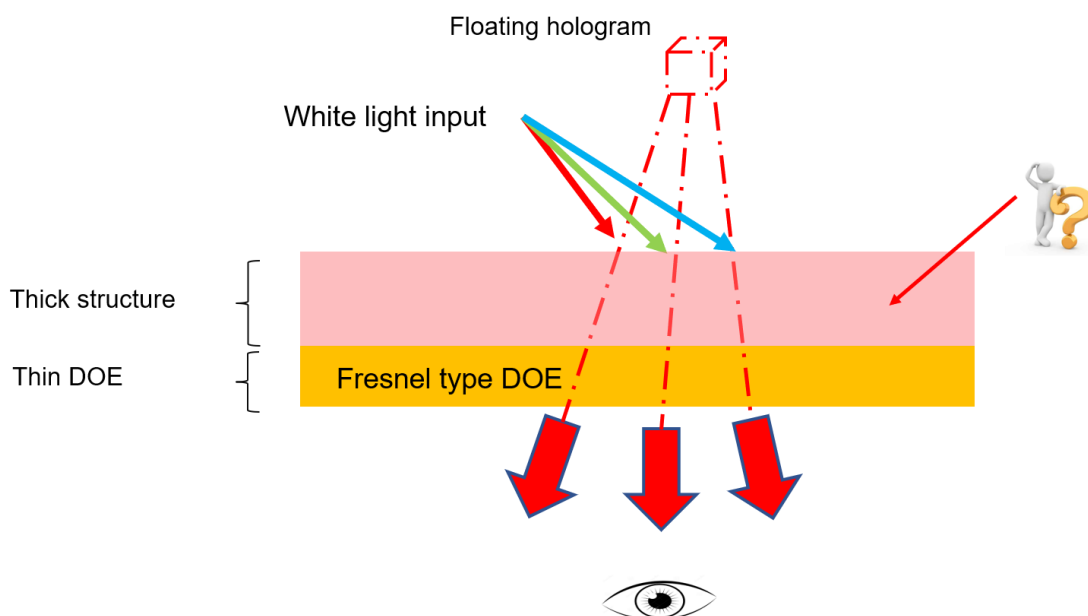


Figure 4-1-Schematic of thick hologram with white light illumination.

Our idea for a first hologram is depicted in **Figure 4-1**. The unit comprises a thick structure and a faceted Fresnel type DOE. The thick structure would work as a wavelength selective device. The faceted Fresnel DOE could produce for example a floating virtual 3D object. When observed under a white light illumination, a single

color virtual object could be perceived. But, the thick structure is not detailed in **Figure 4-1**. How can we design this thick structure?

Before we begin the design, the concept of ‘structure colors’ should be clarified. Structure colors, which results from the interaction of light and subwavelength structures have attracted extensive attention in the optics community [102]. Some researchers developed bio-inspired structures which mimic the nanostructure of the butterfly’s wing [103, 104]. Artificial structures have also been proposed recently [105, 106]. But, the disadvantages of these structures are that they need complex multistep photolithography fabrication, and different materials of different indices. To overcome these problems, a 3D structure with only one material was targeted. Generally, fabricating a patterned narrowband filter is a more complex and costly multistep process, but such kinds of thick structures can be fabricated directly by using two photon polymerization (2PP) lithography which will be described in Chapter 6.

In this chapter, we present an inverse optimization methodology that incorporates the specific fabrication constraints of the 2PP lithography process. The major difficulty is that the structures are thick, so the TEA is invalid because the phase shift is great than 2π . To design the structure, a more rigorous diffraction model should be used. In general, the FDTD and Fourier Modal Method (FMM) are frequently used for full-wave calculations. Although both algorithms are limited to small structures, periodic structures can be usefully designed because they can be repeated spatially during fabrication to create large area photonics structures. Since the FMM is a semi-analytical solution of Maxwell’s equations, the calculation is usually less heavy than FDTD. Thus, we chose FMM to optimize a single period of the thick structure. The longer-term aim of this approach is to enable the extension of thick diffractive optical elements to an expanded realm in other fields of optics research, such as grating splitters, angle selective devices, and so on. Next, we will present the original idea and the design algorithm of our optimization model.

4.2 Kogelnik theory

Before we present the proposed design method, Kogelnik theory is introduced here whose the original idea originates from the volume Bragg grating (VBG) [107]. In 1969, Kogelnik first proposed the coupled-wave theory based on a group of differential equations used in the holography community. The various diffraction phenomena including transmission and reflection by gratings which occur in VBG were investigated comprehensively. The core of Kogelnik coupled-wave theory (KCWT) is to resolve the coupled wave differential equations of the incident and diffracted light waves with different optical constants based on Maxwell’s equations. The most important parameter of the VBG is the diffraction efficiency at the Bragg incident angle, which can be obtained directly from the solution of the KCWT equations. KCWT has been widely used to predict VBG diffraction characteristics since the obtained analytical solutions match well with the experimental results of the real fabricated VBG. However, the KCWT is an approximate theory. The hypotheses in the derivation are as follows:

1. The interference light field of the hologram is a cosine-shaped intensity distribution;

2. The spatial modulation of the dielectric constant of the recorded medium and its conductivity vary according to a cosine law. The light and medium interaction is linear;
3. The illuminating light is incident at the Bragg angle, thus only the illumination light and the first-order diffracted light exist, all the other diffraction orders are ignored, i.e., only the Bragg regime is considered in this model.
4. The second order differential of the light's amplitude is ignored, this is the so called slow envelope approximation.

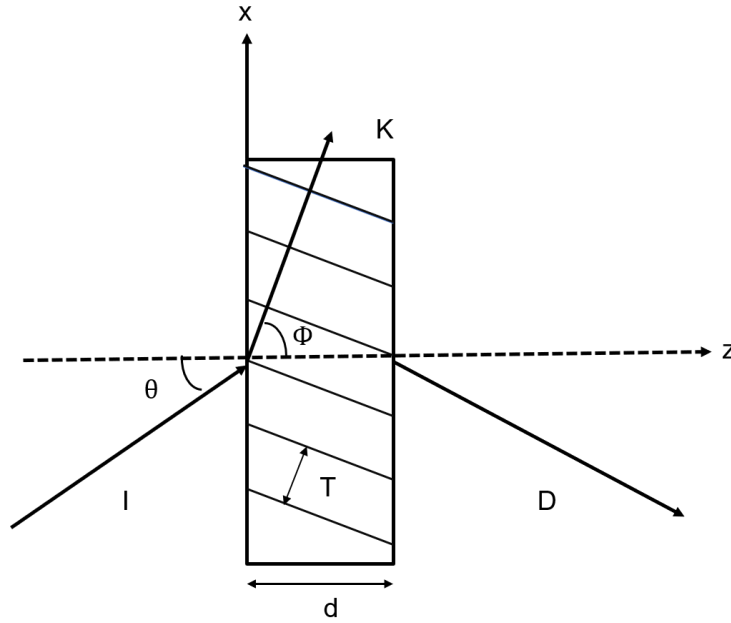


Figure 4-2- Schematic of the VBG's diffraction.

The geometric parameters of the VBG are sketched in **Figure 4-2**. The thickness of the VBG is marked as d , and its period is T . The grating vector K is in the x - z plane, and the angle between K and the z axis is Φ . Here, 'I' represents the incident illuminating light, and 'D' is the diffracted light by the VBG.

According to assumption 2, the dielectric constant and conductivity in the grating ($z=0$ - d) can be expressed as

$$\begin{cases} \varepsilon_g = \varepsilon_{r0} + \varepsilon_g' \cos(\vec{K} \cdot \vec{r}) \\ \sigma_g = \sigma_0 + \sigma_g' \cos(\vec{K} \cdot \vec{r}) \end{cases} \quad (4.1)$$

Where, ε_{r0} and σ_0 are the average dielectric constant and average conductivity respectively. ε_g' and σ_g' are their corresponding spatial modulation amplitude, and \vec{r} represents the spatial coordinate in the VBG. Since the relationship between the refractive index and dielectric constant is $n = \sqrt{\varepsilon_r}$, and $\varepsilon_g' \ll \varepsilon_{r0}$, the spatial variation of refractive index in the VBG can be simplified as

$$n = \sqrt{\varepsilon_{r0}} + \frac{\varepsilon_g'}{2\sqrt{\varepsilon_{r0}}} \cos(\vec{K} \cdot \vec{r}) \quad (4.2)$$

The propagation of the electromagnetic wave in the VBG can be described using the scalar Helmholtz equation.

$$\nabla^2 E + k^2 E = 0 \quad (4.3)$$

In eq. (4.2), $k^2 = \omega^2 \mu_0 \varepsilon_0 \varepsilon_r - j\omega \mu_0 \sigma$, then substituting the eq.(4.2) into k ,

$$k^2 = \beta^2 - 2j\alpha\beta\kappa\beta\cos(\vec{K} \cdot \vec{r}) \quad (4.4)$$

In eq.(4.4), $\beta = \omega(\mu_0 \varepsilon_0 \varepsilon_{r0})^{\frac{1}{2}}$, $\alpha = \frac{\sigma_0}{2}(\mu_0/\varepsilon_0 \varepsilon_{r0})^{\frac{1}{2}}$, $\kappa = \frac{\pi n_1}{\lambda} - j\frac{\alpha_1}{2}$, β is called the propagation constant, and κ is the coupling constant. According to hypothesis 3, the electric field inside the VBG can be determined by superimposing the complex amplitude of the incident illumination light I and the diffracted light D .

$$E = I(z) \exp(-j\vec{k}_I \cdot \vec{r}) + D(z) \exp(-j\vec{k}_D \cdot \vec{r}) \quad (4.5)$$

Where, the amplitude of $I(z)$ and $D(z)$ change slowly along the z axis, and \vec{k}_I and \vec{k}_D contain the propagation constant and wave vector direction. The relationship between \vec{k}_I and \vec{k}_D can be written as

$$\vec{k}_D = \vec{k}_I - \vec{K} \quad (4.6)$$

As shown in **Figure 4-3**, if the incident light fulfills the Bragg condition, the wave vector of incident light, the grating vector and the vector of diffracted light form a closed isosceles triangle. The direction of diffracted light can thus be predicted according to the K vector. When the incident light deviates from the Bragg condition, the direction of the diffracted light is hard to determine, that means the end of the K vector is not on the circle, see **Figure 4-3** (b). So, $|\vec{k}_D| \neq |\vec{k}_I|$.

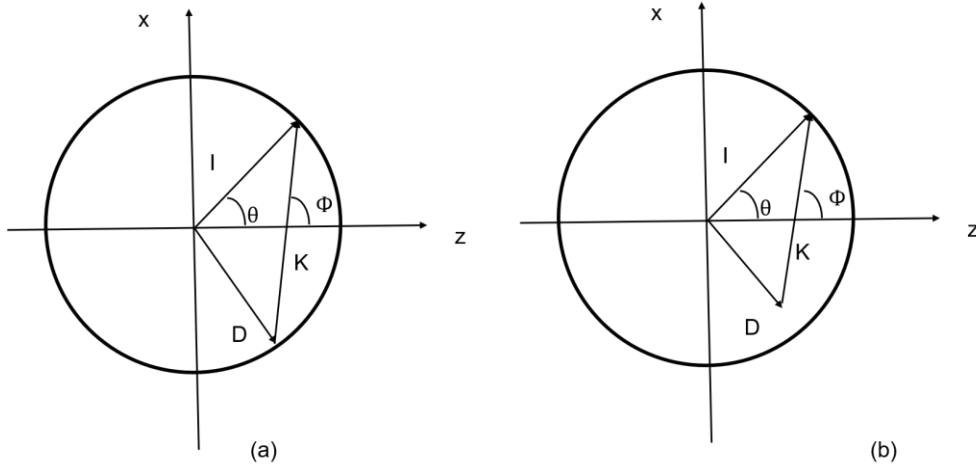


Figure 4-3-Vector diagram for a volume Bragg grating. (a) Incident light at the Bragg angle. (b) Incident light deviated from the Bragg angle.

Based on the above assumptions, the wave vectors of \vec{k}_I and \vec{k}_D can be expressed as

$$\vec{k}_I = \begin{bmatrix} \rho_x \\ 0 \\ \rho_z \end{bmatrix} = \beta \begin{bmatrix} \sin \theta \\ 0 \\ \cos \theta \end{bmatrix} \quad (4.7)$$

$$\vec{k}_D = \begin{bmatrix} \delta_x \\ 0 \\ \delta_z \end{bmatrix} = \beta \begin{bmatrix} \sin \theta - K \sin \Phi / \beta \\ 0 \\ \cos \theta - K \cos \Phi / \beta \end{bmatrix} \quad (4.8)$$

When the Bragg condition is satisfied, $K = 2\beta \cos(\Phi - \theta)$. The coupled wave equations can be derived by combining eq. (4.1)-eq. (4.7):

$$c_I I' + \alpha I = -j\kappa D \quad (4.9)$$

$$c_D D' + (\alpha + j\chi)D = -j\kappa I \quad (4.10)$$

Among eq. (4.9) and eq. (4.10), $\chi = \frac{\beta^2 - k_D^2}{2\beta}$, and the inclination factors are defined as

$$c_I = \cos \theta \quad (4.11)$$

$$c_D = \cos \theta - \frac{K \cos \Phi}{\beta} \quad (4.12)$$

If the Bragg condition is not satisfied, $\chi = K \cos(\Phi - \theta) - \frac{K^2 \lambda}{4\pi n_0}$. The physical nature of the diffraction process can be seen from eq. (4.11) and eq. (4.12). The variation of the amplitude of the light wave along the z axis is caused by the coupling process of another light wave. The coupling constant describes the coupling strength between the incident light and the diffracted light. The larger the value, the stronger the coupling. Especially, coupling is zero when $\kappa = 0$. The general solution of the coupled wave equations can be expressed as

$$I(z) = i_1 \exp(\gamma_1 z) + i_2 \exp(\gamma_2 z) \quad (4.13)$$

$$D(z) = d_1 \exp(\gamma_1 z) + d_2 \exp(\gamma_2 z) \quad (4.14)$$

Where, $\gamma_{1,2} = -\frac{1}{2} \left(\frac{\alpha}{c_I} + \frac{\alpha}{c_D} + \frac{j\delta}{c_D} \right) \pm \frac{1}{2} \left[\left(\frac{\alpha}{c_I} - \frac{\alpha}{c_D} - \frac{j\delta}{c_D} \right)^2 - \frac{4\kappa}{c_I c_D} \right]^{\frac{1}{2}}$. Based on the general solution and the boundary conditions of the volume grating, the complex amplitude of the diffraction light and the diffraction efficiency can be obtained. For a transmission VBG, there is no light reflected by the VBG, thereby the boundary conditions of the transmission VBG are written as

$$I(0) = 1, \quad D(0) = 0 \quad (4.15)$$

Where I is the incident light, and D is the diffracted light.

For a reflective VBG, there is no light transmitted by the VBG. Thus, the boundary conditions of the reflective VBG can be written as

$$I(0) = 1, \quad D(d) = 0 \quad (4.16)$$

By combining eq. (4.13)-eq. (4.16), the amplitude of the diffracted light for transmission and reflective VBG can be expressed as:

Transmission VBG:

$$D(d) = -j \sqrt{\frac{c_I}{c_D}} \exp\left(-\frac{ad}{c_D}\right) e^{\xi \frac{\sin \sqrt{v^2 - \xi^2}}{\sqrt{1 - \frac{\xi^2}{v^2}}}} \quad (4.17)$$

Reflective VBG:

$$D(0) = \sqrt{\frac{c_I}{c_D}} \frac{s \hbar(jvcha)}{ch} (a + j v c \hbar a) \quad (4.18)$$

In eq.(4.17) and eq.(4.18), $\xi = \frac{d}{2} \left(\frac{\alpha}{c_I} - \frac{\alpha}{c_D} - \frac{j\delta}{c_D} \right)$, $v = \frac{\kappa d}{\sqrt{c_I c_D}}$. The diffraction efficiency of the VBG is defined as the ratio of the diffraction energy flow along the z direction to incident energy, which can be calculated by the following formula.

Transmission VBG:

$$\eta = \left(\frac{c_D}{c_I} \right) D(d) D^*(d) \quad (4.19)$$

Reflective VBG:

$$\eta = \left(\frac{c_D}{c_I} \right) D(0) D^*(0) \quad (4.20)$$

with the above equations, a wavelength selectivity device, for example VBG, can be designed.

Based on this theory, we give our first design result when illuminated by red light in the TE polarization state. In general, photo-polymers are frequently used in holography community since they are sensitive to the majority of the visible spectrum. For example BAYFOL HX photopolymer from Bayer Material Science AG is used to fabricate the reflective VBGs. Through optimization, the thickness is 16.8 microns meters, the spatial frequency is 4984 lines/mm, the average refractive index is 1.55 with a modulation of 0.07 and Φ is 35 degrees. Such parameters are optimal for operation at a wavelength of 633nm. By using these parameter in eq.(4.19), the spectrum near the center wavelength was plotted in **Figure 4-4**, near 100% diffraction efficiency is obtained for the design wavelength with a spectral width of 20nm.

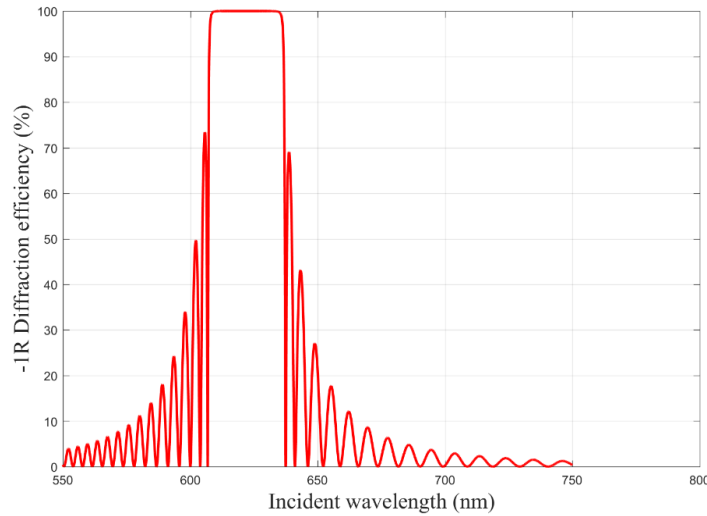


Figure 4-4-The diffraction efficiency against the incident wavelength near the center wavelength for a VBG with a Bragg incidence.

Different color selectivity can be obtained by adjusting the spatial frequency. For example, 5930 lines/mm for a center wavelength 525nm, and 6670 lines/mm for blue light with center wavelength 470nm. These results are shown in **Figure 4-5**.

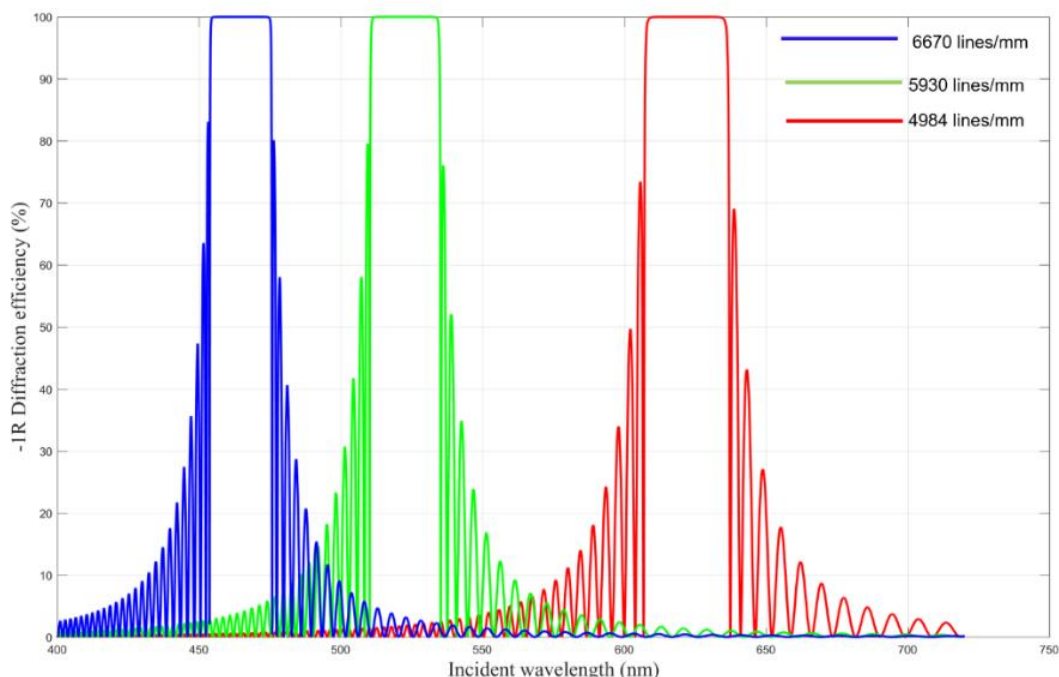


Figure 4-5-The diffraction efficiency against the incident wavelength with different spatial frequencies.

From **Figure 4-5**, it is clear that with the KCWT we can obtain a good simulation result, the FWHM of each center wavelength is narrow enough to satisfy our requirements. However, a high accuracy interference optical bench is needed with accurate exposure control, and the real result is sensitive to the refractive index modulation.

In our cleanroom, we are developing a 2PP lithography machine, which makes it possible to envisage the manufacture of synthetic thick holograms to realize wavelength selectivity. But, current 2PP processes can't make the continuous refractive index changes as does VBG. We have to develop a thick structure with a single material in air. As we know, the refractive index of VBG varies continually along the z axis, i.e., the modulation is in the z axis. This is the reason why the VBG has wavelength selectivity. Usually, other than the VBG approach it is difficult to modulate the refractive index along the depth with a single material in air. Inspired by the VBG, we propose the structure shown in **Figure 4-6**. To the best of our knowledge, this is the first time such synthetic structures have been reported. The structure is similar to a VBG, but has a single material in air. Although, we can't change the refractive index in each layer, the effective dielectric constant can be modulated with the proposed structure by modulating the relative density of the material and air. This means we have the possibility to reach the desired diffraction performance by optimizing the structure's parameters with a suitable algorithm. The initial parameters can be determined using

KCWT, the angle is determined by $\theta = \arccos(\lambda/2nT)$, T is the period of the VBG.

Because the proposed structure is thicker than one wavelength, the TEA model is invalid. The optimization process must be based on a rigorous diffraction model. The algorithm is presented in detail in the next section.

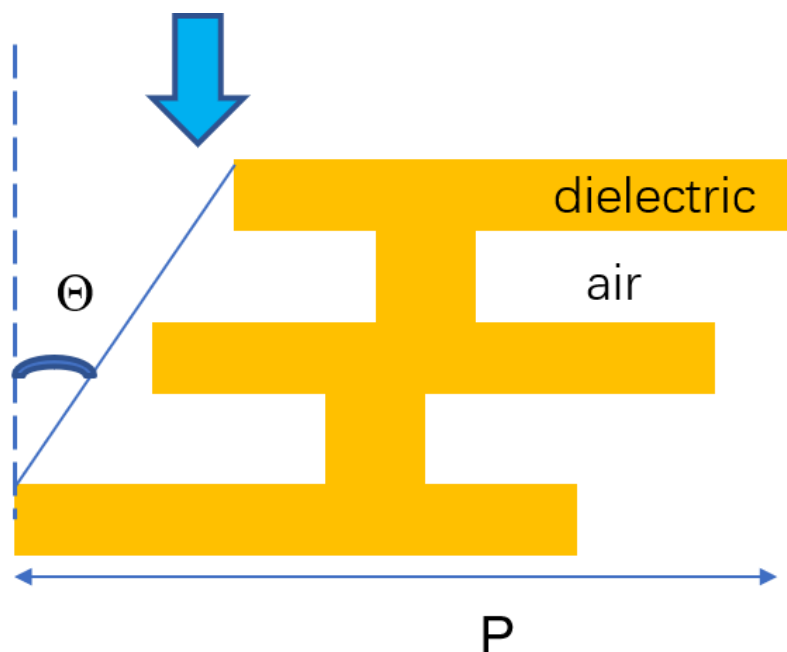


Figure 4-6-The proposed thick 3D diffractive structure to create wavelength selectivity.

4.3 Rigorous theory for thick structure design

The theoretical models of scalar diffraction and rigorous vector diffraction were presented in chapter 2. In scalar diffraction models, the interaction between the illuminating light field and the DOE surface is regarded as a phase retardation in a single plane. The phase shift is added directly to the incident light field, when the light passes through the DOE. The diffracted field can be calculated using scalar diffraction models such as the TEA model. However, this theory fails to predict the diffraction characteristics when the feature size is at the subwavelength scale or the thickness is larger than one wavelength. This is because considers only two EM field components with no coupling to other components, i.e. $E_y e^{i\varphi}$ and $H_x e^{i\varphi}$ when TE polarization light field pass through the DOE. To clarify the differences between scalar diffraction models and rigorous diffraction models, the simulation results of a binary phase grating based on different models are shown in **Figure 4-7**.

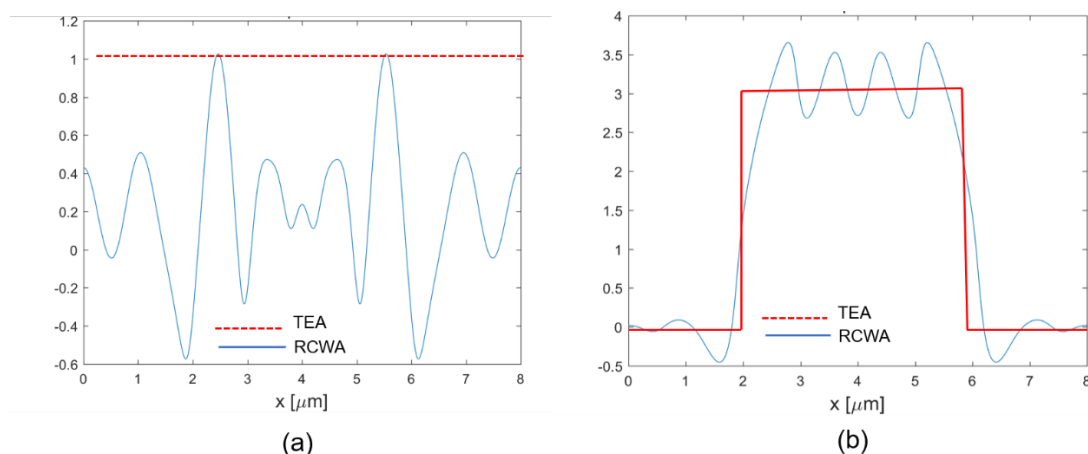


Figure 4-7- (a) The amplitude of the diffraction field through the binary phase grating. The results are obtained using TEA model are compared with the RCWA simulation model. (b) The phase distribution of the diffraction field through the binary phase grating. The results obtained using TEA model are compared with RCWA simulation model.

In these simulations, the wavelength was $1\mu\text{m}$ with the TE polarization state, the grating period and the fill factor are $8\mu\text{m}$ and 0.5 , respectively. The corresponding etch depth d is predicted by the TEA model to be $d=\lambda/2(n-1)=1\mu\text{m}$, where the refractive index n of the substrate is 1.5 . From **Figure 4-7**, we can see that the calculation results of interaction of the incident light with the structure profile of the DOE are not the same by employing scalar diffraction theory and the rigorous diffraction model. Hence, the value of the phase and the amplitude are not the same after the DOE. The TEA model incorrectly predicts the diffraction field as a simple function (see red dashed line), while the RCWA simulation shows a more complicated function (see blue solid line). In the RCWA model, oscillations obviously appear along the boundary of the DOE structure. The TEA model cannot predict this phenomenon since it neglects coupling effects. This will lead to errors when the features of DOEs are less than one wavelength of the incident illumination light. If we design such a DOE by employing scalar diffraction models, the optical performance of a real fabricated DOE, such as diffraction efficiency and noise will be significantly worse than that predicted by the scalar diffraction model. Therefore, rigorous models must be used to calculate the real diffraction behavior of the interaction between incident electromagnetic field and the DOE .

Because the proposed device is a periodic structure, the RCWA model can be used to estimate the diffraction results. In chapter 2, we simply presented the RCWA model for a binary grating. Here, in this design work, we must model more complex multilayer structures. Therefore, we now introduce the RCWA model for multilayer structures. The schematic of the multilayer grating is show in **Figure 4-8**.

The RCWA model belongs to the ‘modal method’ family. In modal methods, the electric permittivity and magnetic permeability are expanded into an orthogonal set of functions. In the RCWA model, they are expanded as Fourier modes [31], which is the reason why it has another name ‘Fourier modal method’ (FMM). The one dimensional grating being described is a multilayered grating, shown in **Figure 4-8**. The grating is divided into a number of sufficiently thin planar slabs along the z axis. The permittivity in each layer can be expanded into a Fourier series.

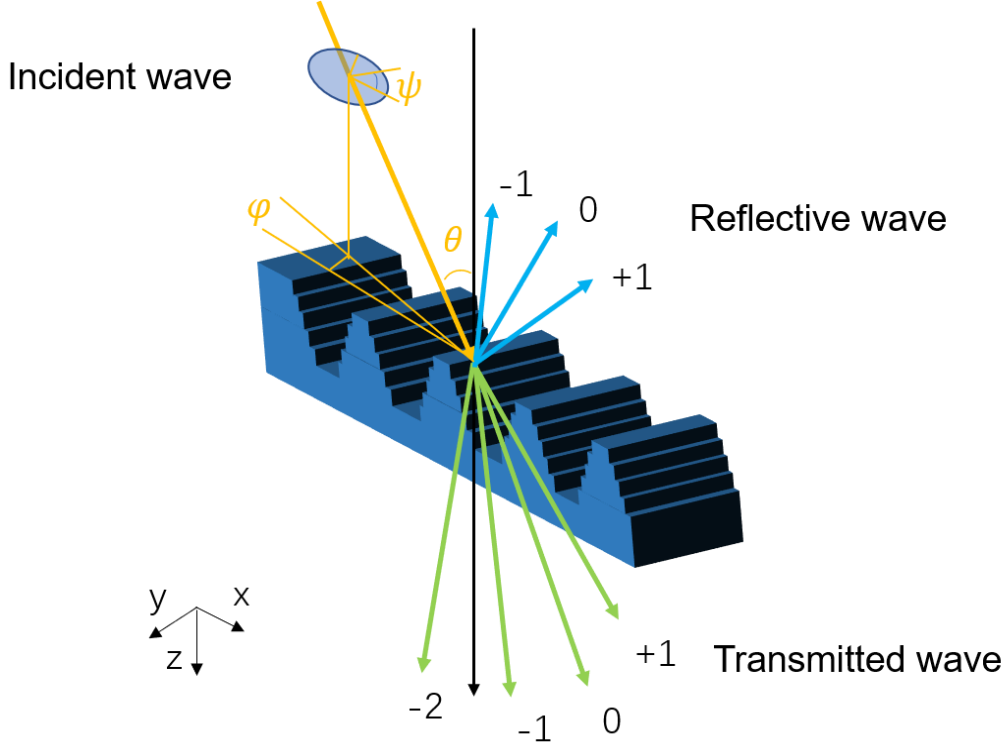


Figure 4-8-Geometrical schematic of the multi-layer grating diffraction.

$$\varepsilon^l = \sum_m \varepsilon_{l,m} \exp \left[\frac{j2\pi m}{p} x \right] \quad (4.21)$$

In eq. (4.21), p is the period of the grating, $\varepsilon_{l,m}$ is the m -th Fourier coefficient of the permittivity in the l -th layer of the grating, which is given by

$$\varepsilon_{l,m} = \frac{1}{T} \int_0^T \varepsilon^l \exp \left[-2j\pi \frac{m}{T} x \right] dx \quad (4.22)$$

The electric field in the incidence space $E_{inc,y}$ and the transmittance space $E_{out,y}$ can be written as [31]

$$E_{inc,y} = \exp[-jk_0 n_1 (\sin\theta x - \cos\theta z)] + \sum_i R_i \exp[-j(k_{xi}x - k_{1,zi}z)] \quad (4.23)$$

$$E_{out,y} = \sum_i T_i \exp \left[-j \left(k_{xi}x - k_{2,zi}(z - d) \right) \right] \quad (4.24)$$

Where R_i and T_i are the amplitude of the i -th harmonic component of the reflected and transmitted diffraction light, respectively. The vector k_{xi} is calculated according the Floquet condition.

$$k_{xi} = k_0 n_1 \sin\theta \cos\varphi + \frac{2\pi i}{T} \quad (4.25)$$

$$k_{\tau,zi} = (k_0^2 n_\tau^2 - k_{xi}^2)^{\frac{1}{2}}, \quad \tau = I, II \quad (4.26)$$

Similar to eq.(4.21), the electric field and magnetic field in the l -th layer can be expanded as Fourier series, giving as below:

$$E_{l,gy} = \sum_i \epsilon_{l,yi}(z) \exp(-jk_{xi}x) \quad (4.27)$$

$$H_{l,gx} = -j \left(\frac{\epsilon_0}{\mu_0}\right)^{\frac{1}{2}} \sum_i \Theta_{l,xi}(z) \exp(-jk_{xi}x) \quad (4.28)$$

In eq. (4.27) and eq. (4.28), $\epsilon_{l,yi}(z)$ and $\Theta_{l,xi}(z)$ are the normalized amplitude of the i^{th} component of the harmonic diffraction field, which satisfy Maxwell's equations:

$$\frac{\partial E_{l,gy}}{\partial z} = j\omega\mu_0 H_{l,gx} \quad (4.29)$$

$$\frac{\partial H_{l,gx}}{\partial z} = j\omega\epsilon_l\epsilon_0 E_{l,gy} + \frac{\partial H_{l,gz}}{\partial x} \quad (4.30)$$

In eq. (4.30), $H_{l,gz} = \frac{j}{\omega\mu_0} \frac{\partial E_{l,gy}}{\partial x}$. Then, the coupled wave equations can be derived by substituting eq. (4.27) and eq.(4.28) into eq.(4.29) and eq.(4.30).

$$\frac{\partial \epsilon_{l,yi}}{\partial z} = k_0 \Theta_{l,xi} \quad (4.31)$$

$$\frac{\partial \Theta_{l,xi}}{\partial z} = \left(\frac{k_{xi}^2}{k_0}\right) \epsilon_{l,yi} - k_0 \sum_p \epsilon_{l,i-p} \epsilon_{l,yp} \quad (4.32)$$

Through further derivation, the equations can be simplified as

$$\frac{\partial^2}{\partial(k_0z)^2} \epsilon_{l,yi} = \left(\frac{k_{xi}^2}{k_0}\right)^2 \epsilon_{l,yi} - \sum_p \epsilon_{l,i-p} \epsilon_{l,yp} \quad (4.33)$$

For fast calculation, eq. (4.33) can be written in a matrix form as

$$\left[\frac{\partial^2 \epsilon_{l,yi}}{\partial(k_0z)^2}\right] = [A_l][\epsilon_{l,y}] \quad (4.34)$$

In eq. (4.34), matrix A can be written as

$$A = K_x^2 - E \quad (4.35)$$

Where, K_x is a diagonal matrix containing diagonal elements k_{xi}/k_0 , and matrix E is a Toeplitz matrix when the i, p element is equal to $\epsilon_{l,i-p}$. The harmonic field in the l -th grating layer can be obtained by calculating the eigenvalues and eigenvectors associated with matrix A, which are presented as below.

$$\epsilon_{l,yi}(z) = \sum_{m=1}^n w_{l,i,m} \{c_{l,m}^+ e^{-k_0 q_{l,m}(z-D+d_l)} + c_{l,m}^- e^{k_0 q_{l,m}(z-D)}\} \quad (4.36)$$

$$\Theta_{l,xi}(z) = \sum_{m=1}^n v_{l,i,m} \{-c_{l,m}^+ e^{-k_0 q_{l,m}(z-D+d_l)} + c_{l,m}^- e^{k_0 q_{l,m}(z-D)}\} \quad (4.37)$$

Where $w_{l,i,m}$ are the components of the eigenvector matrix W_l for the l -th layer, and the $q_{l,m}$ are the positive square roots of the matrix A's eigenvalues at the l -th layer. Also, $v_{l,i,m}$ are the elements of the matrix $V_l = W_l Q_l$, and Q_l is a matrix with elements $q_{l,m}$. To get the coefficients $c_{l,m}^+$ and $c_{l,m}^-$ of the propagation waves, the

boundary conditions should be applied in each grating layer.

The first boundary is between the incident light region and the first grating layer, where $z=0$. This gives as below by matching the tangential electromagnetic fields.

$$\begin{bmatrix} \delta_{i0} \\ jn_1 \cos\theta \end{bmatrix} + \begin{bmatrix} I \\ -jY_I \end{bmatrix} R = \begin{bmatrix} W_1 & W_1 X_1 \\ V_1 & -V_1 X_1 \end{bmatrix} \begin{bmatrix} c_1^+ \\ c_1^- \end{bmatrix} \quad (4.38)$$

Where I is the identical matrix, Y_I is the diagonal matrix which consists of elements $k_{l,zi}/k_0$. Similarly, the boundary condition between grating layer $l-1$ and l can be written as

$$\begin{bmatrix} W_{l-1} X_{l-1} & W_{l-1} \\ V_{l-1} X_{l-1} & -V_{l-1} \end{bmatrix} \begin{bmatrix} c_{l-1}^+ \\ c_{l-1}^- \end{bmatrix} = \begin{bmatrix} W_l & W_l X_l \\ V_l & -V_l X_l \end{bmatrix} \begin{bmatrix} c_l^+ \\ c_l^- \end{bmatrix} \quad (4.39)$$

The last boundary condition between the last grating layer and the substrate is

$$\begin{bmatrix} W_L X_L & W_L \\ V_L X_L & -V_L \end{bmatrix} \begin{bmatrix} c_L^+ \\ c_L^- \end{bmatrix} = \begin{bmatrix} I \\ jY_{II} \end{bmatrix} [T] \quad (4.40)$$

Where the diagonal matrix X_l consists of elements $\exp(-q_{l,m} d_l)$, the diagonal matrix Y_{II} consist of elements $k_{II,zi}/k_0$, respectively. The reflection and transmittance of a multilayer structure are linked to successive the operation (using product of the sequence) of boundary conditions for the different layers. By combining eq. (4.38)-eq. (4.40), the equation including R and T can be written as:

$$\begin{bmatrix} \delta_{i0} \\ jn_1 \cos\theta \end{bmatrix} + \begin{bmatrix} I \\ -jY_I \end{bmatrix} R = \prod_{l=1}^L \begin{bmatrix} W_l & W_l X_l \\ V_l & -V_l X_l \end{bmatrix} \begin{bmatrix} W_L X_L & W_L \\ V_L X_L & -V_L \end{bmatrix}^{-1} \begin{bmatrix} I \\ jY_{II} \end{bmatrix} [T] \quad (4.41)$$

With these above equations, the reflected light R and transmitted light T can be solved, then the diffraction efficiency of each order can be obtained based on the following equations.

$$DE_{ri} = R_i R_i^* Re \left[\frac{k_{l,zi}}{k_0 n_l \cos\theta} \right] \quad (4.42)$$

$$DE_{ti} = T_i T_i^* Re \left[\frac{k_{II,zi}}{n_l^2} \right] / \left[\frac{k_0 \cos\theta}{n_l} \right] \quad (4.43)$$

Now that, the basic theoretical model for designing Bragg like thick DOE structures have been presented. In next section, we will describe the design algorithm built around this rigorous theory model.

4.4 Algorithm and design results

The layout of our proposed Bragg like structure was depicted in **Figure 4-9**.

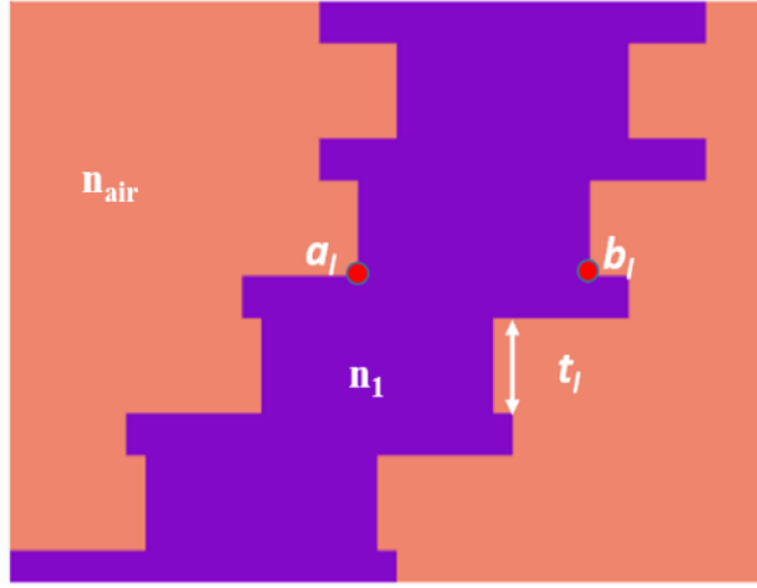


Figure 4-9-The Bragg like structure. A Multilayer structure with single material in air which can be fabricated using 2PP lithography. All the thicknesses t_l and transition points a_l, b_l in each layer are variables to be optimized.

The structure is a multilayer structure, all the thickness t_l and transition point a_l, b_l in each layer are variables to be optimized. The structure represents a single unit which would be repeated periodically in the X and Y directions. It shows periodic Bragg like features in the z direction thanks to the t_l layer thickness variations that enable Bragg like diffraction efficiency and wavelength selectivity to appear. It also shows slanted grating like asymmetry to enable blazed grating like high diffraction efficiency in a single diffraction order.

In this work, our goal is to design a wavelength selective optical component which belongs to a multi-object optimization problem. The figure of merit (FOM) is defined as follows.

$$\text{FoM} = \omega_1(\eta_c - \eta_t)^2 + \omega_2 \sum_{i \neq c} \eta_i^2 \quad (4.44)$$

Where η_c is the first diffraction order efficiency of the center wavelength, and η_t is the target diffraction efficiency, ω_1 and ω_2 are weighting factors for the center wavelength and other wavelengths, respectively. Considering the current 2PP fabrication limitations, the following values were used for these constraints.

$$|b_l - a_l| \geq 0.5 \mu\text{m}, \quad t_l > 1.5 \mu\text{m} \quad (4.45)$$

Both the FoM and the constraints in eq. (4.45) are functions of the electric E field, which satisfies Maxwell's equation:

$$\nabla \times \frac{1}{\mu} \times \mathbf{E} - \varepsilon_l \frac{\omega^2}{c^2} \mathbf{E} = 0 \quad (4.46)$$

$$\varepsilon_l = \varepsilon_1 |b_l - a_l| + (\Lambda - |b_l - a_l|) \quad (4.47)$$

Where ε_l is the relative permittivity, and μ is 1. The electric field \mathbf{E} in the grating can be solved using the RCWA model presented in the previous section. To solve the parametric optimization problem, the particle swarm optimization (PSO) algorithm was combined with eq. (4.44) -eq. (4.47) due to its strong global optimization capability. The flowchart of the proposed algorithm is depicted in **Figure 4-10**.

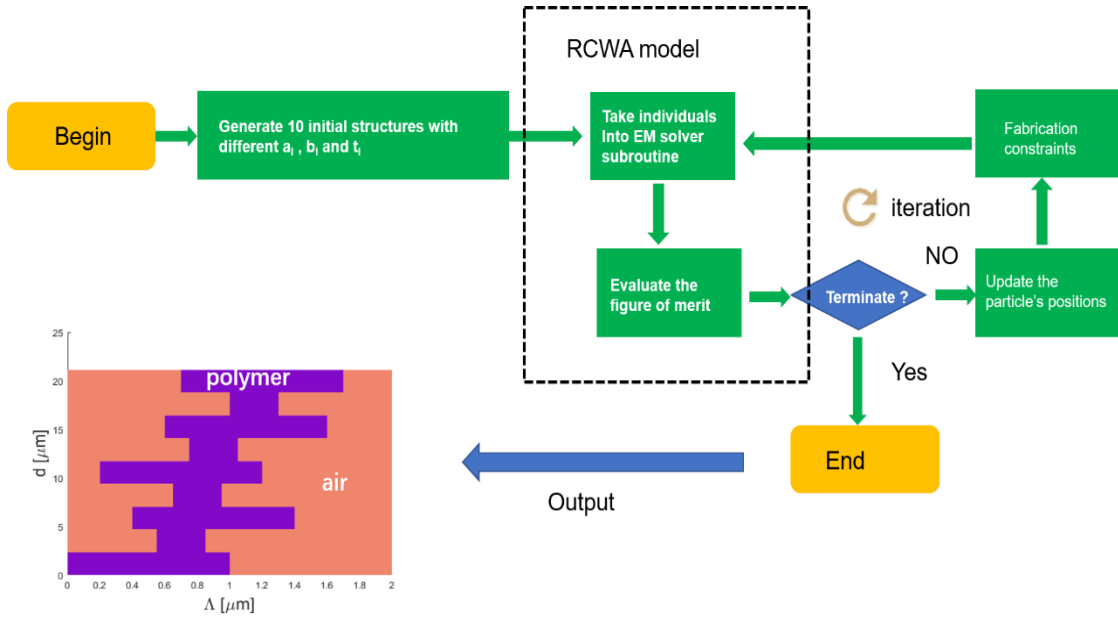


Figure 4-10-The flowchart of the design algorithm for the synthetic Bragg like structure design.

Since the basic idea of the PSO has already been described in chapter 2, here we directly present the algorithm. The specific steps of the proposed iterative optimization can be described as follows:

1. Generate 10 individual structures (“particles”). In PSO the position of the particle is a possible solution to the problem. In order to help the algorithm converge fast, the first individual structure is produced according to the Bragg condition, see **Figure 4-6**. The other nine structures are produced randomly with different t_l and transition points a_l, b_l in each grating layer.
2. Call the EM solver subroutine to calculate the first diffraction order efficiency of each individual in the current generation, and evaluate the FOM. If the termination condition is reached, the optimization process ends.
3. If the termination condition is not satisfied, the particles are updated to produce next generation. The updated positions of the particles are calculated as follow

$$x_i^{new} = x_i^{old} + v_i, \quad i = 1, 2, \dots, N \quad (4.48)$$

$$v_i = c_w v_i + c_1 t_1 (pbest_i - x_i) + c_2 t_2 (gbest_i - x_i) \quad (4.49)$$

Where c_w is a inertial weight, c_1 and c_2 are weighting factors, t_1 and t_2 are constants. x_i^{old} is the position of the i -th individual structure in the current generation, x_i^{new} is the updated position of the i -th individual structure for the next generation, v_i is the i -th individual structure's velocity, $pbest_i$ and $gbest_i$ are the i -th individual structure's individually best position and the globally best position, respectively.

4. Fabrication constraints are incorporated into the optimization process by controlling the feature size and individual thickness, see eq. (4.45).
5. Repeat from step 2 until the maximum number of iterations or the FOM are reached, then the designed structure is output.

Before the optimization process starts, the convergence characteristic of the RCWA model should be considered to allow us to determine the number of the harmonic orders to be used. Usually, the zeroth order is used to evaluate the convergence characteristic in the RCWA model. The diffraction efficiency of the zeroth order against the number of different harmonic orders used in the RCWA model was presented in **Figure 4-11**.

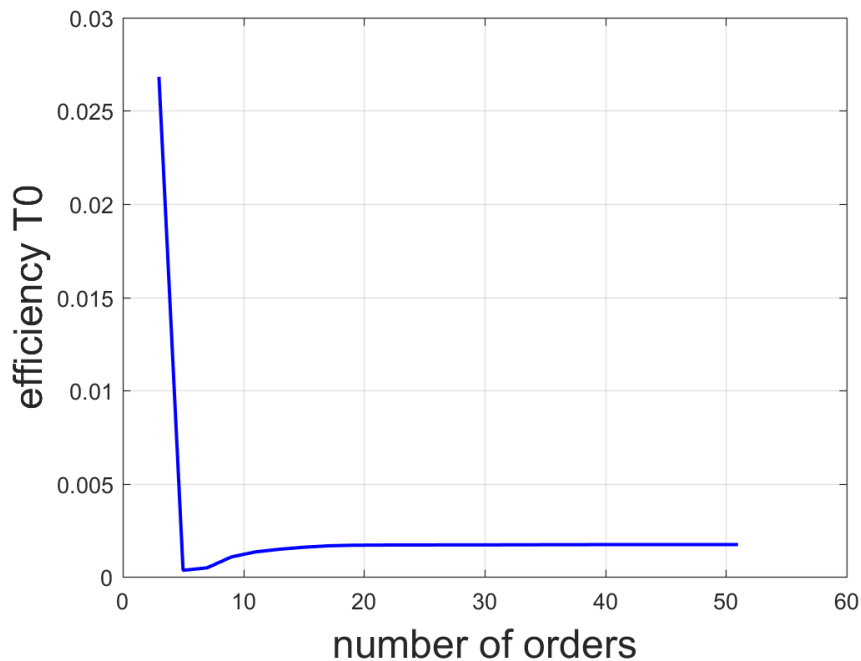


Figure 4-11-The diffraction efficiency of the zeroth order against the number of harmonic orders used in the RCWA model.

From **Figure 4-11**, we can see that the curve is convergent when the number of harmonic orders is larger than 15. For more accurate calculations, 20 harmonic orders were used in our optimization process (using higher number of harmonic orders leads to slow convergence). With the proposed algorithm, a multilayer structure optimization for a center wavelength of 633nm was carried out to verify the proposed method. The FOM against generation is plotted in **Figure 4-12**. After 3500 iterations (optimization using MATLAB2014 software, with a time cost of eight hours on a standard personal

computer) the curve is convergent. The resulting optimal optically thick structure is shown in **Figure 4-13**. The structure's dimension is larger than 400nm.

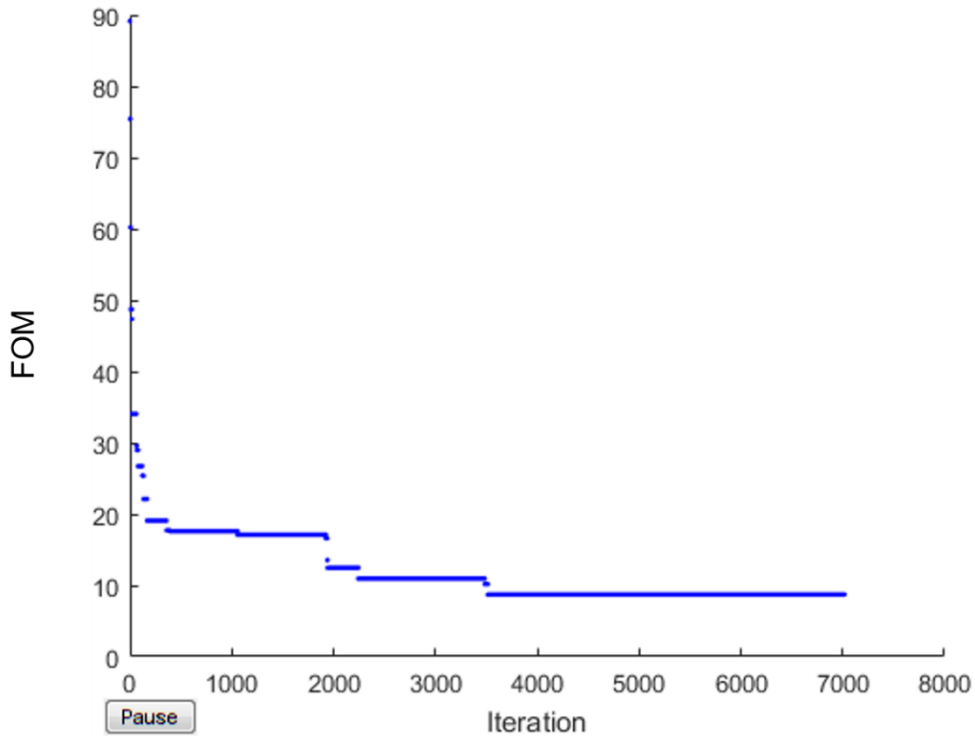


Figure 4-12-The FOM against iterations.

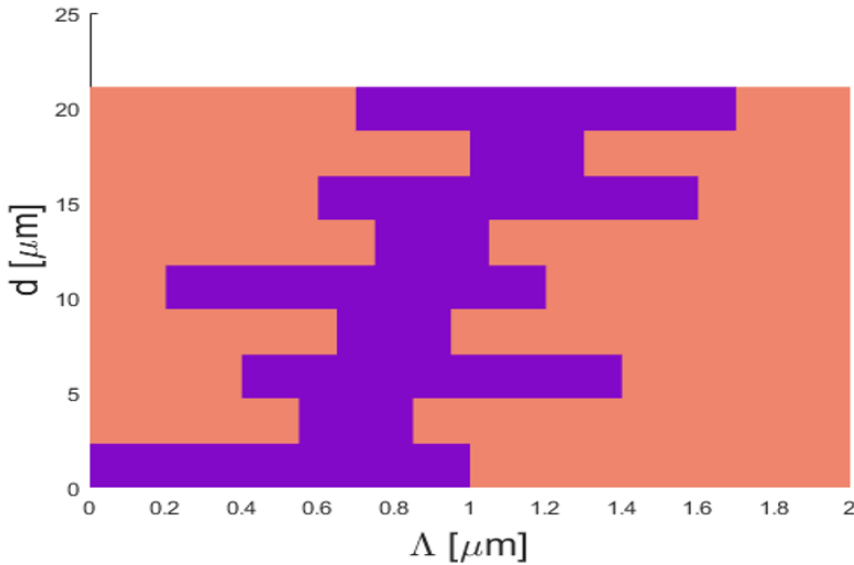


Figure 4-13-The optimal thick structure.

The optimized optical performance of the final structures is shown in **Figure 4-14**. From **Figure 4-14 (b)**, we can see that the spectral width of the first diffraction order of the optimized structure is about 30nm (FWHM), and the diffraction efficiency of the center wavelength is about 62.5%. The FWHM is narrow enough to be used as a

narrowband filter. **Figure 4-14** (a) shows the EM field intensity distribution inside this structure, the output field has a displacement in the X direction compared to the incident light field since the diffraction phenomenon occurs.

The numerical simulation experiments indicate that the multilayer periodic structure designed by the proposed methodology performs well, and are close to the desired target which demonstrate that the proposed optimization strategy is feasible.

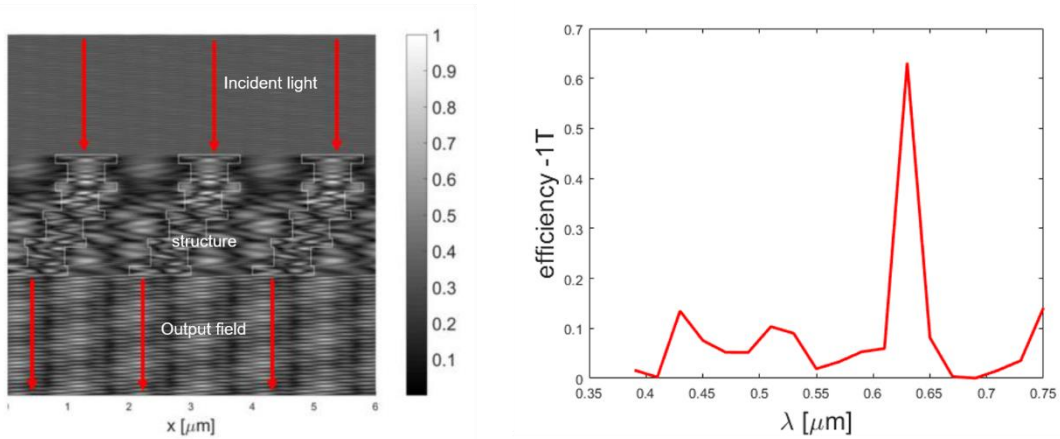


Figure 4-14-Optimization results for 650nm. (a) Intensity distribution inside the multilayer periodic structure. (b) Spectrum curve.

To validate the accuracy of the proposed design model, the diffractive response of the optimized structure was simulated using the FMM model in the commercial VirtualLab fusion software which we used as a bench mark. The optical path diagram of the 3D grating simulation is shown in **Figure 4-15**.

The proposed structure is similar to a multilayer Dammann grating which can be imported into the ‘Transition Point List Grating’ box. The specific manipulation to verify the reported structure in the VirtualLab fusion software is presented in **Figure 4-16**.

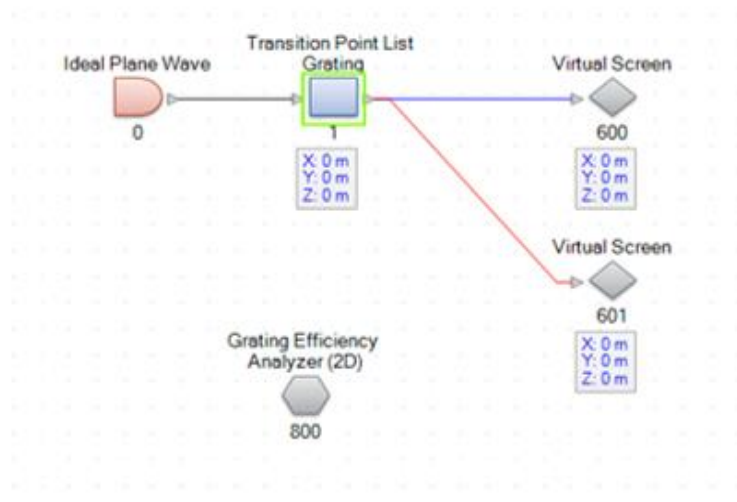


Figure 4-15-Light path view of 3D grating in VirtualLab fusion.

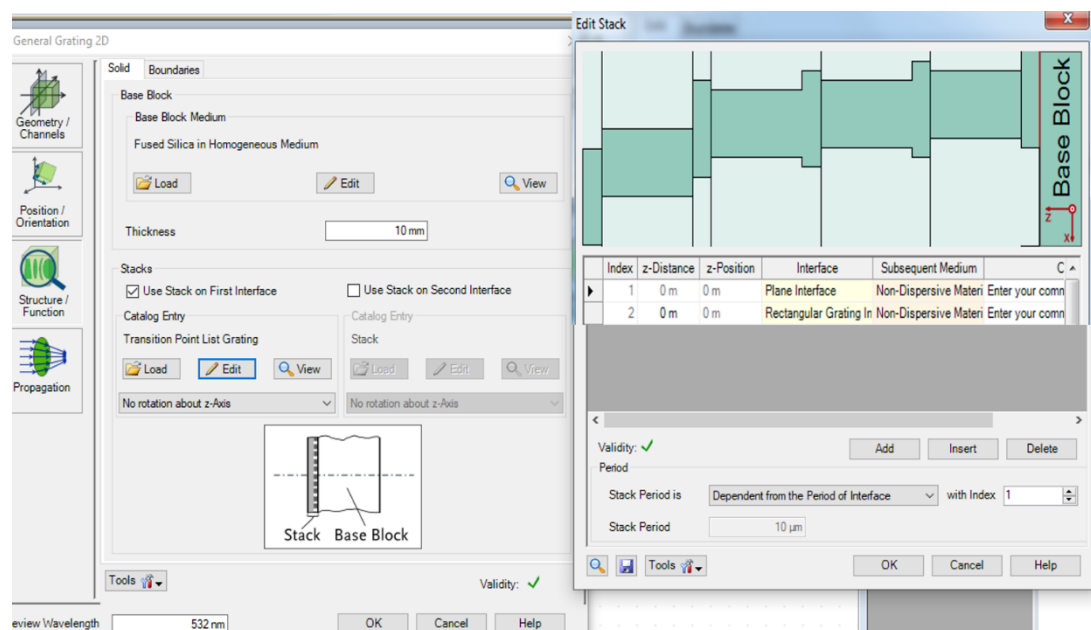


Figure 4-16-The setting parameters for the designed Bragg like structure in VirtualLab fusion software

Table 4.1 compares the result of the FMM model in the VirtualLab fusion software and the proposed design model. All the calculations are based on the same parameters. These simulation results show that the differences between the two methods are small enough to be explained by the numerical precision errors. Our proposed design method is therefore validated as a useful way to design thick diffractive structures.

Table 4.1 Diffraction efficiency (%) of the first diffraction order against wavelengths by using different calculation method

Wavelength	VirtualLab fusion	The design result
540nm	4.7944%	4.7953%
570nm	3.2956%	3.3165%
600nm	5.6611%	5.6629%
633nm	63.1420%	63.1159%
660nm	8.9793%	8.9908%
690nm	0.0205%	0.0215%
720nm	4.7615%	4.7596%

As the fabrication technology proposed for the fabrication of this kind of thick structure is little tested, it was important to estimate the system's fabrication tolerances.

Figure 4-17 shows that the diffraction efficiency varies with errors in the thickness of the different layers.

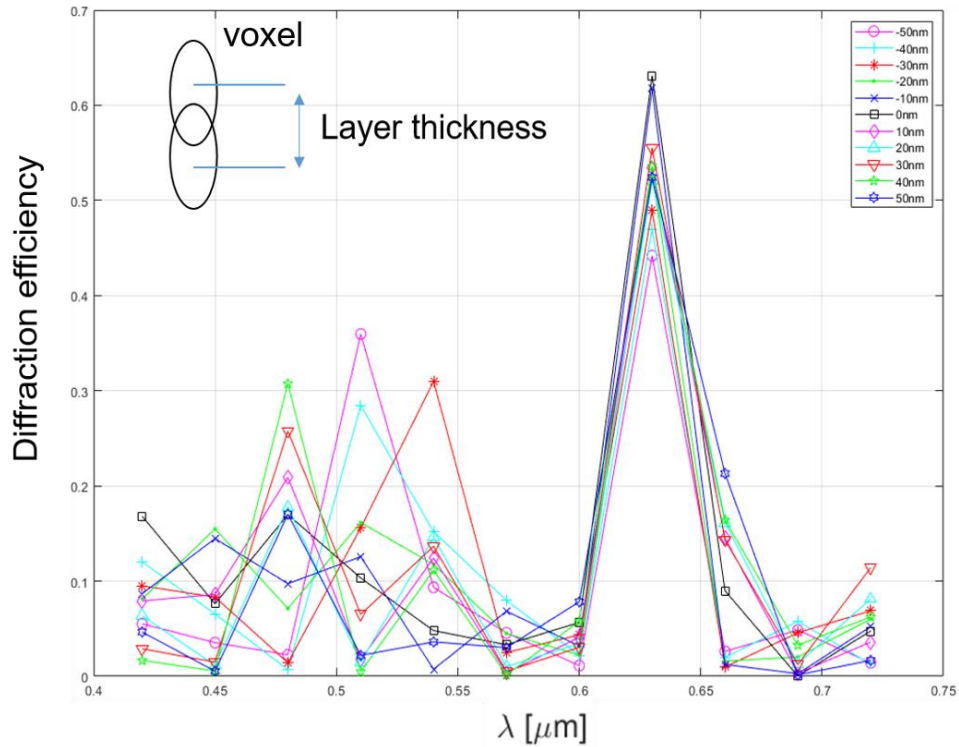


Figure 4-17-Spectrum curve with different layer thickness errors.

From the calculation results in **Figure 4-17**, we see that errors in layer thickness mainly reduce the diffraction efficiency of the center wavelength, and increase the diffraction efficiency of the other wavelengths. The side lobes reduce the wavelength selectivity. Nevertheless, the result can be accepted if the depth tolerance is controlled in the range [-30nm, 30nm]. The corresponding lateral fabrication tolerances are plotted in **Figure 4-18**.

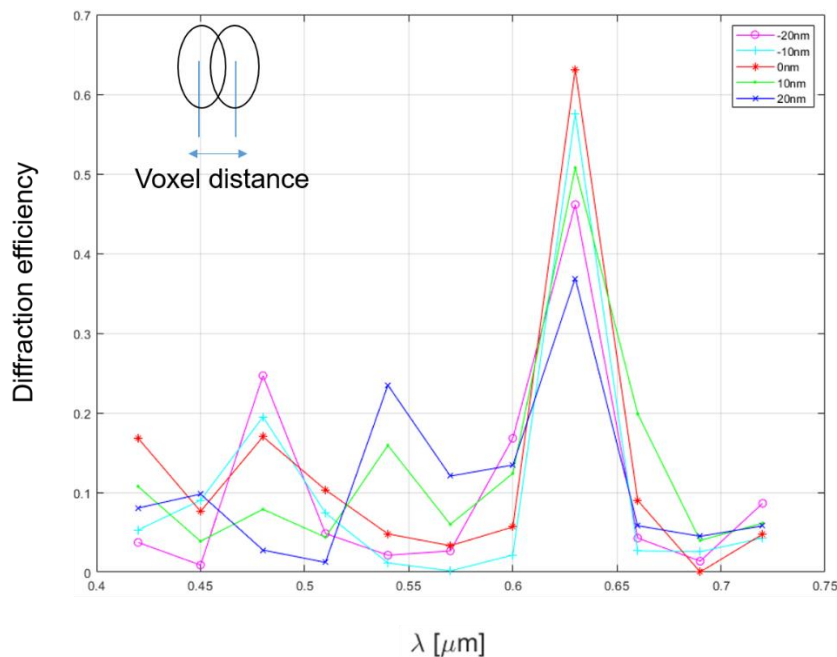


Figure 4-18-Spectrum curve with different lateral errors.

Based on the simulation results in **Figure 4-18**, we can see that the tolerances should be limited in [-20nm, 10nm]. Lateral errors appear to be more sensitive compare to that of the depth tolerances. These results can provide a fabrication guide through the tolerance analysis.

4.5 Conclusion

In conclusion, two different types of coupled wave theory models have been introduced for designing optically ‘thick’ diffractive structures. Kogelnik theory was used to model and design conventional Bragg gratings so as to obtain wavelength selectivity. However, to fabricate such gratings, high accuracy optical interference benches and special photopolymers are needed. We described now here researchers have proposed some artificial structures to produce structural color, however these structures are composed of at least two different materials, and complex experimental multi-step lithography process are required for their fabrication. To overcome these problems, a thick structure with a single material in air was investigated as a solution. Inspired by Bragg volume grating structures, a Bragg like structure was proposed which is specially adapted to fabrication by newly available 2PP lithographic techniques. As far as we know, this is the first time such design strategies and structures have been reported in the optics community.

The practical limitations of the TEA model in describing the electromagnetic field inside the DOE structure was investigated in detail by comparing it with a rigorous diffraction model. The calculation results obtained by using the RCWA model indicate that the TEA model fails to predict the diffraction characteristics such as the amplitude and phase after the DOE plane. Therefore, a multilayer RCWA model was presented implemented to model and design the desired Bragg like structure by combining the RCWA model and the particle swarm optimization algorithm. In addition, the expected fabrication limitations of 2PP lithography were incorporated into the design algorithm in our design to improve the fabrication performance. The design results were verified using the commercial VirtualLab fusionTM software which demonstrated that the proposed design method can be an efficient way for optimizing such optically thick structures. The multilayer structure is targeted for fabrication by the parallel 2PP fabrication system currently under construction in the IMT-A cleanroom for experimentally verifying the performance of the proposed structures. A basic unit of the proposed structures is presented in Chapter 6.

Chapter 5 DOE fabrication and experimental analysis

5.1 Introduction

In the previous chapters, we numerically demonstrated several optimization methods for designing DOEs capable generating real and virtual 2D and 3D images under LED illumination based on the scalar diffraction model, and also developed a novel method for optimizing optically thick structures for white light illuminated DOEs by combining a rigorous diffraction model and the particle swarm optimization algorithm. In this chapter, we present the corresponding experimental fabrication of these devices and the experimental evaluation of the optical performance of the fabricated DOEs. The numerical simulations are verified by comparing their predictions to the experimental performance. The DOE samples were all fabricated and characterized in IMT Atlantique (IMT-A) cleanrooms. The core fabrication equipment is our home built parallel direct-writing photoplotter which is used for fabricating the DOE microstructures usually in a layer of photoresist on a glass.

This chapter first gives a brief introduction to the fabrication facilities, the fabrication process, the characterization instruments and the optical benches. Then, the experimental results for each DOE are described in detail and compared to the design. Finally, we conclude our works.

5.1.1 IMT Atlantique DOE fabrication and characterization facilities

Photo-lithographic machines are the core equipment to manufacture a DOE. The standard photo-lithographic techniques were introduced in Chapter 2. In this thesis, the parallel direct-write grayscale photoplotter method is used to exposure a photoresist layer because it is a flexible tool for producing DOE prototypes offering high writing speed with a resolution better than 1 micron. The write speed can reach 20 mega pixels per second. A photograph of the photoplotter in our IMT-A cleanroom is shown in **Figure 5-1**. It consists of the controller unit, the illumination unit, the projection optics, the moving *XY* stage, and the auto focus unit. The detailed description of each unit can

be found in reference [67].

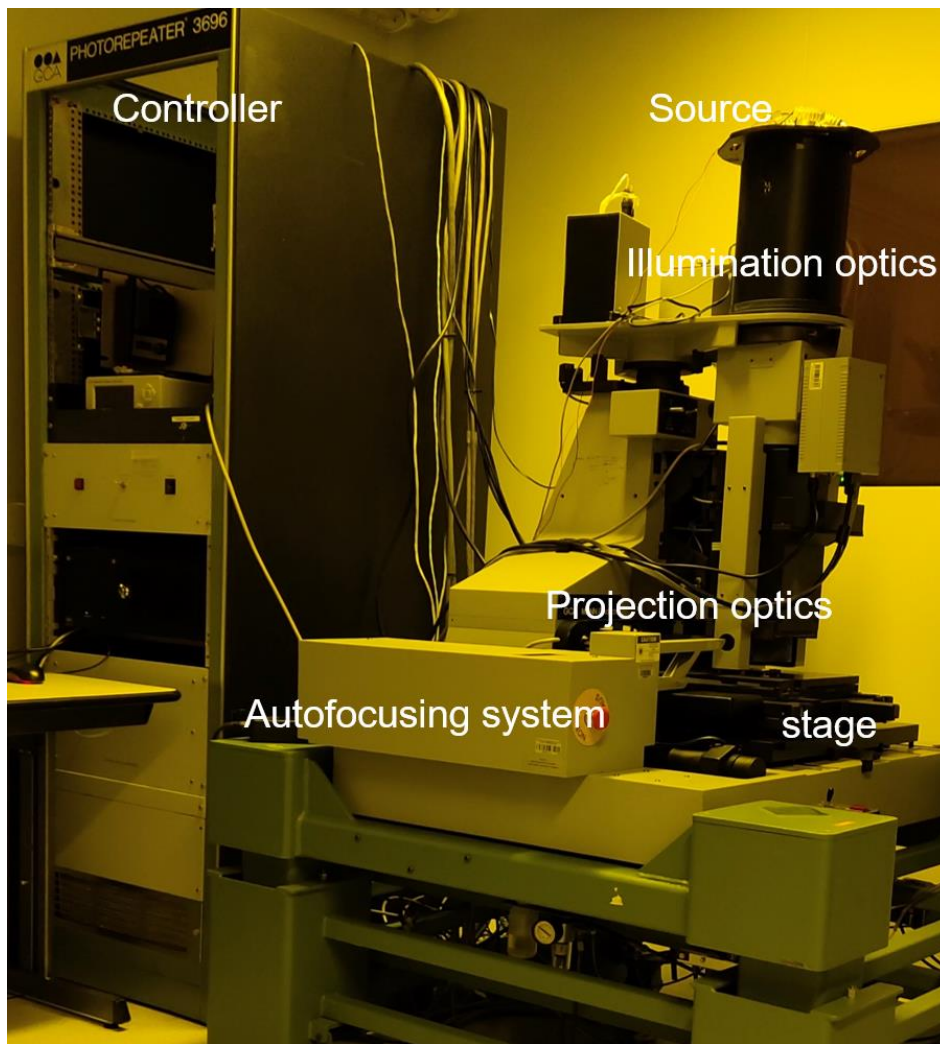


Figure 5-1-Photograph of the photoplotter in IMT-A cleanroom.

The basic process and the photographs of the spin-coating equipment, parallel direct write photoplotter and metal coating machine are illustrated in **Figure 5-2**.

In this thesis, the grayscale lithography technique was used to produce multi-level pure phase type microstructures. The fabrication process for DOEs holograms in the IMT-A cleanroom is briefly as follows.

1. The glass substrate is first cleaned by ultrasonic washing. Then, a positive photoresist film, which is usually of the S1800 series from Micro Resist Technology, is spin coated onto the cleaned glass substrate with an appropriate spin speed to give a relatively uniform layer of the required thickness (the variation of the thickness across the substrate is about 30nm).
2. The photoresist layer is then exposed using our home built photoplotter. The target DOE pattern is transferred from spatial light modulator (SLM) to the photoresist

surface, and the exposure time can be varied by using the drive current send to the LED illumination optics.

3. The post-exposure photoresist is developed in Microposit 303A developer to etch the exposed pattern. Then, deionized water is used to rinse the DOE, and stop development.
4. If a reflection type DOE is needed, the metal coating machine is used to deposit a thin metal film (about 10nm) on the DOE profile, see **Figure 5-2(c)**.
5. The DOE profile etched into the photoresist layer is characterized using optical microscopes or a scanning electron microscope (SEM). The diffraction performance such as diffraction efficiency and reconstructed image fidelity are measured on an optical bench.

The photographs of these characterization instruments and the optical bench in our cleanroom at IMT-A are shown in **Figure 5-3**. **Figure 5-3 (a)** shows the 3D interferometric microscope (Nikon Optihot100) used to measure the DOE profile with a lateral resolution of about 1 micron and a depth error of about 10nm. The optical microscope (Reichert-Jung Polyvar Met) in **Figure 5-3 (b)** is used to photograph and measure the pattern of the fabricated DOE, and the SEM of **Figure 5-3 (c)** is used to characterize the profile of submicronic structures. The optical bench is used to measure the diffraction pattern and diffraction efficiency is shown in **Figure 5-3 (d)**.

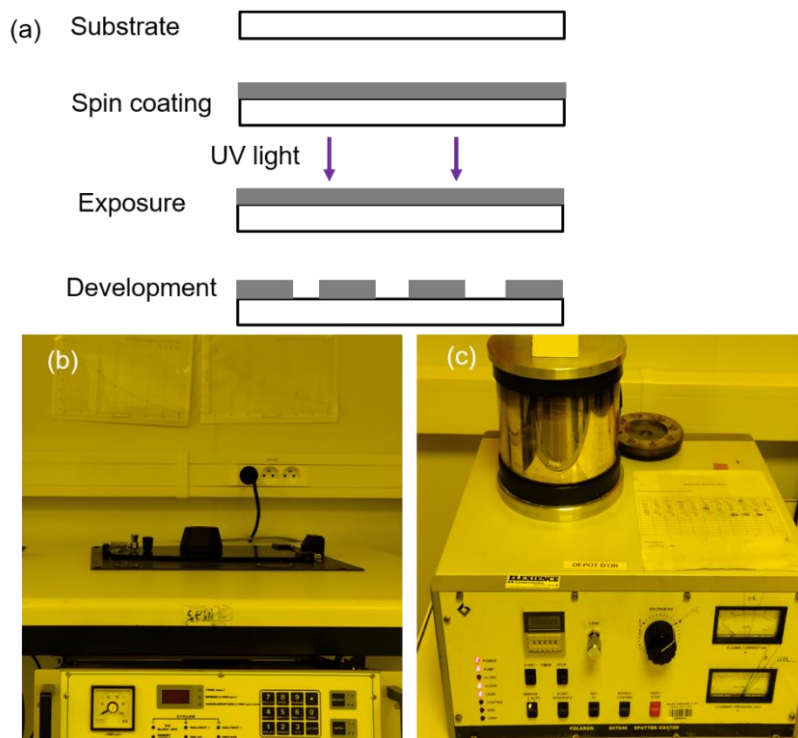


Figure 5-2-(a) The basic DOE fabrication process in the IMT-A cleanroom. (b) Spin-coater unit. (c) coating machine.

All the fabrication and optical measurements are conducted in our cleanroom. In the next section, we will present the 2D output pattern DOE.

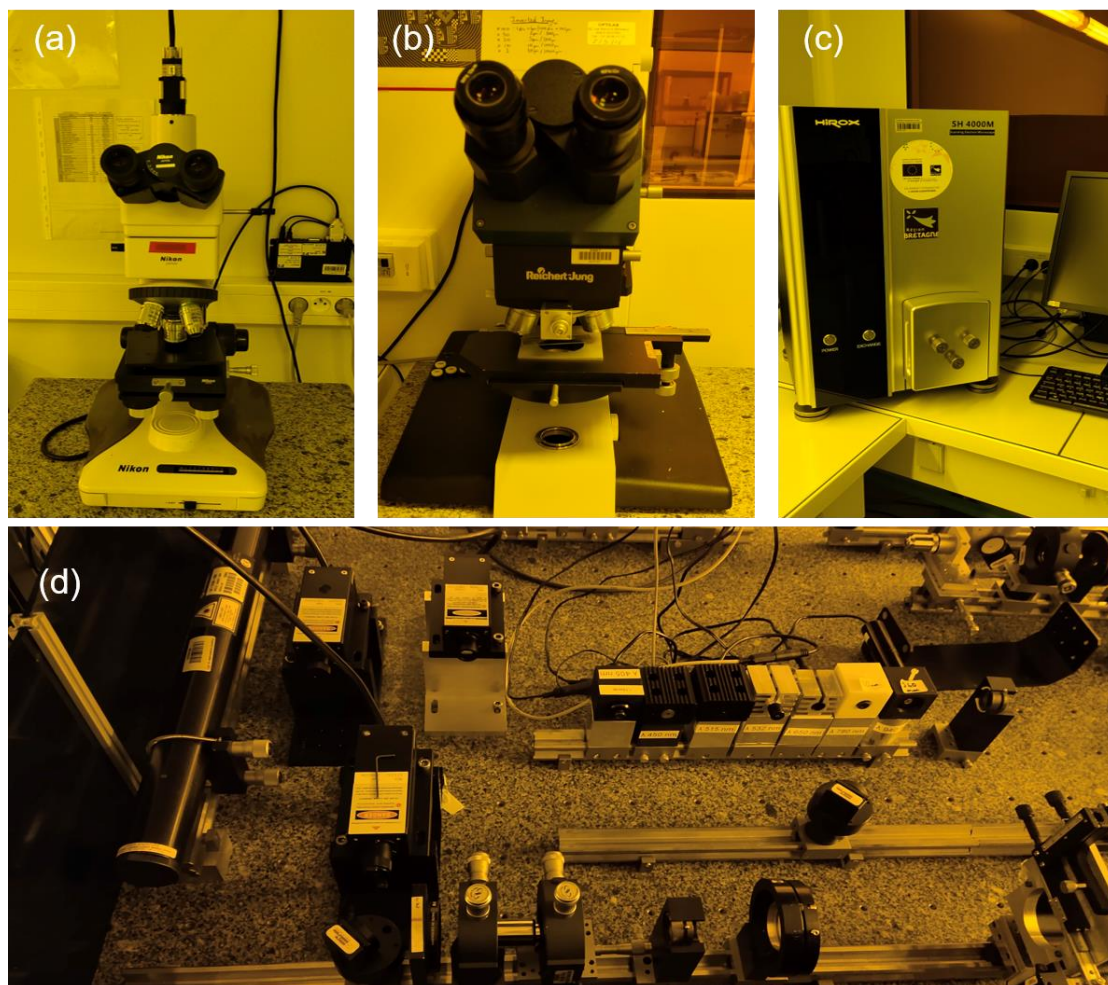


Figure 5-3- (a) 3D interferometric microscope for measuring the DOE profile. (b) Optical microscope. (c) SEM for submicron structure measurement. (d) Optical bench for DOE diffraction characterization.

5.2 Experimental verification of the projection type 2D security holograms illuminated by a divergent light source

5.2.1 DOE sample test with divergent light illumination

To validate the design model of the Fresnel type DOE for divergent illumination presented in section 3.1, a DOE was designed for operating at a wavelength of 525nm. After optimization, the optimal multi-level DOE image file with size $12 \times 12 \text{mm}^2$ was loaded onto the photoplotter memory. Then, the DOE sample was fabricated using the

home built photoplotter and tested using the optical bench in our cleanroom. In this work, the more viscous photoresist S1813 was used since the DOE has eight phase levels (a thicker resist layer was required). The experimental characterization setup is shown in **Figure 5-4** (a). It consists of a LED source, a diaphragm, the DOE sample (shown in the inset of **Figure 5-4**) and an observation screen on which the output image is formed. The divergent angle of the LED source was 120 degrees. A diaphragm was used after the LED source to limit the effective illumination area on the DOE plane which depends on our designed divergent angle. The diffraction pattern on the screen was captured by a camera. When the fabricated DOE was illuminated by the divergent LED (wavelength of 525 nm), the reconstructed image obtained is shown in **Figure 5-4** (c). The experimental reconstruction result shows a good agreement with the simulation of **Figure 5-4** (b). From **Figure 5-4** (c), the qualitative signal to noise ratio (SNR) of the reconstructed image appears high enough, and the zeroth order diffraction spot is almost invisible using the DOE optimized by the developed optimization algorithm. The DOE diffraction efficiency in the signal area was about 50% as measured using a Newport photodetector [108].

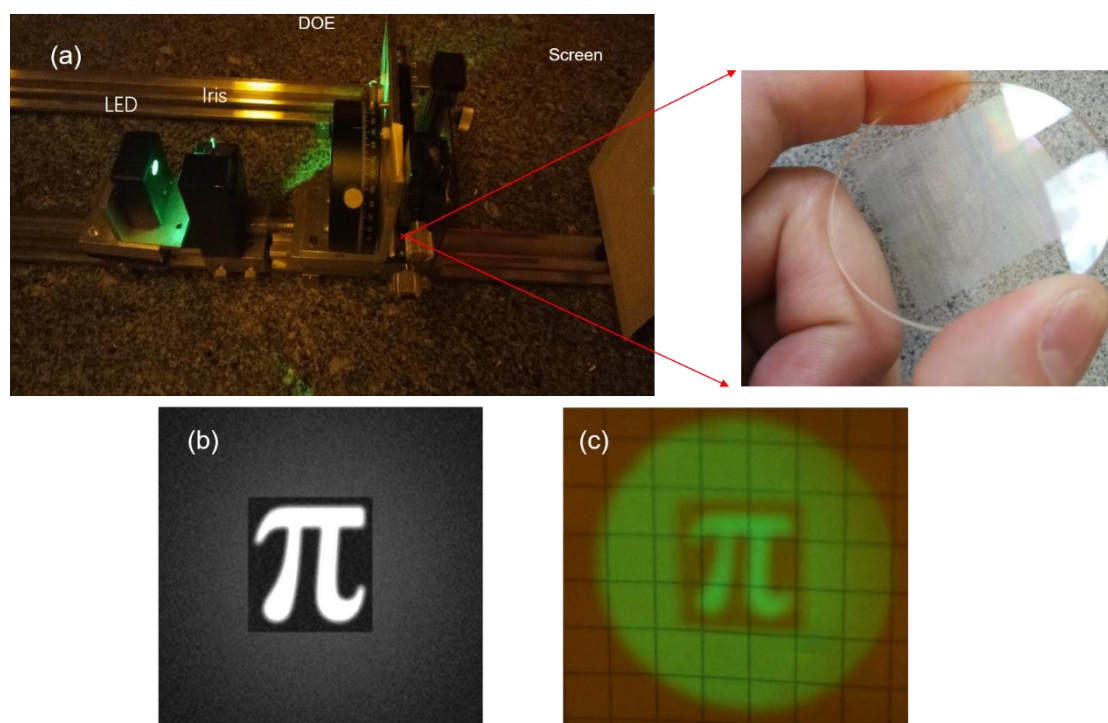


Figure 5-4-(a) Experiment setup of testing the DOE sample. (b) Numerical simulation output pattern.
(c) Experimental output pattern.

The successful technique also avoids the difficulties usually met in fabricating DOEs with low zeroth order energy. In general to reduce the zero order energy we have to fabricate several identical DOE samples on the same substrate with slightly different exposure times to finely adjust the etch depth. In this work, only a single DOE sample was fabricated, but the zeroth order is invisible without any fabrication process optimization. The reason for this interesting phenomenon is that with a Fresnel type

DOE and the divergent light source used here the zeroth order's energy is diffused to other regions. This particular virtue opens new opportunities in security holograms applications, as it greatly simplifies mass production by reducing the need for heavy lithography process optimization.

5.2.2 Fabrication and experimental verification of the faceted grating array DOE

To verify the proposed design algorithm, a DBA (diffractive blazed grating array method presented in chapter 3) was fabricated and characterized. With the design algorithm presented in section 3.2, a DBA was designed with 200*200 grating cells, each grating cell contained 100*100 pixels with a pixel size of 0.75 μm , and the collective divergent angle was about 16 degrees. The total calculation time was about 10 minutes on a personal computer (Intel Core™ I7-8750H CPU@2.2GHz, GPU GTX1060). According to the proposed method in Section 3.2, the maximum diffraction angle can be reduced by considering the real fabrication performance, as shown in **Figure 5-5**.

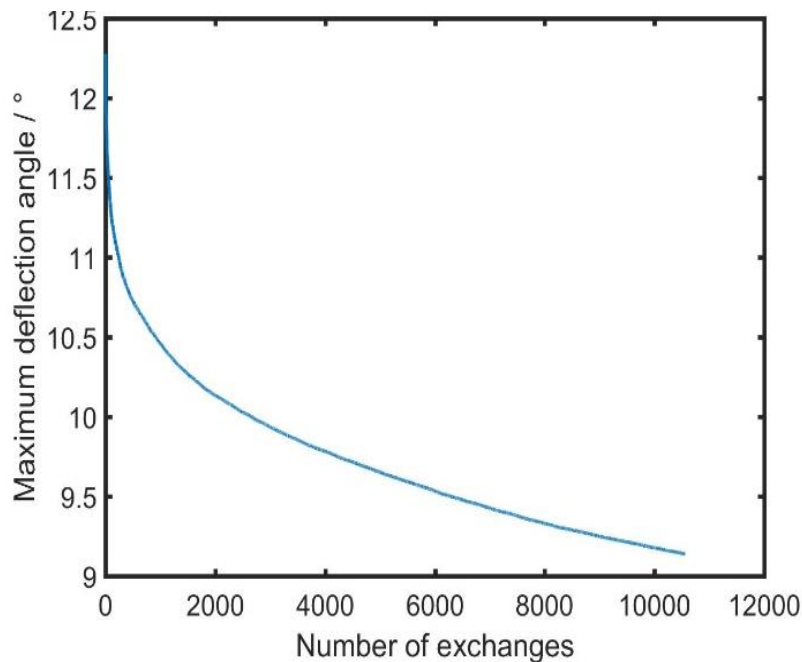


Figure 5-5-Maximum deflection angle against with the cumulated number of exchanges of the real DBA.

The fabrication facilities we used to make the DBA were again our home-built direct-write photo-plotter. The photoresist was S1813 from Micro Resist Technology, with the refractive index of 1.66 at a wavelength of 525nm.

The fabrication process was the same as for the previous DOE (see section 2.5.2). **Figure 5-6(a)** shows a part of the grating cell array, captured by the optical microscope. The height profile of single cell obtained by the interference microscope can be seen in **Figure 5-6 (b)**. The etch depth of the fabricated grating is about 750nm, it is not exactly the designed depth (790nm) due fabrication errors. This depth error decreases the

diffraction efficiency. To know how it affects the diffraction efficiency, we calculated the diffraction efficiency as function of the grating depth based on the RCWA model, as shown in **Figure 5-6 (c)**. The calculated theoretical diffraction efficiency of the first diffraction order is near to 90% at a depth of 750nm.

An experiment to measure the grating's first order diffraction efficiency was also implemented. The experimentally measured first diffraction order's diffraction efficiency was about 82%, a slight deviation from the theoretical prediction. It has 8% difference with the theoretic computation, can be explained mainly by the Snell reflection losses of the glass. The diffraction pattern was captured on an optical bench, as shown in **Figure 5-7**.

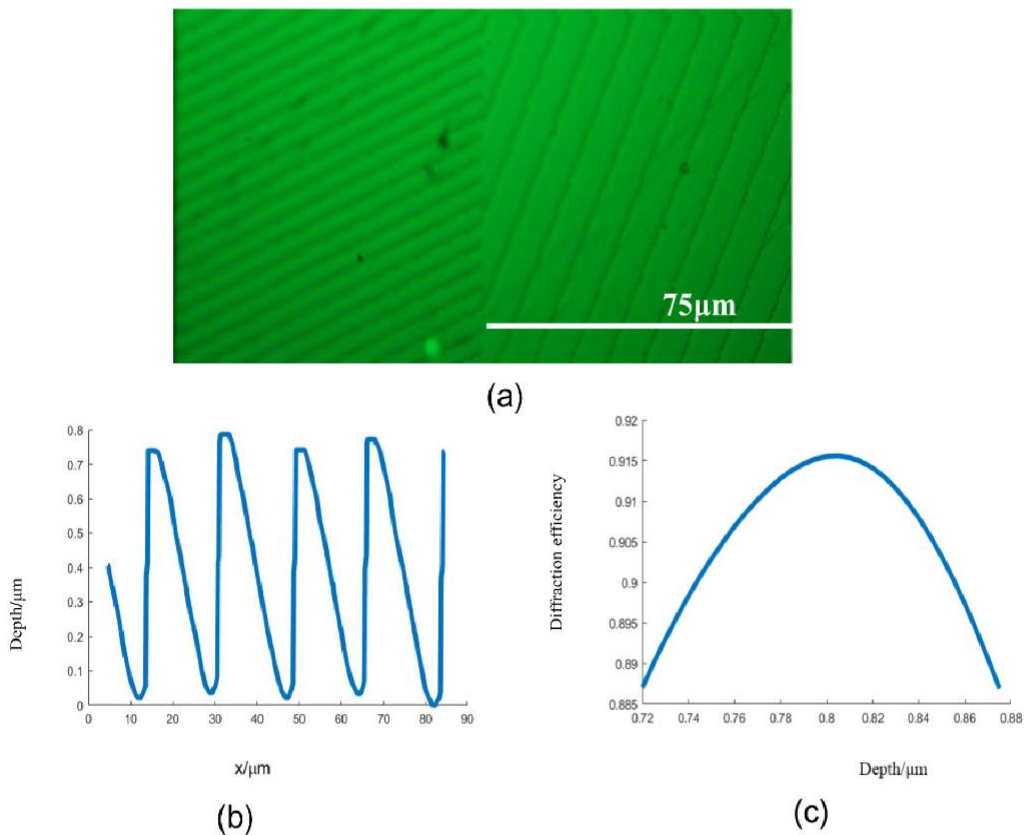


Figure 5-6-Surface structure and surface profile. (a) Partial view of the fabricated grating cell array. (b) Height profile of single fabricated grating cell. (c) Normalized theoretical first order diffraction efficiency against depth.

Figure 5-7 (a) shows the experiment setup used to capture the reconstructed pattern. The testing system consists of a divergent source, an iris, the fabricated DBA and a screen. Here, the iris is used to block other non-useful light. When the DBA is illuminated by a divergent green LED source, the reconstructed diffraction pattern formed on the screen and captured by a camera, is shown in **Figure 5-7 (b)**. A reconstructed pattern illuminated by a white light LED of a smart-phone is also shown in **Figure 5-7 (c)**. The feature pattern can still be clearly recognized with relatively low color dispersion even under white light illumination. As for the previous DOE, and for

similar reasons, the zeroth order is once again invisible. The experiment results demonstrate that the proposed faceted grating array method functions correctly and is feasible in optical security hologram applications. The proposed design method is more suitable to the use of divergent light compared to the iterative method in previous section when large DOEs are required since its calculation time cost is much lower. The structure of each DOE is simple and is easy to mass production with nanoimprint technology [109].

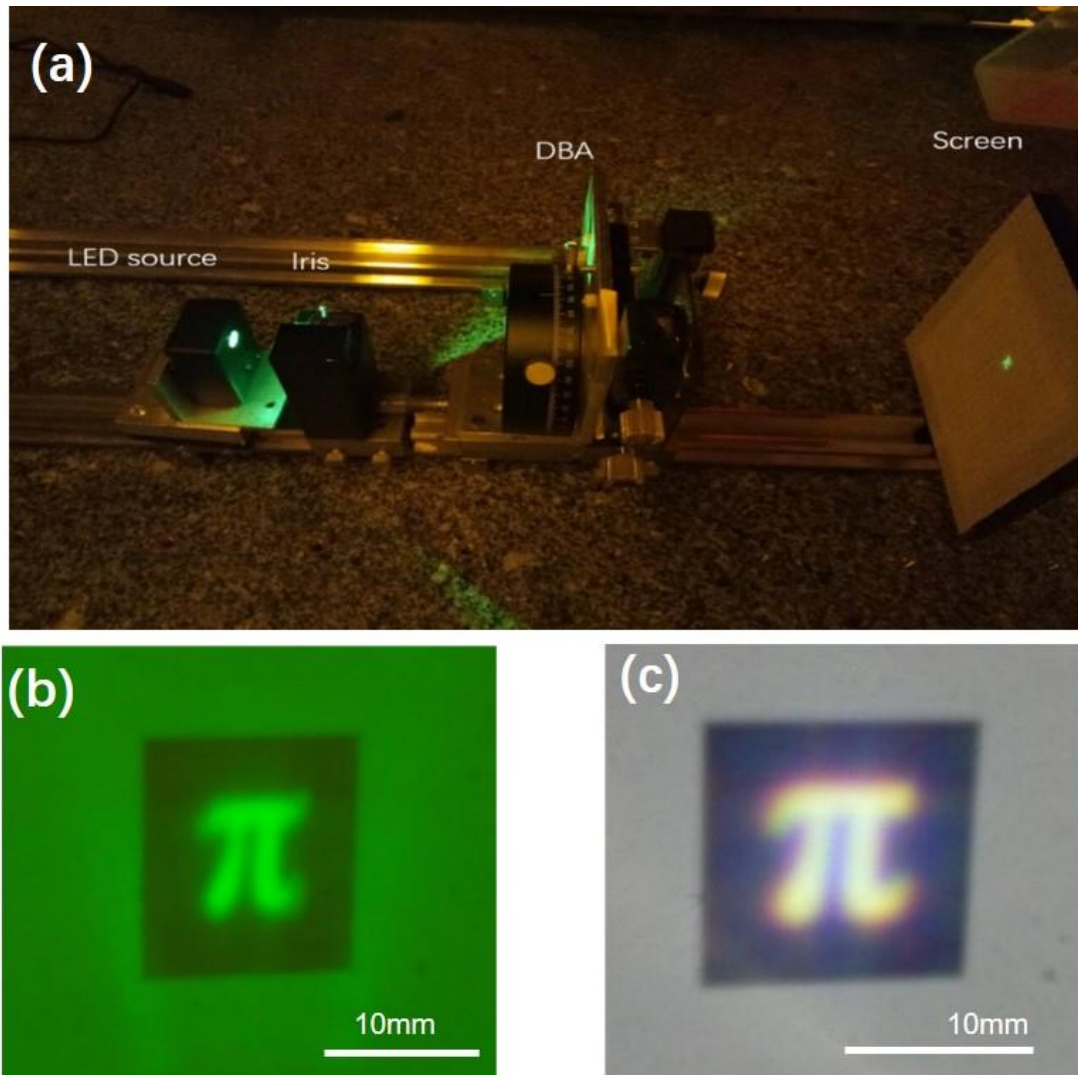


Figure 5-7- (a) Experiment setup. (b) The intensity distribution on the target plane as a result of illuminating the DBA with a green LED source. (c) Intensity distribution on target plane when illuminated by a white LED of a smart-phone.

5.2.3 Fabrication and experimental verification of a 2D optically variable device

In chapter 3.3, we presented the design principle of the blazed grating based OVD.

To investigate its optical performance, a reflective type OVD was fabricated using the photoplotter and characterized with an inverted interferometric microscope. The pixel size of the OVD was $0.75\mu\text{m}$ with 15000×15000 sampling points. In this design, the blazed grating period was chosen as $20\mu\text{m}$ to produce a sufficiently large diffraction angle to increase the visibility of the optical effect while avoiding the grating's shadow effect which affects the diffraction efficiency. A description about the grating's shadow effect can be found in reference [110].

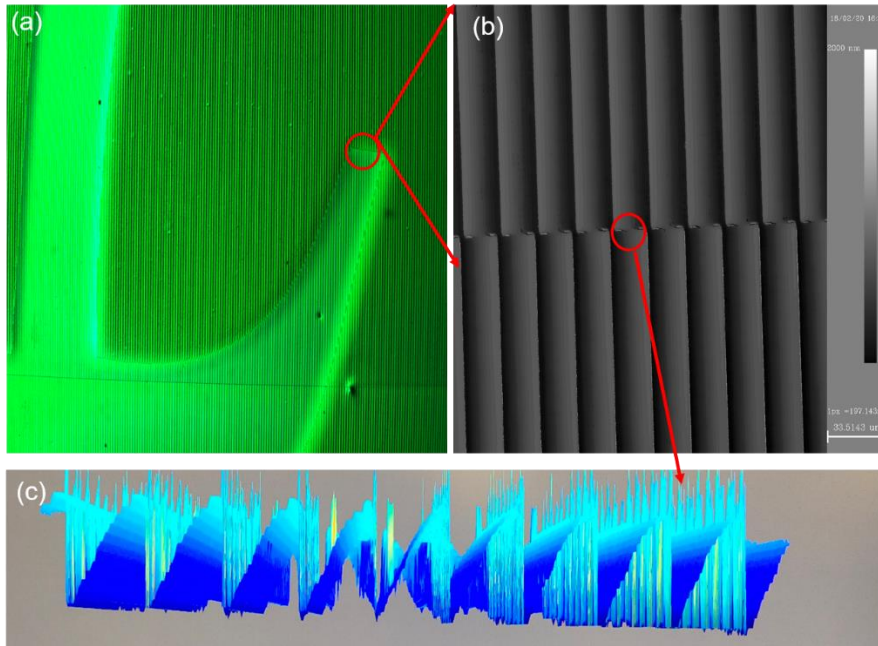


Figure 5-8-(a) Optical microscope photograph of part of the OVD. (b) Interferometric microscope height map view of the boundary of the pi pattern and the background. (c) Interferometric microscope generated 3D view of the structure on the boundary.

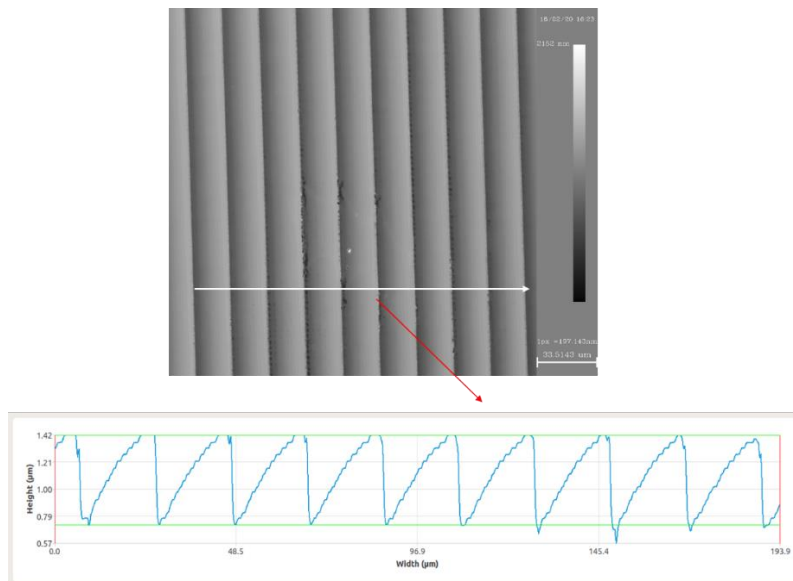


Figure 5-9-Height map surface structure image and surface profile of the OVD blazed gratings.

Figure 5-8(a) shows part of the OVD, which with **Figure 5-8 (b)** and (c) demonstrates that the grating orientation is inverted across the boundary which is matched with the desired structure shown in **Figure 3-23**. The 3D interferometric microscope was used to characterize the surface profile of the OVD which is depicted in **Figure 5-9**. The depth of the blazed grating was about 705nm with a period of 20 μ m. The measured first order diffraction efficiency was 84%. A result obtained by using the photodetector and optical bench described in section 5.1. To better approach security hologram observation conditions, the transmission OVD was coated by a thin metal layer. The observation experiment was conducted by illuminating the OVD with a yellow extended light source (fluorescent tube) in our cleanroom. According to the OVD design spirit, we should see different patterns when the OVD is tilted. **Figure 5-10(a)** is the image of the background, which is consistent with **Figure 3-24 (b)**. While in **Figure 5-10 (b)**, the pattern π appears brightly. These experimental results demonstrate successfully the design principle as they are very close to the numerical simulation results presented in section 3.3.

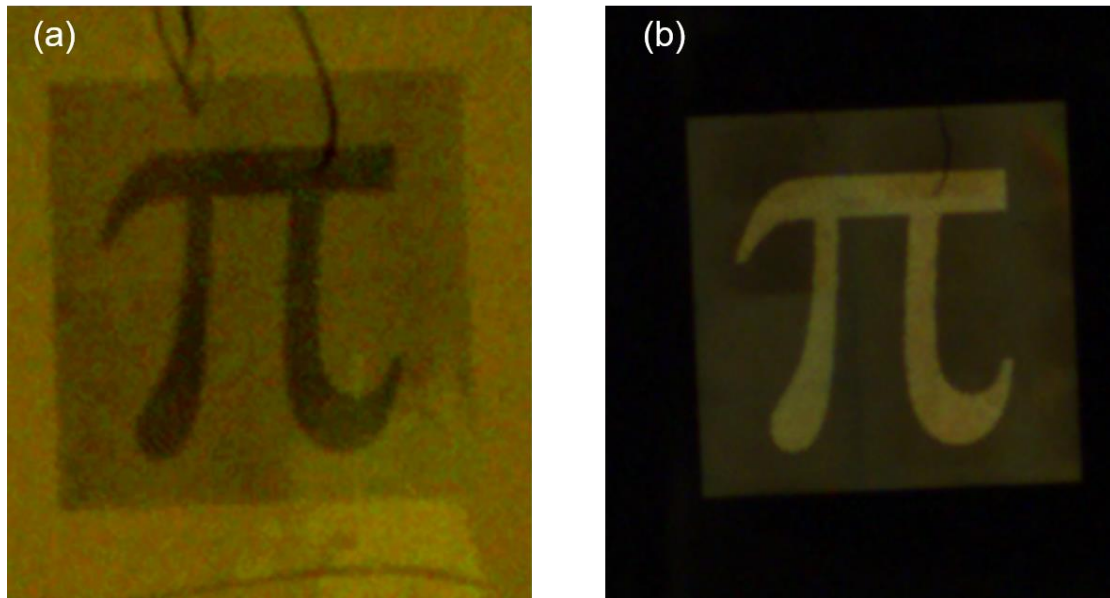


Figure 5-10-Experimental results.(a) Optically reconstructed result with tilt angle -6 degrees.(b) optically reconstructed result with tilt angle 6 degrees.

Similarly to the structure demonstrated in the previous section, the surface structure of the OVD can also be mass produced using standard roll to roll nano-imprint techniques [109]. In this work, only a 2D pattern on the OVD was demonstrated. However the proposed technique can be extended to produce the visual impression of a 3D pattern. But by the end of this thesis, the new design for 3D pattern is not completed due to lack of time. The basic principle of the design can be found in the Appendix. Researches continues into this effect is in optics department at IMT-A.

5.3 Experimental verification of the “floating 3D image” DOE

5.3.1 Experimental verification for faceted Fresnel DOEs

In order to validate the design algorithm for “floating 3D image” DOEs presented in chapter 3, a FDOE was fabricated and tested in our cleanroom. With the algorithm described in section 3.4, the FDOE was designed with 11*3 facets. The smallest pixel size of our direct write photoplotter is 0.75 μm , but here we use 1.5 μm as the design pixel size. This helps minimize pixel effects during fabrication in the off-axis configuration which tends to decrease the DOE fringe size. Each DOE facet contained 1800*1800 pixels, with a pixel size of 1.5 μm , the total FDOE size was 29.7mm \times 8.1mm. In this work, the FDOE was multi-level phase, the photoresist S1813 from Micro Resist Technology is used. The etch depth is chosen to give a maximum phase difference of each cell of 1.75π . The etch depth is dependent on the wavelength λ of the incident light and the refractive index of the resist. According to the TEA model, the groove depth of the surface relief structure can be written as

$$d = \frac{N-1}{N} \frac{\lambda}{2(n_{\text{material}} - n_{\text{air}})} \quad (5.1)$$

The number of phase levels, $N=8$, n_{material} is the refractive index of photoresist, its value is 1.66 at a wavelength of 532nm. According to this formula, the maximum depth d is about 691nm. The spin coating speed was 3200rpm, giving a photoresist thickness about 1.3 μm ; this depth is enough to etch the multi-level DOE. Exposure was implemented using our home-built parallel direct-write photo-plotter with a lookup table (LUT) to establish a linear relation between the addressed gray phase level and the etch depth. The exposed pattern is mapped from the LCD screen to photoresist plane. The exposure time was controlled to ensure the optimum etching depth.

A part of the FDOE and final fabricated FDOE are shown in **Figure 5-11** (a) and (b), respectively. The photo of **Figure 5-11** (a) was captured by the optical microscope (Reichert-Jung Polyvar Met Microscope), with a 100x objective. The FDOE was designed so that a floating 3D virtual image can be observed with a divergent LED source illuminating the FDOE. The schematic of experimental set up used to capture the output views is shown in **Figure 5-12**. This optical system comprises an LED source, the FDOE and a camera. A green LED source placed behind the transmissive FDOE was used as the illumination source for reproducing the expected 3D virtual image. The camera was mounted on a support, which could be rotated to obtain different viewing angles equivalent to those an observer sees moving his head to view the apparent 3D object. **Figure 5-13** shows the real experimental system (mounted in a vertical arrangement), the inset is the spectrum of the LED source. In **Figure 5-13**, the window is used to limit the observation area which can act as a reference to judge whether the reconstructed virtual object is located at the same position. The distance between the LED and the FDOE was about 155mm, and position of the virtual image is about 70mm behind the FDOE. The position of virtual image can be calculated according to the

imaging formula of eq. (5.2).

$$d_{image} = \frac{f_{fresnel} d_{obj}}{d_{obj} - f_{fresnel}} \quad (5.2)$$

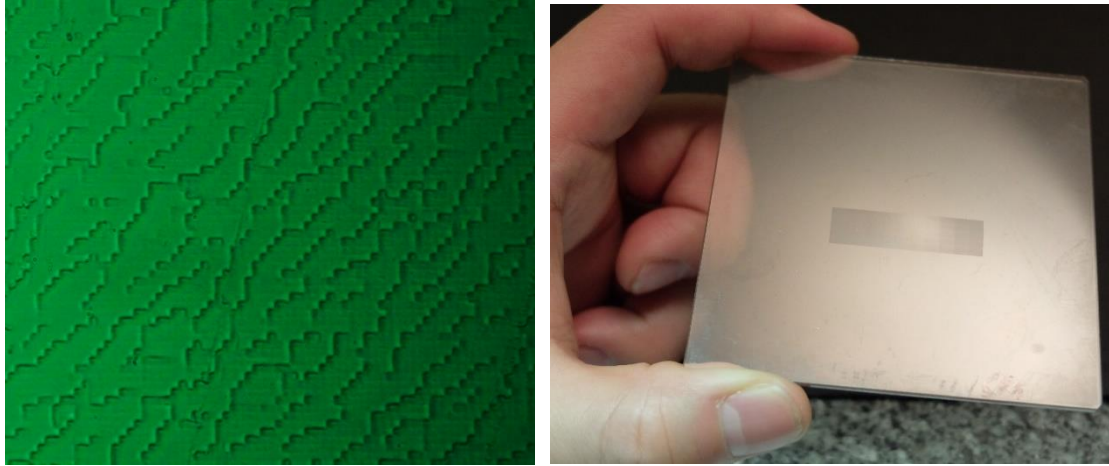


Figure 5-11-View of the fabricated FDOE and real sample. (a) Microscope view of the part of the FDOE. (b) Photograph of the real sample etched into photoresist on the glass substrate.

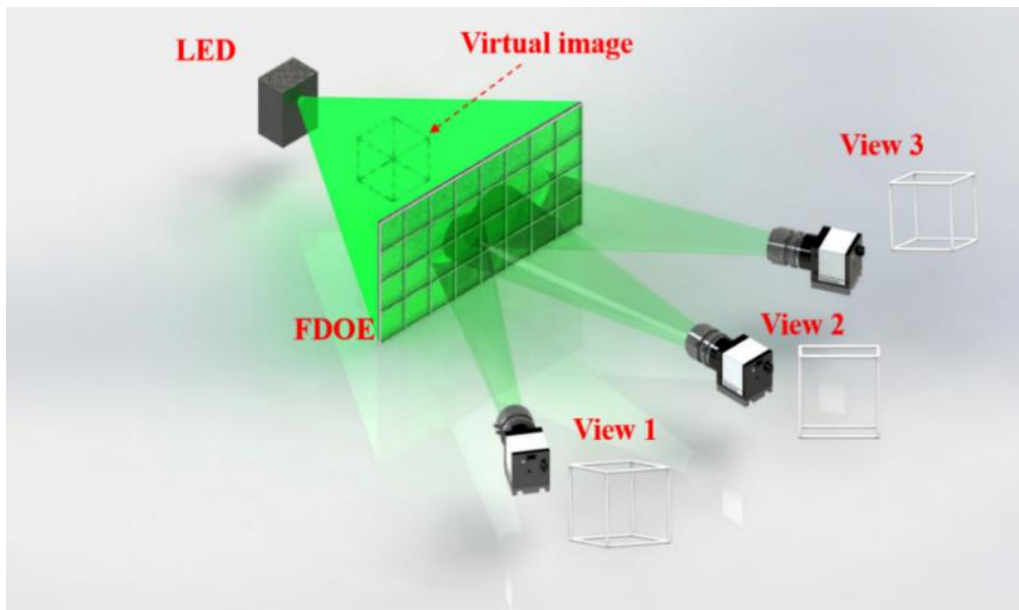


Figure 5-12-Schematic diagram of the 3D floating virtual object reconstruction capture setup.

In eq.(5.2), $f_{fresnel}$ is the focal length of the Fresnel type DOE, and d_{obj} is the distance between the source and the FDOE plane. With the LED illumination, the diffracted light propagates to human eye and the 3D virtual image is perceived in the air between the DOE plane and the LED source.

Figure 5-14 shows one perspective view of the 3D model “cube”. When the hologram is optically replayed, a floating virtual object appears hanging in the air, A finger is visible near to the virtual object cube, and the bright spot is the image of the

LED source. The effect created is of the “augmented reality” type in which artificial generated contents is superposed onto the real scene.

An observer also can see a realistic 3D image effect by looking at the virtual object from different angles. **Figure 5-15(a)-(f)** show six experimentally reconstructed virtual object views obtained by illuminating the FDOE. They were captured from six different viewing angles by rotating the camera from left to right, see **Figure 5-13**. The different views all locate the perceived virtual object at the same position hence giving a convincing impression of a single 3D object. The total field of view (FOV) is about 10 degrees, which can be calculated using the grating equation. The brightness of the reconstructed images is slightly different because the exposure time of camera was slightly different for the different views, and capture angles. In practice, the visual effect perceived by the observer is of a 3D virtual image with more uniform brightness.

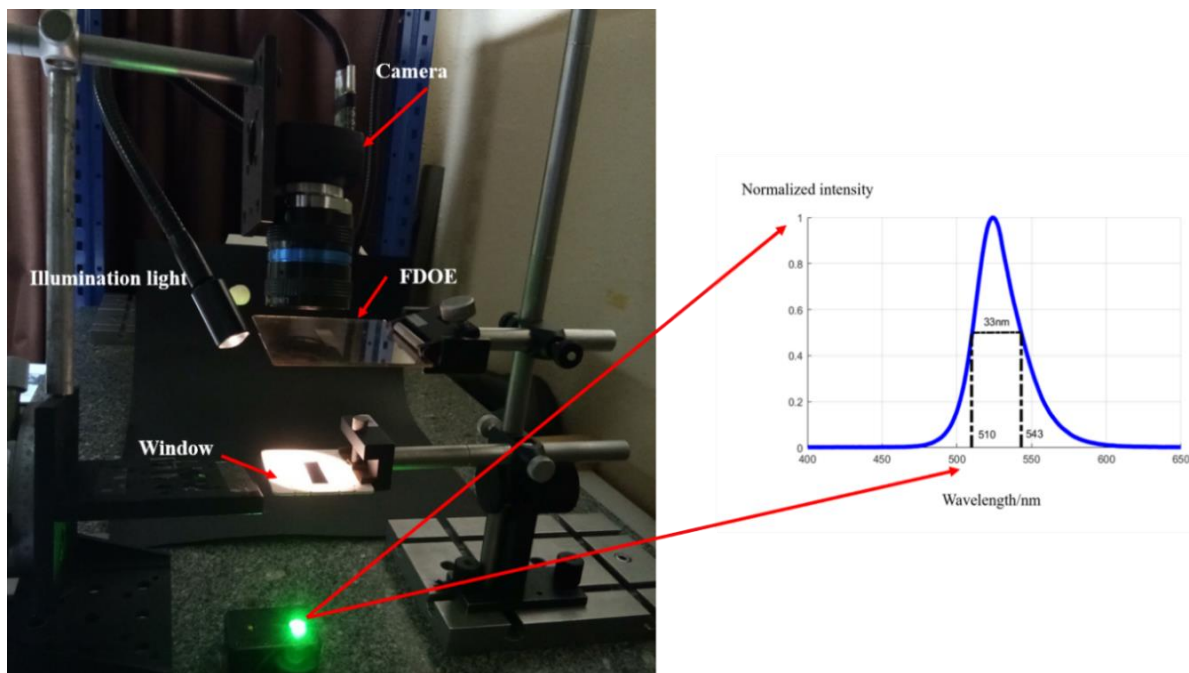


Figure 5-13-Experiment setup for 3D floating virtual image reconstruction. Inset: spectrum of the LED source obtained using an Ocean Optics HR4000CG-UV-NIR. The center wavelength is 525nm.

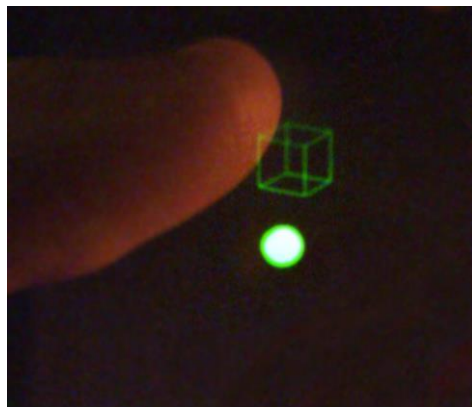


Figure 5-14-One perspective of the 3D virtual object “cube” floating in air.

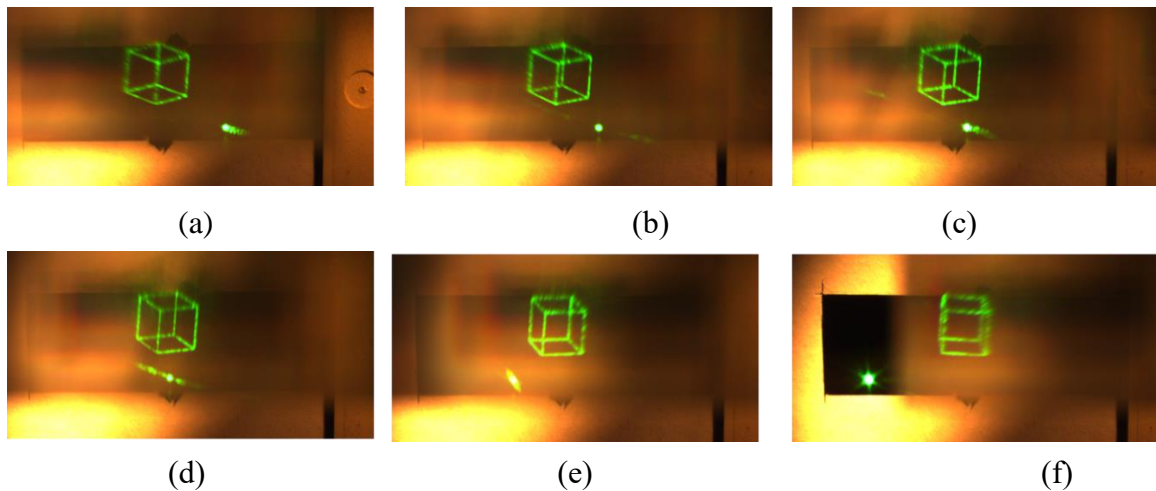


Figure 5-15-Virtual image taken from different angles of the object “cube” with the FDOE is illuminated by the LED.

Figure 5-16 shows the real experimental setup for evaluating the diffraction efficiency. The basic principle for measuring the diffraction efficiency was described in detail in section 3.4. Here, the setup consists of an LED source, a diaphragm, the DOE, a condenser lens and a photodiode. A real reconstructed image was imaged onto the photodiode using the condenser lens. In this way we obtained a DOE diffraction efficiency estimate of 46%. The DOE zeroth order was estimated in a similar way at 20%. The remaining light losses are due mainly to Fresnel reflection (~10%) and light in higher diffraction orders. The measurement results are close to that of the theoretical prediction of section 3.4. However, even with the current diffraction efficiency of 46%, the observed image is already clearly visible in daylight with a readily available LED.

As we discussed in chapter 3, one effective way of increasing the diffraction efficiency is to improve fabrication resolution. The parallel 2PP lithography system is currently being developed now in our cleanroom at IMT-A, should improve the fabrication resolution significantly. When the new fabrication facility is ready, the DOE will be designed using the same algorithm, but with a smaller pixel size. Due to the lack of time, FDOE fabrication using the new developed parallel 2PP lithographic machine was unfortunately not completed before the end of this thesis. Fabrication of new higher performance FDOE are planned for the end of 2020 when the new machine should be operational.

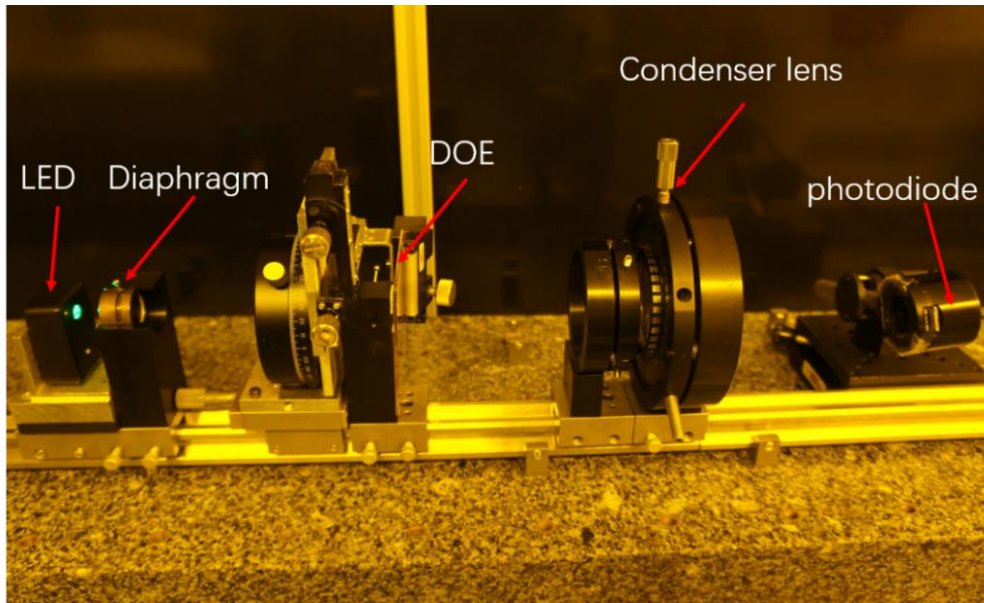


Figure 5-16-Setup for diffraction parameters measurement.

5.3.2 Experimental verification of Frequency multiplexing DOE design method

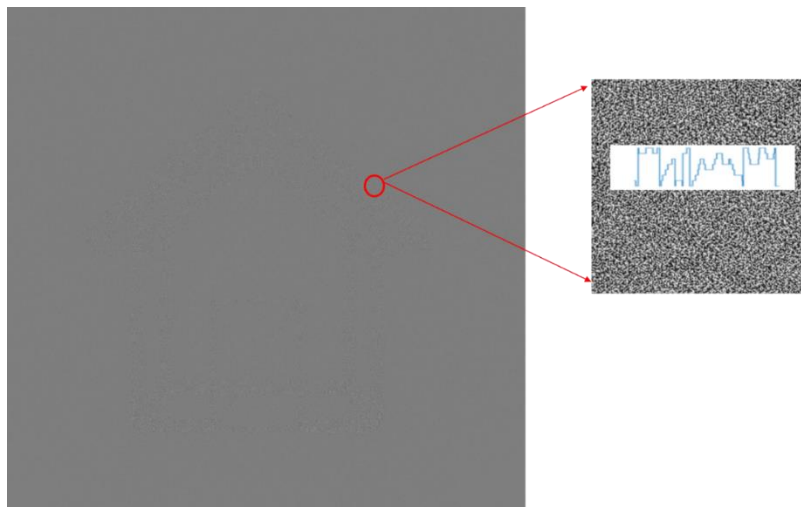


Figure 5-17-The calculated hologram using Frequency multiplexing method. The inset is a part of the hologram.

To validate the optical performance of the frequency multiplexing design algorithm of section 3.5, we experimentally fabricated a corresponding hologram operating in transmission and generating a perceived 3D image. The basic design principle was presented in section 3.5. A horizontal parallax hologram generating a virtual 3D house with 15 views was designed. The number of the DOE sampling points was 20000×20000 with the pixel size of $1.5\mu\text{m}$. In this work, the resolution of our home built photoplotter is $0.75\mu\text{m}$. The reason why we use $1.5\mu\text{m}$ in this design is to reduce

the pixel smear effect which comes from the optical proximity limitations of the lithography process, and is particularly strong with this algorithm which tends to produce many isolated pixels. The center wavelength used in this design was 650nm and the diffraction propagation distance was 50mm. The maximum field of view of this hologram was about 20 degrees. The final designed hologram is shown in **Figure 5-17**.

At full resolution (not visible here), we can see the contour of the target pattern in **Figure 5-17**. A possible reason is that the angular spectrum propagating method is used and the holograms corresponding to the 15 views are superposed on one hologram. The multi-level hologram (see inset) was fabricated using the same technique that was already described in detail in the previous sections.

To show the motion parallax, experiments were conducted using the same experimental setup as in **Figure 5-13**. **Figure 5-18(a)-(h)** are captured views of eight optically reconstructed virtual objects obtained when illuminating the hologram with a red LED. The photos were captured from eight viewing angles by rotating the camera from left to right. The real view angle here is 20 degrees which is twice the result demonstrated in the previous section with the FDOE approach.

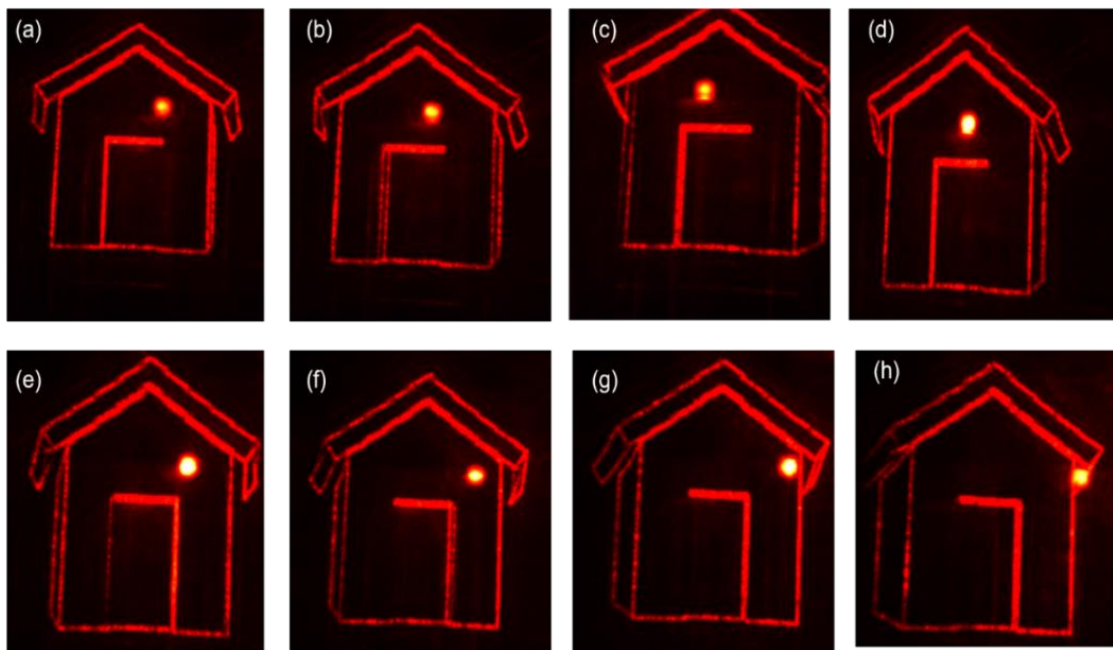


Figure 5-18-Different angular virtual image views of the object “house” when the DOE is illuminated by a LED source.

Compared to the method proposed in the previous section and traditional interference recording techniques, the proposed design method is more suitable for calculating large holograms because it greatly reduces the DOE calculation time and remove the requirement for an optical bench for the interference recording technique. This technique is currently being adapted to a vehicle 3D holographic augmented reality display application with a major automobile manufacturer.

The view angle of the hologram could be further expanded by reducing the hologram’s pixel size which is determined by the photo-lithography machine. Once the

parallel 2PP lithography machine in our cleanroom is ready, an even greater view angle hologram could be obtained. This research continues to be investigated by the optics department of the IMT-A.

5.4 Conclusion

In conclusion, in this chapter we have experimentally presented the optical performances of the proposed DOE design methods described in chapter 3. In all cases the experimental results are closed to their corresponding numerical simulation results. The developed and fabricated DOEs are all surface relief structures which can be mass produced using standard nano-imprint techniques. The zeroth order is almost invisible without any lithographic process optimizations when the Fresnel type DOE are used under divergent illumination. This is because the zeroth order is diffused under divergent illumination. This phenomenon provides an effect way to avoid the high power zeroth order and can be a good candidate for security holograms applications. However, its calculation load is heavy that cannot be suitable for calculating large size holograms. Therefore a faceted blazed grating array method was developed to overcome this issue. This method is based on optimizing the blazed grating's orientation angle and period in each facet using ray-tracing method. A desired diffraction pattern can form in the observation plane when illuminated by a divergent monochrome light source. In this way, the calculation load is mitigated so the technique can be used for large hologram calculation. Similarly, the zeroth order is also almost invisible which indicates this developed design method can also find applications in security holograms.

The blazed grating based OVD was investigated as a candidate solution for making 3D holograms by using our developing 2PP lithographic system in the near future. The desired pattern can be perceived on the hologram surface at a specified observation angle through tilting the hologram substrate. Unlike the projection type DOEs, it does not need an observation plane, it is more convenient to be used for banknote and brands for anti-counterfeit.

To further explore the DOE applications under divergent illumination, the faceted Fresnel DOEs method was deployed to produce a floating 3D virtual image. A convincing 3D virtual image can be perceived behind the hologram substrate when illuminated by a monochrome LED source. The eyebox can be extended using faceted Fresnel DOEs method. This developed method can find applications in advanced security hologram and holographics display. Nevertheless the calculation load is heavy since it requires numerous iterations for each facet. To address this drawback, a frequency multiplexing design was used, which it is a non-iterative method. A large hologram (30mm×30mm) was obtained using this method. A floating 3D image can also be observed using divergent illumination with this technique.

The residual discrepancies between the experimental results and simulation results come mainly from the fabrication limitations. In particularly, the fabrication resolution affects the real diffraction efficiency. During the DOE design, the discrete Fourier

transformation is used which assumes the high diffraction orders outside the calculation window are zero, thus the diffraction efficiency will often be overestimated. The high diffraction orders reduce the real diffraction efficiency and can introduce noise into the signal window, which would damage the reconstructed image quality. An effective way to improve the real diffraction efficiency is to improve the facility's fabrication resolution. To address this problem, a new parallel photoplotter based on 2PP is under development in our cleanroom. During my PhD, I participated in the design of illumination optical system for this new facility, which is described in the next chapter.

Chapter 6 Contributions to DOE fabrication facilities at IMT-A

In the previous chapters, we described the design methods for DOE generating 2D and 3D output pattern with successful experimental results. Many of these designs have reached the fabrication resolution limitations of our current home-built direct write photoplotter. The fabrication resolution is determined by the optical system of the photo-lithography machine, for example the illumination optical system and the optical projection system. In our photoplotter, a liquid crystal display based spatial light modulator (LCD-SLM) is used as a digital mask, then the projection optics transfer the pattern on the LCD-SLM into the photoresist layer on the glass substrate. The illumination uniformity of the LCD-SLM is very important in determining the lithographic performance. If the uniformity of the LCD-SLM is insufficient, the etch depth will be not uniform across the whole sample which will reduce the real DOE diffraction efficiency and introduce stray light which damages the reconstructed image quality. To address this problem, we need to design a compact illumination optical system with high illumination uniformity. As a part of my PhD research work, I contributed to design and development of two kinds of illumination optical system based on LED sources and one for a laser source. The first illumination system, based on a LED source was for an improved version of our current photoplotter in the cleanroom. The other illumination optical system designs were for the new parallel-write 2PP photoplotter currently being built in the European project Phenomenon, which is supported by Horizon 2020 [111].

As mentioned in the previous chapters, the fabrication resolution is vital parameter. Usually, the fabrication resolution is determined by the numerical aperture (NA) of the projection optics. High diffraction orders can be avoided and fabricating subwavelength photonic structures for visible wavelengths becomes possible only if higher resolution fabrication facility are used such as EBL. Such structures include 3D photonics structure which are now emerging in the optics community for example metasurface device [70], optical holograms [71] and photonics structures [69]. However, EBL fabrication is time consuming and expensive for machining large area DOEs. To attempt to overcome this problem, numerous 2PP fabrication techniques have been published in recent years. Especially, by Nanoscribe GmbH and Multiphoton Optics GmbH (our partner in the project Phenomenon) who has already developed commercial 2PP lithography machines. Nevertheless, the fabrication process is still slow. Therefore, there is an urgent need to investigate the possibility of developing new parallel 2PP lithography techniques and machines which are able to rapidly fabricate 3D submicron

structures. Such a new 2PP lithography machine is currently being built by Quentin Carlier in our cleanroom. Towards the end of my PhD research, I contributed to this work by designing the optical illumination system for this 2PP lithography machine. In this illumination system, the illumination source is based on a fibered laser. We will now present the illumination system design methods in detail

6.1 Illumination system design for the current parallel direct write photoplotter

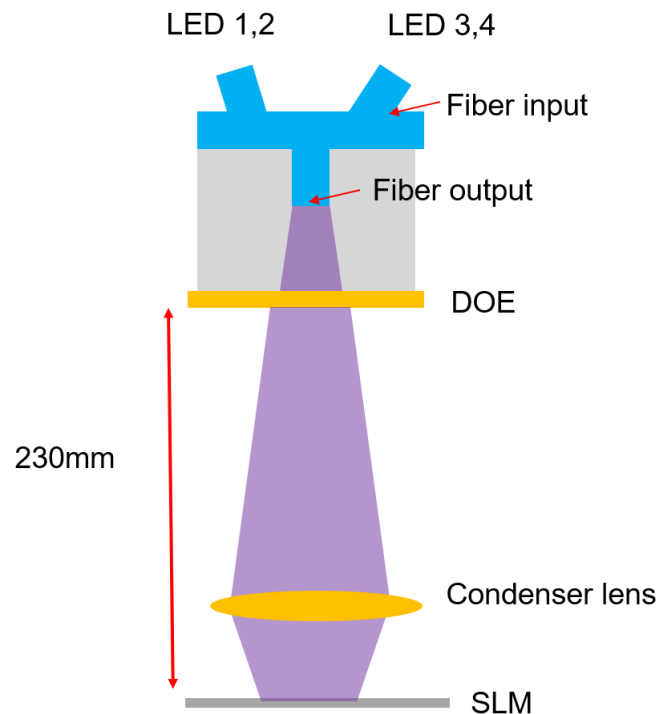


Figure 6-1- Schematic of the illumination system of the current parallel photoplotter in the cleanroom at IMT-A.

The main aim of this contribution was to improve the illumination uniformity of our current parallel photoplotter. **Figure 6-1** shows the schematic of the new illumination optical system. In the previous illumination optical system, there was no DOE. The illumination system uses four LED sources injected into homogenizing fibers for improving the light uniformity. Uniformity is improved by the multi-source superposition and the multimode fiber bundles. The LED sources are coupled into a multimode fiber, such that the light at fiber output is spatially partially coherent light. The fiber output divergence angle is about 20 degrees (full angle). Despite this system measured illumination uniformity across the SLM was still less than 70% (see definition

in eq. (6.1)), which is strong enough to produce very observable etch depth differences on the fabricated DOEs. To solve this problem, a DOE for improving the illumination uniformity was designed, fabricated and assembled into the illumination optical system as shown in **Figure 6-1**. In general, DOE design is based on an incident plane wave. But, in this system, the light from the fiber output is divergent. Hence, the traditional IFTA method for DOE design cannot be used directly. Here, we proposed a new way to design the DOE by measuring the real far field intensity distribution of the light from the fiber end. Then a DOE can be designed according to the real far field intensity distribution. The schematic of the experimental setup for measuring the far field diffraction pattern is depicted in **Figure 6-2**. In this measuring system, the coupler is used for coupling the light from LED into the fiber. The real far field diffraction pattern was captured by a camera as shown in **Figure 6-3**.

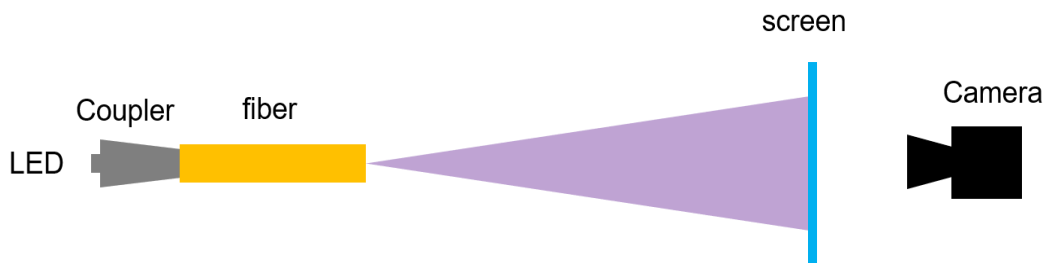


Figure 6-2- Schematic of the experimental setup for measuring the farfield diffractive intensity distribution of the illumination system.

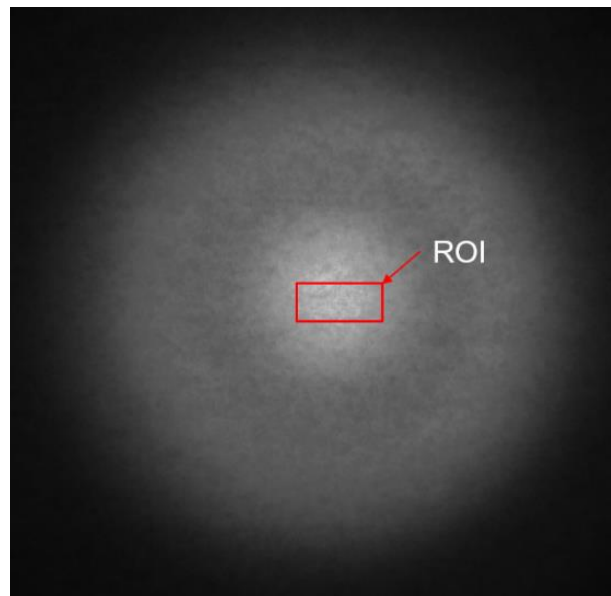


Figure 6-3-Farfield intensity distribution of the light from fiber end. The “ROI” corresponds to the SLM size and position.

The region of interest (ROI) corresponding to the size and position of the photoplotter SLM is in the central part of the diffraction field. Therefore, we have no need to control the illumination uniformity across the whole diffraction field. In our work, the ROI is

about $3\text{cm}\times 2\text{cm}$ at a distance of 23cm from the fiber output. An effective way of enhancing the illumination uniformity is to use a DOE beam splitter to generate several (here 9) different spatially separated copies of the far field fiber output pattern and to overlap these copies as shown in **Figure 6-4**.

The optimal illumination uniformity can be obtained through optimizing the shifting distance between the different copies of the light field. We obtained an optimal illumination uniformity when the displacement in X direction was 5.46mm, and the displacement in Y direction was 3.03mm. The corresponding DOE grating periods in the X and Y directions are $10\mu\text{m}$ and $17\mu\text{m}$ according to the grating equation [2], respectively. The numerical simulation results of the whole superposition diffraction intensity distribution and the intensity distribution in the ROI are shown in **Figure 6-5**. The illumination uniformity in the ROI is about 90%. With this method the light outside the ROI is lost, but it is not a problem since the light level is more than sufficient and exposure time (100ms) cannot be shorter because of the SLM refresh rate.

The corresponding binary DOE was designed by using a modified three-step IFTA method. The center wavelength of this design is 435nm, the pixel size of the DOE was $0.75\mu\text{m}$ and the photoresist etch depth for the binary DOE was 315nm. After the DOE optimization, the DOE was fabricated using our home built photoplotter. The real diffraction efficiency was about 80% as measured with a photo detector on an optical bench.

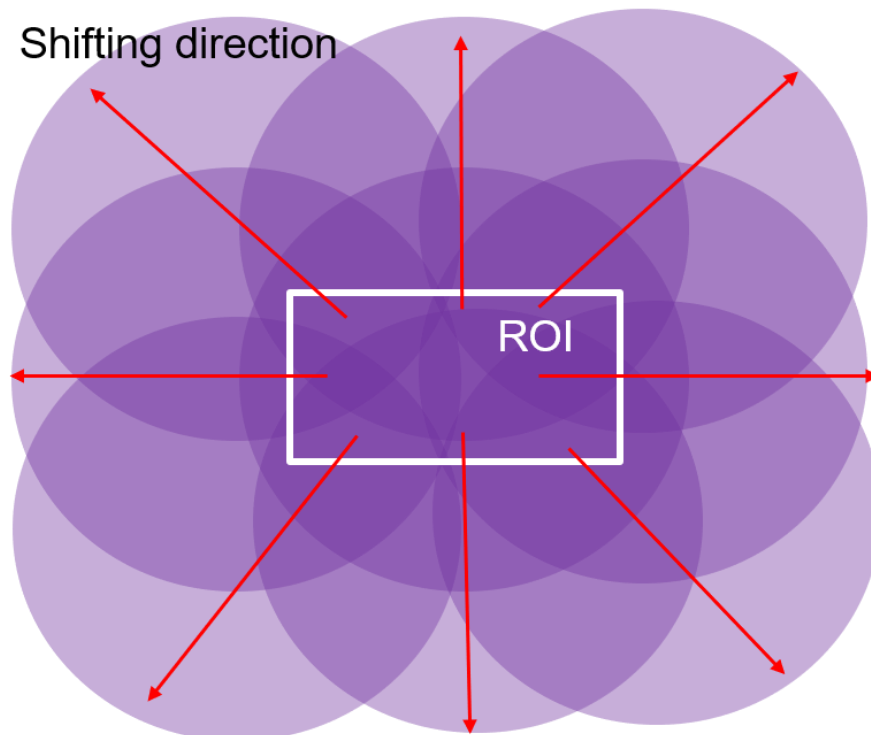


Figure 6-4-The principle of improving the illumination uniformity in the ROI. Each circle represents a copy of the far field fiber output pattern.

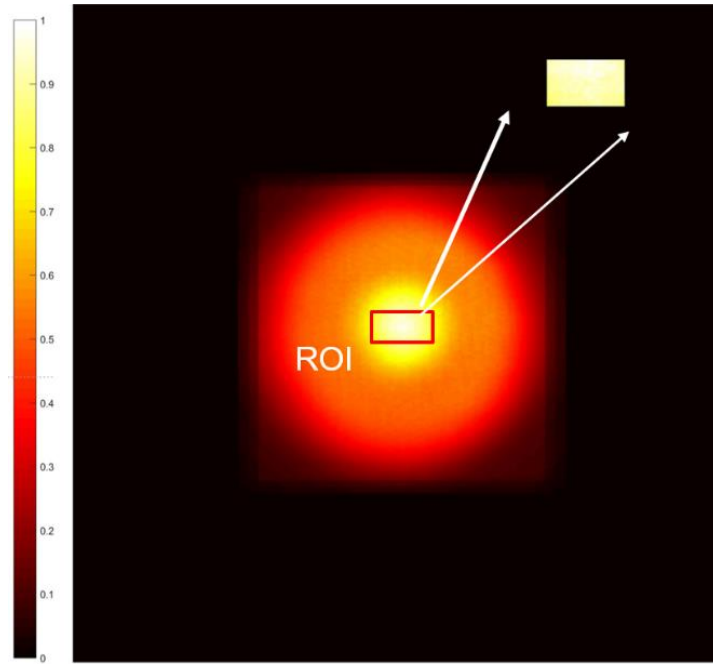


Figure 6-5- Numerical simulation of the DOE homogenized intensity distribution in the ROI.

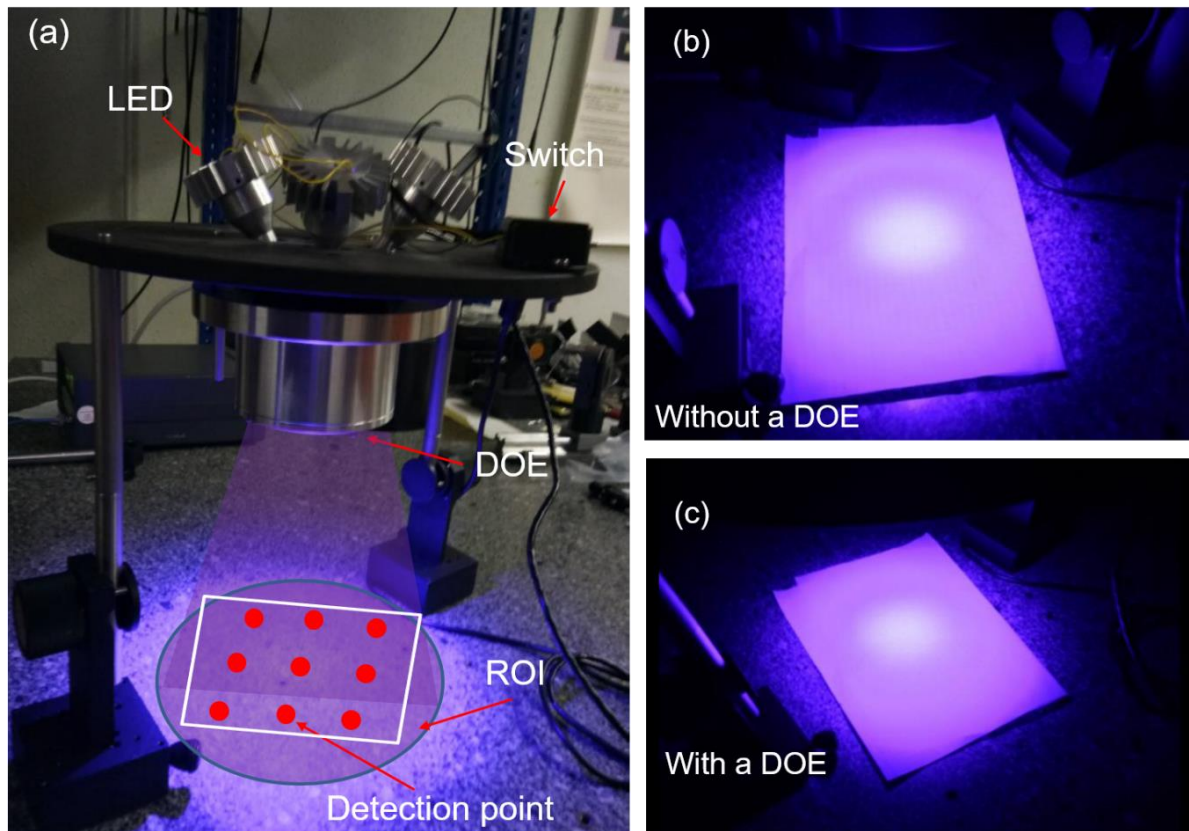


Figure 6-6- (a) Experimental evaluation setup of the photoplotter illumination system. (b) The illumination intensity distribution without a DOE diffuser. (c) The illumination intensity distribution with the DOE diffuser.

When its characterization was finished, the DOE was mounted in the illumination

system. The experimental setup is shown in **Figure 6-6 (a)**. To validate the illumination optics design, a controlled experiment was conducted to measure the illumination intensity distribution with a DOE and without a DOE as shown in **Figure 6-6 (b)** and **Figure 6-6 (c)**, respectively. The illumination uniformity was characterized by measuring the light power at nine different locations of the ROI. Here, the uniformity is defined as below.

$$uniformity = \left(1 - \frac{I_{max} - I_{min}}{2I_{ave}}\right) \times 100\% \quad (6.1)$$

Here, I_{max} represents the maximum measurement intensity, I_{min} is the minimum measurement intensity, and I_{ave} means the average measurement intensity. The experimental measurement results are given in **Table 6.1**.

Table 6.1-experimental results

Parameters	Experimental results with a DOE	Experimental results without a DOE
Maximum intensity:	27.8 μ w/cm ²	35.1 μ w/cm ²
Minimum intensity:	21.2 μ w/cm ²	17.3 μ w/cm ²
Average intensity:	22.3 μ w/cm ²	25.5 μ w/cm ²
Total power in ROI:	1.71mw/cm ²	2.26mw/cm ²
Illumination uniformity:	85.2%	65.1%

From **Table 6.1**, we can see that the illumination uniformity of the new illumination optical system including a DOE is significantly higher than that of the previous illumination optical system. However, the total power in the ROI of the new illumination optical system is lower than that of the previous illumination optical system due to the use of the DOE (reflection losses and light spread out of the ROI). To compensate, the illumination power should be increased or the exposure time should be calibrated when the new illumination optical system is used. The new DOE based illumination optical system has now been mounted into our parallel photoplotter, where it is used daily to fabricate different kinds of DOEs in our cleanroom. For example the DOE samples already demonstrated in the previous chapters.

6.2 Illumination system design for a new hybrid parallel write lithography machine

The task of designing a new 2PP parallel write lithography machine was in the

framework of Project Phenomenon which aims to develop a novel manufacturing approach for rapid machining sub-micron resolution large area 2D and 3D optical structures. In this research, we decided to build a hybrid machine, capable of one photon polymerization (1PP) and 2PP fabrication, to simplify system design, testing and give greater flexibility. The basic principle of the new lithography machine is similar to our current home built photoplotter which is used for DOE fabrication in our cleanroom. The schematic of the new hybrid lithography machine is illustrated in **Figure 6-7**.

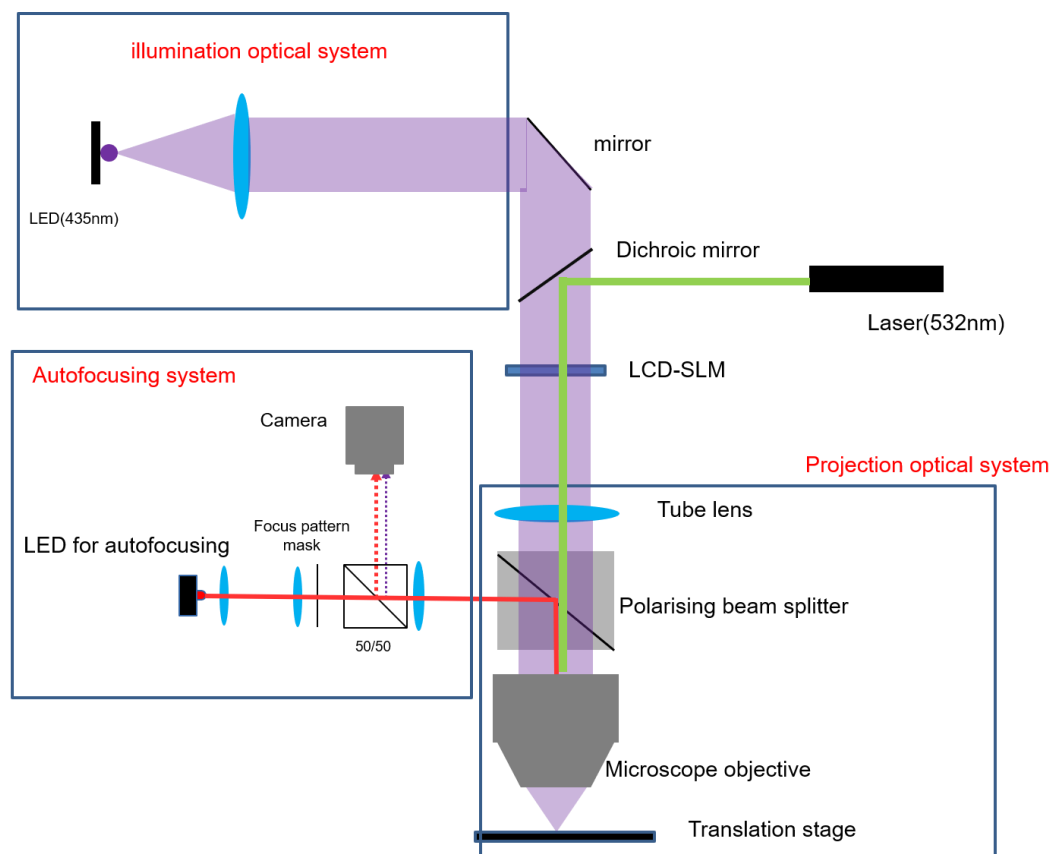


Figure 6-7-Schematic of the digital mask based lithography machine using an LCD-SLM.

The 1PP arm of the lithography machine consists of three sub systems which are optical illumination system, autofocusing system and the projection optics system. Since it is a parallel direct write lithography machine, an SLM is used reconfigurable as a digital mask, where the digital mask pattern can be imaged onto the photoresist via a projection optical system. The main components are the microscope objective and tube lens for the projection optical system. The autofocusing system is used to find the best focal position of the sample substrate. In our autofocusing system, a black and white mask pattern for example a checkerboard is projected to the wafer by the microscope objective. The camera is used to capture the image reflected by the wafer. The focal position can be obtained through shifting the microscope objective in the z direction until the captured image is at maximum contrast. The microscope objective is driven by a piezoelectric linear translation stage.

In this design work, I mainly focused on the design of the illumination optical system

during my PhD. Before designing the illumination system, we first determined the most adapted light source. Laser sources are frequently used in much photolithography equipment since laser beam can be easily collimated and shaped to a flat-top intensity distribution by using commercially available optical components. But, the main disadvantage of the laser source is the speckle noise which can severely damage the fabrication performance. In addition, the appearance of interference fringes is almost inevitable by using a coherent source in our system since parallel optical elements are used. As a result, a significantly more complicated optical system design is needed to reduce the laser speckle and interference fringes. To avoid these issues, we choose a high power LED source which produces much lower speckle compared to a laser source. The technical details of the LED source are given in **Table 6.2**. The suitable choice of the SLM and the homogenization optics remains challenging. In existing parallel 1PP lithography machines an SLM is used instead of physical masks. The SLM can be a digital mirror device (DMD) or an LCD. Compared to the transmissive LCD, the reflection DMD is more sensitive to the collimation and alignment tolerances, which significantly increases the complexity of such parallel 1PP lithography machines. As an engineering compromise, we integrated transmissive LCD into our setup. The detailed information of the LCD is provided in **Table 6.3**.

Table 6.2- The main parameters of the LED source utilized in the 1PP lithography machine

Light source	Wavelength(nm)	Optical power(mw)	Photoresist	Divergent angle
M420-L3	420	750	S1813	125 degrees

Table 6.3- The LCD-SLM utilized in the 1PP lithography machine

Type	Resolution	Size	Active area	Pitch
Epson L3C07U	1920x1080	0.74 inches	16.32x9.18	8.5 μ m

Once the source and SLM were determined, the next design step was to homogenize and collimate light on the LCD. To overcome these problems, we investigated several kinds of optical illumination systems which can be divided into two categories: Critical illumination configuration and Kohler illumination configuration [3]. Their basic working principles are illustrated in **Figure 6-8**, respectively. In the Critical illumination configuration, the condenser lens is used to directly image the source to the SLM. The non-uniformity of the source significantly impacts the uniformity of the SLM. Thus, the critical illumination configuration is not suitable for a system requiring large area uniform illumination. The Kohler illumination configuration overcomes this drawback because the illumination uniformity on the SLM is less dependent on the light source's non-uniformity than in the Critical illumination configuration.

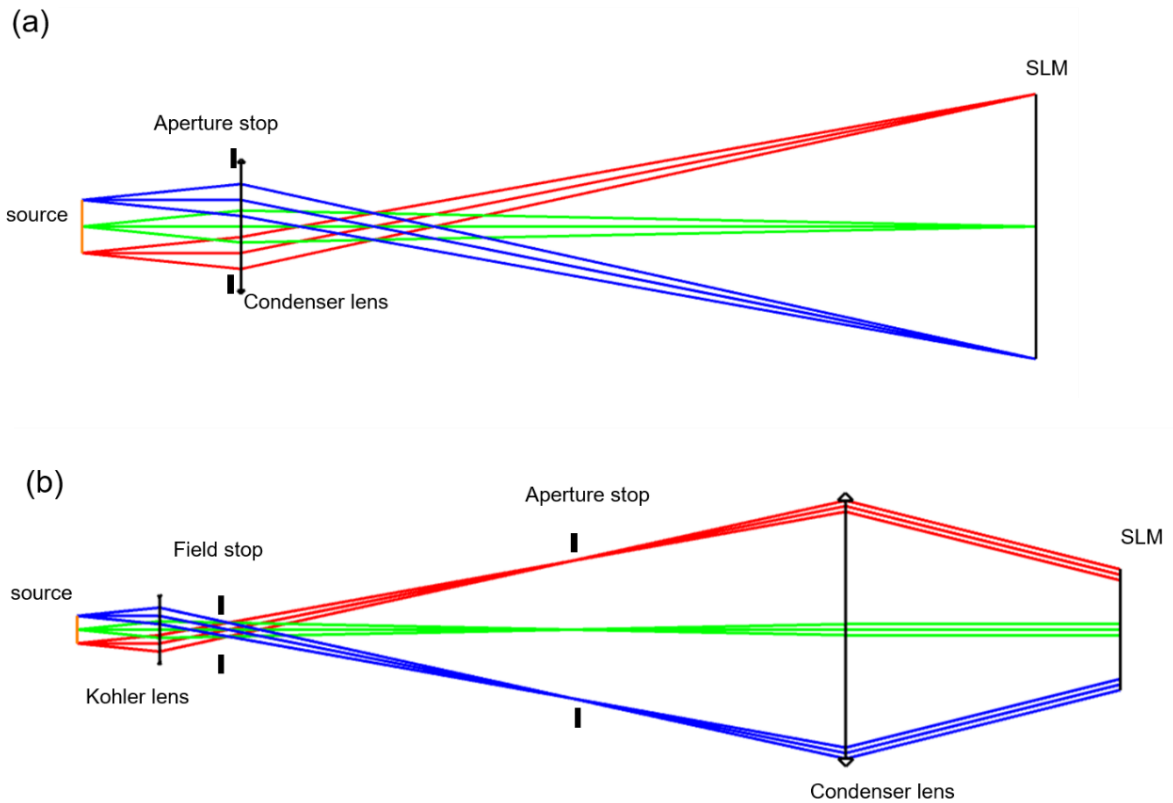


Figure 6-8-Illumination optical configurations. (a) Schematic of the Critical illumination configuration. (b) Schematic of the Kohler illumination configuration.

The Kohler illumination configuration is sketched in **Figure 6-8 (b)**. The light emitted by the light source is imaged by the Kohler lens to the aperture stop. The aperture stop is placed at the front focal plane of the condenser lens, therefore the aperture stop is imaged by the condenser lens to infinity, i.e. the secondary image of the light source is at infinity, thereby forming a telecentric illumination. The field diaphragm of the Kohler illumination configuration is placed behind the Kohler lens, which is imaged onto the SLM by the condenser lens. Hence the illumination uniformity on the SLM depends on the intensity distribution at the field stop. In addition, the Kohler illumination configuration is more flexible because the illumination area and the illumination aperture angle on the SLM can be controlled by adjusting the field diaphragm and the aperture diaphragm. Based on the above analyses, the Kohler illumination configuration was selected as our basic illumination design solution in this work. Usually, the optical system design includes the lens design, lens fabrication and lens group assembly, which are often challenging and time consuming. Nowadays, the design with off-the-shelf optical components has become popular, because the price of the standard optical component is much cheaper than that of the customized lens fabrication. Considering the time cost and the price, we used the off-the-shelf optical elements from Thorlabs to design the illumination optical system.

In our design, the LED source used is an extended source with a divergent angle 125 degrees (full angle). Such high divergent sources cannot be collimated by a single lens.

Here, an aspherical condenser lens (ACL2520U-A) was used to collect part of the light emitted from the LED source. As the SLM illumination uniformity is determined by that at the field diaphragm, a DOE diffuser was used to homogenize the light intensity in this plane. The DOE diffuser is placed near to the image plane of the LED source. The DOE diffuser was designed based on the IFTA method and was fabricated using our photoplotter in our cleanroom. The detailed IFTA design method of the diffuser was described in the previous chapters. The condenser lens (AC254-100-A) was used to collimate the light passing through the DOE diffuser. The whole illumination configuration was modeled using ZEMAX [112] software as shown in **Figure 6-9**.

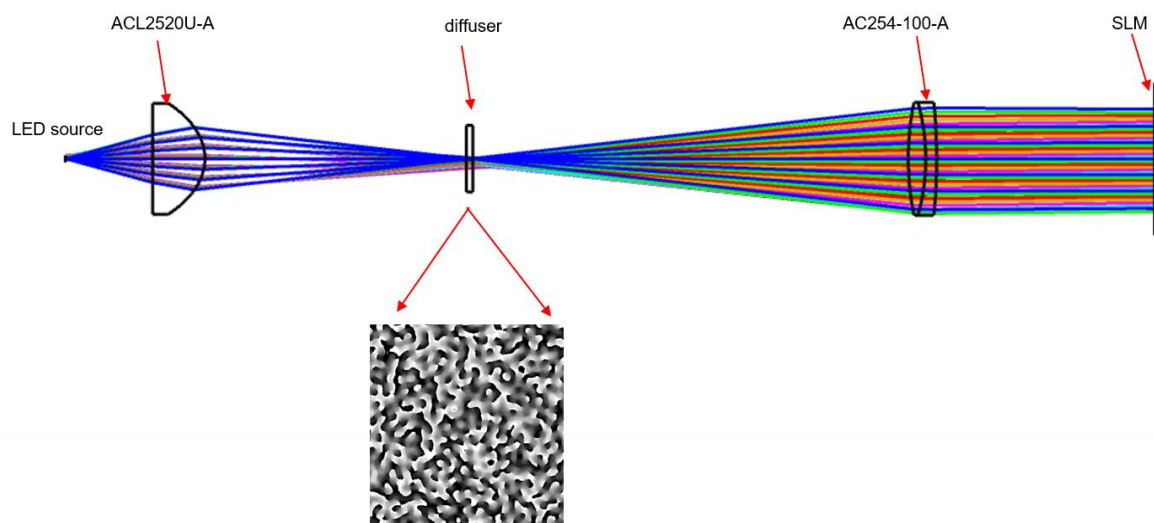


Figure 6-9-The ZEMAX ray-tracing simulation of the illumination system for homogenizing the SLM in the hybrid lithography machine.

However, when we integrated the assembled designed illumination system into the lithography machine, we observed that the LCD-SLM produces higher diffraction orders due to the pixelated structure of the LCD-SLM. These high diffraction orders cannot be all collected by the microscope objective. From the perspective of Abbe's theory of imaging, individual SLM pixel sized structures can be fabricated by the lithography machine only if the higher diffraction orders all contribute to the imaging process. To help collect more of these higher diffraction orders in the microscope objective and hence improve the fabrication performance, we added a long focal length condenser lens (AC254-200-A-ML) to form a convergent illumination light field on the SLM. The modified illumination system using ZEMAX simulation is presented in **Figure 6-10**. **Figure 6-11** shows the intensity distribution on the SLM and in the rear aperture of the microscope objective. In this system, the diameter of the incident light ray on the SLM and the rear aperture of the microscope are about 20mm and 4mm, which are obtained by using nonsequential raytracing. The diameter of the rear aperture of the microscope objective is about 6mm, so most of the light passing through the SLM will be collected by the microscope objective improving system resolution and light

efficiency. When the modified illumination system was assembled into the prototype lithography machine, we observed that the most of the higher diffraction order were indeed collected by the microscope objective. A photograph of the illumination optical system in our cleanroom is shown in **Figure 6-12**.

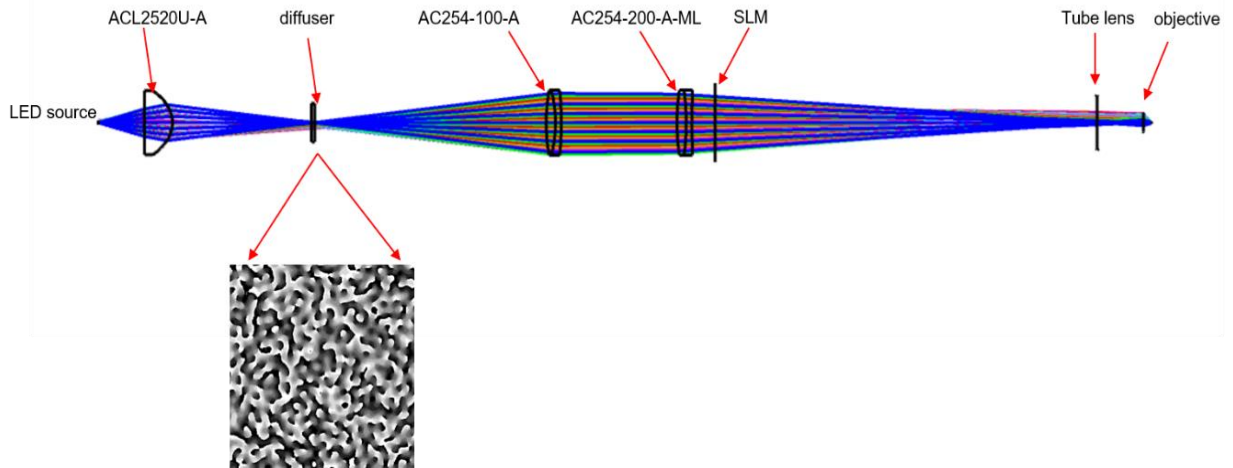


Figure 6-10- ZEMAX simulation of the modified illumination system for homogenizing the SLM.

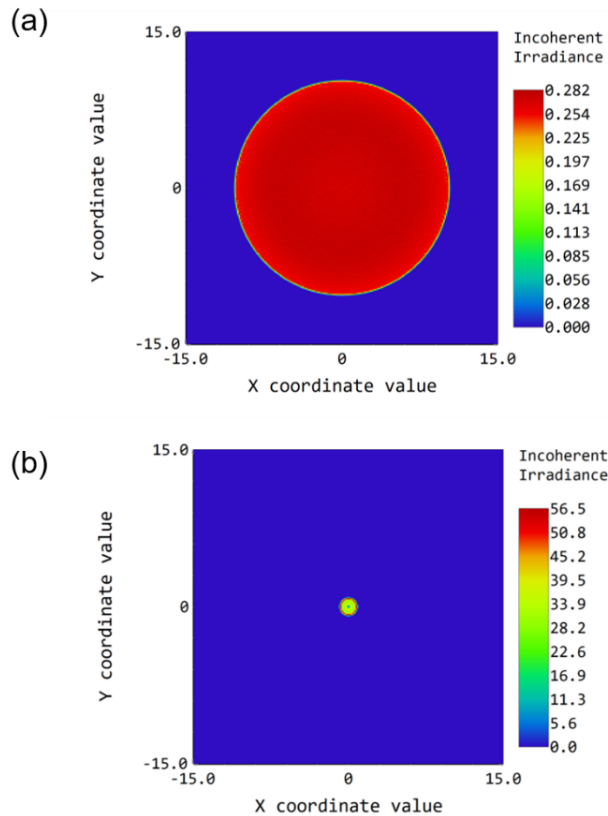


Figure 6-11- (a)The simulated intensity distribution on the SLM , a circle of diameter is 20mm (The diagonal length of the SLM is about 18mm). (b) The intensity distribution at the rear aperture of the microscope objective, a rough circle of diameter about 4mm.

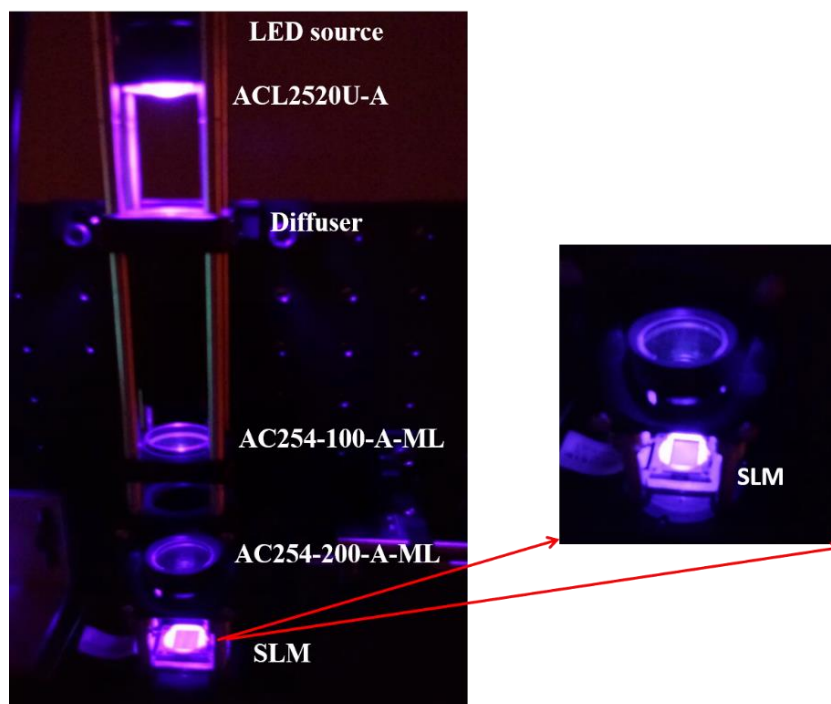


Figure 6-12-Photography of the designed LED based optical illumination system assembled into the prototype lithography machine.

The illumination uniformity on the SLM can be measured using the same method presented in section 6.1. The measured illumination uniformity was near to 90% and the optical power was about $1.23\text{mW}/\text{cm}^2$ on the SLM. The optical power collected by the objective was $0.2\text{mW}/\text{cm}^2$. The photograph of the whole parallel prototype lithography machine is shown in **Figure 6-13**. The optical components, mirrors and the optical cages are all from Thorlabs. The microscope objective is from ZEISS (NA0.4, 20X, or NA 0.85, 40X). The XY stage, the LED source and the LCD-SLM are synchronized by the computer.

To demonstrate the current fabrication performance, we show two example samples in **Figure 6-14**. From these results, we can clear see that $1\mu\text{m}$ feature sizes can be resolved using this fabrication facility. The feature size can be further decreased by using a higher NA microscope objective, but the FOV of the fabrication area is reduced. Therefore, the field stitching technique is needed if we wish to fabricate a large size DOEs .

Nowadays, with the development of the nanoscale devices, the nanofabrication of arbitrarily complex 3D structures is highly desired. This requirement drives us to develop a similar parallel 2PP photoplotter to leverage the 3D fabrication possibility of 2PP process. Such a possibility is currently being investigated using the “2PP arm” of the same hybrid parallel write lithography machine. In this task, I focused on developing the illumination system for laser source. The detailed design method will be presented in next section.

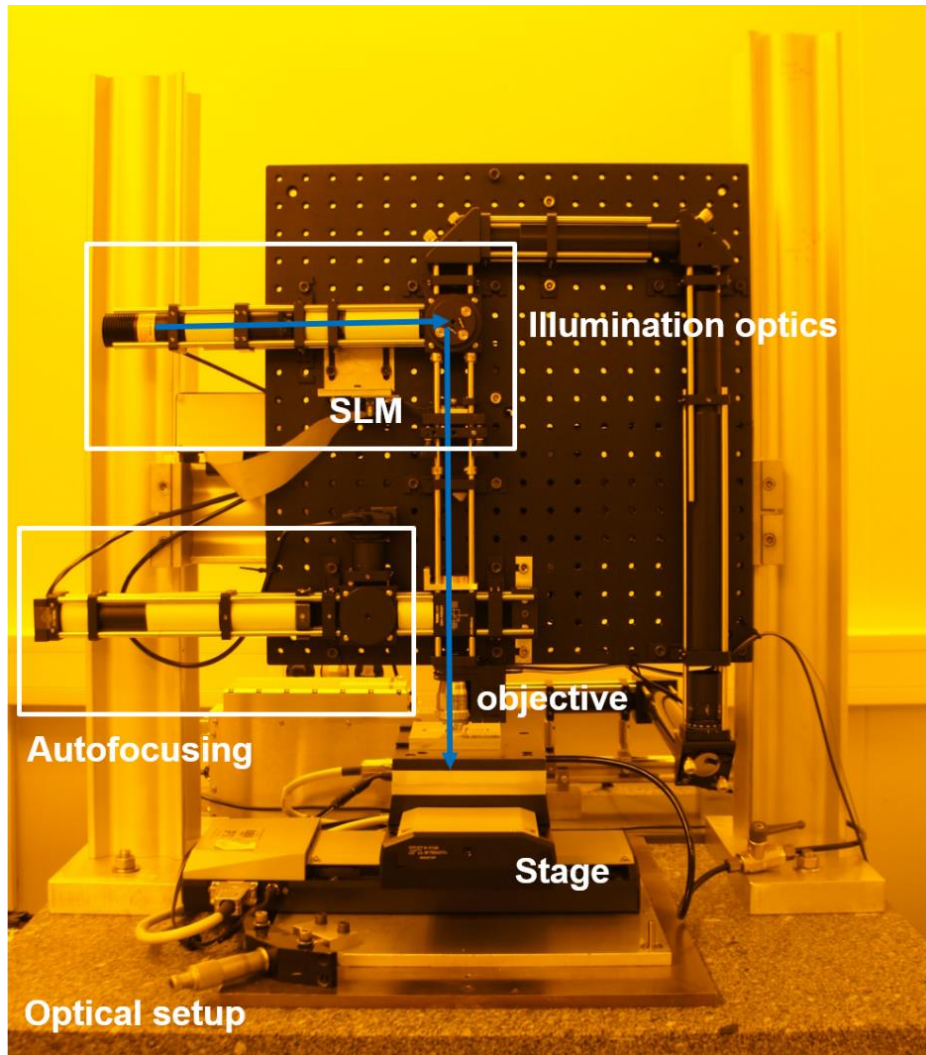


Figure 6-13- Optical setup of the hybrid parallel write lithography machine.

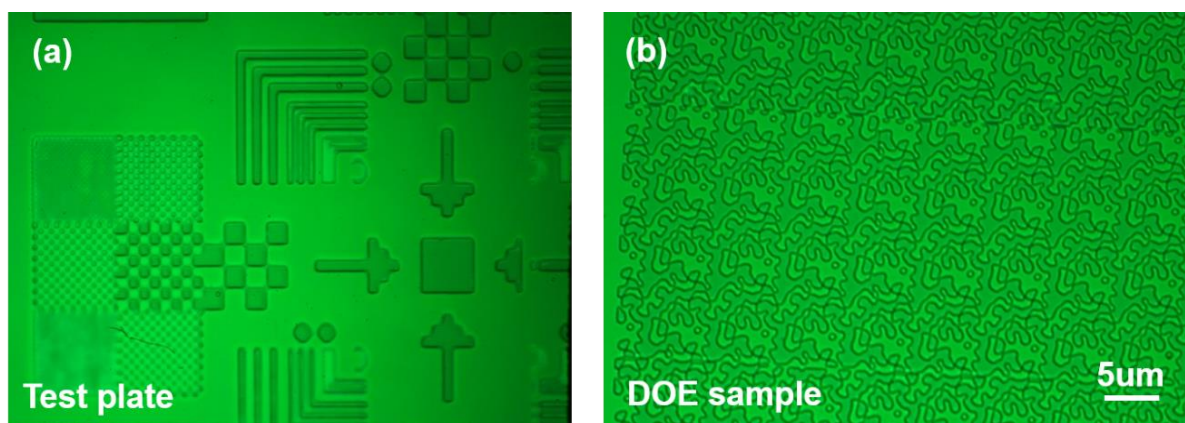


Figure 6-14-Microscope images of the patterns fabricated using the 1PP arm of the hybrid parallel write lithography machine. (a) Test pattern (smallest lines are 1 micron width). (b) DOE sample.

6.3 Illumination optical system design for the 2PP Photoplotter

6.3.1 The basic principle of 2PP

As explained previously, to overcome the limited resolution of conventional photoplotters, researchers have proposed two-photon lithographic technology. Two-photon polymerization is a layer-by-layer method which can provide unprecedented flexibility for manufacturing arbitrary 3D micro or nano structures.

2PP fabrication technology depends on the two-photon absorption (TPA) photochemical process in which a photosensitive material simultaneously absorbs two photons of a tightly focused beam generated by a high NA microscope objective. Through two-photon absorption process illustrated in **Figure 6-15(b)**, the molecule of the polymer is excited to a higher state from the ground state. TPA is one of several multi-photon absorption (MPA) processes. The reason we call it TPA is because the energy level difference between the ground state and excited state is the sum of the energies of the two photons.

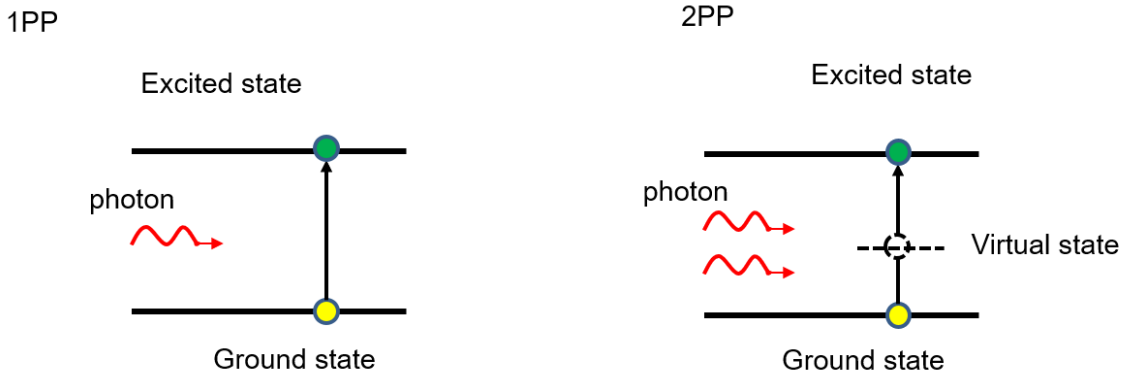
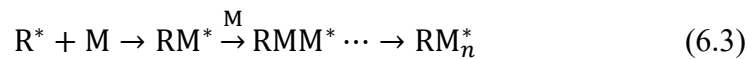


Figure 6-15- (a) One photon absorption process of the 1PP photoplotter. (b) Two-photon absorption process of the 2PP photoplotter.

The standard polymerization process can be illustrated using eq. (6.2), eq. (6.3) and eq.(6.4) [85] [113].



According to these equations, the polymerization process can be divided into three main phases: the initiation phase, the propagation phase and the terminal phase. During the initiation phase, photoinitiators (PI) are promoted to their excited state PI^* when two photons are absorbed. Then, PI^* decomposes to radicals R^* . The R^* combine with monomer molecules to generate monomer radicals RM_n^* in the propagation phase. When the two monomer radicals are combined in the termination phase, the photo-

polymerization process ends.

The TPA process is different from the one-photon absorption process. It is a linear optical process for one-photon absorption, while TPA is a third-order nonlinear optical process in which the absorption rate of energy is proportional to the square of light intensity, as illustrated in eq.(6.5) [113].

$$\frac{dP}{dt} = \frac{8\pi^2\omega}{n^2c^2} I^2 \text{Im}(\chi^3) \quad (6.5)$$

In eq.(6.5), c represents the speed of light in vacuum, n is the refractive index of the polymer, ω is the light optical frequency of the focused beam inside the polymer, $\text{Im}(\chi^3)$ is the imaginary part of the third-order susceptibility, and I is the light intensity. Since the cross section for TPA is several order of magnitude lower than that for one-photon absorption, a high light intensity laser is required. Usually, an ultra-short pulsed laser is preferred because it can produce high intensity pulses (of the order of TW/cm^2) during a very short time (ps). The polymerized spot is formed only in the focal volume of the focused light, this volume is usually called ‘voxel’. An arbitrary 3D structure can be polymerized in the resin by scanning and moving the focused light spot for example with a 2D galvanometer scanner and a piezoelectric stage.

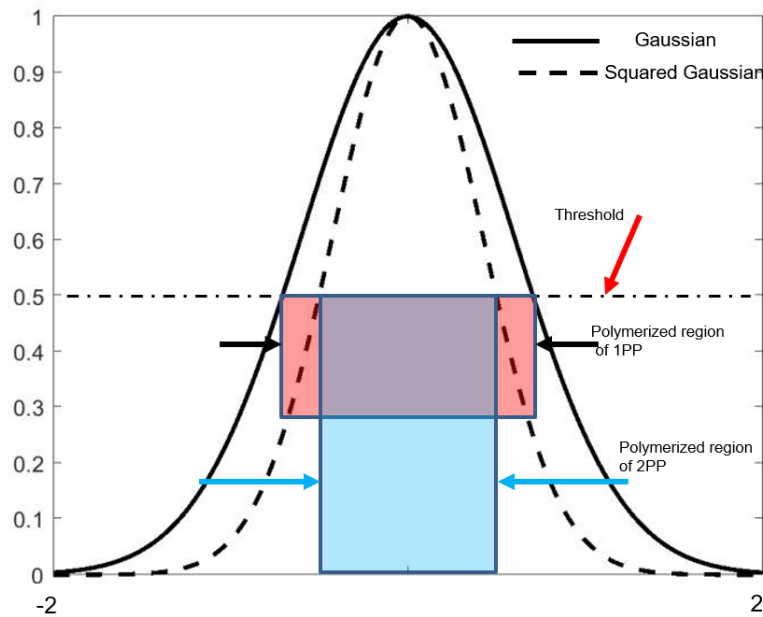


Figure 6-16-The intensity profile of the Gaussian light and squared Gaussian light.

Generally, the resolution of an imaging optical system is bounded by the diffraction limit. Specifically, the lateral resolution limitation is given by eq. (6.6) in an optical microscope according to Abbe imaging theory [3].

$$\sigma = \frac{\lambda}{2NA} \quad (6.6)$$

where NA is the numerical aperture. Usually, the lateral resolution limit is about half the wavelength when NA equals to 1. The TPA process can go beyond this diffraction limit since its exposure is proportional to the square of the focused light's intensity, as illustrated in **Figure 6-16** [113]. The modified formula for the lateral resolution for TPA is expressed as below.

$$\sigma = \frac{\lambda}{2\sqrt{2}NA} \quad (6.7)$$

Therefore, the minimum feature size of TPA can be less than 150nm for example when the wavelength is 532nm and the NA is 1.4. The fabrication resolution can still be further improved by developing new resins: resolution has reached to 9nm according to the recent literature [86].

In addition to the lateral resolution, the longitudinal resolution is a very important parameter for 3D manufacturing. To show the differences, the intensity distribution of one photon absorption and two-photon absorption along the light propagation are presented in **Figure 6-17**. The numerical simulation results are based on the Richard and Wolf integral [114].

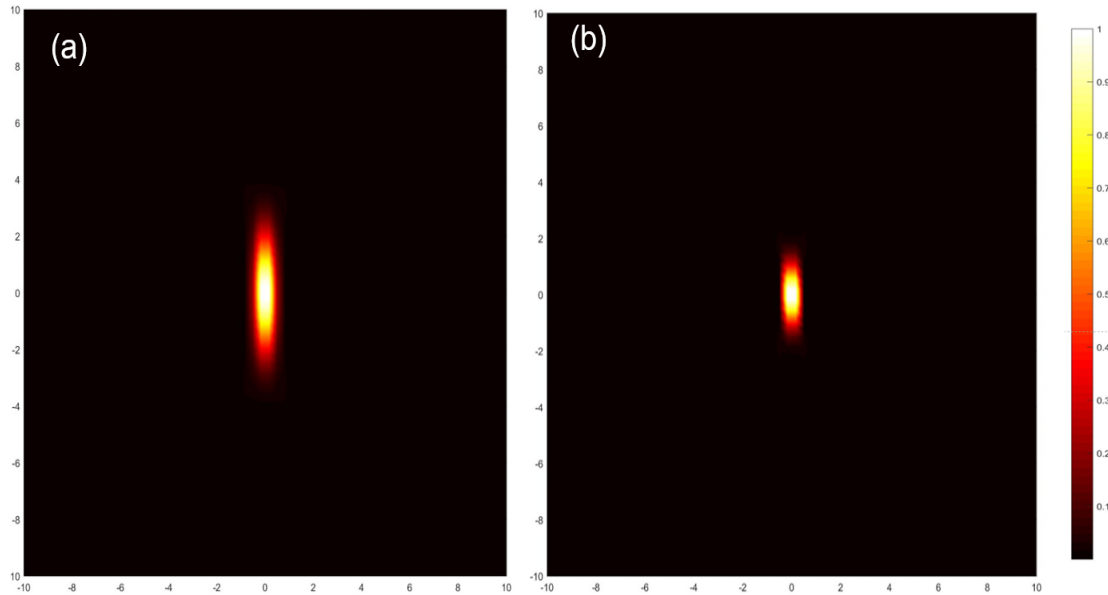


Figure 6-17- (a)The simulated intensity distribution along the axis of one-photon absorption.(b) The simulated intensity distribution along the axis based on two-photon absorption.

From the simulation results, we can see that the voxel resembles an ellipsoid since the lateral diameter is smaller than the axial length. The polymerized voxel is bounded at the focal volume in the TPA process, with a size much less than that of the one photon absorption process. The simulated lateral resolution and axial resolution for the TPA process are about 200nm and 1 μ m, respectively. While the axial resolution for one photon absorption process is about 3 μ m. Compared to 1PP lithography, 2PP lithography is clearly more suitable for 3D structure manufacturing. However, the current 2PP lithography write speed in terms of volume/min is very slow since it is based on point-by-point fabrication. To overcome this disadvantage, considerable research related to parallel 2PP fabrication configurations has been proposed, recently [89-91]. However,

for nearly all of these proposed configurations, an expensive ultra-short pulsed laser is essential. Through collaborating with our project partner at CNRS Lyon who are developing a new kind of resin, we have been able to propose a new type of parallel write 2PP photoplotter based on an imaged LCD-SLM with a continuous laser. Toward to the end of this PhD, I participated in the design of the illumination optical system for the new parallel 2PP arm of the hybrid lithographic machine. This contribution is described in the next section.

6.3.2 The experimental parallel 2PP photoplotter

The basic principle of the parallel 2PP photoplotter is similar to our current parallel 1PP photoplotter. The parallel 2PP photoplotter reshapes the illumination light beam to project 2D pattern or produces multiple focal spots to accelerate the writing speed. To the best of our knowledge, there are two mainstream strategies for building a parallel 2PP photoplotter (reconfigurable mask imaging and holographic projection). Example publications of parallelizing a 2PP photoplotter by imaging a 2D image onto the photoresist layer with a reconfigurable digital mask (such as DMD) can be found in [115]. References on building a parallel 2PP photoplotter based on holographic methods which are usually realized by a phase only SLM (PSLM) or DOEs can be found in [91].

Holographic methods project diffraction patterns into the photoresist through a hologram which is usually designed by IFTA. A PSLM is an active device which can be used to produce dynamic diffraction patterns. This enables the use of the same PSLM to fabricate complicated structures. However, a PSLM usually suffers from relatively low efficiency (the relatively big pixel size compared to fabricated DOEs leads to more high diffraction orders) and often generate a significant zeroth order and so require more complex techniques and more effort to increase pattern light intensity and block the zeroth order. Higher diffraction efficiency can be reached with a high quality fixed DOEs since we can use submicron pixel size to design the DOE and reduce the zeroth order through lithographic process optimization. As a DOE is a passive device which can only produce a fixed diffraction pattern for example spots array, it is mostly suitable for polymerizing periodic structures. Therefore, in our first configuration of the parallel 2PP photoplotter, a DOE was used to parallelize the light beam, as shown in **Figure 6-18**. (This work is being performed in the ongoing PhD of Luis Covarrubias. My contribution was mainly in the DOE design).

In this configuration, a pulsed laser is expanded to illuminate the whole area of the beam splitter DOE. Since the beam splitter DOE is placed at the rear aperture of the microscope objective, the diffraction pattern at the focal plane is the Fraunhofer diffraction pattern. Therefore, the beam splitter DOE can be designed easily using the IFTA method. In the very recent result shown in **Figure 6-19**, a 11×11 spots array in the photoresist was scanned to produce periodic 3D structures. The polymerized 3D structure is a basic unit of the type required for wavelength selective device which was demonstrated in Chapter 4. Due to lack of time, the complete wavelength selective device is not yet available at the time of writing this manuscript. This fabrication result

is an indication of the current continuing into the research the parallel 2PP photoplotter by the optics department of IMT Atlantique. It is hoped that new structures closer to those of Chapter 4 will be available by the time of the oral thesis defense.

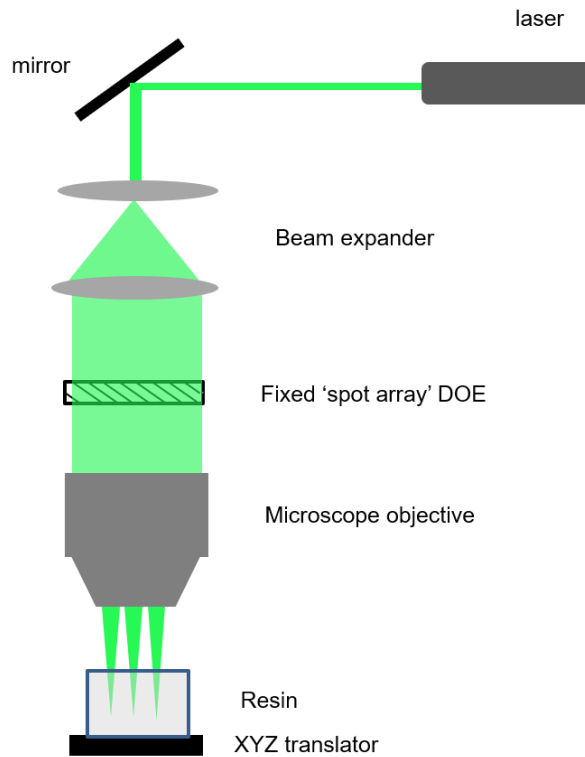


Figure 6-18- Schematic diagram of the parallel 2PP photoplotter based on a beam splitter DOEs.

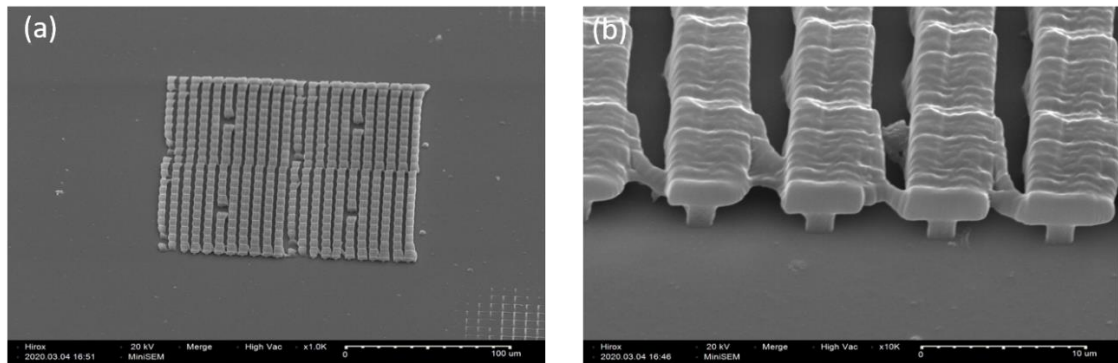


Figure 6-19- SEM images of a parallel 2PP fabricated “T” like 3D structure array. (a) Top view of the whole 3D array. (b) Side view of part of 3D structures, showing the individual 3D “T” structure.

This first configuration of the parallel 2PP photoplotter is highly efficient from the new point of view of energetic efficiency but is limited to the fabrication of periodic structures. To overcome this drawback and fabricate more complicated non-periodic 3D structures, we have developed a new optical system configuration using an LCD-SLM, where the LCD-SLM is used to modulate the light pattern. The pattern on the LCD-SLM is imaged into the photoresist via projection optics. In this updated configuration, a continuous green laser (MDL-SD-520, Changchun New Industries Optoelectronics

Tech) was used whose center wavelength is 520nm. The laser output power is 1.5W, delivered by a multimode fiber to homogenize the light beam. The output power can be controlled from the drive electronics as can the pulse triggers for TTL modulation to synchronize with the XY table position and the LCD-SLM. Unlike the LED source in the previous section, the divergence angle of the beam exiting the fiber is only 20 degrees. Therefore, an off-the-shelf optical component (AC127-019-B-ML) from Thorlabs can be used to collimate the light beam exiting the fiber. A diffuser is then used to further homogenize the light intensity distribution on the LCD-SLM. The diffusion angle of the diffuser in this configuration is 5.8×2.9 degrees to adapt the illumination pattern to the 16:9 rectangular of the SLM. For this method, there are two issues: 1) when we overlap the output pattern of the fiber output, they tend to be more light in the center; 2) Vignetting by the microscope objective reduces light intensity in the image corners. We compensate these effects by sending extra light to the SLM corner.

To do this, the DOE diffuser target pattern was modified, as shown in **Figure 6-20**. In the modified target pattern, the intensity near the edge is slightly higher than that in the center area. After the optimization with IFTA method, the binary diffuser was manufactured using the current 1PP photoplotter in our cleanroom. Through the characterization on the optical bench, the measured diffraction efficiency was about 72%.

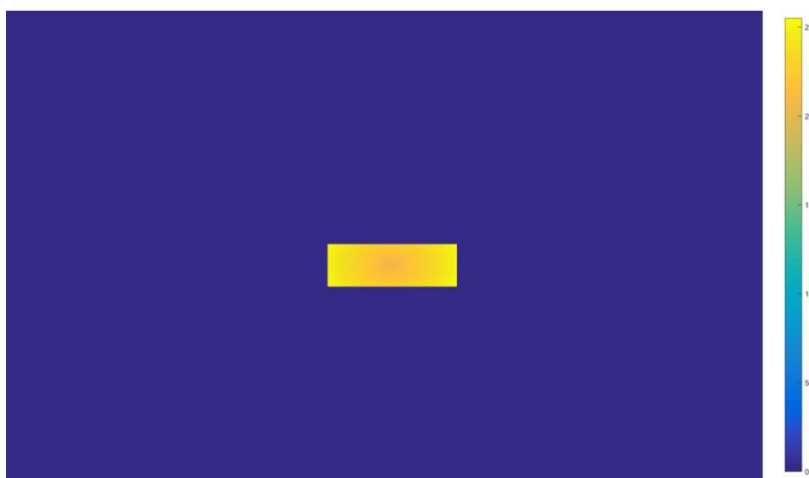


Figure 6-20-The DOE diffuser target pattern for parallel 2PP photoplotter illumination system.

Similar to the illumination system of 1PP photoplotter demonstrated in the previous section, a condenser lens (AC254-150-B-ML) was added to ensure more light diffracted by the pixelated structure of the LCD-SLM enters into the microscope objective. To optimize the design, the whole optical illumination system up to the microscope objective was modeled in ZEMAX software, as shown in **Figure 6-21**. The diffuser was modeled in ZEMAX software based on the diffuser diffraction angle data. The intensity distribution on the LCD-SLM with and without a diffuser is shown **Figure 6-22**. The illumination area is matched to the size of the LCD-SLM ($16\text{mm} \times 9\text{mm}$). The illumination uniformity is near to 90%.

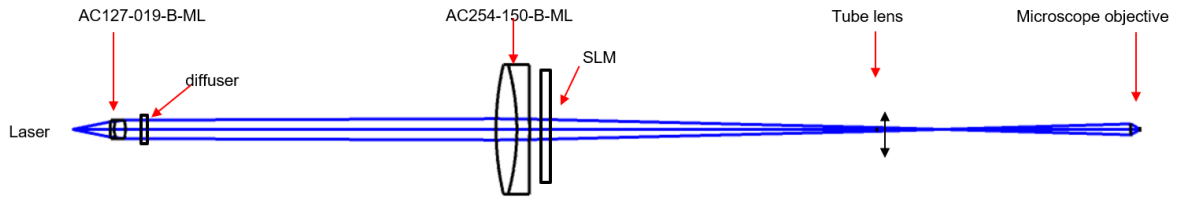


Figure 6-21- The optical system for parallel 2PP photoplotter.

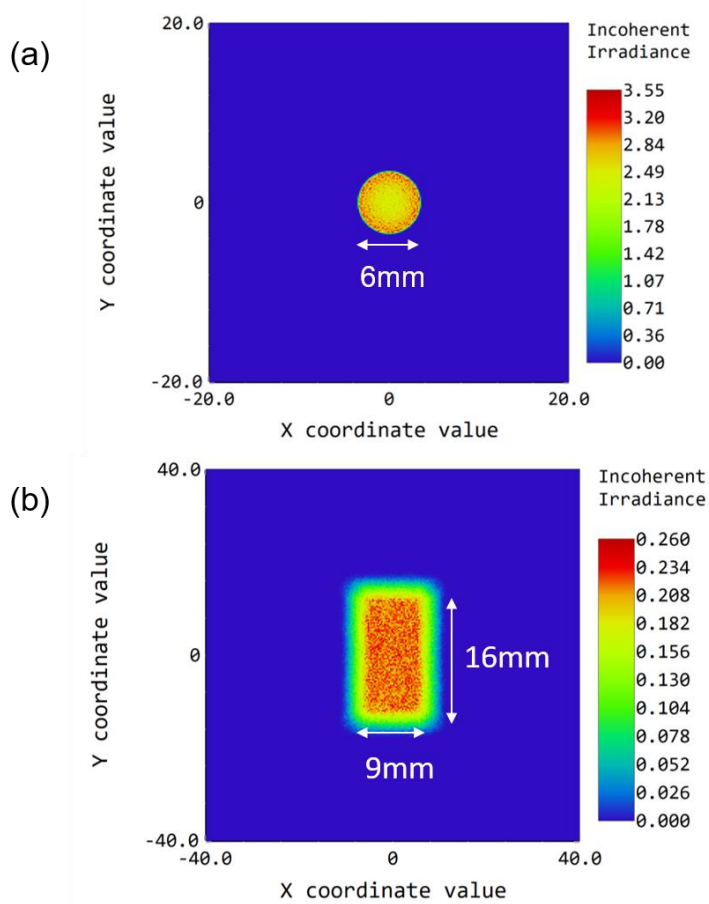


Figure 6-22- Zemax simulation of the illumination module intensity distribution in the SLM plane. (a) without a diffuser. (b) with the DOE diffuser.

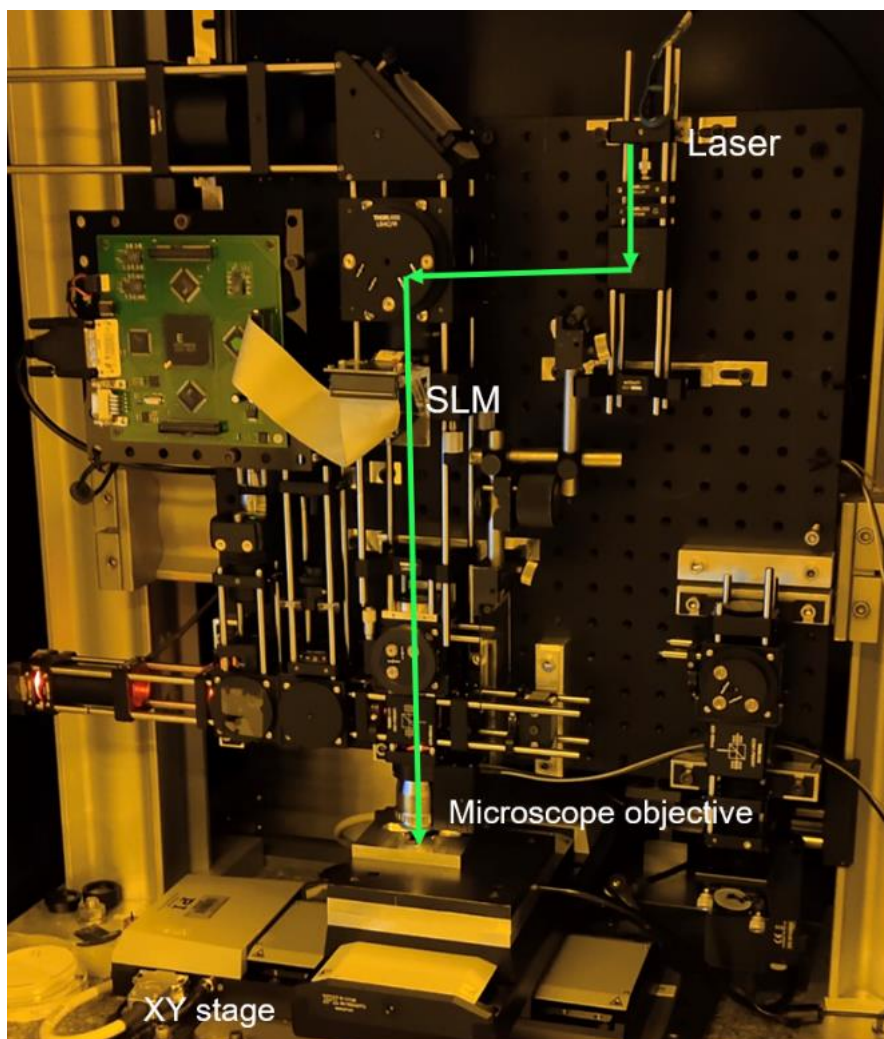


Figure 6-23- The photograph of the latest parallel 2PP photoplotter optical setup.

The designed illumination optics were then mounted in the parallel 2PP photoplotter. A photograph of the latest parallel 2PP photoplotter optical setup in our cleanroom can be found in **Figure 6-23**. The green line shows the light propagation from the fibred continuous wave laser. Specific software written by Quentin Carlier was used to control the laser, the XY-stage and their synchronization. Since the FOV of the polymerization area is small, the stitching technique is used to polymerize large area structures by moving the XY stage. To check the system alignment, illumination uniformity, and fabrication performance, a grid test pattern was loaded on the LCD-SLM and plotted into standard S1813 1PP photoresist. The fabrication results are shown in **Figure 6-24**.

From **Figure 6-24(a)**, the obtained pattern result is clearly not uniform, the light intensity around the center area is obviously stronger than that at the edge. When the homogenizing diffuser is used, the fabrication result is much more uniform, the smallest observable fabricated feature size is about 800nm.

However, when we zoom in on the fabrication result in **Figure 6-24 (b)**, a residual rugosity becomes visible. This appears to be due to laser speckle problems as shown in **Figure 6-25**. An effective way of reducing the laser speckles is to vibrate the fiber. Such a system has been acquired and is currently being investigated by the optics department

of IMT Atlantique.

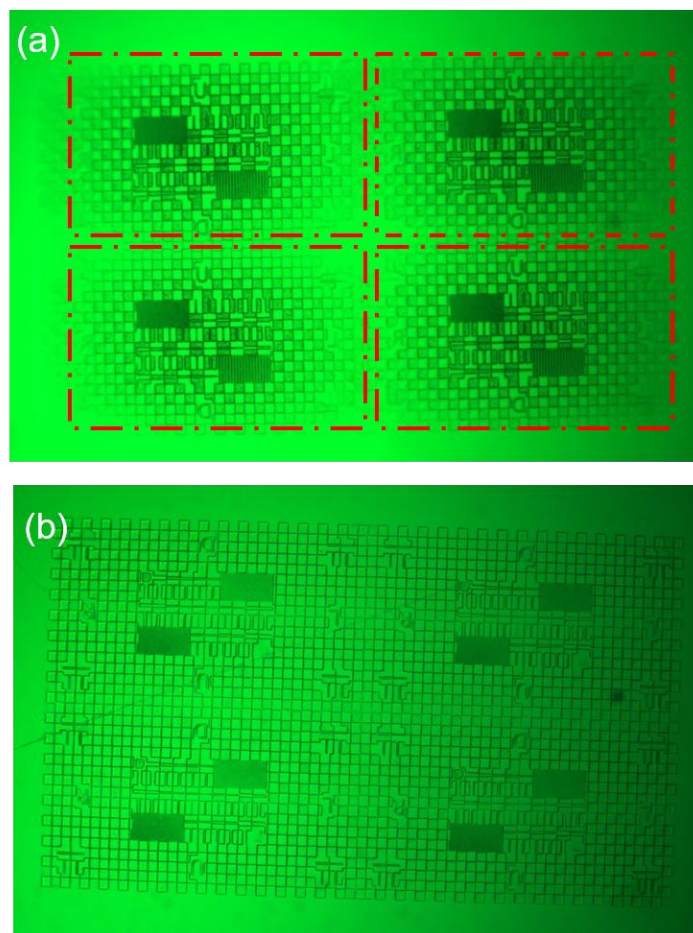


Figure 6-24- Microscope image of the fabricated grid pattern. (a) The fabricated grid pattern without a diffuser for homogenizing the LCD-SLM illumination (the step and repeated SLM patterns are visible). The red dotted line represents the contour of SLM. (b) The fabricated grid pattern with a diffuser for homogenizing the LCD-SLM illumination.

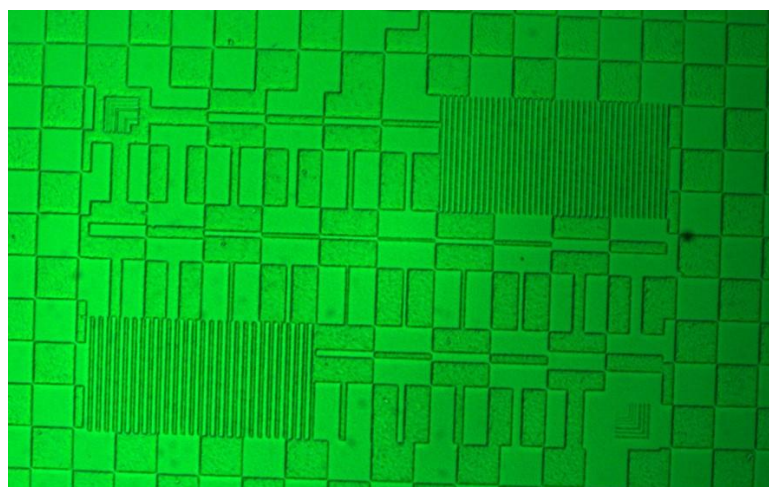


Figure 6-25- Partial microscope image of the written grid pattern.

6.4 Conclusion

In conclusion, in this chapter I have described my contribution to the design and experimental demonstration of three optical illumination systems for different types of parallel direct write photoplotters in our cleanroom. All these designs have significantly improved input illumination uniformity.

The first illumination system has already been integrated into our current “production” parallel direct write photoplotter in our cleanroom, which is now being successfully used to fabricate a wide variety of diffractive optical elements. All the designed DOEs in this thesis were manufactured using the updated photoplotter in our cleanroom.

The second illumination system design was for the more versatile 1PP/2PP parallel direct write photoplotter prototype currently being built in the Phenomenon EU project. The uniformity of the real lithographic fabrication results validates the excellent optical performance of the illumination optical system. But the fly in the ointment is the low optical efficiency which increases exposure time and decreases plot rate. This is because the illumination shape (circular) on the LCD-SLM is not matched to that of the LCD-SLM itself (rectangular). This leads to energy loss since the energy outside of the LCD-SLM is blocked. To address this problem, more sophisticated illumination optics are needed since a divergent LED source is used in this optical setup (alternatively an laser source could be used). The development of an upgraded illumination optics design for this 1PP arm of the hybrid lithography machine continues at the optics department in IMT Atlantique.

My third illumination system design was used for the parallel 2PP photoplotter based on a photochemical process which is totally different to the previous illumination systems. For realizing TPA, a high power laser is usually needed. Unlike the LED source, such laser source can produce strong laser speckle, which will damage the fabrication results. To overcome this drawback, in our illumination system design, we used a multimode fiber to reduce the laser source coherence. In addition, a DOE diffuser was used to homogenize the LCD-SLM, the DOE diffuser was successfully modeled in ZEMAX software to optimize the design before fabrication. The illumination optics were then assembled into the parallel photoplotter setup, and the comparative fabrication results verified the illumination optics design. The feature size is smaller than 800nm in the current parallel hybrid photoplotter using the 1PP approach and structures of about 500nm have been obtained in 2PP approach. A direct way to further improve the fabrication resolution is to use a higher NA microscope objective (for example NA=1.4). On the other hand, the manufactured sample at present is not totally uniform probably due to laser speckles. At the time of writing work continues to find an effective way of reducing the laser speckles to reach an acceptable level. This research shows further improve on the current parallel 2PP fabrication performance. It is that the 2PP performance hoped will soon reach the point where the highly innovative “Bragg” like wavelength selective structures designed in Chapter 4 can be fabricated directly.

Chapter 7 General Conclusion and Perspectives

In the general introduction to this thesis, we identified a number of limitations of both Diffractive Optical Element (DOE) design models/algorithms and DOE fabrication techniques which currently reduce DOE performance and restrict their applications. This allowed us to fix the main objectives of the thesis with a view to addressing these limitations and attempting to overcome or reduce them to improve on current DOE performance. After introducing, in chapter 2, the main DOE concepts, models, design algorithms and fabrication techniques to give an overview of the current state of the art in the field, we addressed the identified limitations systematically in the succeeding chapters.

Chapter 3 attacked the question of DOE illumination by developing new approaches, models and algorithms capable of designing DOEs for use with divergent, non-monochromatic and reduced coherence sources. Traditionally, most DOEs have been designed for, and used with, monochromatic, coherent laser light sources, which limit the scope of applications, particularly in visualization applications such as security holograms and 3D holographic display, because of eye safety and cost constraints. The ability to use DOEs with readily available and cheap LED sources would clearly be of major benefit in these applications. To work towards this goal, we developed four new design strategies for DOEs working with divergent incoherent illumination for visualization applications of 2D or 3D patterns such as security holograms and an automotive “virtual button”. The first approach was an extension of the basic IFTA algorithm to allow for illumination by a divergent, temporally incoherent but near monochromatic LED light source. This produced the desired output image but with a low overall system efficiency and computation load limitations on DOE size. The second approach used a novel, optimised faceted grating array DOE to overcome this size limitation. It also resulted in clearly visible output patterns that remained acceptable even when illuminated by a white LED as found on nearly all smartphones. The next approaches, aimed specifically at visualisation applications, attempted to produce virtual output images rather than images projected onto an observation screen. Based on a modified Fresnel IFTA, an initial approach was able to produce a perceived virtual 2D image when the DOE was illuminated by an LED source. By extending the approach to an innovatively optimised array of off-axis Fresnel DOEs it became

possible to produce a convincing visual perception of a 3D virtual object floating behind the DOE surface. Here also, computation load constraints limited DOE size to a few cm^2 so a final, spatial frequency multiplexing technique was developed which enabled the efficient design of large surface (tens of cm^2) DOEs producing the visual perception of a 3D virtual object floating close to the surface of a DOE illuminated with a divergent LED source. These design algorithms were all verified by fabricating real DOE samples (Chapter 5) and three of the techniques published, two in journals and one at an international conference.

Despite these advances, the algorithms and designed structures were still limited by a more fundamental restriction of nearly all current synthetic DOE design: conventional DOEs are usually surface relief structures (optically ‘thin’ structures). Such “thin” DOEs are mostly strongly limited in their usable wavelength range and diffraction efficiency, unlike optically “thick” structures which can use Bragg grating effects to increase, for instance, diffraction efficiency and spectral selectivity. Chapter 4 attempted to address this limitation through the development of a highly innovative algorithm for the design of synthetic 3D Bragg-like diffractive structures. The algorithm, based on a rigorous diffraction model with a swarm optimization algorithm, successfully designed novel 3D diffractive structures showing high spectral selectivity and diffraction efficiency performance. This research work was presented at the international Diffractive Optics conference held in Jena, Germany.

However, the fabrication of such fully 3D micro- and nano-structures is currently a serious challenge since the traditional fabrication techniques (mask and direct-write photolithography or e-beam lithography) are usually limited in practice to the fabrication of 2D or 2.5D structures. Two-photon polymerisation (2PP) is a feasible technology for fabricating such complex, high resolution 3D structures but, 2PP fabrication speeds and write volumes are currently severely limited by the sequential single laser beam approach. After presenting the present IMT Atlantique DOE facilities used to fabricate, characterise and experimentally validate the DOE designs of chapter 3, chapter 5 described current research into the development, by the IMT Atlantique and its project partners, of a new, massively parallelised 2PP photoplotter for the fast fabrication of large area/volume fully 3D photonic structures. My contribution to this project mainly centred on the design and assembly of the DOE based, high uniformity illumination modules for the new photoplotter. Recently obtained initial results show that very promising fully 3D structures can indeed be fabricated in parallel by the new photoplotter: the fabrication of the novel 3D structures designed in chapter 4 is clearly within reach.

The further development of this novel 2PP photoplotter is clearly one of the major perspective directions for the continuation of the work of this thesis. In particular laser speckles are still observed in some fabricated structures. Novel, speckle reducing homogenising DOEs and a system to vibrate the laser delivery fibre have been identified as promising solutions to minimise these speckle effects. Similarly, the use of higher NA microscope objectives – and adaptation of the illumination system to these objectives – will help decrease plot feature size.

On the modelling/algorithm side, although we successfully demonstrated DOE

generation of the visual perception of 3D object floating behind the DOE surface, perceiving a floating 3D virtual object in front of the synthetic hologram substrate remains a long-sought-after goal. The future work will focus on developing algorithms capable of producing the virtual object in front of the hologram. But it is becoming increasingly clear to us that this is as much a human perception problem as it is an optical design problem. A particularly interesting collaborative human perception/optical design appears to be the most appropriate future line of attack.

Appendix

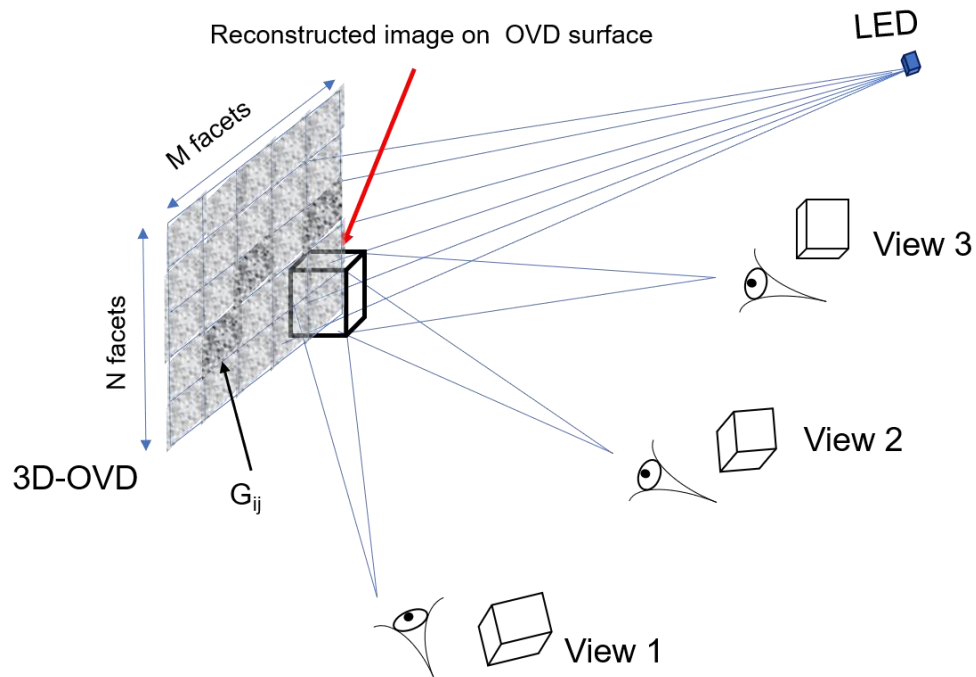


Figure A.1-Configuration of the 3D OVD.

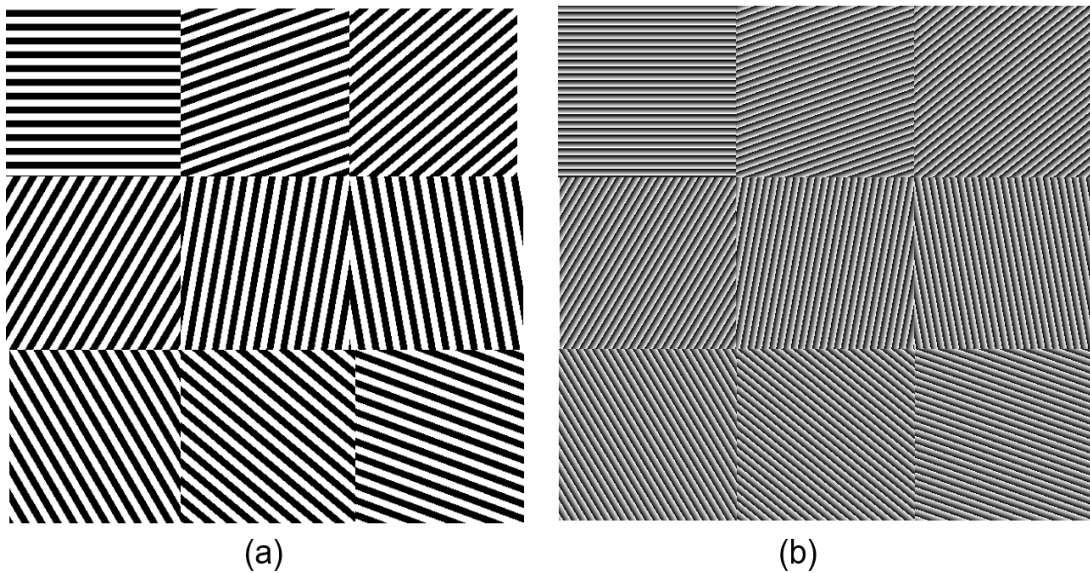


Figure A.2-(a) Binary gratings array in one facet. (b) Blazed gratings array in one facet.

The schematic of producing a 3D feature pattern (here is a “cube”) on the OVD surface is shown in Figure A.1. The configuration consists of a LED source and a 3D-OVD.

The 3D-OVD is a reflective DOE, hence the LED source is placed in front of the 3D-OVD. The overall 3D-OVD is separated into a matrix of individual gratings. M and N are the number of the facets in X and Y direction, which determine the resolution of the targeted 3D feature pattern. G_{ij} is a facet (or a “diffractive pixel”) which consist of binary gratings or blazed gratings (see Figure A.2). Binary gratings are easier here to fabricate but with low diffraction efficiency. Although blazed gratings are more difficult to fabricate, their diffraction efficiency is higher. In each facet, the orientation angle of these sub-gratings are different. Therefore, they can diffract the light into different directions. When an observer moves his eyes from side to side at the 3D-OVD plane they could perceive different views of the 3D “cube”. The overall effect is that of perceiving a 3D object on the surface of the 3D-OVD.

Bibliography

- [1] J. Turunen and Frank. Wyrowski, *Diffractive Optics: Industrial and Commercial Applications*. Akademie Verlag, 1997.
- [2] B. C. Kress and P. Meyrueis, *Applied Digital Optics: From Mirco-optics to Nanophotonics*, Chichester, UK: John Wiley & Sons, Ltd, Oct, 2009.
- [3] J.W. Goodman, *Introduction to Fourier Optics*, McGraw-Hill, 1996.
- [4] L.G. Neto, “Design, fabrication and characterization of a full complex-complicated modulation diffractive optical element,” *Journal of Micro/Nanolithography, MEMS, and MOEMS*, vol.2, p.96, 2003.
- [5] Alexander Goncharsky, Anton Goncharsky, and Svyatoslav Durlevich, “*Diffractive optical element for creating visual 3D images*,” *Opt. Express*, **24**(9), 9140-9148(2016).
- [6] G.-N. Nguyen, “Modeling, design and fabrication of diffractive optical elements based on nanostructures operating beyond the scalar paraxial domain”, PhD thesis., Télécom Bretagne ; Université de Bretagne Occidentale, 9 December. 2014.
- [7] Haichao Wang, Weirui, Yue, Qiang Song, Jingdan Liu, Guohai Situ, “A hybrid Gerchberg–Saxton-like algorithm for DOE and CGH calculation,” *Opt. Lasers Eng*, **89**, pp.109-115(2017).
- [8] Abbas Albarazanchi, Philippe Gérard, Pierre Ambs, Patrick Meyrueis, Giang-Nam Nguyen, and Kevin Heggarty, “Smart multifunction diffractive lens experimental validation for future PV cell applications,” *Optics Express*, **24**(2), A139-A145(2016).
- [9] Omri Barlev and Michael A. Golub, “Multifunctional binary diffractive optical elements for structured light projectors,” *Optics Express*, **26**(16), 21092-21107(2018).
- [10] Vladimir Oliker, “Optical design of freeform two-mirror beam-shaping systems,” *J. Opt. Soc. Am.* **24**(12), 3741-3752(2007).

-
- [11] Weitao Song, Dewen Cheng, Yue Liu, and Yongtian Wang, "Free-form illumination of a refractive surface using multiple-faceted refractors," *Appl. Opt.*, **54**(28), E1-E7(2015).
- [12] B. Gu, "Review - 40 years of laser-marking - industrial applications," *Proc. of SPIE*, **6106**, 61061(2006).
- [13] An. Firsov, A. Firsov, B. Loechel, A. Erko, A.Svintsov, and S.Zaitsev, "Fabrication of digital rainbow holograms and 3-D imaging using SEM based e-beam lithography," *Opt. Express*, **22**(23) 28756-28770(2014).
- [14] Alexander Goncharsky, Anton Goncharsky, and Svyatoslav Durlevich, "Diffractive optical element for creating visual 3D images," *Opt. Express*, **24**(9) 9140-9148(2016).
- [15] Alexander. Goncharsky, Anton. Goncharsky, and S. Durlevich, "Diffractive optical element with asymmetric microrelief for creating visual security features," *Opt. Express*, **23**(22), 29184–29192 (2015).
- [16] Kevin T.P. Lim, Hailong Li, Yejing Liu and Joel K.W. Yang, "Holographic colour prints for enhanced optical security by combined phase and amplitude control," *Nat. Commu*, 10, 25(2019).
- [17] Anton Goncharsky and Svyatoslav Durlevich, "Cylindrical computer-generated hologram for displaying 3D images," *Opt. Express*, **26**(17), 22160-22167(2018).
- [18] Qiang Song, Yoran Eli Pigeon, Kevin Heggarty, "Faceted Fresnel DOEs creating the perception of a floating 3D virtual object under divergent illumination," *Opt. Comm*, 451(15), 231-239(2019).
- [19] Rui Guo, Shizhou Xiao, Xiaomin Zhai, Jiawen Li, Andong Xia, and Wenhao Huang, "Micro lens fabrication by means of femtosecond two photon photopolymerization," *Opt. Express*, **14**(2), 810-16(2006).
- [20] Yanqin Chen, Xin Jin, and Qionghai Dai, "Distance measurement based on light field geometry and ray tracing," *Opt. Express*, **25**(1),59-76(2017).
- [21] K. S. Yee, "Numerical solution of initial boundary value problems involving Maxwell's equation in isotropic media," *IEEE Trans, Antennas and Propagation*, 302-307(1966)
- [22] M. G. Moharam, Eric B. Grann, Drew A.Pommet, and T.K.Gaylord, "Formation for stable and efficient implementation of the rigorous coupled-wave analysis of binary grating," *J.Opt.Soc.Am.A*, **12**(5),1068-10276(1995).

-
- [23] Lifeng Li, "Use of Fourier series in the analysis of discontinuous periodic structures," *J. Opt. Soc Am A*, **13**(9), 1870–1876(1996).
- [24] M. Born and E. Wolf, *Principles of Optics: Electromagnetic Theory Propagation, Interference and Diffraction of Light*. Cambridge University Press, 1999.
- [25] H. P. Herzig, *Micro-Optics: Elements, Systems And Applications*, CRC Press, 1997.
- [26] B. C. Kress and P. Meyrueis, *Digital Diffraction Optics: An Introduction to Planar Diffractive Optics and Related Technology*, vol.2000. Wiley, 2000.
- [27] F. Wyrowski, "Diffractive optical elements: iterative calculation of quantized, blazed phase structures," *Journal of the Optical Society of America A*, **7**(6), 961-969(1990).
- [28] R. Gerchberg and O. Saxton, "A practical algorithm for the determination of the phase from image and diffraction plane pictures," *Optik*, **35**(2), 237-246(1972).
- [29] F. Wyrowski and O. Bryngdahl, "Iterative Fourier-transform algorithm applied to computer holography," *Journal of the Optical Society of America A*, **5**(7), 1058-1065(1988)
- [30] Aamir Gulistan, M. M. Rahman, Souvik Ghosh, and B. M. A. Rahman, "Elimination of spurious modes in full-vectorial finite element method based acoustic modal solution," *Optics Express*, **27**(8), 10900-10911(2019).
- [31] M. G. Moharam, D.A. Pommet, E. B. Grann, and T. K. Gaylord, "Stable implementation of the rigorous coupled-wave analysis for surface-relief gratings: enhanced transmitted matrix approach," *Journal of the Optical Society of America A*, **12**(5), 1077-1086(1995).
- [32] K. Matsushima, H. Schimmel, and Frank. Wyrowski, "Fast calculation method for optical diffraction on tilted planes by use of the angular spectrum of plane waves," *Journal of the Optical Society of America A*, **20**(9) 1755-1762(2003).
- [33] T. Kozacki, "Numerical errors of diffraction computing using plane wave spectrum decomposition," *Optics communications*, **281**(17), 4219-4223(2008).
- [34] D. G. Voelz and M. C. Roggemann, "Digital simulation of scalar optical diffraction revisiting chirp function sampling criteria and consequences," *Applied Optics*, **48**(32), 6132-6142(2009).
- [35] K. Matsushima and T. Shimobaba, "Band-limited angular spectrum method for

-
- numerical simulation of free-space propagation in far and near fields,” *Optics Express*, **17**(22),19662-19673(2009).
- [36] G. C. Sherman, “Application of the Convolution Theorem to Rayleigh’s Integral Formulas,” *Journal of the Optical Society of America A*, **57**(4), 546-547(1967).
- [37] Peng Bao, Guohai Situ, Giancarlo Pedrini, and Wolfgang Osten, “Lensless phase microscopy using phase retrieval with multiple illumination wavelengths,” *Applied Optics*, **51**(22), 5486-5494(2012).
- [38] W. H. Southwell, “Validity of the Fresnel approximation in the near field,” *Journal of the Optical Society of America A*, **71**(1), 7-14(1981).
- [39] D. Mendlovic, Z. Zalevsky, and N. Konforti, “Computation considerations and fast algorithms for calculating the diffraction integral,” *Journal of Modern Optics*, **44**(2), 407-414(1997).
- [40] H. Kim, B. Yang, and B. Lee, “Iterative Fourier transform algorithm with regulation for the optimal design of diffractive optical elements,” *Journal of the Optical Society of America A*, **21**(12), 2353-2365(2004).
- [41] B. K. Jennison, J. P. Allebach, and D. W. Sweeney, “Efficient design of direct-binary-search computer-generated holograms,” *Journal of the Optical Society of America A*, **8**(4), 652-660(1991).
- [42] M. A. Seldowitz, J. P. Allebach, and D. W. Sweeney, “Synthesis of digital holograms by direct binary search,” *Applied Optics*, **26**(14), 2788-2798(1987).
- [43] Jörgen Bengtsson, “Kinoform design with an optimal-rotation-angle method,” *Applied Optics*, **33**(29), 6879-6884(1994).
- [44] Sourangsu Banerji, Berardi Sensale-Rodriguez, “A computational design framework for efficient, fabrication error-tolerant, planar THz diffractive optical elements,” *Scientific Reports*, **9**, article number:5801(2019).
- [45] Q. Song, H. Huang, X. Lv, J. Zhu, H. Huang, “An approach for generating the first order structure of multi-movable zoom lens,” *Optics Communications*, **359**(15), 399-404(2015).
- [46] Guangya Zhou, Yixin Chen, Zongguang Wang, and Hongwei Song, “Genetic local search algorithm for optimization design of diffractive optical elements,” *Applied Optics*, **38**(20), 4281-4290(1999).
- [47] Jean-Numa Gillet and Yunlong Sheng, “Multiplexed computer-generated

-
- holograms with polygonal-aperture layouts optimized by genetic algorithm,” *Applied Optics*, **42**(20), 4156-4165(2003).
- [48] Aleksandra B. Djurišić, Jovan M. Elazar, and Aleksandar D. Rakić, “Simulated-annealing-based genetic algorithm for modeling the optical constants of solids,” *Applied Optics*, **36**(28), 7097-7103(1997).
- [49] W. Yue, Q. Song, J. Liu, and G. Situ, “An iterative algorithm for computer-generated holograms calculation,” *Digital Holography and Three-Dimensional Imaging 2015*, Paper DW2A.8, Shanghai, China, 2015.
- [50] X. Lv, Q. Song, D. Li, Y. Qiao, J. Zhu, H. Huang, “Modified iterative algorithm for the design of wide-diffraction angle diffraction optical element,” *Optical engineering*, **54**(9),093106, 2015.
- [51] S. Teiwes, B. Schillinger, T. Beth, and F. Wyrowski, Efficient design of paraxial diffractive phase elements with descent search methods,” in Photonics West 95, pp.40-49, *International Society for Optics and Photonics*, Apr. 1995.
- [52] J. C. C. Mak, C. Sideris, J. Jeong, A. Hajimiri, J.K. S. Poon, “Binary particle swarm optimized 2×2 power splitters in a standard foundry silicon photonic platform,” *Optics Letter*, **41**(16), 3868-3871(2016).
- [53] Zhongtao Cheng, Jiamiao Yang, and Lihong V. Wang, “Intelligently optimized digital optical phase conjugation with particle swarm optimization,” *Optics Letter*, **45**(2), 431-434(2020).
- [54] S. S. Vaezi, S. Nikmehr, and A.Pourziad, “Nano-antenna synthesis for an arbitrary far-field radiation pattern and polarization based on vector spherical wave functions expansion,” *Applied Optics*, **59**(8), 2431-2442(2020).
- [55] H. Huang, T. Zhai, Q. Song, X. D. Yin, “Wide angle 2D beam splitter design based on vector diffraction theory,” *Optics Communications*, **434**(1), 28-35(2019).
- [56] Qiang Song, Yoran-Eli Pigeon, Xavier Theillier, Kevin, Heggarty, “An optimization approach of computer generated hologram(CGH) for divergent light shaping”, *Digital Holography and Three-Dimensional Imaging*, 19-23 May, Bordeaux France, 2019
- [57] Kevin Murphy, Vincent Toal, Izabela Naydenova, and Suzanne Martin, “Holographic beam-shaping diffractive diffusers fabricated by using controlled laser speckle,” *Optics Express*, **26**(7), 8916-8922(2018).
- [58] O. Ripoll, V. Kettunen, and H.P. Herzig, “Review of iterative Fourier-transform algorithms for beam shaping applications,” *Optical Engineering*, **43**(11), 1

November 2004.

- [59] <https://www.asml.com/en>
- [60] A. Selimis, V. Mironov, M. Farsari, “Direct laser writing: Principles and materials for scaffold 3D printing,” *Microelectronic Engineering*, **132**(25), 83-89(2015).
- [61] Yifang Chen, “Nanofabrication by electron beam lithography and its applications: A review,” *Microelectronic Engineering*, **135**(5), 57-72(2015).
- [62] Colin J. R. Sheppard and Zoltan Hegedus, “Resolution for off-axis illumination,” *Journal of the Optical Society of America A*, **15**(3), 622-624(1998).
- [63] V.V. Ivin, T. M. Makhviladze, K. A. Valiev, “Practical Aspects of Off-Axis Illumination in Optical Nanolithography,” *Russian Microelectronics*, **33**,209-219(2004).
- [64] Yijiang Chen, “Lithographic source and mask optimization with narrow-band level-set method,” *Optics Express*, **26**(8), 10065-10078(2018).
- [65] Yijiang Shen, Fei Peng, and Zhenrong Zhang, Semi-implicit level set formulation for lithographic source and mask optimization,” *Optics Express*, **27**(21), 29659-29668(2019).
- [66] Ningning Jia and Edmund Y. Lam, “Pixelated source mask optimization for process robustness in optical lithography,” *Optics Express*, **19**(20), 19384-19398(2011).
- [67] M. M. Kessels, M. El Bouz, R. Pagan, K. Heggarty, “Versatile stepper based maskless microlithography using a liquid crystal display for direct write of binary and multilevel microstructures,” *Journal of Micro/Nanolithography, MEMS and MOEMS*, **6**(3),033002 (2007).
- [68] G. N. Nguyen, K. Heggarty, A. Bacher, P.J. Jakobs, D. Häringer, P. Gérard, P. Pfeiffer, and P. Meyrueis, “Iterative scalar nonparaxial algorithm for the design of Fourier phase elements,” *Optics Letter*, **39**(19), 5551-5554(2014).
- [69] Y. Yang, Y. Yamagami, X. Yu, P. Pitchappa, J. Webber, B. Zhang, M. Fujita, T. Nagatsuma, and R. Singh, “ Terahertz topological photonics for on-chip communication,” *Nature Photonics*, **14**, 446-451 2020.
- [70] Qian. C, Zheng. B, Shen. Y, *et al.* “Deep-learning-enabled self-adaptive microwave cloak without human intervention,” *Nature Photonics* **14**, 383-390(2020).
- [71] Kwon, H, Arbabi. E, Kamali. S, *et al.* “Single-shot quantitative phase gradient

-
- microscopy using a system of multifunctional metasurfaces,” *Nature Photonics* **14**, 109–114 (2020).
- [72] Bekenstein. R, Pikovski. I, Pichler. H, *et al.* “Quantum metasurfaces with atom arrays,” *Nature Physics*. **16**, 676-681(2020).
- [73] Y. Hu, X. Luo, Y. Chen, Q. Liu, Xin Li, Y. Wang, N. Liu, H. Duan, “3D-Integrated metasurfaces for full-colour holography,” *Light Science & Applications*, **8**, article number:86(2019).
- [74] Y. Hu, L. Li, Y. Meng, *et.al*, “Trichromatic and Tripolarization-Channel Holography with Noninterleaved Dielectric Metasurface,” *Nano Letter*, **20**(2):994-1002(2019).
- [75] L. Li, T. Cui, W. Ji, S. Liu, *et.al*, “Electromagnetic reprogrammable coding-metasurface holograms,” *Nature Communications*, **8**, Article number: 197(2017).
- [76] G. Zheng, H. Muhlenbernd, M. Kenney, G. Li, T. Zentgraf, S. Zhuang, “Metasurface holograms reaching 80% efficiency,” *Nature nanotechnology*, **10**, 308-312(2015).
- [77] <https://heidelberg-instruments.com/en/products/dwl-66.html>
- [78] <https://www.raith.com/>
- [79] https://www.jeol.co.jp/en/products/list_ebx.html
- [80] <https://www.hitachi.com/>
- [81] V. Pavelyev, V. Osipov, D. Kachalov, B. Chichkov, “Diffractive optical elements with radial four-level microrelief fabricated by two-photon polymerization,” *Optics Communications*, 286(1), 368-371(2013).
- [82] Jesper Serbin, Aleksandr Ovsianikov, and Boris Chichkov, “Fabrication of woodpile structures by two-photon polymerization and investigation of their optical properties,” *Optics Express*, **12**(21), 5221-5228(2004).
- [83] Tommaso Baldacchini, Scott Snider, and Ruben Zadoyan, “Two-photon polymerization with variable repetition rate bursts of femtosecond laser pulses,” *Optics Express*, **20**(28), 29890-29899(2012).
- [84] Helmut Schiff; Robert Kirchner; Nachiappan Chidambaram; Mirco Altana, “Surface smoothing of the inherent roughness of micro-lenses fabricated with 2-photon lithograph,” *Proc. SPIE*, 10456(2018).

-
- [85] Shoji Maruo, Osamu Nakamura, and Satoshi Kawata, “Three-dimensional microfabrication with two-photon-absorbed photopolymerization,” *Optics Letter*, **22**(2),132-134(1997).
- [86] Z. Gan, Y.Cao, R.A. Evans, M. Gu, “ Three-dimensional deep sub-diffraction optical beam lithography with 9 nm feature size,” *Nature communications*, **4**, Article number:2061(2013).
- [87] D. Wu, Q. Chen, L. Niu, J. N. Wang, J. Wang, R. Wang, X. Hong, H.B. Sun, “Femtosecond laser rapid prototyping of nanoshells and suspending components towards microfluidic devices,” *Lab on a Chip*, **9**,2391-2394(2009).
- [88] D. Yang, S. H. Park, T. W. Lim, H. J. Kong, S. W. Yi, H. K. Yang, K. S. Lee, “ Ultraprecise microreproduction of a three-dimensional artistic sculpture by multipath scanning method in two-photon photopolymerization,” *Applied Physics Letter*, **90**, 079903(2007).
- [89] Lóránd Kelemen, Sándor Valkai, and Pál Ormos, “Parallel photopolymerisation with complex light patterns generated by diffractive optical elements,” *Optics Express*, **15**(22), 14488-14497(2007).
- [90] F. Hilbert, J. Wiedenmann, B. Stender, W. Mantei, R. Houbertz, “Impact of massive parallelization on two-photon absorption micro- and nanofabrication,” *Proc. SPIE 11271*, Laser 3D Manufacturing VII, 1127105(2 March 2020).
- [91] K. Obata, J. Koch, U. Hinze, B. Chichkov, “Multi-focus two-photon polymerization technique based on individually controlled phase modulation,” *Optics Express*, **18**(16), 17193-17200(2010).
- [92] J. H. Liu, J. B. Liu, Q. Y. Deng, J. H. Feng, S. L. Zhou, and S. Hu, “Intensity modulation based optical proximity optimization for the maskless lithography,” *Optics Express*, **28**(1), 548-557(2020).
- [93] X. Ma, X. J. Zhao, Z. Q. Wang, Y. Q. Li, S. J. Zhao, and L. Zhang, “Fast lithography aerial image calculation method based on machine learning,” *Applied Optics*, **56**(23), 6485-6495(2017).
- [94] F. Wyrowski, O. Bryngdahl, “Speckle-free reconstruction in digital holography,” *Journal of the Optical Society of America A*, **6**(8), 1171-1174(1989).
- [95] Qiang Song, Yoran Eli Pigeon, and Kevin Heggarty, “Faceted gratings for an optical security feature,” *Applied Optics*, **59**(4), 910-917(2020).

-
- [96] D. Asoubar, C. Hellmann, H. Schweitzer, M. Kuhn, and F. Wyrowski, "Customized homogenization and shaping of LED light by micro cells arrays," *Proc. SPIE* 9383, 93831B (2015).
- [97] S.L. Yeh, "Using random features of dot-matrix holograms for anticounterfeiting," *Applied Optics*, **45**(16), 3698-3703(2006).
- [98] <https://vtk.org/>
- [99] Yuanbo Deng, Daping Chu, "Coherence properties of different light sources and their effect on the image sharpness and speckle of holographic displays," *Scientific Report*, **7**, Article number: 5893(2017).
- [100] Hao Zhang, Liangcai Cao, and Guofan Jin, "Three-dimensional computer-generated hologram with Fourier domain segmentation," *Optics Express*, **27**(8), 11689-11697(2019).
- [101] X. Yang, H. Wang, Y. Li, F.Y. Xu, H.B. Zhang, J.H. Zhang, "Large scale and high resolution computer generated synthetic color rainbow hologram," *Journal of Optics*, **21**, 025601(2019).
- [102] K. T. P. Lim, H. L. Liu, Y. J. Liu, J. K. W. Yang, "Holographic colour prints for enhanced optical security by combined phase and amplitude control," *Nature Communications*, **10**, Article number: 25 (2019).
- [103] G. England, M. Kolle, P. Kim, M. Khan, et.al, " Bioinspired micrograting arrays mimicking the reverse color diffraction elements evolved by the butterfly pierella luna," *Proceedings of the National Academy of Sciences*, **111**(44), 15630-15634(2014).
- [104] N. N. Lal, K. N. Le, A. F. Thomson, M. Brauers, T. P. White, et. al, "Transparent Long-Pass Filter with Short Wavelength Scattering Based on Morpho Butterfly Nanostructures," *ACS photonics*, **4**(4), 741-745 (2017).
- [105] A. F. Kaplan, T. Xu, L. J. Guo, "High efficiency resonance-based spectrum filters with tunable transmission bandwidth fabricated using nanoimprint lithography," *Applied Physics Letters*, **99**, 143111(2011).
- [106] S. Kroker, T. Kasebier, F. Bruckner, et. al, "Reflective cavity couplers based on resonant waveguide gratings," *Optics Express*, **19** (17), 16466-16479(2011).
- [107] Herwig Kogelnik, "Coupled Wave Theory for Thick Hologram Gratings," *Bell System Technical Journal*, **48**(9), 2909-2947(1969).
- [108] <https://www.newport.com/f/calibrated-photodiode-sensors-918d>

-
- [109] D. Wu, N. Rajput, X.C. Luo, “Nanoimprint Lithography - the Past, the Present and the Future,” *Current Nanoscience*, **12**(6), 712-724(2016).
- [110] Thomas Hessler, Markus Rossi, Rino E. Kunz, Michael T. Gele, “ Analysis and optimization of fabrication of continuous-relief diffractive optical elements,” *Applied Optics*, **37**(19), 4069-4079(1998).
- [111] <http://www.phenomenonproject.eu/>
- [112] <https://www.zemax.com/>
- [113] Xiaoqin Zhou, Yihong Hou, Jieqiong Lin, “ A review on the process accuracy of two-photon polymerization,” *AIP Advances*, **5**, 030701(2015).
- [114] B. Richards and E. Wolf, “Electromagnetic diffraction in optical systems. II. Structure of the image field in an aplanatic system,” *Proc. R. Soc. Lond. A Math. Phys. Sci*, **253**(1274), 358–379 (1959).
- [115] B.Mills, M.Feinaeugle, C.L. Sones, N. Rizvi, R.W. Eason, “Sub-micron-scale femtosecond laser ablation using a digital micromirror device,” *Journal of Micromechanics and Microengineering*, **23**, 035005(2013).
- [116] <https://www.lighttrans.com/>
- [117] https://en.wikipedia.org/wiki/Rainbow_hologram
- [118] Detlef Leseberg, “Computer-generated three-dimensional image hologram,” *Applied Optics*, **31**(2), 223-229(1992).
- [119] Detlef Leseberg, “Sizable Fresnel-type hologram generated by computer,” *Journal of the Optical Society of America A*, **6**(2), 229-233(1989).
- [120] Detlef Leseberg, Christian Frere, “Computer-generated holograms of 3-D objects composed of tilted planar segments,” *Applied Optics*, **27**(14), 3020-3024(1988).
- [121] Shunsuke Igarashi, Tomoya Nakamura, Kyoji Matsushima, and Masahiro Yamaguchi, “Efficient tiled calculation of over-10-gigapixel holograms using ray-wavefront conversion,” *Optics Express*, **26**(8), 10773-10786(2018).

Titre : Conception de structures diffractantes synthétiques pour les applications de visualisation 3D et leur fabrication par un processus parallélisé, innovant de polymérisation à deux photons

Mots clés : éléments optiques diffractifs, hologramme de sécurité, polymérisation à deux photons

Résumé : Les éléments optiques diffractifs (EOD) sont maintenant largement utilisés dans les applications universitaires et industrielles grâce à leurs caractéristiques ultra-minces et compactes et à leur très flexible manipulation des fronts d'ondes lumineuses. Malgré ces excellentes propriétés, la portée d'application des EOD est souvent limitée par le fait que la plupart des DOE sont conçus pour générer uniquement des motifs projetés en 2D, et plus important encore, pour être utilisés uniquement avec des sources laser monochromatiques, cohérentes, souvent collimatées. Les contraintes de coût et de sécurité oculaire des sources laser limitent fortement les applications de visualisation des EOD telles que les hologrammes de sécurité, et la nature 2D des motifs générés limite les applications de réalité virtuelle ou augmentée. Pour surmonter ces restrictions, cette thèse vise la conception et la fabrication de structures diffractives 3D sélectives en longueur d'onde qui peuvent produire un objet 3D "flottant" perçu à plusieurs angles de vue derrière le substrat EOD lorsqu'il est éclairé par des sources LED blanches facilement disponibles et bon marché. Dans une première approche, nous développons et validons expérimentalement une série de nouveaux algorithmes de conception pour des structures EOD conventionnelles, optiquement "minces" sous un éclairage incohérent et divergent ; d'abord pour projeter des motifs 2D, puis pour créer des images 2D virtuelles et enfin des motifs 3D virtuels.

Dans un deuxième temps, nous exploitons les capacités des structures optiquement "épaisses" de type Bragg pour introduire une sélectivité spectrale (vers des modèles de sortie de couleur) et améliorer l'efficacité de la diffraction. Comme l'approximation des éléments minces n'est pas valable pour la conception de structures photoniques 3D optiquement épaisses, nous développons un algorithme d'optimisation des essais de particules basé sur un modèle de diffraction rigoureux pour concevoir des structures diffractives synthétiques optiquement épaisses très innovantes. La fabrication rentable de ces structures micro et nano-photoniques entièrement 3D proposées est très difficile lorsqu'on utilise les techniques lithographiques traditionnelles actuelles qui sont généralement limitées, en pratique, à la fabrication de structures 2D ou 2.5D. À cette fin, le département d'optique de l'IMT Atlantique met actuellement au point un prototype avancé de photoplotter de polymérisation à deux photons massivement parallélisés (2PP) pour la fabrication de structures photoniques entièrement tridimensionnelles de grande surface. Nous présentons nos contributions à la conception et au développement des modules d'illumination critiques et de haute uniformité pour le nouveau prototype de photoplotter 2PP. La recherche et le développement de cette thèse contribuent à l'élargissement des applications de l'EOD à des domaines actuellement inaccessibles. Les méthodes de conception développées peuvent également trouver des applications dans des domaines d'affichage holographique tels que la réalité augmentée automobile.

Title : Design of synthetic diffractive structures for synthetic 3D visualization applications and their fabrication by a novel parallel-write two-photon polymerization process

Keywords: diffractive optical elements, security hologram, two-photon polymerization

Abstract : Diffractive Optical Elements (DOEs) are now widely used in academic and industrial applications due to their ultra-thin, compact characteristics and their highly flexible manipulation of light wave-fronts. Despite these excellent properties, the scope of DOE applications is often limited by the fact that most DOEs are designed to generate only 2D projected patterns, and even more importantly, for use only with monochromatic, coherent, often collimated, laser sources. The cost and eye safety constraints of laser sources severely restrict DOE visualisation applications such as security holograms, and the 2D nature of the generated patterns limits virtual or augmented reality applications. To overcome these restrictions, this thesis targets the design and fabrication of wavelength selective 3D diffractive structures which can produce a perceived multiple view-angle "floating" 3D object behind the DOE substrate when illuminated by readily available and cheap white LED sources. In an initial approach we develop and experimentally validate a series of novel design algorithms for conventional optically "thin" DOE structures under incoherent, divergent illumination; first to project 2D patterns, then to create virtual 2D images and finally virtual 3D patterns. In a second stage, we leverage the capacities of optically "thick", Bragg-like structures to introduce spectral selectivity (towards colour output patterns) and improve diffraction

Since the thin element approximation is invalid when designing optically thick 3D photonic structures we develop a particle swarm optimization algorithm based on a rigorous diffraction model to design highly innovative optically thick synthetic diffractive structures. The cost-effective fabrication of such proposed fully 3D micro- and nano-photonics structures is highly challenging when using current traditional lithographic techniques which are generally limited, in practice, to the fabrication of 2D or 2.5D structures. To this end, an advanced prototype massively parallelized two-photon polymerization (2PP) photoplotter for the fabrication of large area fully 3D photonic structures is currently being developed by the IMT Atlantique Optics Department. We present our contributions to the design and development of the critical, high uniformity illumination modules for the new prototype 2PP photoplotter. The research and development in this thesis contributes to the broadening of DOE applications to fields which are currently inaccessible. The developed design methods can also find applications in holographic display fields such as automotive augmented reality.